UNIVERSITÀ
DEGLI STUDI
FIRENZE

PhD in
International Doctorate in Atomic and Molecular Photonics

CYCLE XXXIV

COORDINATOR Prof. Wiersma Diederik

Development and characterization of systems for optical wireless and visible light communication

Academic Discipline (SSD) FIS/03

Doctoral Candidate
Seminara Marco
MSeminara
(signature)

Supervisor
Dr. Catani Jacopo
JCatani

Coordinator
Prof. Wiersma Diederik

(signature)

Years 2018/2021

Università degli Studi di Firenze, European Laboratory for Non-Linear Spectroscopy (LENS).

Thesis submitted in partial fulfillment of the requirements for the degree of Doctor of Philosophy in Atomic and Molecular Photonics.

Abstract

This doctoral Thesis deals with several aspects of communication through visible and infrared light by exploiting and building on the expertise of our research group at LENS in the study and manipulation of light. Over the course of three years, the project has focused on the investigation and implementation of an optical wireless communication system in several application scenarios. A pivotal aspect is the use of appropriately modulated LED light sources, allowing for the realization of long-range (10–100 m) optical channels for the delivery of information over even shorter times than those achieved in radiofrequency transmissions. One of the key applications herein demonstrated is within the field of intelligent transportation systems: this contribution provides methods to increase vehicular safety, such as the real-time relaying of traffic information for quick response in critical road situations and platooning. Some original indoor applications are also proposed, including the first full optical characterization of a communication link exploiting the existing illumination system of a real museum to deliver dedicated information and services. Furthermore, efficient long-range transmission through free space is achieved using a mid-infrared laser source, whose behavior is modeled according to different possible extents of atmospheric absorption and scattering. Finally, we present a preliminary characterization of a new reception system consisting of an optical antenna coupled with a photodiode to overcome the étendue principle and achieve fast data transmission up to 100 m even under direct sunlight irradiation. In summary, this work shows the capabilities and potential of optical wireless communication, which is now almost mature for implementation in synergy with radiofrequency-based technologies to accomplish fast, reliable, and secure pervasive communication networks.

Contents

Acknowledgements

First of all, I would like to thank my patient supervisor, Dr. Jacopo Catani, for his support and encouragement; his experience has been precious in establishing the research questions and methods that eventually brought forth this Thesis. Your observant feedback has prompted me to refine my thought and taken my work to a higher level.

My heart-felt acknowledgements are due to Dr. Marco Meucci, Dr. Tassadaq Nawaz, and Mr. Ali Umair, who have helped, supported, and borne with me! With their aid, these three years of work have gone by smoothly indeed. I shall never forget the never-ending July days that we spent working together under the scorching sunlight.

Special thanks are extended to all the people who have taken part in this project, starting with Prof. Lorenzo Mucchi and Dr. Stefano Caputo, who have shared their knowledge of communication protocols, thereby allowing us to implement our entire work. I would like to acknowledge Prof. Francesco Saverio Cataliotti, Dr. Cristiano Riminesi, and Dr. Fabio Tarani for the help and support lent during the redaction of various publications.

My appreciation goes to our industrial partners ILES s.r.l. and Glass 2 Power s.p.a. and, in particular, to Eng. Lorenzo Tabani, Prof. Franco Meinardi, and Prof. Sergio Brovelli, for their helpful discussions, collaboration and assistance in providing advanced materials and instruments for our research.

Many thanks to all of LENS, who have provided the most advanced tools and staff and allowed me to improve myself over the last three years. A special acknowledgement goes to the “boys” of the electronics workshop (Alessio, Mauro, and Roberto) for their help and advice.

I acknowledge all of my co-workers with whom I have shared even a tiny bit of this experience, and particularly (I hope you won't mind me calling you all by name): Giammarco, Naomi, Francesco, Tecla, Nicola, Alessia, Maja, Giovanni, Andrea, Lorenzo, Daniele, Paolo, Joep, and anyone else I might have forgotten.

I am grateful to my family, who have been understanding and helpful during the difficult times that I have gone through; thank you in advance for those that are yet to come.

I am also grateful to my friends, whom I will not mention one by one because I fear I might forget some. Without your advice, I would certainly have failed to overcome such challenging times.

Finally, thank you Chantal. You have been at my side during my entire doctorate by listening, advising, supporting and encouraging me at all times. You have spurred me in the difficult times, laughed with me in the happy ones, cast away all my doubts and worries. Without you, I never would have had it in me to face this experience. I love you.

1. Introduction

1.1. Visible light communication

The use of light as a means to convey messages across large distances dates back to ancient times. The practice of communicating through fire and smoke signals is reported in the Bible [1], while the Greek and the Roman were probably the first to use mirrors to reflect and modulate sunlight: according to historians such as Tacitus, a complex system of mirror stations existed in Southern Italy, which could carry messages with this method across a distance of approximately 44 miles [2]. In the absence of sunlight, fire could serve as an appropriate light source. Fire beacons were also used in lighthouses to signal ships approaching ports; the most famous example from ancient eras is certainly the legendary *Pharos* of Alexandria [3]. More recently, Claude Chappe, a French clergyman, invented the first terrestrial semaphore-based telegraph in 1792: this consisted of a series of towers placed between 10 and 30 km apart, which allowed relaying messages over very large distances [4]. Soon after, in the early 1800s, the US military developed a solar telegraph, termed heliograph. This consisted of a simple mirror that could reflect sunlight beams in flashes following precise sequences according to the Morse code [5]. Similarly, signal lamps have been used for ship-to-ship communications based on the Morse alphabet for centuries [6]. In 1880, Alexander Graham Bell invented the photophone: this was based on a flexible plane mirror that vibrated when exposed to sound such as human voice, thereby modulating the reflection of light beams and practically enabling the wireless transmission of voice for the first time [7]. However, further development of optical communications was halted by Italian physicist and Nobel prize winner Guglielmo Marconi's invention of wireless telegraphy, a radio frequency (RF)-based transmission system, in the 1890s [8]. We need to wait until 1960 for the realization of the first He-Ne gas laser (an acronym for "light amplification by stimulated emission of radiation") by Theodore Maiman [9], which paved the way to the development of fiber optics beginning in 1970 [10]. In 1979, Gfeller and Bapst proposed the first wireless communications system based on infrared (IR) radiation, which was able to transmit data at high rates (hundreds of Mbps) in short-range indoor settings [11]. However, it was only in the early 2000s that a research group from Keio University in Japan saw the potential of light-emitting diodes (LEDs) to handle fast modulation and perform as a light source for indoor wireless communications, giving birth to the field of visible light communication (VLC) [12].

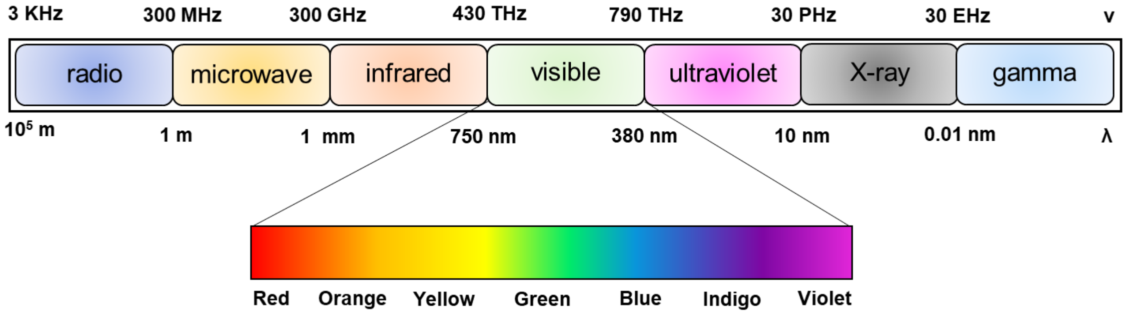

Figure 1-1. Schematic representation of the radiation spectrum highlighting the visible light region.

At present, optical wireless communication (OWC) technology is one of the best candidates for the implementation of modern data transfer networks. This covers the IR, visible, and ultraviolet (UV) portions of the light spectrum [13]. In particular, as shown in Figure 1-1, VLC exploits the range of frequencies from 430 to 790 THz, corresponding to the wavelength spectrum between 380 and 750 nm. This is a particularly promising technology for the present era owing to the increasing demand for high-capacity, ubiquitous connectivity by an exponentially growing number of mobile devices, which cannot be met by RF-based technologies owing to the limited RF spectrum. Moreover, RF communication (RFC) suffers from interference: for this reason, mobile phones are not allowed on aircrafts or in hospitals. Also, IR and high-power RF can pose a threat to human health [14]. Another advantage of VLC over RFC is represented by cost efficiency: VLC exploits the same LED lamps used for ambient illumination, saving the supplemental power required by additional communication equipment. Moreover, there is a significant difference in the cost of the devices: $1.7 for a 50 Mb/s VLC link compared to approximately $5 for a 1 Mb/s Bluetooth module [15]. Finally, visible light cannot penetrate solid objects such as building walls: because the light used for data transmission remains confined, it is less prone to being intercepted than radio waves, which allows for improved security and confidentiality of information [16]. The main advantages and disadvantages of the three technologies, RFC, IR communication (IRC), and VLC, are listed in Table 1-1.

Potential applications of VLC include [14]:

1. Implementation of light-fidelity (Li-Fi) networks for indoor data transfer (*e.g.*, in offices, museums, etc.);
2. Vehicle-to-vehicle (V2V) and infrastructure-to-vehicle (I2V) communication for intelligent transportation systems (ITSs);
3. Robots in hospitals;

4. Underwater communication;
5. Signboards;
6. ID systems.

Table 1-1. Comparison of RFC, IRC, and VLC technologies [15,17]. The advantages of VLC technology are evident: for example, light presents 400 THz of unlicensed spectrum and intrinsic safety characteristics owing to the directionality of communications.

Index	**RFC**	**IRC**	**VLC**
Available spectrum	~300 GHz (licensed)	~400 THz (unlicensed)	~400 THz (unlicensed)
Safety	Intensity regulated	Intensity regulated	Unregulated
Noise/Interference	Little	High	High
Security	Limited	High	High
Coverage	Wide	Limited	Limited
Multipath	High	Low	Low
System complexity	High	Low	Low
Electromagnetic interference	Yes	No	No
Infrastructure	Access point	Access point	Illumination
Power consumption for short-range links	Medium	Low	Low (combined with LED illumination)
Range	35−70 m indoor Up to 100 km outdoor, depending on cell type	10 m	100 m [18]
Data rate	Up to 7 Gb/s	~5 Gb/s [19]	Up to 35 Gb/s [20]

Nevertheless, VLC technology is not yet mature, and several challenges still need to be addressed for its development and implementation: these include the interference with ambient light sources and between VLC devices, as well as its integration with existing technologies [14], among others. Figure 1-2 provides a schematic representation of a typical VLC architecture.

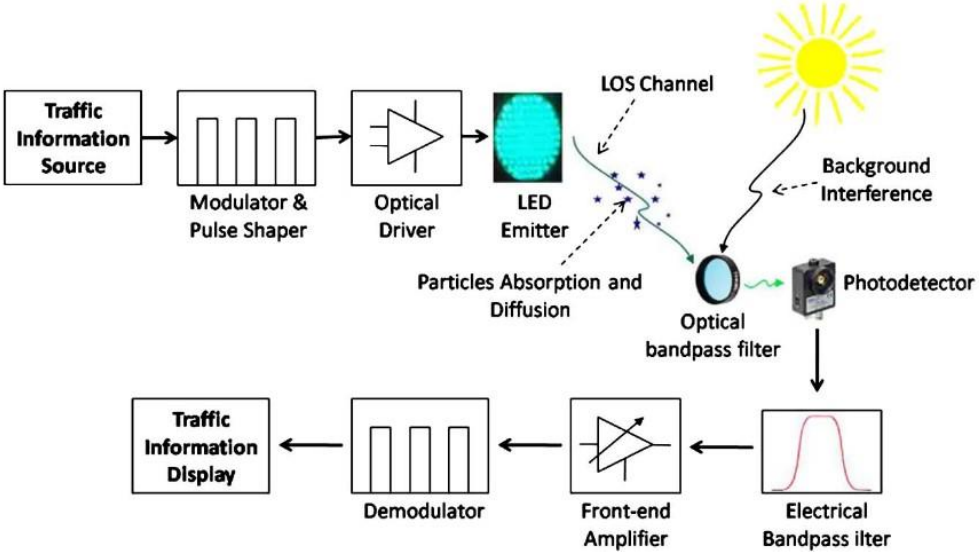

Figure 1-2. Example of VLC architecture: the source, a LED lamp, is modulated and travels across an optical channel, in which it can undergo absorption or scattering effects. The analog signal is eventually captured by a detector, digitized, and decoded. Reproduced from ref. [21].

1.2. Scope of this Thesis

This is the first doctoral Thesis at the European laboratory for non-linear spectroscopy (LENS) to report on the development of innovative systems for OWC. We have developed these systems by building on our ability to manipulate light, from both the time and space standpoints and at both the transmission and reception sides of the communication channels, and to deal with photonic materials as well as optoelectronic systems. During this three-year project, our interest was devoted to several topics:

1) vehicular communication, to solve critical road safety problems;
2) museum applications of VLC technology, where LED light sources can both illuminate and broadcast information concerning the exposed artworks;
3) the implementation of a mid-IR (MIR)-based system for long-range free-space optical communication (FSOC) applications;
4) the characterization of an optical antenna allowing for long-distance OWC.

All the systems presented herein are related by the study and characterization of commercial or novel light sources, such as LEDs and lasers; optical channels for transmission and reception; receivers based on various types of photodiodes (PDs) exhibiting high bandwidth (BW) and low noise; optical and optoelectronic systems for the transmission and reception of luminous signals. The scope of our project was to use semiconductor devices as both light sources and instruments for pervasive digital communications. The first step consisted in the study of advanced transmission and receiving systems based on the digital modulation of LED sources in the visible spectrum. One of the first tasks that were carried out during the first year consisted in prototyping and testing the printed circuit boards to feed the digital modulation into the LED source and the digitization of the received signal. These boards were coupled with two Arduino DUE platforms, used to encode messages into light sources and decode the received signals collected by an amplified photodetector.

Next, we worked at the characterization of the optical channel, realized with commercial sources in realistic environments, by evaluating the behavior of the system when equipping the receiving unit with different lenses. This was done by embedding a message in the light source and transmitting it at different baud rates (115 and 230 kbaud). The performance of our prototype was assessed through two parameters: the ratio between lost packets and total number of packets in the transmission, or packet error rate (PER), and the latency time, that is, the time interval elapsed between the first bit of the transmitted message and the last bit of the relayed message after a correct decoding process.

By the end of the first year, we started our research for new fluorescent materials for the development of a fluorescent concentrator. Such a tool is characterized by a high field of view (FoV), high gain, and high signal-to-noise ratio (SNR), allowing for the use of small-area detectors having high acceptance angles.

During the second year, the experimental work involved mainly field tests of our prototypes for vehicular and museum applications. This included a characterization of commercial motorcycle LED rear lights and headlights as well as museum spotlights. Through our collaboration with the VISIble light COmmunication REsearch group (VISICORE) and ILES srl, a private company that develops advanced traffic lights for VLC, we realized a one-directional communication channel based on a standard museum light as the transmitter and a digital active-decode (AD) unit as the receiver. Furthermore, a bi-directional communication system was developed using commercial vehicular rear lights and headlights as transmitters and a pair of digital active decode-and-relay (ADR) units as receivers.

During the third year, the work focused mainly on two topics. The first was the development of a communication system based on MIR radiation, obtained with a Quantum Cascade Laser (QCL) source, for which we evaluated the communication performance through the characterization of two distinct noise regimes. In the first, the system was limited by the detector noise, while in the second, by the source intensity noise. The other topic of interest was the study of an optical antenna developed by dispersing fluorescent quantum dots (QDs) in a plastic material provided by Glass to Power, a spin-off company of the Università di Milano Bicocca, with the scope of realizing an OWC system. For this, we evaluated the communication performances in outdoor environments and large distances (up to 100 m).

The present Thesis is organized as follows:

1) Chapter 1 introduces the context of the research;
2) Chapter 2 presents the theoretical background on OWC and VLC technologies;
3) Chapter 3 summarizes the characteristics and different architectures of the experimental setups used in this work;
4) Chapter 4 presents the results of the experiments aimed at the development and characterization of a VLC system for ITSs [22–28];
5) Chapter 5 presents the results of the experiments aimed at the development and characterization of a VLC system for museum environments [29,30];
6) Chapter 6 details our results on an FSOC system based on a QCL source emitting in the MIR region of the spectrum [31];
7) Chapter 7 reports our characterization of an optical antenna based on a fluorescent material for applications in long-distance OWC [18];
8) Chapter 8 draws the main conclusions;
9) Chapter 9 discusses the perspectives of the present work.

The articles published after the work outlined in this Thesis are listed in Table 1-2. After Chapter 9, the reader will find an extensive bibliography containing all the works referred to in this Thesis. Owing to the vastity of the topics discussed in this work, each Chapter will be introduced by a brief outline.

Table 1-2. Articles published after the work outlined in this Thesis.

Reference	Publication
[22]	T. Nawaz, M. Seminara, S. Caputo, L. Mucchi, F. S. Cataliotti and J. Catani, "IEEE 802.15.7-Compliant Ultra-Low Latency Relaying VLC System for Safety-Critical ITS," in IEEE Transactions on Vehicular Technology, vol. 68, no. 12, pp. 12040-12051, Dec. 2019, doi: 10.1109/TVT.2019.2948041.
[23]	F. Nizzi et al., "Data dissemination to vehicles using 5G and VLC for Smart Cities," 2019 AEIT International Annual Conference (AEIT), Florence, Italy, 2019, pp. 1-5, doi: 10.23919/AEIT.2019.8893380.
[24]	M. Seminara, T. Nawaz, S. Caputo, L. Mucchi and J. Catani, "Characterization of Field of View in Visible Light Communication Systems for Intelligent Transportation Systems," in IEEE Photonics Journal, vol. 12, no. 4, pp. 1-16, Aug. 2020, Art no. 7903816, doi: 10.1109/JPHOT.2020.3005620.
[25]	Nawaz, T.; Seminara, M.; Caputo, S.; Mucchi, L.; Catani, J. “Low-Latency VLC System with Fresnel Receiver for I2V ITS Applications.” *J. Sens. Actuator Netw.* **2020**, *9*, 35.
[26]	Marabissi, D.; Mucchi, L.; Caputo, S.; Nizzi, F.; Pecorella, T.; Fantacci, R.; Nawaz, T.; Seminara, M.; Catani, J. Experimental Measurements of a Joint 5G-VLC Communication for Future Vehicular Networks. *J. Sens. Actuator Netw.* **2020**, *9*, 32.
[28]	S. Caputo, L. Mucchi, F. Cataliotti, M. Seminara, T. Nawaz, J. Catani, “Measurement-based VLC channel characterization for I2V communications in a real urban scenario, Vehicular Communications”, 2020, 100305, ISSN 2214-2096.
[29]	Marco Seminara, Marco Meucci, Fabio Tarani, Cristiano Riminesi, and Jacopo Catani, "Characterization of a VLC system in real museum scenario using diffusive LED lighting of artworks," Photon. Res. 9, 548-557 (2021)
[27]	M. Meucci, M. Seminara, T. Nawaz, S. Caputo, L. Mucchi and J. Catani, "Bidirectional Vehicle-to-Vehicle Communication System Based on VLC: Outdoor Tests and Performance Analysis," in IEEE Transactions on Intelligent Transportation Systems, doi: 10.1109/TITS.2021.3104498.
[30]	Meucci, M.; Seminara, M.; Tarani, F.; Riminesi, C.; Catani, J. “Visible Light Communications through Diffusive Illumination of Sculptures in a Real Museum”. *J. Sens. Actuator Netw.* **2021**, *10*, 45.
[31]	(Submitted) Seminara M, Gabbrielli T. et al. “Mid-infrared free-space optical communication based on Quantum Cascade Lasers: experimental analysis of noise regimes”.
[18]	(Almost ready for submission) Umair et al. “Long-range, Mbit-class Optical Wireless Communication System based on a large-area, quantum-dot fluorescent antenna”.

2. Fundamentals of optical wireless and visible light communication

In this Chapter, we review some fundamental aspects of VLC. We begin with the Shannon–Hartley theorem, which quantifies the maximum channel capacity as a function of the SNR; we then move to an overview of light sources, receivers, communication standards, and encoding methods; finally, we provide a brief analysis of some VLC applications.

2.1. Shannon–Hartley theorem

In information theory, the Shannon–Hartley theorem establishes a quantitative link between the maximum transmissible data rate with the communication channel in the presence of additive white Gaussian noise (AWGN). The theorem establishes the maximum channel capacity for a communication link for which a certain amount of information can be transmitted without errors at a certain BW in the presence of AWGN.

Let us suppose a certain signal amplitude V. Its average signal power, P, is proportional to the square of the amplitude, V^2, and has a Gaussian distribution around the average value [32]. The AWGN, by definition, is summed to the average signal power, S, under the assumptions that:

1) the average noise amplitude is zero;
2) the noise power is finite, and its variance is N;
3) there is no correlation between the noise and input signal.

Therefore, we can write the channel capacity, C, as a form of entropy and express it in terms of bps. In this way, it can be maximized by finding an upper bound of mutual information equal to:

$$\mathrm{C_{bps}} = \mathrm{BW}\log_2(1+\mathrm{SNR}) \tag{2-1}$$

where BW and SNR are as defined in previous Paragraphs; one can observe that the maximum channel capacity increases for increasing BW and SNR of a system.

2.2. VLC transmitters: Light sources

The common incandescent lamps are being progressively replaced by LED lamps. These and laser diodes (LDs) are the main light sources used in VLC devices [33]. LEDs are solid-state semiconductor devices whose illumination properties originate from an effect known as electroluminescence.

Briefly, the semiconductor material is doped with impurities to create a p-n junction. Here, the charge carriers are electrons and holes (*i.e.*, atoms that lack electrons); when a voltage is applied, an electron meets a hole and falls to a lower energy level while emitting a photon [34]. LED lamps present many advantages compared with traditional means of illumination, such as higher luminous efficacy, better energy efficiency owing to lower heat generation, possibility of controlling the radiation intensity and spectrum, and longer lifetime [35].

The use of white light is common and preferable for indoor purposes. White light is typically obtained using red, green, and blue LEDs (RGB-LEDs) by mixing the three color components. Alternatively, phosphor-converted LEDs (pc-LEDs) can be used, which have the advantages of being less expensive and complex. Traditionally, these devices emit white light by employing a single blue indium-gallium nitride (InGaN) chip coupled with an yttrium-aluminum garnet (YAG) phosphor coating. The latter converts part of the blue light to green, yellow, and red: the mixture of these colors gives rise to white light, which can be categorized as warm-white or cool-white depending on the amount of blue light that is leaked [36]. The disadvantage of pc-LEDs is that, when the blue photon crosses the yellow phosphor, the penetration power and frequency modulation bandwidth (BW) are reduced, which in turn limits the SNR and the transmission capacity of VLC systems [37,38]. However, it should be noticed that the capacitance and area of the blue light are larger, making this the most suitable region of the spectrum for communication applications [15]. The achievable data rate with this type of LEDs is approximately 1 Gb/s [39,40]. While with the RGB -LEDs the obtainable data rate is higher than that of phosphor LEDs and can reach several Gb/s [39,41]. A comparison between the emission spectra of pc- and RGB-LEDs is presented in Figure 2-1. However, traditional LEDs are limited by the photons emitted spontaneously from the active region when stimulated by photons. New types of LEDs, such as resonant cavity LEDs (rc-LEDs) and micro-LEDs (μ-LEDs), have been proposed to overcome this issue owing to their high internal quantum efficiency, light extraction rate, and variable modulation BW [33]. μ-LEDs are miniaturized GaN-based LED arrays, currently employed in flat-panel displays where each diode constitutes a single pixel [42]. Recent research has focused on their use in VLC applications [43]. The allowed data rate is high (~10 Gb/s in OWC). One more type of LED is represented by Organic-LEDs (OLEDs), which consist of several high-reflective-index layers sandwiched between a low-refractive index substrate and a reflective metal electrode. OLEDs exhibit less advantageous properties for high-speed applications (low frequency response, shorter lifetime) and are used mainly for optical displays in consumer electronics [44]. The other type of source used in VLC systems is represented by LDs, characterized by a high coherence, narrow spectral linewidth, and large modulation BW. The analysis and study of the LED modulation characteristics is fundamental to improve their performances. The analog modulation band of an LED is defined as the frequency at which the alternate current (AC) of the LED is reduced by a factor −3 dB compared to a reference value. As a consequence, because the photoelectric response of white LEDs is slow [45], the modulation band is limited to a few MHz, which in turn reduces the data rate of the entire system. Only the use of various modulation schemes (see Section 2.5.) allows for the enhancement of the white LEDs channel capacity. The main characteristics of the light sources described in this Section are summarized in Table 2-1.

Table 2-1. Comparison of different types of LEDs and LDs. Reproduced from ref. *[33]*.

Parameter	**pc-LED**	**RGB LED**	**μ-LED**	**OLED**	**LDs**
Bandwidth	~5 MHz	10−20 MHz	< 1.5 GHz	≤ 1 MHz	10–20 GHz
Power	> 1 W	> 1 W	~μW	> 1 W	> 1 W
Cost	Low	High	High	Lowest	High
Complexity	Low	Moderate	Highest	High	High
Application	Illumination	Illumination	Biosensors	Display	Pointing

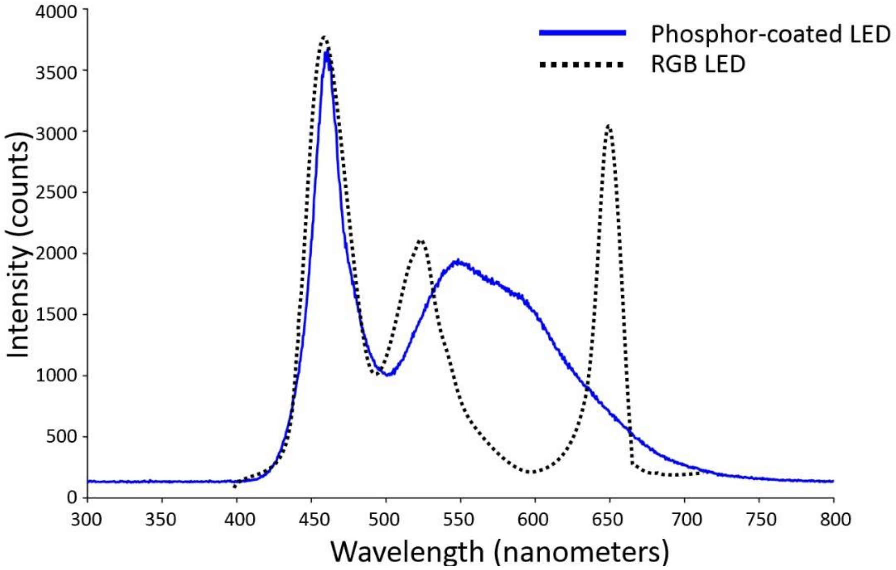

Figure 2-1. Comparison between the emission spectra of a yellow pc-LED and RGB-LED. Reproduced from ref. [35].

An important property of LED transmitters is their luminous flux, which is a crucial design parameter for both illumination and communication technologies. For the evaluation of luminous flux, it is necessary to take into account the luminosity function V(λ), which reflects the ability of the human eye to distinguish different colors with different sensitivities, and the spectral power distribution $S_T(\lambda)$, which represents the power of the LED at all wavelengths in the visible light spectrum [46]. Thus, the luminous flux F_T, measured in lumens, is given by [47]:

$$F_T = 683 \int_{380\ \mathrm{nm}}^{750\ \mathrm{nm}} S_T(\lambda) V(\lambda) d\lambda \tag{2-2}$$

where 683 (lumen/watt) is the maximum luminous efficiency, a measure of the conversion of electricity into visible light. This value corresponds to the wavelength of 555 nm, to which the human eye is most sensitive [48].

Alternatively, the luminous flux can be derived from an LED's spatial emission properties:

- Luminous intensity, $g_t(\theta)$, which measures the LED's brightness in a specific direction;
- Axial intensity (I_0), defined as the luminous intensity at a 0° solid angle;
- Half beam angle (θ_{max}), or the angle at which the light intensity decreases to half of the axial intensity.

Therefore,

$$F_T = I_0 \int_0^{\theta_{max}} 2\pi\, g_t(\theta) \sin\theta \, d\theta \tag{2-3}$$

Path loss, that is, the decline in power density owing to light propagation is also a pivotal property to be taken into account in the design of VLC systems. In line-of-sight (LoS, meaning that the transmitter and receiver are in view of each other) free-space propagation, this is assumed to be independent of the wavelength and calculated as the ratio of luminous flux of the receiver ($F_R = I_0\, g_t(\beta)\, \Omega_r$, where β is the irradiation angle and Ω_r the receiver solid angle as observed from the transmitter) and that of the transmitter (F_T):

$$L_L = \frac{F_R}{F_T} = \frac{g_t(\beta)\, A_r \cos\alpha}{D^2 \int_0^{\theta_{max}} 2\pi\, g_t(\theta) \sin\theta \, d\theta} \tag{2-4}$$

where D is the distance between the transmitter and receiver, r is the radius of the receiver aperture, α is the incident angle, and A_r is the area of the receiver.

2.3. Receivers

One type of receivers employed in VLC is represented by PDs, semiconductor devices based on a p-n junction that converts the received light into current. A photon hitting the diode with sufficient energy creates, according to the photoelectric effect, an electron-hole pair. Holes tend to move toward the anode, while electrons move toward the cathode, generating a photocurrent. The total current of the PD at a certain voltage V is given by the sum of the diode current (Shockley's law) and the inverse current I_{ph}, photo-generated in the depletion region and proportional to illuminance:

$$\mathrm{I} = \mathrm{I_S}\left(e^{\mathrm{qV_D/nkT}} - 1\right) \tag{2-5}$$

where I_s is the saturation current, q the charge of an electron, V_D the potential difference between the PD terminals, n is the ideality factor, k is the Boltzmann constant, and T the temperature expressed in Kelvin. PDs can work in two regimes: photovoltaic and photoconductive. In the latter, a PD delivers a current proportional to the optical power, and the current at the terminals is negative, that is, the diode is counterpolarized. An advantage for communication applications is represented by the increased BW. Indeed, because of the inverse polarization, the PD's rate increases for two reasons: the first is that, through an increase in the depletion region of the p-n junction, the capacity of the junction decreases, leading to a decrease in the time constant RC; the second is the increase in the value of the electric field at the extremities of the junction, which decreases the transit time of the charges. The disadvantage of working in the photoconductive regime is that the photocurrent is summed to the dark current [49].

Two types of PD are the most commonly used in VLC applications and they can work in photoconductive mode [50]:

- PIN PDs, where the "i" in "PIN" stands for an "intrinsic" semiconductor region sandwiched between the usual p and n regions. These have been used predominantly in VLC owing to their speed and low cost;
- Avalanche PDs (APD), whose structure is optimized to operate near the reverse breakdown voltage. They have the advantage of a higher gain and the downside of excess shot noise

generated by the higher photocurrent. They are characterized by a low noise and high sensitivity, but they are prone to saturation in the presence of ambient light and more difficult to be used.

PDs are fabricated with different materials, the most common ones for VLC applications being silicon (having a spectral responsivity in the 200–1100 nm range), InGaAs (800–2000 nm), and germanium (400–1700 nm), despite being very expensive. In particular, silicon PDs have a larger bandgap and generate a lower noise compared to germanium ones. These PDs cannot be used in high-interference scenarios (for example, an external environment exposed to sunlight), unless complex decoupling systems are used to split the AC signal from the DC interference [28].

The abovementioned spectral responsivity is the ratio of the generated photocurrent I and the incident power P for a monochromatic source (otherwise P should be replaced by the integral of the power over all wavelengths), which depends on the wavelength:

$$\mathrm{Responsivity}\ (\lambda) = \frac{\mathrm{I}}{\mathrm{P}} \tag{2-6}$$

In addition to this, other properties of the PDs used in photoconductive regime are:

- dark current, or the current generated by the PD in the absence of light;
- response time, t_r, or the time required by the detector to respond to a luminous signal;
- BW of the detector, determined by t_r and given by:

$$\mathrm{BW} \approx \frac{0.35}{\mathrm{t_r}} \tag{2-7}$$

One parameter limiting the BW is the electronic impedance of the detector circuit, also known as RC parasitic response and equal to $1/(2\pi RC)$, where R is the impedance and C the capacity of the PD. As a consequence, since C scales with area, fast detectors will be characterized by a small area.

The received optical power P_{RO} depends on the transmitter-receiver distance (D), the incident angle (α), and the irradiation angle (β) as shown in Figure 2-2. P_{RO} for a direct LoS optical link can be calculated using the path loss, L_L.

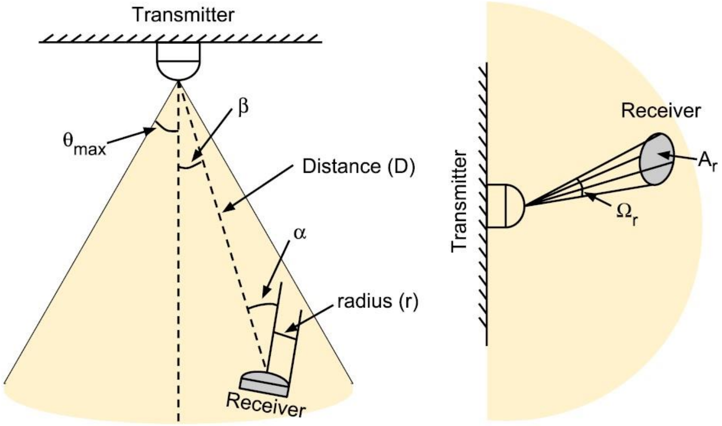

Figure 2-2. Relative position of transmitter and receiver in LoS settings. The transmitter emits a luminous signal toward the receiver, placed at a distance *D*, with an incidence angle α and irradiance angle β. Reproduced from ref. [51].

In the typical case of a receiving detector equipped with an optical filter, we have [47]:

$$P_{RO} = \int_{\lambda_{rL}}^{\lambda_{rH}} S_R(\lambda)\ R_f(\lambda)\ d\lambda \tag{2-8}$$

where $S_R(\lambda) = L_L S_T(\lambda)$; λrL and λrH are, respectively, the lower and upper wavelength cut-off values for the optical filter; and $R_f(\lambda)$ is the spectral response of the optical filter.

In indoor applications, the contribution of non-LoS (NLoS) radiation must be taken into account because most indoor surfaces (such as walls and ceilings) are more or less reflective. NLoS signals can be bounced from several surfaces in a complex multipath fashion before reaching the receiver. In such scenarios, the spectral reflectance is taken in consideration, which represents the reflectivity of a surface as a function of wavelength, and light propagation can be modeled using a power delay profile (PDP) [52] (see Chapter 5).

Moreover, receivers can be affected by noise occurring from three major sources [47]:

- *Ambient light noise:* solar radiation (from windows, doors, *etc.*) and light from other illumination sources (incandescent and fluorescent lamps); it can be mitigated using a high-pass filter.
- *Shot noise,* σ_{shot}: inherent statistical fluctuation in the amount of photons collected by the PD. It follows a Poisson statistics; therefore, the shot noise amplitude increases as the square root

of the number of absorbed photons or generated charges. Such a random fluctuation of the electrical current generates a DC. The spectral noise density is 2eI, where e is the electric charge and I the average current of the electron flux; as a result, the shot noise is often negligible compared to the thermal noise.

- *Thermal noise or Johnson-Nyquist noise, $\sigma_{thermal}$:* originating from the electronic stage PD pre-amplifier. This type of noise is produced by the thermal agitation of the charge carriers. The noise power is kT · BW, where k is the Boltzmann constant, T the temperature in Kelvin, and BW the bandwidth [53].

Once the first type of noise is filtered, the SNR at the receiver is given by:

$$\mathrm{SNR} = \frac{\mathrm{P_R^2}}{(\sigma_{\mathrm{shot}})^2 + (\sigma_{\mathrm{thermal}})^2} \tag{2-9}$$

where σ_{shot} and $\sigma_{\mathrm{thermal}}$ are the standard deviations of the shot noise and thermal noise, respectively [54]. The contribution of σ_{shot} cannot be eliminated, as it a result of statistics fluctuations~~; however, at room temperature, it is usually negligible compared to $\sigma_{\mathrm{thermal}}$~~.

In summary, we can list the ideal characteristics of receivers for VLC systems [33]:

- the wavelength of the photons emitted by the LED should be within the receiver responsivity and sufficiently high to ensure the highest possible photocurrent;
- a fast response, allowing for a high-speed system;
- the noise level should be as low as possible, thereby reducing its impact on the SNR.

The photodetectors typically used for optical communication are APDs and PINs. For example, a silicon APD has recently allowed to establish a 2 Gbps communication using an On-Off modulation [55]. New types of detectors, such as µ-photodetectors, have been used as optical receivers in an orthogonal frequency-division multiplexing (OFDM)-modulated VLC system, achieving high data rates (3.2 Gbps) [56].

2.4. Standardization

A standardization of VLC technology is pivotal to address some current challenges and ensure smooth operations, including the integration with already existing communication standards (such as Wi-Fi) and avoiding interference with ambient light sources as well as between different devices [14]. The earliest efforts toward standardization have started in Japan thanks to the Japan Electronics and Information Technology Industries Association (JEITA), which released the JEITA standards

CP-1221 and CP-1222; then, in 2009, the VLC Consortium and Infrared Data Association (IrDA) published IrDA-like standards [17]. In 2011, a comprehensive 802.15.7 VLC standard was approved by IEEE, which was recently updated in 2018 [57]. At present, this standard provides six operating modes [58]:

- *PHY I:* uses OOK and VPPM modulation schemes. Data rates can reach up to 266 kbps. Used for high-current, low-BW outdoor devices (*e.g.*, traffic lights);
- *PHY II:* uses OOK and VPPM. Data rates can reach up to 96 Mb/s. Used for indoor applications, mobile devices, high-BW displays, and low-power transmitters;
- *PHY III:* uses CSK modulation for multi-chip LEDs. Data rates can reach up to 96 Mbps;
- *PHY IV*: this PHY is intended for use with discrete light sources with data rates up to 22 kbps using various modulations;
- *PHY V*: this PHY is intended for use with diffused surface light sources with data rates up to 5.71 kbps using various modulations;
- *PHY VI*: this PHY is intended for use with video displays with data rates in kbps using various modulations.

The system also supports flicker mitigation, dimming, and multi-access topologies;

2.5. Modulation

In VLC, information is transmitted by modulating the current signals used to switch LEDs at desired frequencies. This is achieved by methods that are common to IRC [59].

Owing to the low BW of most LEDs, complex modulation schemes offer the opportunity of high-speed data transmission. Because the LEDs used in VLC are most often also sources of ambient illumination, any modulation scheme should meet some key requirements about perceived light. For example, people commonly necessitate different levels of illuminance depending on environments and activities. Owing to the advancements in driver circuits, LEDs can be dimmed to save energy and meet specific illuminance requirements. However, it should be noticed that the relation between measured and perceived light is non-linear and is given by [60]:

$$Perceived\ light(\%) = 100 \times \sqrt{\frac{Measured\ light(\%)}{100}} \tag{2-10}$$

Therefore, a lamp that is dimmed by 1% of its measured light is perceived to be 10% dimmed by the human eye. The importance of such a phenomenon for VLC architecture is that the level of dimming chosen by users should not affect the communication, *i.e.*, data modulation must support any desired dimming level. Furthermore, VLC modulation schemes can suffer from a phenomenon termed "flickering," meaning that the fluctuations in the brightness of the light may be perceived by the human eye. Because the exposure to flickering light has been shown to have harmful effects on human health (for example, it can be dangerous for people suffering from epilepsy) [61], any change in light intensity should occur at a rate faster than that perceived by the eye, *i.e.*, a frequency higher than 200 Hz [57]. The most common cause of flickering is represented by long strings of 0s or 1s, which can result in a low frequency domain fluctuation which could be perceived by eye. To mitigate this effect, Run Length Limited (RLL) codes are used, which ensure a balanced repetition of output symbols. Typical RLL codes are:

- *Manchester:* as shown in Figure 2-3, it works by replacing a “0” with a “up” transition (“01”) and a “1” with an “down” transition (“10”);
- *4B6B coding:* maps a 4-bit symbol to a 6-bit symbol with a balanced repetition;
- *8B10B coding:* maps an 8-bit symbol to a 10-bit symbol.

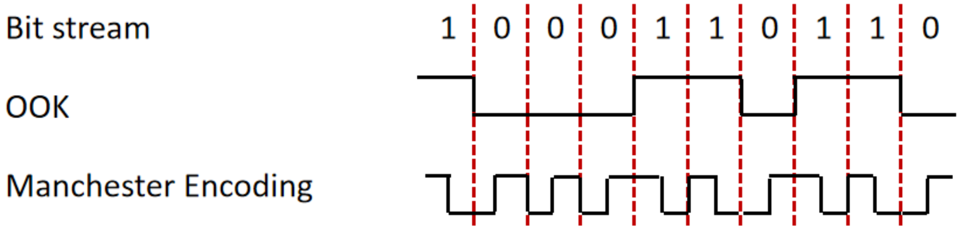

Figure 2-3. Representation of a data stream with OOK and Manchester encoding, ensuring a constant average luminous intensity and avoiding the flickering effect.

Each modulation technique is characterized by a finite number of symbols that can be used to encode data into light. A higher number of symbols ensures a VLC system having a higher data rate; however, a consequent disadvantage is that a higher SNR will be required to achieve the same communication performances as a simpler modulation scheme, because noise can mix neighboring symbols and cause errors.

The most important modulation schemes for VLC are the following:

- *On-Off Keying (OOK).* This is the simplest modulation scheme, based on amplitude shift keying (ASK); it has been widely used and consists in switching the intensity of an LED between a high (bit 1) and low (bit 0) value [62]. Because this method basically turns the LED on and off, one of its major drawbacks is represented by flickering when the frequency with which the modulation is carried out can be perceived by the human eye. This can be avoided using Manchester coding, which encodes the signal with on/off and off/on transitions; in such a way, the luminous intensity is constant. In this case, the relationship between SNR and bit error rate ($\mathrm{BER_{OOK}}$), that is, the ratio of wrong and total sent bits, can be expressed as [63]:

$$\mathrm{BER_{OOK}} = \frac{1}{2}\mathrm{erfc}(\sqrt{\mathrm{SNR}}) \tag{2-11}$$

The amplitude S of the received signal, BER, and SNR (Equation (2-9)) are related to the PER (the ratio between lost packets and total number of packets in the transmission) *via* the following equation [64,65], which is valid for high SNRs and, thus, low BERs and PERs, where the loss of a packet stems from the loss of a single bit:

$$\mathrm{PER} = 1 - (1 - \mathrm{BER})^{\mathrm{N}} = 1 - \left(1 - \mathrm{Q}\sqrt{\mathrm{SNR}}\right)^{\mathrm{N}} = 1 - \left(1 - \frac{1}{2}\mathrm{erfc}\left(\frac{\mathrm{S} - \mathrm{T}}{\sqrt{2}\sigma}\right)\right) \tag{2-12}$$

where N is the packet length, Q is the Q function, erfc is the complementary error function, σ is the standard deviation of the background noise, and T is a parameter that takes into account a possible hysteresis in the receiver resulting from the presence of the comparator.

- *Pulse Position Modulation (PPM).* Here, the width and amplitude of the pulse are constant; a pulse corresponding to a certain bit is transmitted in a given time slot within a symbol period. However, because only one pulse is emitted for each symbol, the data rate is limited [66]. A variation of this scheme, pulse width modulation (PWM), works based on the length of the signal, which determines its value, given a time period [67]. A hybrid PPMPWM modulation scheme has also been proposed [68], exploiting the broadened pulses of PWM to overcome the pulse width and low BW issues of PPM, thereby enhancing power efficiency.
- *Pulse Amplitude Modulation (PAM):* A basic and efficient modulation scheme, in which data are modulated into the amplitude of the signal pulse through multiple intensity levels. However, this may cause nonlinearity in the luminous efficacy of the LEDs and shifts in color temperature [69].

- *Generalized Space Shift Keying (GSSK):* This scheme exploits the spatial domain to modulate information with a higher spectral efficiency than OOK and PPM techniques [70].
- *Phase Shift Keying (PSK):* this is a digital modulation that encodes data by changing or modulating the carrier phase. Binary-PSK (BPSK) is the simplest form, and the phases of the symbols are separated by 180°.
- *Quadrature Amplitude Modulation (QAM):* This is a combination of PSK and ASK with a modification in the two parameters of the carrier (*i.e.*, phase and amplitude).
- *Color Shift Keying (CSK):* The signal is modulated according to the intensity of the three colors making up a multi-chip (typically, RGB) LED [71]: the transmitted bit corresponds to a specific color in the CIE 1931 coordinates (Figure 2-4). The RGB sources can be chosen from seven possible wavelength bands; the three wavelength bands of choice correspond to the vertices of a triangle containing the constellation points (*i.e.*, CIE coordinates) of the CSK symbols. Each symbol's color point is then obtained by modulating the intensity of the LED [17].
- *OFDM:* The previously discussed modulation schemes are affected by high inter-symbol interference owing to the non-linear frequency response of VLC channels. This issue is effectively addressed by OFDM, which is adapted from RFC: it consists in dividing the channel into multiple orthogonal subcarriers to transmit parallel data streams simultaneously [72]. However, the orthogonal sub-carrier frequencies are selected by an inverse fast Fourier transform (IFFT), which converts the frequency-domain input signals into time-domain output signals. To obtain real and unipolar valued signals, Hermitian symmetry is forced on the parallel data streams into the IFFT input, resulting in loss of half the available BW [73].

2.6. Network topologies

A network topology is a geometric modem representing the connectivity relationships between the elements of the network. Three types of link layer topologies are proposed in IEEE 802.15.7, as shown in Figure 2-5:

- *Peer-to-peer:* One device acts as the coordinator for the link between two devices communicating with each other. The client (user) has an uplink to the master (coordinator).
- *Star:* Many clients can connect to a master device (coordinator); this design is quite challenging owing to the presence of many bi-directional links.

- *Broadcast:* The client devices can only receive data from the master LED transmitter. This type is the one we mainly used in our experiments.

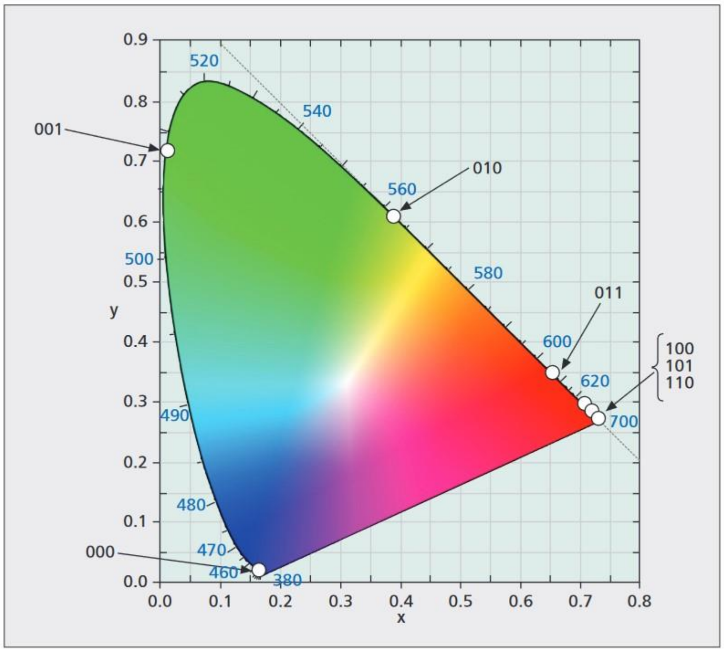

Figure 2-4. CIE chromaticity diagram [74].

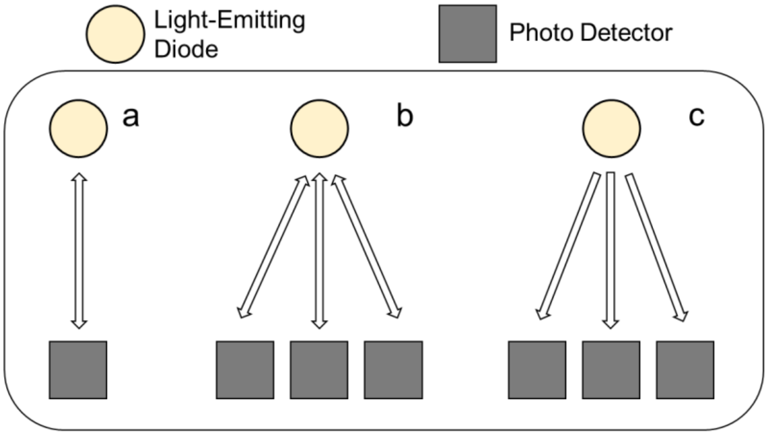

Figure 2-5. VLC link layer topologies: (a) Peer-to-peer; (b) Star; (c) Broadcast. Adapted from ref. *[57]*.

Evidently, many VLC scenarios can involve multiple users connected to an access point (*i.e.*, an LED light bulb). The control and coordination of accesses can follow several possible schemes. Namely, the IEEE 802.15.7 standard proposes the following [57]:

- *Carrier Sense Multiple Access (CSMA):* This scheme can work via two protocols, with coordinator signals either disabled or enabled. In beacon-disabled CSMA, an unslotted random channel access is used, so that any device needing to transmit over the channel must first wait for a random back-off period; whenever the channel is busy, the device will wait for another random period before retrying transmission. In beacon-enabled CSMA, time is divided into beacon intervals termed contention access periods (CAP) and contention free periods (CFP). A device attempting to transmit first needs to locate the start of a back-off slot, wait for a random number of back-off slots and then perform clear channel assessment (CCA). Transmission can begin if the channel is idle; in contrast, if it is found busy, the device must wait for another random number of back-off slots before a new CCA;
- *Orthogonal Frequency Division Multiple Access (OFDMA):* This scheme is practically a medium access control (MAC) extension of physical-layer OFDM. Here, different users are assigned separate resource blocks for communication. Its main challenges are power efficiency and decoding complexity;
- *Optical Code Division Multiple Access (OCDMA):* This scheme provides access to multiple users in the same channel by utilizing optically orthogonal codes (OOCs). Each device is assigned a binary code used to encode data by turning the LED on and off; OOK modulation with LED transmitters can be used. To improve the achievable data rate of devices, cyclic shifts of OOC codes can be implemented.

2.7. Indoor applications

The development of VLC systems in indoor environments has many possible applications, such as visible light positioning (VLP), dedicated services (for example, in museum or commercial scenarios), and pervasive or localized data connections. VLP is similar to the global positioning system (GPS) and complementary to it for those scenarios that cannot be reached by GPS signals (*i.e.*, inside certain buildings and underground locations). Indeed, attempts at developing an indoor positioning system based on Wi-Fi local area networks (LANs) have not yet resulted in sufficiently accurate and cost-effective solutions [75]. Therefore, VLC-based localization can provide a flexible, accurate, and ubiquitous positioning system in areas where LED lighting is present [76]. VLP has been investigated using both white and multi-colored LEDs as light sources [77]. An early test for this technology was carried out at a Korean mall in 2013 and termed "sale navigation" [78]: the experiment consisted in guiding shoppers to discounted items through lighting coupons. Similarly, a

VLP system could be used in theaters to guide customers to their seats or in museums to replace traditional security sensors preventing visitors from stepping too close to artwork [79]. Further use of VLC in museums may involve providing visitors with interactive services [80]. In the work of Gokrem *et al.* [81], a system of courtesy lamps was proposed to communicate through VLC according to a person's position in a museum to provide the same information that a guide would, such as the features and history of the place. A schematic representation of a possible VLC architecture for a typical museum setting is depicted in Figure 2-6. This particular application is one of the focus areas of the present Thesis: in Chapter 5, we will describe for the first time the performance of a PD-based NLoS VLC system exploiting the illumination of artwork in a real museum environment [29,30].

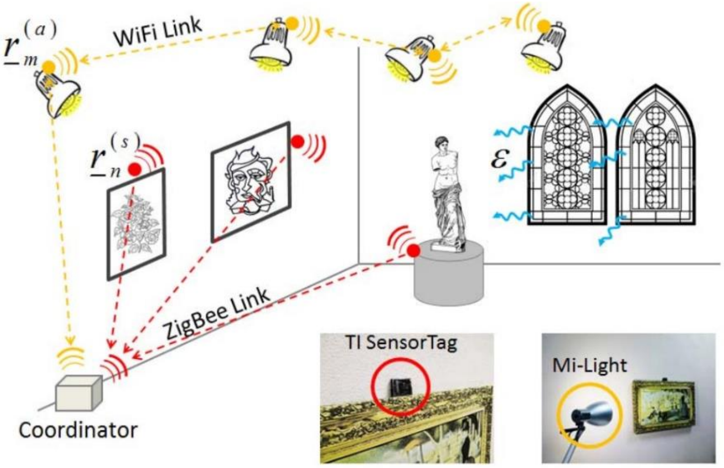

Figure 2-6. Sketch of a smart VLC-RF application for museum environments: multiple sources connected to each other which simultaneously serve as illumination and information transmitters. Visitors are provided with various types of information depending on the received signal through appropriate decoders. Reproduced from ref. [82].

An interesting application of VLC to indoor environments is represented by wireless data transmission networks, especially in office buildings and supermarkets, where illumination systems typically consist of LEDs and can be switched on all day long [17], but also in homes [12]. The VLC-based counterpart of Wi-Fi is Li-Fi, a term coined in 2011 by Harald Haas to refer to a two-way multi-user and high-speed data transmission network [83]. An example of a Li-Fi home network is represented in Figure 2-7. In particular, while Wi-Fi is unsuitable for use in sensitive environments, such as aircrafts, areas sensitive to electromagnetic radiation (such as galvanic factories), and hospitals (owing to interference with other RF signals), Li-Fi is safe to use in these types of settings

[14]. The main challenges to Li-Fi implementation are shadowing and interference. The first refers to the obstructions in the direct link between transmitter and receiver, which can occur in typical settings because of various elements including human body and furniture. To avoid this, multiple lighting points are necessary so that no shadowed areas exist in a room, which leads to the second drawback, interference. These need to be addressed through appropriate coding schemes to ensure adequate spectral efficiency [84]. Furthermore, to achieve ideal performance, the optimal transmitter configuration and receiver FoV must be designed in such a way as to boost communication without affecting lighting operation [85]. Finally, it is worth mentioning that optimum performances have been achieved through hybrid networks based on VLC and other communication media, such as Wi-Fi/Li-Fi integration [86].

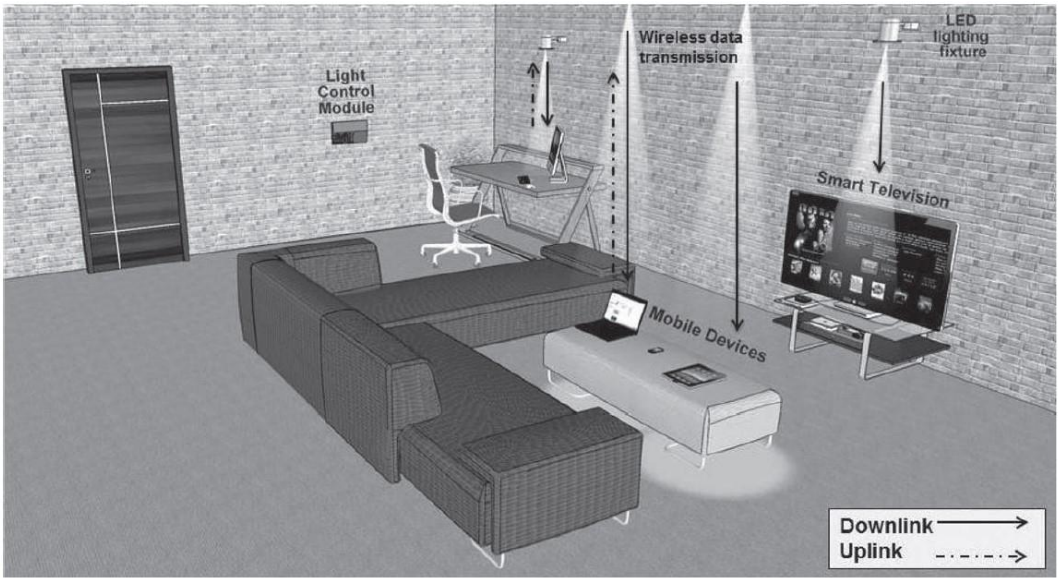

Figure 2-7. Indoor illumination integrated with VLC for next generation smart home lighting. Reproduced from ref. [17].

2.8. Outdoor applications

Compared to the indoor counterpart, the growth of outdoor optical communications has progressed more slowly owing to many environmental constraints. The term FSOC has been coined to refer to large-scale transmissions: the basic concepts are the same as generic OWC, but FSOC especially concerns the transmission of data using IR, visible light, and UV radiation through media without barriers: air, atmosphere, and space [35]. An FSOC network allows broadband wireless communication between two end points; communication is typically LoS and can span distances up to a few kilometers. While extremely high transfer speeds can be achieved, a serious drawback of this technology is represented by the degradation of links owing to atmospheric turbulence. The magnitude of atmospheric turbulence-induced irradiance fluctuations can be estimated through the Rytov variance [87]:

$$\sigma_R^2 = 1.23\left(\frac{2\pi}{\lambda}\right)^{7/6} C_n^2 z^{11/6} \tag{2-13}$$

where C_n^2 is a parameter reflecting the atmosphere's refractive index, and z is the length of the link. Based on this, researchers have been able to estimate the number of nodes in a multi relay FSOC network that would be required to maintain communications [88]. At extreme link lengths, FSOC can be established between satellites and towers on Earth to form a global network providing high-BW services to remote areas, cruise ships, airplanes, *etc.*; such an application clearly requires extremely accurate location pointing during satellite motion [89]. In the present work, we will present an MIR FSOC system (FSOCS) based on quantum cascade lasers to tackle the challenge represented by adverse atmospheric conditions: owing to the larger wavelength, MIR radiation suffers from reduced scattering rate compared to the visible light and UV ones, which strongly suppresses the detrimental effects on link stability.

A very specific application of outdoor OWC is represented by high-speed underwater communication, which is of interest for tactical surveillance, pollution monitoring, oil control and maintenance, offshore explorations, climate change monitoring, and oceanography research [90]. Underwater communication and localization are mostly carried out by means of acoustic waves at present; this technique, however, has many drawbacks including scattering, low propagation speed, high attenuation, low BW, and adverse impact on aquatic animals [91]. Recent development of underwater OWC has particularly involved the development of wireless networks for swimmer and diver communication [92] allowing a 6.25 Mbps, with Manchester encoding, communication up to 2.5 m [93], as well as the maneuvering of remotely operated vehicles in unsafe conditions [94]. The presence of various constituents and impurities can affect the transmission path and radiation absorption in a certain body of water; therefore, the most appropriate operational wavelength should be selected depending on the specific application and environment [17]. Recently, Kong *et al.* have described an amorphous silicon thin-film solar cell characterized by a high light absorption coefficient, which achieved VLC communication over 20 m in air and 2.4 m in turbid pool water [95].

Among the various possible applications in outdoor settings, VLC is currently considered as the most promising approach to realize ITSs by implementing real-time I2V and V2V communication to exchange location or safe driving information and thereby regulate road traffic in an autonomous way [96]: for example, very useful functions consist in collision warning and avoidance, lane change assistance, and cooperative adaptive cruise control [97]. The earliest studies on the subject have taken place in Japan, exploiting the ubiquitous presence of LEDs in streetlights and automobiles [98]. Others have demonstrated a high data rate (50 Mbps) communication using car headlamps for very long distances (up to 70 m) [99].

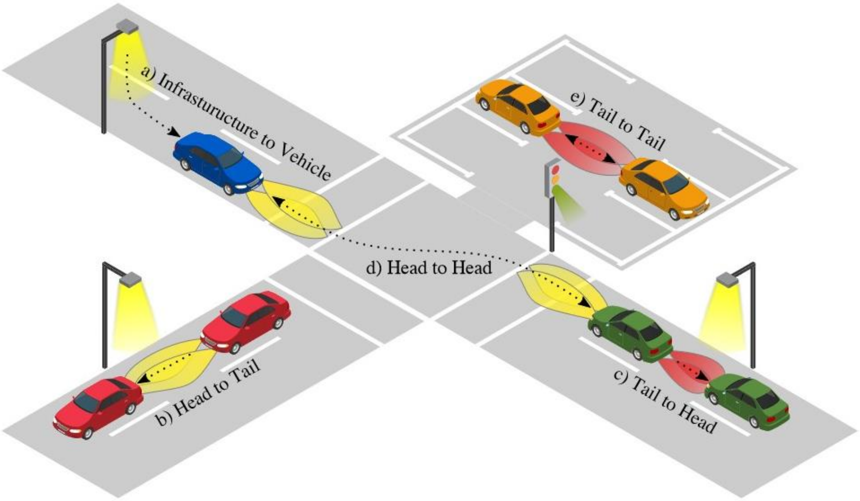

Figure 2-8. Different types of communication in ITSs such as I2V, V2V, and I2V2V achieved through different available light sources (car headlights, rear lights, and traffic lights). Reproduced from ref. *[100]*.

There are many difficulties in VLC-based ITSs; one of these is that the receiver must be able to ensure a stable link with the transmitter while in motion: to address this issue, high-speed cameras [101] and 2D imaging sensors [102] have been proposed as receivers. Other challenges are the non-negligible ambient light interference (background solar radiation and other urban light sources) and light scattering owing to factors such as smoke, smog, ambient humidity, rain, mist, *etc.* [103]. Furthermore, an intrinsic problem of VLC is related to the presence of obstacles that may obscure the detector; for this reason, many studies have focused on the complementarity of several technologies in addition to VLC, such as dedicated short-range communications [104] or Cellular Vehicle-to-everything (C-V2X) [105]. The use of RF sources typically allows longer range communications even in harsh environmental conditions that negatively affect VLC efficiency, such as fog, rain, or snow.

It should be noted that VLC is also compatible with 6G technology because it supports higher data rates in heterogeneous networks with reliable security. Nevertheless, the VLC standard cannot yet be considered mature, and several challenges are still to be tackled in its development such as new methods to increase data rates and avoid interference with ambient light sources and neighboring cells. Regulatory studies also take into account the development of standards for automotive and human safety as well as the impact of spurious RF emissions [106]. In this Thesis, we will report on the experimental investigation of a VLC link comprising a traffic light and a receiving stage in realistic configurations [28], with a special focus on safety through the introduction a low-latency and high-accuracy I2V2V architecture for high-speed transmission of alert messages from a regular traffic light through the vehicular chain [25]. We will propose an optical model for received intensity and effective FoV (EFoV) [24] as well as a low-cost prototype PD receiver equipped with a Fresnel lens as a condenser [25]. Further, bidirectional V2V communication will be tested under direct sunlight conditions in an outdoor scenario using real motorcycle headlights and rear lights [27].

2.9. Fluorescent concentrators as VLC large-area optical antennas

In VLC data links, high speed is achieved via a combination of large BW and SNR for both the transmitter and receiver. Large PDs are typically slow owing to their high capacitance, while those with a BW in the GHz range have active areas below 1 mm^2 [107]. The amount of light collected by these detectors can be increased through the use of a focusing optical element, such as a lens or compound parabolic concentrator. These, however, are based on reflection and refraction: therefore, they conserve étendue, and any gain in SNR comes with the disadvantage of a reduced FoV [108]. For these reasons, alternative methods for concentrating light onto PDs with no loss in BW and FoV are needed. A simple and inexpensive way to tackle this issue is based on the enhancement of light conversion via luminescent solar concentrators (LSCs), also known as fluorescent concentrators (FCs) [109]. An FC is based on the idea of light pipe trapping of molecular or ionic luminescence to provide a concentrated photon flux while reducing the heating due to radiation and increasing the electrical output of coupled devices (typically photovoltaic cells) [110]. Thanks to their intrinsic characteristics, FCs have been proposed as key elements in greenhouses [111] and, more importantly, as an efficient means to integrate photovoltaic architectural elements into buildings, urban furnishings, and wearable fabrics [112]. By extending this concept further, it is possible to develop large optical antennas based on semitransparent polymer sheets containing fluorescent materials, which absorb the incident light and re-emit it at longer wavelengths [113]. The concept of these optical devices is to absorb the light coming from the transmitted and guiding the light re-emitted by the fluorescent material toward the thin edge through internal reflection processed; the edge is coupled with a small, fast PD. To achieve this, the requirements of optical antennas are [107]:

1) the slab's refractive index higher than the surrounding medium, such that the emitted light is caught in the thin fluorescent slab. In this way, the emitted light is partly retained inside the LSC via a mechanism known as total internal reflection (TIR) and can only escape at its edge [107];
2) strong absorption in the emission region of the transmitter, so as to maximize the amount of absorbed light;
3) weak re-absorption of its own fluorescence, so as to minimize further losses;
4) high fluorescence quantum yield of the fluorescent material, so as to maximize the amount of re-emitted light;
5) short lifetime of the excited state (< 10–100 ns). Re-emission processes should be fast so as to prevent the absorption/re-remission process from becoming the rate-limiting step in the communication.

The receiving detector, which is small and fast, is placed at this position in order to collect the emitted light. Such fluorescent antennas are able to exceed the étendue limit for gain because they work based on fluorescence (in which the number of photons is conserved) rather than solely refraction or reflection [114]. For this reason, the superiority of FCs to white LEDs in VLC applications has recently been suggested [115].

Besides the geometric design, the implementation of fluorescent antennas in VLC systems presents other challenges. The selection of the appropriate dye and its processing in the fabrication of the device is a key step in the design of a VLC fluorescent antenna: dye-dye and dye-matrix interactions must be taken into account, as they can be the source of phenomena such as quenching and self-absorption, leading to efficiency losses [116]. A wide range of differently colored organic dyes exists, which can provide extremely high quantum efficiencies, and new molecular species are constantly being developed to achieve better UV stability. The first organic semiconductor solar cell used as an energy-harvesting receiver in an OWC data link was proposed by Haas in 2015: it consisted of a patterned indium tin oxide-coated glass substrate, on which a layer of poly(3,4-ethylene dioxythiophene) and poly(styrenesulfonate) was spin-coated to support the active material, a blend of PTB7 and $PC_{71}BM$, and the cathode [117]. Luminescent detectors for VLC, characterized by omnidirectional sensitivity and multi-Gbps data rates, were realized by [118] using commercially available scintillating fibers. A category of simpler and inexpensive optical antennas for VLC characterized by large signal gain and FoV has been described by Manousiadis *et al.* [108]. An appealing device, based on the combination of a narrow bandgap donor polymer and a nonfullerene acceptor, has been designed by Tavakkolnia *et al.* [119]: the power conversion efficiency was 8.8% under 1 Sun and 14% under indoor lighting conditions, and a VLC data rate of 363 Mb/s was achieved [119]. The importance of dye distribution in the matrix is exemplified in a study by Carbone *et al.* [116], where flexible FCs utilizing a perylene dye and a polydimethylsiloxane waveguide are presented. Bulk doping yielded devices that were less effective in the collection of direct light, while thin-film devices with high dye contents were affected by quenching and self-absorption losses and thus were not effective in light concentration [116].

Another class of interesting fluorescent materials, yet unexplored in VLC applications, is represented by QDs, core-shell semiconductor nanoparticles characterized by broader absorption spectra and higher stabilities compared to those of organic dyes [120]. Moreover, the red-shift between absorption and fluorescence of QDs is quantitatively determined by the distribution of the nanoparticle sizes, which can be appropriately tuned during the synthesis process to achieve the desired fluorescence properties [121]. In this work, we will present the first reliable VLC link obtained under direct solar irradiance with the use of a large-area optical antenna based on $CuInS_2$ (CIS) QDs. These were dispersed in a poly(methyl methacrylate) (PMMA) slab provided by Glass 2 Power spa, a spin-off company of UNIMIB (Università Milano - Bicocca). We will provide a physical characterization of the antenna in terms of conversion efficiency, FoV, temporal response to variable optical signal, and BW. Finally, the system's communication performance will be described for distances up to 100 m.

2.9.1. Fluorescent concentrator model

Several models have been developed to describe the optical efficiency of antennas. For example, for an LSC of length w and thickness d, we can define an effective photon-concentrating factor (EPCF) as [122]:

$$\mathrm{EPCF} = \mathrm{T} \times \mathrm{F_i} \times \eta_{\mathrm{FLQY}} \times \mathrm{F_r} \times \mathrm{w/d} \qquad (2\text{-}14)$$

where T is the transmittance, which depends on the incidence angle as described by Fresnel's laws, F_i the probability of an incident photon being absorbed, η_{FLQY} the fluorescence quantum yield, and F_r the probability of an emitted photon of reaching the detector. For an LSC to be considered in VLC applications, its EPCF or it must exceed the geometric gain $G = n^2/\sin^2\varphi$ [122], which could be achieved by a conventional concentrator with the same FoV, where n is the refractive index of the concentrator and φ is the FoV half-angle; alternatively, a significantly higher FoV is required compared to conventional concentrators. A graphical representation of different achievable FoVs and gains is depicted in Figure 2-9. Among various recent applications, an interesting study by Dong *et al.* described the fabrication of nanopatterned LSCs on flexible substrates by lithography, which presented a large FoV (up to ± 60°) and high efficiency for VLC (400 Mbps). The device achieved a 100% enhancement in optical gain in comparison to classic rectangular LSCs [107].

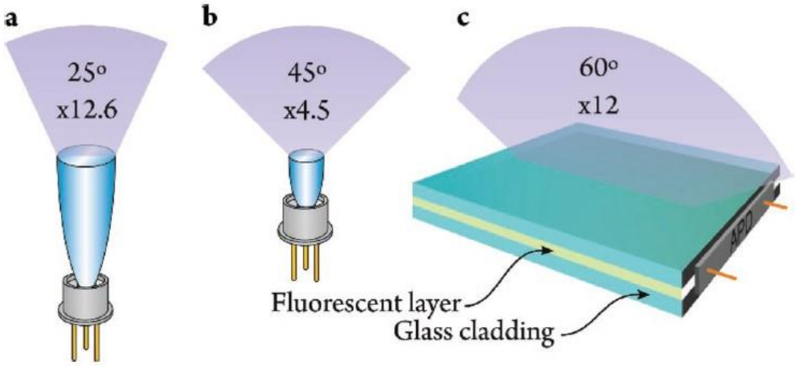

Figure 2-9. Examples of achievable FoVs and optical gain for different optical receivers. a) Maximum theoretical gain for a compound parabolic concentrator with an FoV of 25°. b) Maximum theoretical gain for a compound parabolic concentrator with an FoV of 45°. c) Experimental results for the FoV and gain of a fluorescent antenna. Reproduced from ref. [123].

Here, we propose a more accurate model to describe an antenna's optical efficiency. Let us assume an FC of dimensions length × width × depth (l × w × d) as the one represented in Figure 2-10. When this is hit by a radiation of luminous intensity I(0) varying over z, the intensity decays as a function of the wavelength λ according to the Lambert–Beer law:

$$I(z,\lambda) = I(0)\, S_{LED}(\lambda) e^{-\alpha_{Tot}(\lambda) z} \tag{2-15}$$

where $\alpha_{Tot}(\lambda)$ is the total attenuation coefficient, given by the sum of the attenuations of the QDs and the matrix in which they are dispersed: $\alpha_{Tot}(\lambda) = \alpha_{QD}(\lambda) + \alpha_{Matrix}(\lambda)$; and S_{LED} is the spectrum of the light source (in our case, a 405 nm LED) as in Figure 2-11.

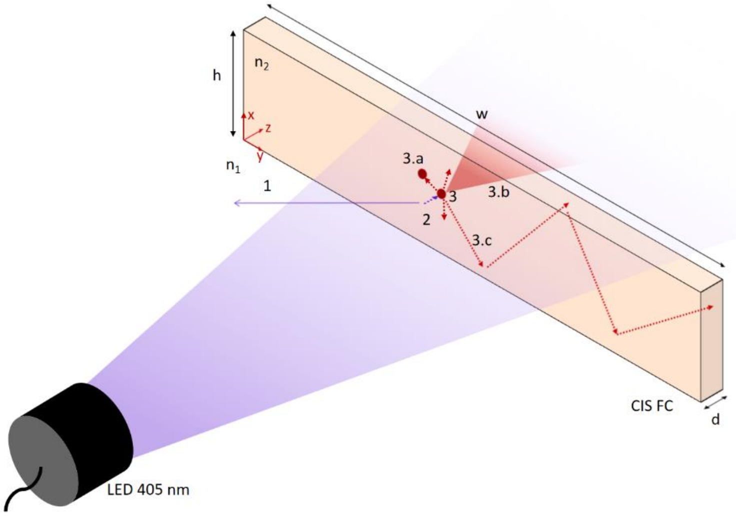

Figure 2-10. Representation of the model FC used in this study: a 405 nm LED is shone on a slab doped with CIS QDs. Some of the photons emitted by the LED can be reflected by the surface (1), while others can go through the slab without interaction (purple shadow) or cross the surface along the z direction until they meet a QD (2). Once the QD absorbs the incident radiation, it re-emits it isotropically in all directions. Some of these re-emitted photons will be re-absorbed by other QDs (3a) while others will leave the slab (3b) or be guided toward the border of the slab owing to TIR.

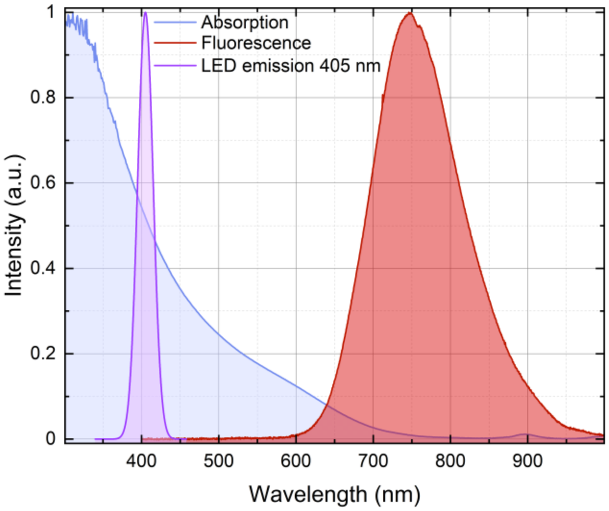

Figure 2-11. Typical normalized emission spectrum of the 405 nm LED (purple); absorption (blue) and fluorescence (red) spectra of the CIS QDs.

In a spatial interval dz, located in z, the intensity absorbed by the slab is equal to:

$$\mathrm{dI} = (1 - \mathrm{R})\, \mathrm{I}(0)\, \mathrm{S}_{\mathrm{LED}}(\lambda)\mathrm{S}_{\mathrm{Abs}}(\lambda)\mathrm{e}^{-\alpha_{\mathrm{Tot}}(\lambda)\mathrm{z}}\, |{-\alpha_{\mathrm{Tot}}(\lambda)}|\mathrm{dz} \tag{2-16}$$

where R is the Fresnel reflection coefficient, which depends on the incidence angle and, for non-polarized light, is equal to the average of the *p*-polarized and *s*-polarized reflection coefficients; and $\mathrm{S}_{\mathrm{Abs}}(\lambda)$ is the absorption spectrum of the QDs. Of the absorbed light, the QDs will re-emit only a fraction $\eta_{\mathrm{PLQY}}\alpha_{\mathrm{QD}}(\lambda)/\alpha_{\mathrm{Tot}}(\lambda)$, where η_{FLQY} is the fluorescence quantum yield. Naturally, the light will be emitted isotropically at a wavelength λ' and with a probability $\mathrm{S}_{\mathrm{Fluo}}(\lambda')\mathrm{d}\lambda'$. Therefore, the average path owing to the TIR effect from a point (x,y,z) to the extremity of the slab is indicated as <l(x,y,z)>. The outgoing power, considering a loss of photons emitted from the cone of light owing to the difference in refraction indices, which will be $\eta_{\mathrm{Trap}} = \sqrt{1 - (\mathrm{n}_1/\mathrm{n}_2)^2}$, and the re-absorption of light by other QDs or the dispersing matrix ($(1 - \eta_{\mathrm{ReAbs}})$ and $(1 - \eta_{\mathrm{Matrix}})$, respectively), will be equal to the integral in the volume l × w × d and wavelength λ of $\mathrm{dI}_{\mathrm{Out}}(\lambda')$:

$$\begin{aligned}\mathrm{dI}_{\mathrm{Out}}(\lambda') &= \\ &= (1 - \mathrm{R})\, \mathrm{I}(0)\, \mathrm{S}_{\mathrm{LED}}(\lambda)\, \mathrm{S}_{\mathrm{Abs}}(\lambda)\, \mathrm{S}_{\mathrm{Fluo}}(\lambda')\, \mathrm{e}^{-\alpha_{\mathrm{Tot}}(\lambda)\mathrm{z}}\, \mathrm{e}^{-\alpha_{\mathrm{Tot}}(\lambda')<\mathrm{l(x,y,z)}>} \\ &\quad \alpha_{\mathrm{QD}}(\lambda)\eta_{\mathrm{FLQY}}\eta_{\mathrm{Trap}}\, (1 - \eta_{\mathrm{ReAbs}})(1 - \eta_{\mathrm{Matrix}})\, \mathrm{dx\, dy\, dz\, d}\lambda\end{aligned} \tag{2-17}$$

Assuming an incidence normal to the surface for both refraction indexes $\mathrm{n}_1 \approx 1$ (air) and $\mathrm{n}_2 \approx 1.54$ (FC slab), we obtain a Fresnel reflection coefficient R ≈ 4% and $\eta_{\mathrm{Trap}} \approx 76\%$. Moreover, considering typical values of $\eta_{\mathrm{ReAbs}} \approx 5\%$ and $\eta_{\mathrm{FLQY}} \approx 85\%$ and neglecting the re-absorption by PMMA for our case, we can already estimate, independently on the amount of absorbed light, a loss factor (as a first approximation, for the simplest path w within the slab) equal to:

$$\frac{\mathrm{dI}_{\mathrm{Out}}(\lambda')}{\mathrm{I}(0)\, \mathrm{S}_{\mathrm{LED}}(\lambda)\, \mathrm{S}_{\mathrm{Abs}}(\lambda)\, \mathrm{d}\lambda} \approx \frac{0.6}{\overline{\alpha}_{\mathrm{Tot}}}\; \mathrm{S}_{\mathrm{Fluo}}(\lambda')(1\text{-}\, \mathrm{e}^{\overline{-\alpha}_{\mathrm{Tot}}\mathrm{d}})\, \mathrm{e}^{-\alpha_{\mathrm{Tot}}(\lambda')\mathrm{w}/2} \tag{2-18}$$

and distributed over the fluorescence wavelengths, where $\overline{\alpha}_{\mathrm{Tot}}$ is (for simplicity) the average value of the absorption coefficient at the emission wavelength of the LED (in our case, we assume this to be monochromatic at 405 nm). The above equation highlights the exponential decay of the signal as the light propagates inside the slab; as a consequence, longer slabs will exhibit greater losses.

3. OWC system architecture and implementation

3.1. Introduction to the Chapter

For this Thesis, we decided to design and test an open-source and versatile VLC system encompassing our expertise in the creation, manipulation and measure of light. The versatility of our system is one of its main advantages, together with its low cost and the possibility of driving these commercial sources at high currents (up to 1 A) and relatively high baud rates (up to 2 Mbaud UART). The choice of utilizing commercial light sources, open-source microcontrollers, and simple communication protocols clearly presents the disadvantage of being unable to achieve the best performances in terms of communication speed. In this Chapter, we will describe the hardware and software components of such a system for all experiments; concerning the study on the MIR QCL, its experimental setup being different despite having a similar architecture, it will be described in detail in Chapter 6.

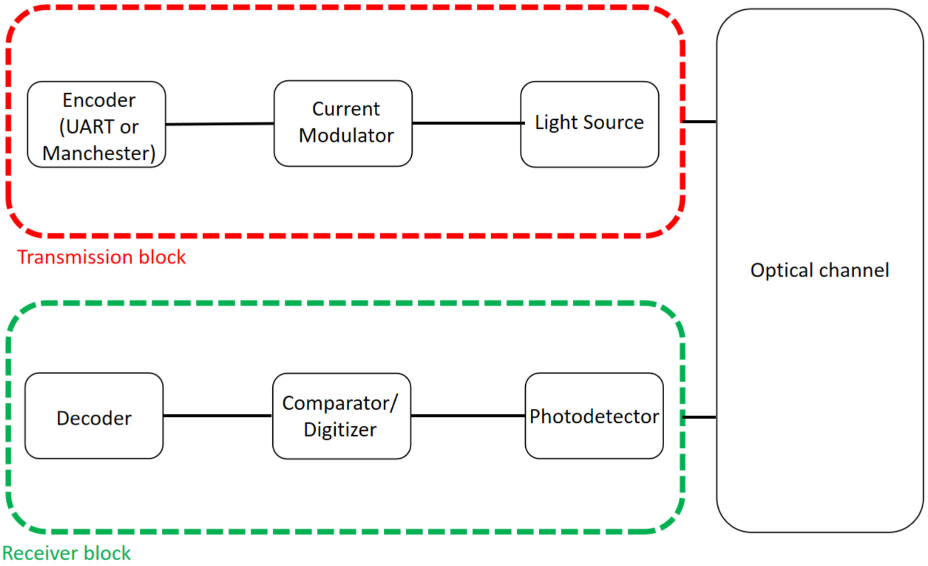

Figure 3-1. Schematic block diagram of our VLC experimental setup. Transmission block: the Arduino DUE encoder generates an AC digital message that is added on top of the DC provided by the current modulator to the light source. The modulated light travels across the optical medium and is collected by an AC-coupled detector in the receiver block that removes all spurious stray light. The AC-coupled photodetector consists of a PD and a transimpedance amplifier. The analog signal is digitized before being compared with a prestored message in the Arduino DUE decoder board.

As exemplified in Figure 3-1, our experimental setup typically consisted of a light source modulated through a driver (*i.e.*, a current modulator), which added an AC digital signal to the direct current (DC) required by the light source; such a digital signal was produced by an encoder. The light wave thereby modulated traveled across the optical medium and was collected by an AC-coupled photoreceiver capable of working even under direct sunlight [28]. The received signal was first amplified, then digitized and compared with a prestored message in the decoder. In the following, the receiver unit will be sometimes abbreviated as RX and the transmitter unit as TX.

The transmission block consisted of an encoder, a current modulator, and a light source; the receiver block consisted of a detector (which in turn was made up of reception optics, a detector, and the amplifying front-end), a comparator, and a decoder. At the end of this Chapter, we will present a table summarizing the hardware employed in each experiment.

3.2. Transmitter

In this Section, we will provide a general description of the components that make up the transmitting unit and present their characterization.

3.2.1. Encoder

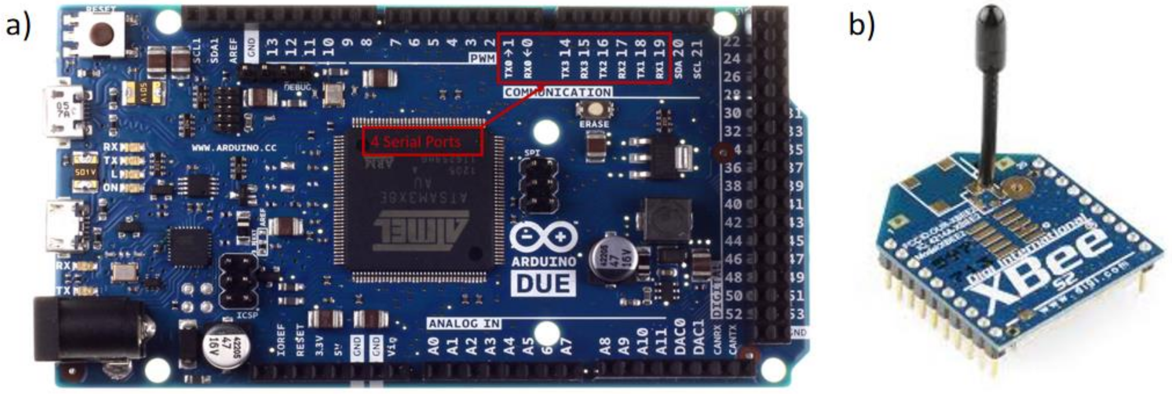

Figure 3-2. a) Photograph of our Arduino DUE board. The red box highlights the four serial ports used for communication; b) photograph of the Zigbee platform.

In our experiments, an open-source, low-cost platform named Arduino DUE (Figure 3-2a) was used as both the encoder and decoder. This was a microcontroller board based on a 32-bit central processing unit, with 54 digital input/output pins, 12 analog inputs, four universal asynchronous receiver-transmitter (UART) serial ports, an 84 MHz clock, 96 kB of random-access memory, and

512 kB of flash memory for storing code. It could be connected to a computer via a micro-USB cable or powered with an AC-to-DC adapter or battery and could also communicate with another Arduino or other microcontrollers as well as different devices like phones, tablets, or cameras.

3.2.2. Encoder software

Owing to the versatility of these boards and an accurate study of its register, we were able to achieve baud rates up to 2 Mbps with UART and 1 Mbps with Manchester [124]. Our system evaluated the communication performance based on the PER metric, that is, the ratio of the lost and sent data packets. For baud rates up to 0.5 Mbps, we could also evaluate the BER, owing to two developed programs. As mentioned above and highlighted in Figure 3-2, four serial ports were available and were used for communication on the Arduino DUE: in both types of programs, UART0 operated the connection between the board itself and a computer, that is, by accessing the serial monitor of the Arduino with a computer, we were able to communicate with the platsofmr through the UART0. Serial ports UART1 and UART2 were dedicated to VLC; specifically, UART2 was used for the transmission of data messages and was directly connected to the current modulator (see Paragraph 3.2.3.), while UART1 was used for the reception of data messages (such as backward messages in a bidirectional system, see Section 4.5.). UART3 communicated with a Zigbee platform; indeed, each Arduino DUE board had an associated Zigbee, as shown in Figure 3-2b. This port was utilized solely for the configuration of both boards via one computer (independently on either the transmitter or the receiver side): indeed, besides starting the communication, it allowed to set various parameters of the Arduino DUE board used for VLC (*e.g.*, the number of messages), reboot the board, vary the baud rate between 9.6 kbps and 2 Mbps, and set either a UART or Manchester communication by altering the microcontroller registers following the directions provided in the official datasheet [124]. Using the command *USART1->US_WPMR = 0x55534100*, the write protection in register mode was disabled (in this example, for serial port number 1). For a Manchester communication, the following code lines were entered: *USART1->US_MR = 0xA00008C0* and *USART1->US_MAN = 0x60000000*. For UART communication, the following was used: *USART1->US_MR = 0x000008C0* and *USART1->US_MAN = 0x60000000*.

The baud rates were selected between 9.6 kbps and 2 Mbps (with UART; 1 MBps with Manchester) when we meant to evaluate the system performances in terms of PER and between 9.6 kbps and 0.5 Mbps for a bitwise control with Manchester encoding.

Going into further detail, let us now discuss the transmission software that evaluated the communication performance through PER measurements. First, for each baud rate, we initialized the variables defining i) the delay between one packet and the next, ii) the number of packets to be sent, and iii) the baud rates of the four serial ports. Then, we initialized the sent message as a code line formed by the equalization bytes ("ð" in ASCII, whose number could be varied depending on the light source and baud rate used: indeed, when the baud rate is increased, more bytes are required to equalize the system, up to a maximum of 8 bytes; see further for detail), the starting byte ("Z" in ASCII), the reference message ("AL" from alert), and the end byte ("\n," which is a new line). Moreover, we also defined the end transmission packet to inform the reception system (see Paragraph 3.3.4.): this packet had the same structure as the sent message, except for the reference end message, which was "ST" (as in "stop").

As shown in Figure 3-3, which presents the shape of the packet acquired by the receiving system, the equalization bytes (red box) were required to bring the system to a steady state. Indeed, as explained in the next Paragraphs (3.2.3. and 3.3.1.), the message coming from the encoder was added on top of the DC and then received by an AC-coupled detector. Therefore, a transient was present, in which the signal was able to stabilize. Should these bytes be absent, the transient would prevent setting a common threshold, compatible with the start and end bytes, in the comparator (see Paragraph 3.3.3.).

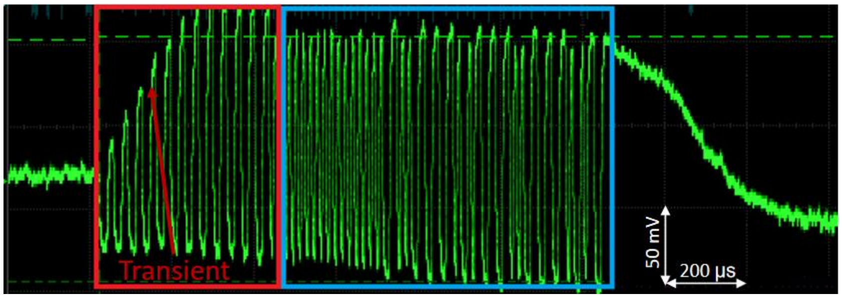

Figure 3-3. Example of a packet received by the PD. The red box shows the pre-equalization bytes required to bring the system to a steady state. The blue box contains the starting, reference message, and end bytes.

During setup, using a predefined function which runs only once, after each powerup or reset of the board [125], the different serial ports were initialized at a specific baud rate (which, as mentioned above, could be modified whenever no data were being transmitted). Generally, during an experiment, the UART0 baud rate was left unaltered at 230.4 kbaud, as this port regulates the communication between the platform and computer.

As explained in more detail further in the text, most experiments were carried out with distances of tens of meters occurring between transmitter and receiver units; therefore, it is paramount to be able to set the communication parameters simultaneously on both boards in wireless mode (which is done using a Zigbee platform directly attached to the UART3 of both transmitter and receiver boards at a baud rate of 9.6 kbaud). Before moving to the subsequent loop section, the instructions were printed on the serial monitor; the buffers of all serial ports were wiped so as to remove any data left in them; and finally, through the command *while(Serial.available()){Serial.read()}* (example for UART0), we allowed the system to await an external input (equivalent code lines were used for the other serial ports).

The loop part began by awaiting the reception of the various parameters from the computer through the functions *serialEvent()* and *serialEvent3()*. These acted as *interrupt* functions, that is, anytime an input was received from the UART0 (UART3), they interrupted the loop function. These functions were similar and had the scope of aggregating characters to form strings until they found a pre-established character ("*"); then, they compared such strings with reference ones, allowing to change the number of packets to be sent, rested the board, modify the baud rate of each port, choose a Manchester or OOK encoding, and start the communication. Moreover, every time a string was composed, it was also printed (using *Serial.print* and *Serial3.print*) both on the terminal and UART3, where the Zigbee platform was connected, which transferred the parameters to the other board *via* a wireless link.

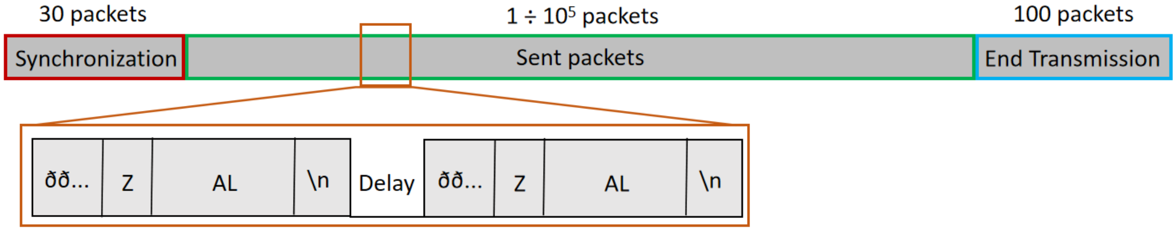

Figure 3-4. Schematic representation of the transmission (not in scale). At the start of the transmission, 30 packets are sent to synchronize the boards. The, the VLC transmission (usually, 100000 packets) begins. At the end of the transmission, a set of 100 packets with different reference messages are sent. The inset shows the structure of the packets, separated by a constant delay: "ð" are the pre-equalization characters, which are a variable number; "Z" the starting byte; "AL" the reference message; and "\n" the end byte. The synchronization packets have different starting byte ("Y") and reference message ("JU"). The end transmission packets have an "ST" in the reference message instead of "AL".

Next, as shown in Figure 3-4, for each communication, approximately thirty packets were sent through the UART2, which was directly connected to the current modulator (see Figure 3-5b). These packets were the same byte size as the correct ones but with different starting byte ("Y") and reference message and were used solely for synchronizing the boards. Thus, a number of packets equal to the established number (usually 100000) were sent through the UART2 port; these packets could be separated by a certain interpacket delay time, depending on the relative baud rate. This is necessary because a computational time is required for the string comparison by the Arduino DUE board: for this reason, the interpacket delay time was set to be slightly longer than the packet time, so as to allow the platform the necessary time to compute. However, in most experiments, we used an interpacket delay and a message to be resent by the received to perform a real-time evaluation of the transmission success.

At the end of the transmission, 100 packets (having the same structure as the communication packets but a different reference message, "ST") were sent to inform the system of the end of the transmission. Such a number of packets was chosen in a redundant way to prevent the system from freezing. Indeed, as long as the decoder has not received at least one end transmission packet, it remains in listening mode. This could happen in case of a high PER, where only a few correct packets are received. Notably, we have observed that information such as the number of correctly received packets and PER should be preferably printed at the end of the transmission to minimize the communication time and interpacket delay.

The second software that we realized allowed for a bitwise control in Manchester encoding up to 0.5 Mbps. In this second case, the packet was formed by 72 bits, of which 24 pre-equalization bits required to stabilize the signal, 16 preamble bytes (composed by 16 bits "0"), and 32 reference message bits. The preamble bytes had a similar function as the starting byte: if they were all received correctly, the system evaluated the following bits; otherwise, the packet was considered lost owing to a synchronization error and was not accounted for in the final result. The end transmission string was formed by 124 bits (24 pre-equalization bits "UUU" and 100 bits "1"). In a similar way as what described previously, the setup function initialized the serial ports and set them into listening mode to receive an input from the serial monitor or Zigbee platform. The loop function within consisted only of functions *serialEvent()* and *serialEvent3()*, which were slightly different from those described above. Function *serialEvent()* (*serialEvent3()*) obtained the inputs from the computer (Zigbee), which were similar to those described previously as for what concerned the number of packets to be sent and other parameters. The main difference consisted in the selection of the baud rate: a *flag* would kick start the transmission at the selected baud rate, while waiting for the other board to synchronize according to the received parameters, and send the packets formed by the 72 bit, Manchester-encoded stream. Depending on the bit to be sent, the system would remain high (low) during half the bit time and then move to the low (high) state for the remaining bit time, which is inversely proportional to the baud rate. By performing a control of the length of the bit string, the system inserts an opportune delay (different for each baud rate) every 72 bits (1 packet). Finally, as in the previous software, the 124-bit end transmission string was sent. Once a certain number of consecutive "1" (10 bits) was received, the decoder printed the results on screen, including the total number of sent bits (*i.e.*, the number of messages per number of data bits) as well as the number of correctly received bits (compared with a pre-stored message) and packets (*i.e.*, a group of 4 data bytes).

3.2.3. Current modulator

Owing to their small dynamic resistance, LEDs are highly sensitive to even slight changes in current, which determines the emitted intensity; for this reason, controlling and dimming them is quite challenging. LEDs used for both illumination and VLC have further requirements concerning driver design, such as the integration of multiple functions (performance, data, and luminance control) on a single die [126] to ensure VLC functionality without compromising illumination control. More generally, driver circuits must present the following three characteristics: 1) use of low power; 2) long lifetime; 3) use of pulsed current to drive the LEDs; and 4) large BW.

The current modulator (Figure 3-5) designed and exploited in this work allowed us to add the AC modulation from the encoder on top of the DC used to power the light sources at their nominal current and supply voltage. In this way, a data stream could be inserted into the optical carrier wave for each modulation scheme. The modulator was based on a quad-precision, high-speed operational amplifier (Analog Devices OP467); its main features were the high slew rate (170 V/μs), wide unitary-gain BW (28 MHz), and fast settling time (< 200 ns to 0.01%).

Referring to Figure 3-5b, the first stage of the OP467 was used as a non-inverting buffer; here, a DC set point from 0 to 1 A was set, which was the current travelling through the diode after the subsequent stages of feedback signal control. The second stage, characterized by a unitary gain, was used in inverting mode in order to obtain a compatible signal to sum to the modulation one coming from the encoder. The modulation stage was placed after a proportional integral regulation stage, which was used to stabilize the supply current from DC to approximately 1.5 kHz by adjusting the servo resistor-capacitor (RC network). The op-amp chain could reach open-loop BWs in the order of several MHz, but these would be reduced by two main factors: i) the large parasitic capacitance of the LED light sources and ii) the non-linear response of the actuation chain.

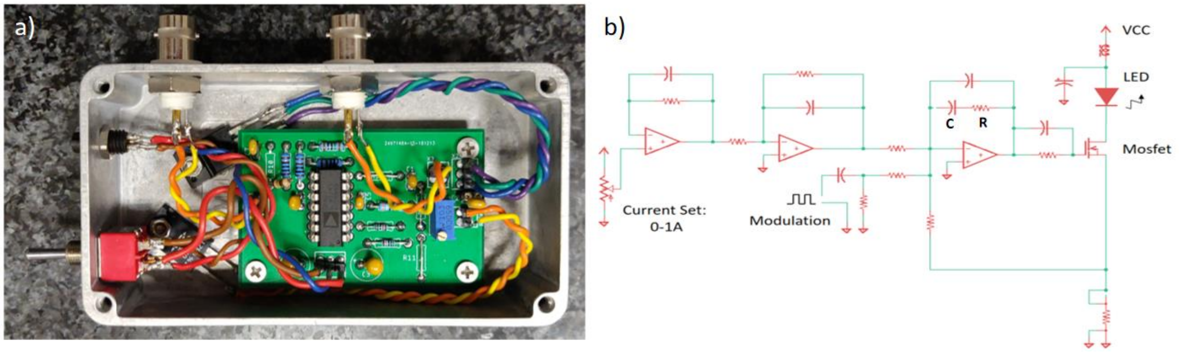

Figure 3-5. a) Photograph of the current modulator. b) Current modulator schematics: a regulation stage stabilizes the DC value so that the source emits the nominal luminous intensity. On top of this, a high-frequency AC is fed into the light source by the modulation stage for data transmission.

3.2.4. Light sources

In all our experiments (except those involving the FSOC QCLs, described in Chapter 6. Mid-infrared free-space optical communication based on quantum cascade lasers), we employed commercial LED light sources (Figure 3-6) which were characterized using an Ocean Insight HR2B1359 spectrometer; the only exception was the light source used for the experiments with the fluorescent antenna (Chapter 7), for which the spectrum was provided by the supplier and was available in the datasheet (Thorlabs M405L4-C1). For each source, five spectra were acquired and averaged, and the background was subtracted (Figure 3-7).

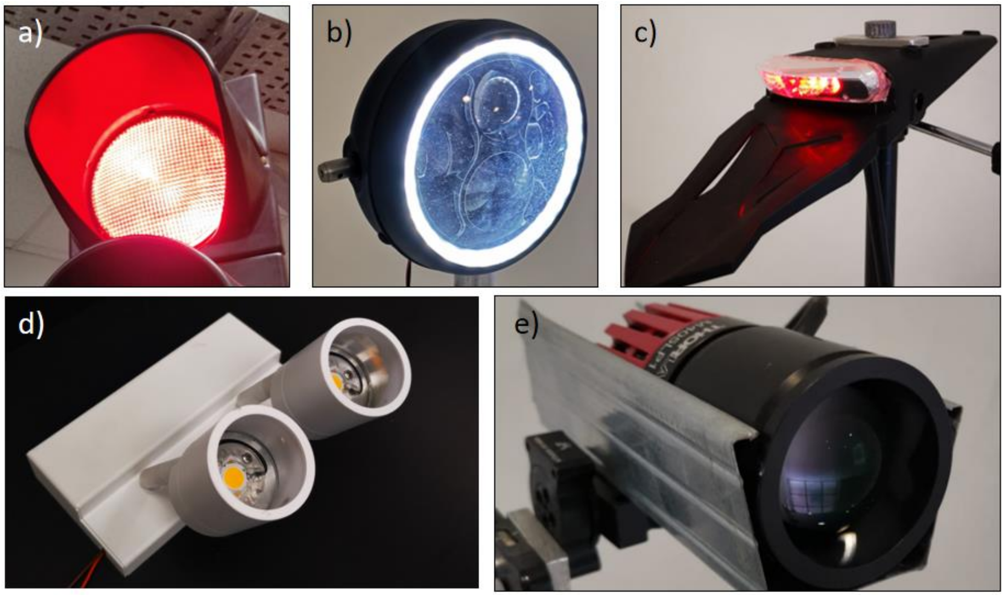

Figure 3-6. Photographs of the main LED sources used in our experiments: a) red traffic light; b) motorbike headlight; c) motorbike rear light; d) museum spotlights; and e) 405 nm collimated LED light source.

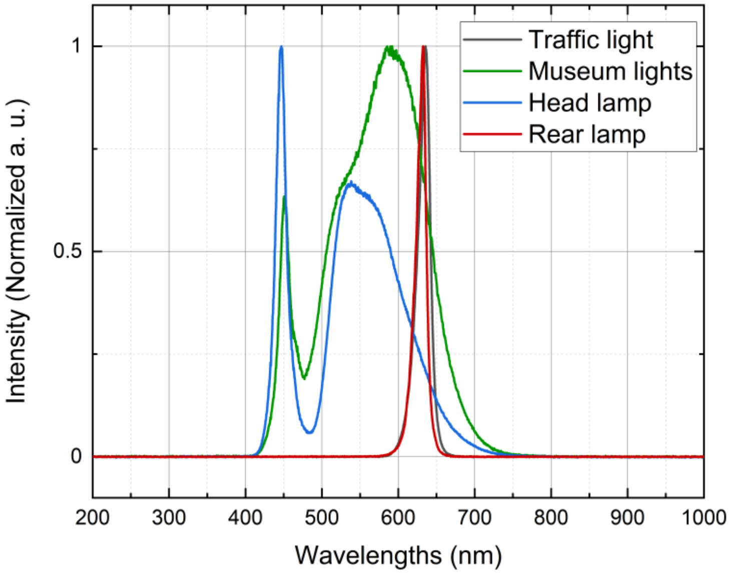

Figure 3-7. Spectra of the different LED light sources used in this work. Gray line: traffic light; green line: museum lights; blue line: head lamp; red line: rear lamp.

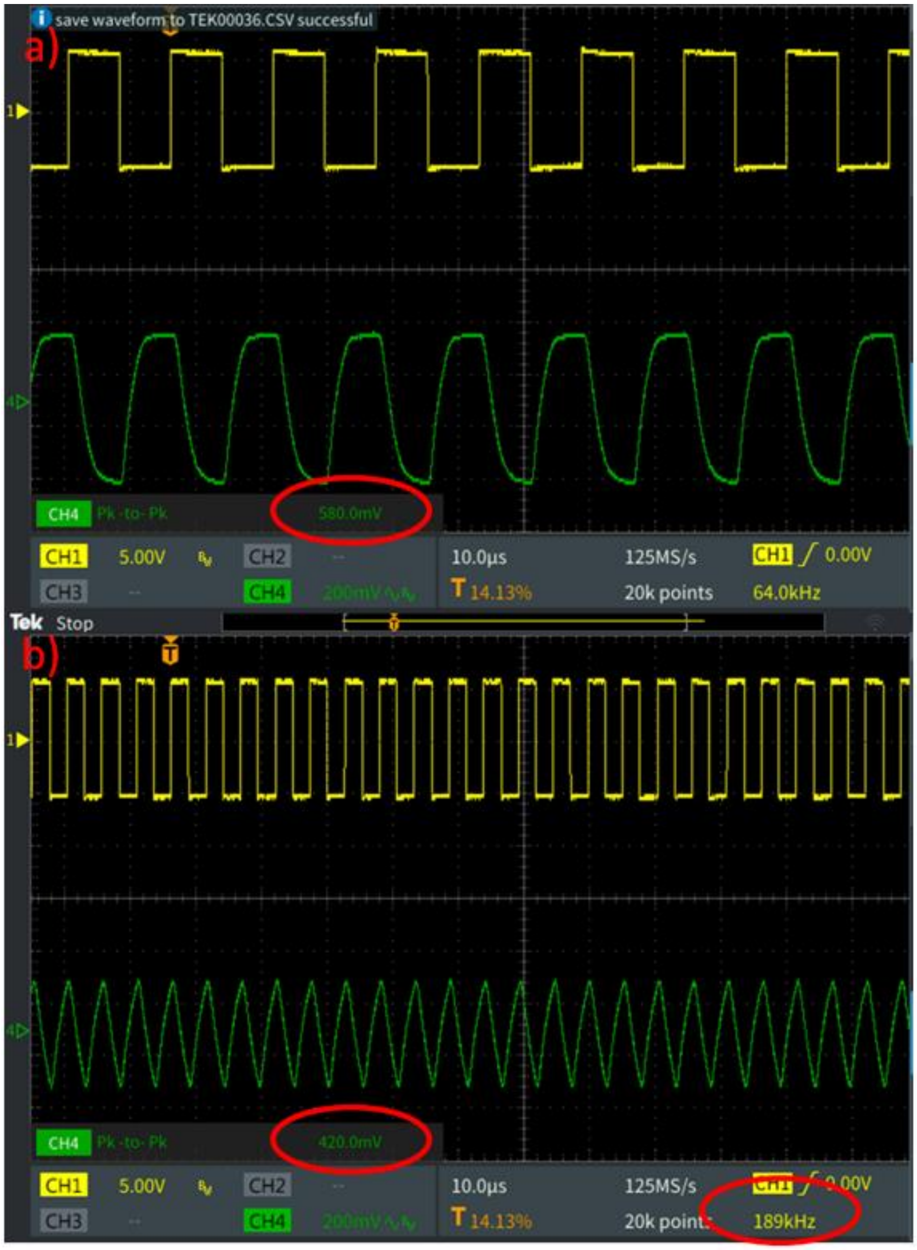

save waveform to TEK00036.CSV successful

Figure 3-8. Images acquired by the oscilloscope to evaluate the digital BW of the headlight source. Yellow lines represent the digital signal coming from the wavefunction generator, while the green traces are the signals originating from the PD (Thorlabs, APD430A/M, BW = 400 MHz). The upper panel (a) is used for the signal inside the BW, while the bottom one (b) is used for the signal at −3 dB BW.

Further, we characterized the analog (see Section 2.2.) and digital bands of each light source by powering them with their nominal currents through the modulator (see Paragraph 3.2.3.). We defined the cut-off frequency of the digital band in the same way as that of the analog band, that is, the point at which the signal amplitude decreases by 3 dB with respect to a reference value. The signal amplitude is the one from peak to peak in the plateau; clearly, owing to the nature of the digital signal, as we leave the band, the received square wave tends to transform into a triangular wave, and the amplitude to be considered is the peak-to-peak one in the triangular wave (see Figure 3-8b). A wavefunction generator (Siglent SDG5022X) was used to add the modulation signal to the source. The modulated luminous signal was collected by a fast APD (Thorlabs, APD430A/M) and acquired by a digital oscilloscope (Siglent SDS1204X-E). We considered the peak-to-peak values for varying frequencies until the signal amplitude diminished by a factor √2 (corresponding to −3 dB) with respect to the reference signal, that is, the one where the signal was not cut. Figure 3-8 shows an example regarding the motorbike headlight: the digital BW of this light source was 190 kHz, as shown in the bottom panel of the oscilloscope (Figure 3-8b).

Table 3-1. List of the main LED sources used in this work along with their digital BWs and nominal working currents.

LED source	Digital BW (MHz)	Supply voltage (V)	Current (mA)	Wavelength (nm)	Optical Power (W)	Supplier and model
Red traffic light	1	12	700	630	12	Lux Potentia OJ200-R07
Headlights	0.2	12	160	420–600	2	Qiilu QL04156
Rear lights	0.2	12	90	630	1	Alchemy Parts, UPC: 5060502564597
Museum spotlights	0.4	20	700	420–650	9	Exenia
405 nm LED	5	12	700	405	0.75	Thorlabs M405L4-C1

Table 3-1 reports some characteristics of the various sources, including the digital band, which is a useful feature to consider in a VLC system. The light intensity of each source was modulated between 0% and 200% through the current modulator. Such a range was chosen to obtain an on-off modulation of the LED while maintaining the average value of the luminous intensity as the nominal value. We noticed that, with a 0–200% modulation, the RMS of the light intensity was 100%, and we observed that this fact did not reduce the lifetime of the LED lamps. An exception was the LED used with the fluorescent antenna (Thorlabs M405L4-C1), which was modulated between 0% and 100%; the mean LED current value corresponded to half the DC nominal value (0.7 A) for a 50% duty cycle modulation, because it ensured an adequate signal at long distances and, being more expensive and fragile, should be operated within the indicated working parameters.

3.3. Receiver

The modulated light, after traveling across the optical channel, was collected by a photoreceiver; in our experiments, this consisted in a PD with its amplification electronics. The PD could be coupled with an optical collector.

3.3.1. Photodetectors

In this work, we employed customized, switchable-gain silicon amplified PDs (Figure 3-9a). These detectors exhibited a relatively high BW/gain product (11–12 MHz) which allowed us to perform outdoor, long-distance experiments using high gains (30–40 dB) while being compliant with IEEE 802.15.7 PHY I [57].

In the receiver, the signal collected by the photodiode was AC-decoupled before being sent to the trans-impedance amplifier (TIA) stage according to a time constant of approximately 5 kHz obtained via a multielement RLC network. A schematic representation of the AC decoupling circuit is presented in Figure 3-10. The parameters were chosen so as to allow the modulation signal alone into the receiving electronics and filter out stray light of low frequencies. In this way, a high receiver gain (chosen as the highest possible that would allow for a BW higher than 150 kHz) could be obtained while preventing the saturation of the amplifier. Moreover, with such a configuration, in our experiments, no colored filter was required at the RX, contrary to the example scheme in Figure 1-2, where the use of a colored filter was required to screen the stray light component coming from the sun.

Thorlabs photodetectors include a low-noise, low-offset, high-gain TIA that allows for gain adjustment over a 70 dB range, thereby converting photocurrent into voltage (see Section 2.3.). The gain is adjusted by rotating a gain control knob, located on the detector. There are eight gain positions incrementing by 10 dB steps. It is important to note that the BW will decrease as the gain increases. We used detectors PDA36A2 (Figure 3-9b; Silicon Amplified Photodetectors, wavelength range = 350–1100 nm, BW range = DC-12 MHz, active area = 3.6 × 3.6 mm^2) and PDA100A2 (Figure 3-9c;

Silicon Amplified Photodetectors, wavelength range = 320–1100 nm, BW range = DC-11 MHz, circled active area = 75.4 mm^2) by Thorlabs, Inc., except in the FC experiment, for which we customized a PDA100A2 model by replacing the original PD with an S3588-09 by Hamamatsu while keeping the original TIA (Figure 3-9d; Silicon PIN PD, wavelength range = 340–1100 nm). This modification was required to better match the PD size (L = 30 mm, d = 3 mm) to that of the CIS QD-doped slab while maintaining the same electronic performance, especially the digital BW/gain product (Figure 3-11).

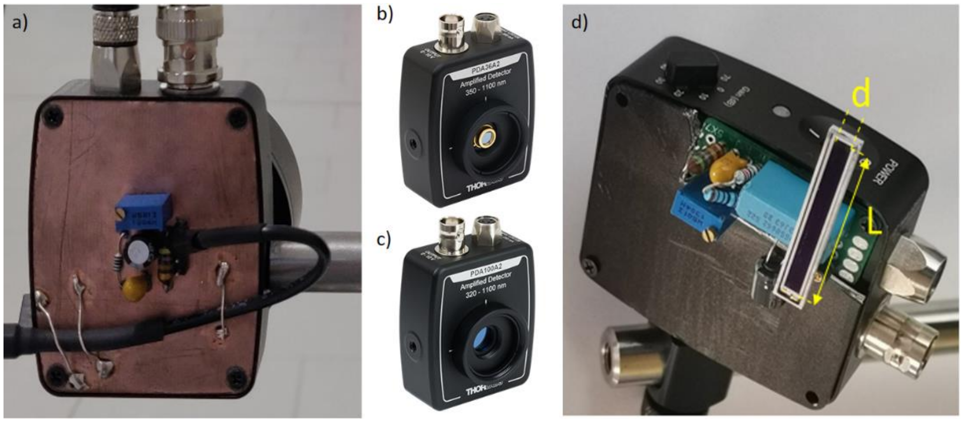

Figure 3-9. a) Photograph of the custom circuit of the switchable-gain silicon amplified PD. b) Photograph of the Thorlabs PDA36A2. c) Photograph of the Thorlabs PDA100A2. d) Photograph of the Hamamatsu S3588-09 connected to the PDA100A2 TIA, used to collect the light from a thin FC doped with CIS QDs; the dimensions of the slab, h = 80 mm and d = 3 mm, are a perfect match for the PD (L = 30 mm and d = 3 mm).

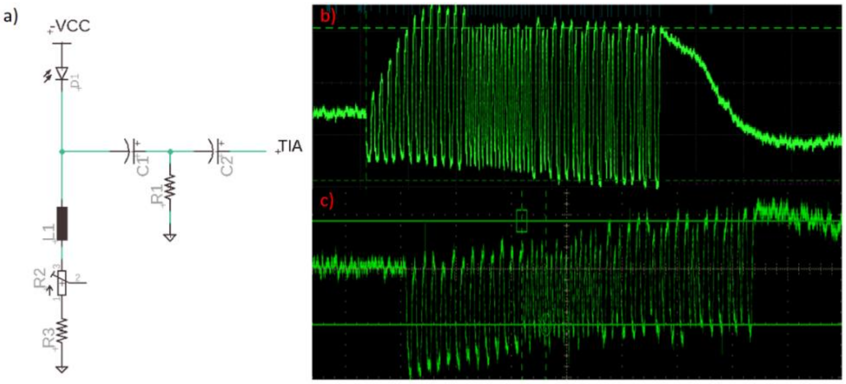

Figure 3-10. a) Schematic of the AC-decoupling circuit of the PD through an RLC circuit network before the TIA. Effects of the filter in two different experiments, working in the presence (b) and the absence (c) of artificial lights. The filter is adjusted to remove the 100-Hz effect typical of neon lights. In this case (b) the average value of the received signal is centered around 0 V.

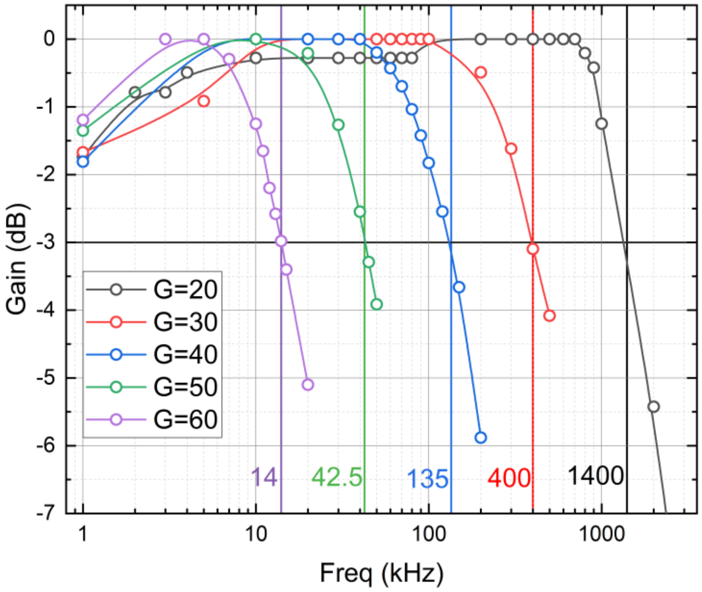

Figure 3-11. Graph of the various digital BWs for the different gains of the PD composed by the Hamamatsu S3588-09 PD and Thorlabs TIA. From an electronic point of view, no differences were observed with respect to the datasheet of the PDA100A2 Thorlabs PD. The low-frequency cut-off of approximately 1–2 dB was due to our definition of digital band (see Paragraph 3.2.4.). Because the square wave is a sum of sinusoidal waves, the values of signal amplitude received at low frequencies are slightly cut off by the filter, while remaining above the cut-off frequency at –3 dB.

3.3.2. Optical collectors: lenses and fluorescent antenna

Depending on the type of experiment, different optical collectors were used. In our paper [24], we have provided a detailed description of a selection of lenses that allowed for increasing the signal significantly while reducing the FoV, thereby decreasing the communication distance. In the FC experiments, we overcame the étendue principle and obtained optical antennas with FoVs of 120°: these were based on the absorption and re-emission of light at higher wavelengths by fluorescent substances enclosed in a substrate.

The lenses used in this work were typically non-custom, 1" or 2" in diameter, and characterized by the shortest possible focal lengths (see Table 3-2 and Figure 3-12a). With their low costs (between €5 and €40) and large angles of FoV (AFoV), these were the most suitable choices as condensing optical elements for our VLC experiments. Our analysis involved two classes of lenses:

1) molded glass aspheric lenses (high cost, high optical performance);
2) plastic Fresnel lenses (low cost, thickness, and weight; higher optical aberrations).

In our receiver system, the most significant aberration was coma, which affected the signal reception when large TX-RX angles were used. In contrast, other types of aberration (*i.e.*, spherical, chromatism, field curvature, and image distortion) had a non-significant impact on the system performance because only non-imaging detectors were used.

Table 3-2. List and main characteristics of the lenses used in this Thesis.

Diameter	Focal length	Type	Vendor/code	Acronym
1"	30 mm	Plastic Lens	-	PL
1"	16 mm	Aspheric molded glass	Thorlabs ACL25416U	AS1
2"	32 mm	Aspheric molded glass	Thorlabs ACL50832U	AS2
1"	25 mm	Fresnel plastic	Thorlabs FRP125	FR1
2"	32 mm	Fresnel plastic	Thorlabs FRP232	FR2

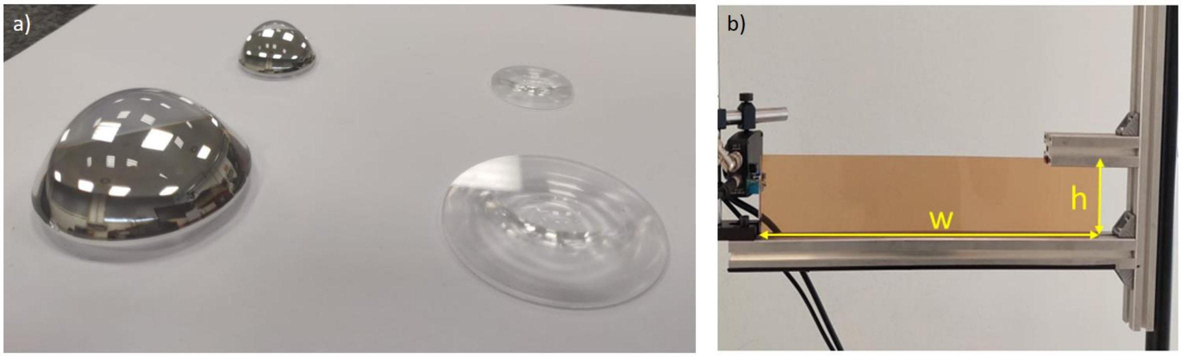

Figure 3-12. Photographs of a) the lenses used as optical concentrators in front of the PDs in our experiments and b) the slab doped with CIS QDs, where w represents its width and h its height.

In addition to the lenses mentioned above, we used a fluorescent slab doped with CIS QDs. As already explained, such an architecture allowed overcoming the étendue principle owing to absorption and re-emission processes. The slab used in our experiments was 38 cm in width and 8 cm in height (w and h in Figure 3-12b, respectively). The PMMA slab, in which the QDs were dispersed, enabled an FoV of approximately 120°, which is significantly higher than those achieved by typical lenses (of the order of 20°–40°). As further detailed in Section 4.4., the optical collectors for light sources placed at an infinite distance define, together with the detector size, an AFoV as:

$$\mathrm{AFoV} = 2\tan^{-1}\left(\frac{\mathrm{a}}{2\mathrm{f}}\right) \tag{3-1}$$

where a is the size of the active area of the detector (assumed of a square shape) and f the focal length of the optical collector [127].

3.3.3. Comparator

The analog signal coming from the PD was digitized and compared before being sent to the encoder board. We employed a single-threshold, UltraFast Precision 10ns Comparator LT1016 (shown in Figure 3-13), which is particularly suitable for high-precision applications. This apparatus responded very quickly to fast, low-level signals thanks to its high BW/gain product, allowing for BWs in the order of the MHz. A variable DC offset was added on top of the analog signal, and the result was compared to a reference value of 1.6 V. Indeed, the signal coming out of the TIA had a variable average value close to 0 V (owing to being AC-coupled); therefore, by adding a DC offset, the modulation signal could be compared with the reference one.

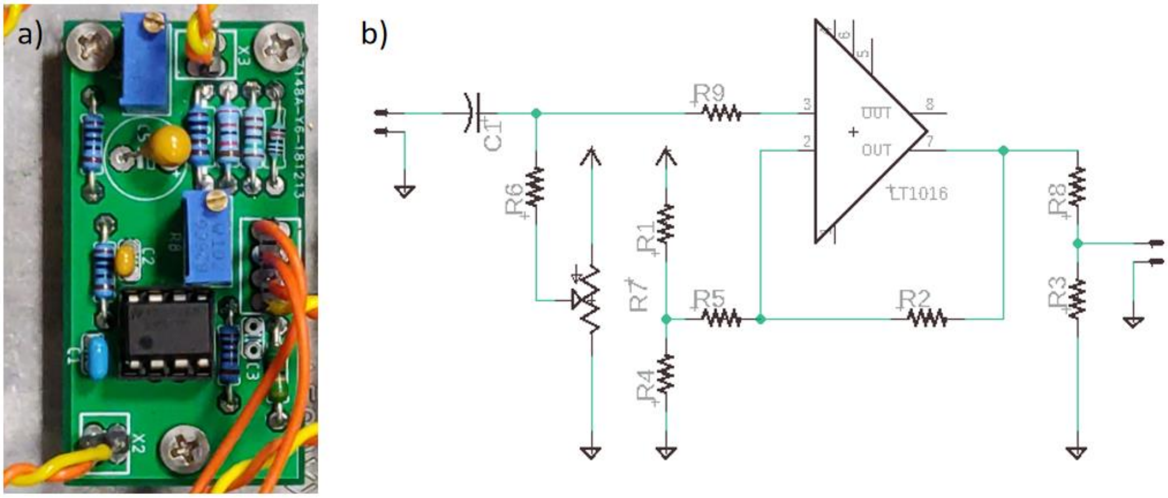

Figure 3-13. a) Photograph of the comparator. b) Circuit schematics: the analog signal is compared to a variable reference value after a variable DC signal has been added to the analog one. The outgoing signal (0–5 V) is reduced to 0–3.3 V to be compatible with the decoder.

Moreover, there was a 250 μV hysteresis, following the configuration of the Schmitt trigger comparator, realized through the resistors R2 and R5; this prevented background noise from continuously commuting the comparator, thereby increasing its stability. The Schmitt trigger is a threshold comparator that transforms the analog signal into a binary output (in our case, 0 and 5 V) depending on whether or not the incoming signal is above he reference value (1.6 V). Since the maximum input voltage on the receiver Arduino DUE platform is 3.3 V, the output signal, digitized at 0–5 V, was reduced to 0–3.3 V through a voltage divider to be compatible with the decoder board.

3.3.4. Decoder software

The digital signal coming from the comparator was read and analyzed by the decoder. In this Paragraph, we will describe the two software programs corresponding to those described for the encoder, starting with the one allowing exclusively for an evaluation of the PER.

The reception program on the Arduino DUE decoder was also structured in three parts: the definition and *setup()* ones were substantially the same as those used by the transmitter, except for the variable counting the number of correctly received packets, which was reinitialized to 0 at each communication. The *loop()* function contained only three lines of code, so as to minimize the time used for computation and signal elaboration. Thus, the *serialEvent()* and *serialEvent3()* functions, which were used to acquire the initial parameters, were identical to those of the transmitter; *serialEvent()* was used when communicating with this board through the computer, while *serialEvent3()* was employed when the board was far and received the parameters from the other platform *via* the Zigbee connected to the UART3. Further, the *serialEvent1()* function was also recalled for receiving and decoding the message: this function read the characters reaching UART1 and, each time a packet containing the starting byte was received, began a comparison of such a message with the pre-stored reference; whenever the comparation yielded a positive result, the correctly received packets count was increased. When an end transmission packet was received which had the same structure (pre-equalization "ð…" + starting byte "Z" + reference end message "ST" + end byte "\n", see Paragraph 3.2.2.) as the other packets but contained a different message, it stopped reading from the serial port and printed the number of correct packets and PER on the screen (and UART3, if the RX was distant and the computer was communicating with the TX board); then, all counters were reset, and serial buffers wiped.

As mentioned previously, the receiving board retransmitted each correct message through the UART2, which ensured:

- the possibility of using the board as an RX-TX (decoder-encoder), that is, using these messages to communicate with another device. This is useful in ITS applications (*e.g.*, platooning, replying to the first TX, *etc.*: see Section 4.5.);

- the possibility of carrying out a real-time check of the communication performance by displaying the messages through an oscilloscope, thereby allowing us to maximize the amount of relayed packets, if necessary, by modifying the comparator threshold (see Paragraph 3.3.3.).

The second program allowed for a bitwise decoding of the Manchster-encoded packets. The bit strings composing the message and the end transmission string were initialized in a similar way as done in the encoder. The parameters were initialized through functions *serialEvent()* e *serialEvent3()*, equivalent to those described for the encoder. The software printed the results on screen at the end of the communication so as to minimize the computing time. This program was based on the Arduino *interrupt()* functions, which paused the board every time a signal reached the reception pin (UART1). The system remained idle for a time proportional to the bit time (thus, each baud rate had a different idle time), to which some microseconds were added to account for jitter effects in the Arduino (estimated at approximately 1–2 μs). At this point, the system began reading the various bits, comparing them pre-stored ones and checking the length of the preambles (16 bits "0"’). If the process went through correctly, the counter of the messages sent with a correct preamble was increased by one unit, and the next 32 bits of information were verified; if all 32 bits were correct, the correct packets counter was increased by one unit. One received the end transmission string, the results were printed on screen, showing the numbers of packets with a correct preamble, correct packets (*i.e.*, packets having correct preamble and subsequent 32 bits), total bits (corresponding to the number of packets with a correct preamble multiplied by 32), and correct bits over the total ones.

3.4. Summary

We report here a table summarizing the apparatus employed in the main experiments carried out for this Thesis, except for what concerns the study on the MIR QCL system for FSOC, which is described in Section 6.2..

Table 3-3. Summary of the components used in our various experiments. Orange columns: TX hardware; green columns: RX hardware.

Reference	Encoder and current modulator	Light source	Optical collectors	Photodiode and electronic front end	Comparator and Decoder
	Transmitter		**Receiver**		
[28]	Arduino DUE + custom current modulator	Traffic light	PL	AC-coupled PDA36-A (old version of PDA36-A2)	Custom comparator + Arduino DUE
[22]		Traffic light	AS2	AC-coupled PDA36-A2	
[24]		Traffic light	AS1, AS2, FR1, FR2	AC-coupled PDA36-A2	
[25]		Traffic Light	FR1, FR2	AC-coupled PDA36-A2	
[27]		Motorbike headlight and rear light	AS2	AC-coupled PDA100-A2	
[29]		Museum spotlight	none	AC-coupled PDA100-A2	
[30]		Museum spotlight	none	AC-coupled PDA100-A2	
[18]		Collimated 405 nm LED	CIS Fluorescent Concentrator	AC-coupled Hamamatsu S3588-09 connected to the PDA100A2 TIA	

4. Intelligent transportation systems

4.1. Introduction to the Chapter

According to the World Health Organization, road accidents are one of the first ten causes of death in the world [128]. New technologies are required to increase the efficiency of transportation systems by advancing their safety protocol capabilities in response to critical events. Moreover, sharing dynamic information on the real-time state of roads and traffic between vehicles and infrastructures can allow driving units in controlled close formations (platoons), thereby increasing traffic fluidity and reducing environmental pollution [129]. In recent years, research has focused on ITSs through the development of both I2V and V2V communications, facilitated by the emergence of the IEEE 802.11p standard for short- to medium-range vehicular communications [130]. VLC technology finds one of its most interesting applications in this context, where fast communication, high reliability, and low latency are paramount requirements [131]. In addition, VLC can provide energy saving as well as low implementation and maintenance costs because it can function through the already existing road illumination and signaling infrastructures [132].

Despite the growing interest in this technology [133], however, an accurate characterization of the VLC channel for I2V and V2V applications in real-life scenarios is still lacking. For example, most studies propose the assessment of communication systems through measurements of the PER, which is a well-established parameter. However, PER alone is often insufficient in active road safety applications, where an accurate evaluation of the awareness level of receiving units in case of sudden events is paramount. In such scenarios, a statistically-averaged latency (SAL) value is a more appropriate performance indicator; however, to the best of our knowledge, no studies have reported this type of analysis so far. In view of VLC implementation in real ITSs, moreover, the relative positions of vehicles and infrastructures are dependent on road geometries and signaling regulations, so that LoS conditions are hardly achieved. In such a scenario, angular misalignments between transmitter and receiver units have significant consequences on the quality of the VLC link. Nevertheless, no studies have reported a detailed characterization of the optical performance of such a VLC setup in terms of communication cast and EFoV.

In this Thesis, we undertake such a characterization in a real urban environment, with regulatory LED sources and infrastructures, to assess the suitability of the VLC channel for safety-critical and smart driving applications [28]. In Section 4.2., we present a measurement campaign carried out in an urban setting to provide an extensive characterization of the VLC channel. The experiments are performed in the city of Prato (Italy) in collaboration with ILES srl, a private company that develops urban signaling systems. The results of this work allow for the extraction of a mathematical model of the channel taking into account the presence of stray light sources such as sunlight or other car headlights.

While most modern vehicles and urban roads are equipped with cameras (e.g., for pedestrian and lane detection), these cannot provide sufficient data rates for vehicular communications, and high-speed cameras are still too expensive for their comprehensive implementation in vehicular networks [134]; therefore, dedicated PD receivers are still the most efficient solution for this application [135]. However, there is a lack of studies demonstrating the low-latency performance of communication links. For this reason, we assess the experimental implementation of an IEEE 802.15.7-compliant VLC-based I2V2V architecture with the aim of validating the low-latency, high-speed, and high-accuracy transmission of alert messages from a regular traffic light to an on-board receiving unit [22]. Such high-quality performances can foster the development of new safety standards for cooperative ITS implementations: envisaged applications include collision avoidance, automatic braking, and car platooning through the continuous exchange of information between vehicles and infrastructure, with significant advantages in comparison to the performances obtainable via traditional RF-based technologies [136]. Herein, we demonstrate the possibility to achieve sub-ms ADR communication in a realistic urban scenario using the standard traffic light and experimental setup mentioned in the previous Paragraph. The results discussed in Section 4.3. lay grounds for the future development of VLC relay chains in ITSs, such as assessing the effects of a relative misalignment between transmitter and receiver units, implementing active tracking strategies, and analyzing the overall performance throughout the ADR chain by assessing the quality of the position, speed, and unit data relayed to incoming vehicles.

Among the many interesting characteristics of VLC technology, the intrinsic directionality of the optical channel is crucial for ITS applications. Lenses and compound parabolic concentrators may be employed at the RX and TX stations [137–140] to increase the optical gain and thereby improve communication quality even at high distances. However, in real ITS scenarios, ideal LoS conditions are rarely achieved because the relative positions of vehicles and infrastructures depend on road geometries and regulations, often resulting in significant angular misalignment between the transmitting and receiving units [141]. At present, no detailed studies exist on the optical performance of a realistic VLC setup of the kind just described. In this work, we perform an experimental campaign with the scope of determining the optical and transmission properties of our VLC link in realistic configurations [24,25]: we measure the AFoV, PER, and received amplitude for different TX-RX distances as well as orientations of the RX stage with respect to the traffic light to determine the advantages and disadvantages of each lens (including low-cost, commonly available plastic Fresnel lenses). In this framework, we evidence the importance of an accurate angular alignment between the transmitter and receiver when short distances are involved. This allows us to extend our previous findings and provide an angle-dependent optical model of the received intensity. As discussed in Section 4.4., these results represent a significant advancement for the implementation of real VLC-based ITSs.

Finally, we take a step further toward the integration of cooperative technology for active safety applications in ITSs by implementing a bidirectional VLC link for V2V and I2V communications. For this scope, we use real motorcycle head- and rear lights and characterize the transmission performances in an outdoor scenario under direct sunlight conditions. We consider typical road distances and relative positions between vehicles to evaluate SNR maps and PER values in various configurations and at different baud rates. Our findings are compared with the predictions of a physical model that takes into account non-ideal orientations of the RX unit, resulting in a very good agreement between the two sets of data.

The experimental setup used in this part of the work is represented in Figure 4-1 (see also Table 3-3). The digital encoder/modulator (Arduino DUE board and custom current modulator) is the same for all the experiments. For the different studies carried out in the framework of ITSs, we use a regular traffic light provided by ILES srl, our partner company for this work, as the TX light source (except for Section 4.5., for which more details will be provided further in the text) and a fast, high-gain RX unit equipped with various optical collectors and an AC-coupled detector. The setup is completed by a digitizer/decoder and a 1 Gs/s digital oscilloscope for signal recording and analysis. In addition to the DC supply required by the LED, the TX stage includes an AC modulator, consisting in a DC current generator with an AC external input to translate the modulation signal (provided by a digital encoder) into the corresponding current modulation. This achieves digital data transmission up to 230 kbaud through the optical carrier emitted by the traffic light. Digital modulation is based on OOK with Manchester encoding as recommended by IEEE 802.15.7 PHY I for outdoor VLC [142]. Our work focuses mainly on demonstrating the feasibility of I2V, V2V, and I2V2V communications through semiconductor-based sources and receivers, achieving significant transmission rates (for the considered instrumentation) and thereby increasing road safety.

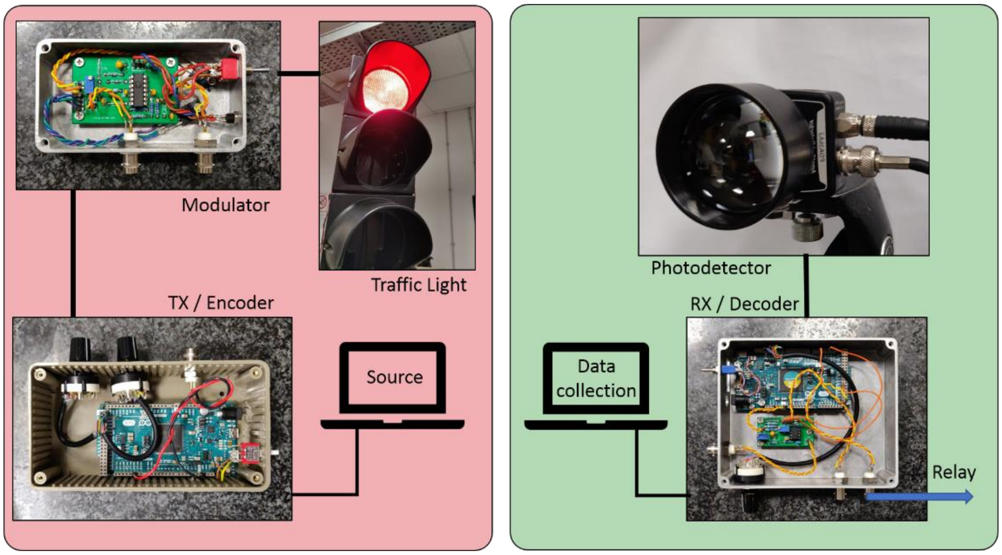

Figure 4-1. VLC hardware blocks used in the present part of this work. Left panel: TX-modulator block and regulatory traffic light source. Right panel: RX-ADR block.

4.2. Traffic light channel model

The characterization of a VLC channel can proceed via either a theoretical or empirical approach. The former is typically based on simplified scenarios, such as mathematical approximations for Lambertian emission and reflection pattern [98] or software-based physical simulations [143]. The latter, in contrast, requires measurement campaigns aimed at gathering empirical data for the development of a mathematical model of the channel [144] and is the far less common approach owing to intrinsic difficulties (*e.g.*, influence of ambient light and irregular LED emission patterns). In this work, we chose to perform a comprehensive characterization of the VLC channel in a realistic outdoor scenario using a regulatory traffic light equipped with a LED lamp that emits a VLC signal to a receiver placed along the same road.

4.2.1. Theoretical model

Let us first describe the fundamental elements of the VLC system: these are two electronic circuits (*i.e.*, the transmitter and the receiver) and an optical channel. The latter, in turn, consists of two optical stages (one installed on the transmitter and one on the receiver) and one final element corresponding to propagation in free space. Each element can be represented mathematically by its transfer function

H(f), which corresponds to the Fourier transform of the impulse response h(t). The transmitted signal can be represented by a time-dependent rectangular function:

$$s(t) = \sum_{j=0}^{\infty} s_j(t - jN_b T) \tag{4-1}$$

$$s_j(t) = A \sum_{i=0}^{7} s_k \cdot \mathrm{rect}\left(\frac{t - \frac{T}{2} + kT}{T}\right) \tag{4-2}$$

where A is the amplitude, T the pulse duration, s_k the transmitted symbol, and N_b the number of symbol sequences being transmitted. The chosen sequence was s = {1, −1, 1, −1, 1, 1, −1, −1}, encompassing all possible logic transitions of Manchester encoding, and is represented by the blue curve in Figure 4-2.

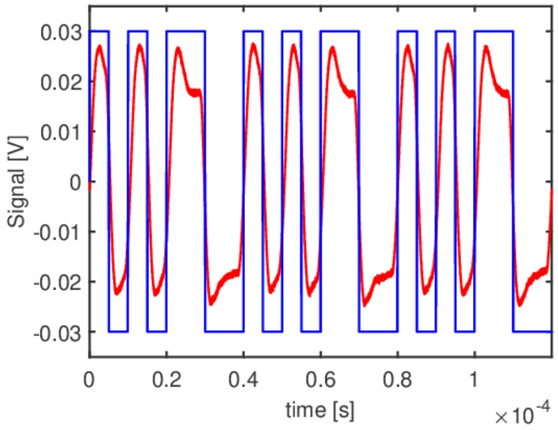

Figure 4-2. Blue curve: transmitted signal, modulated with OOK Manchester Non-Return-to-Zero (NRZ) scheme, as indicated in standard IEEE 802.15.7 for outdoor VLC. Red curve: received signal averaged over 4 acquisition periods. Data packages are constructed by attaching two square-wave blocks with frequencies of 50 kHz and 100 kHz and a global periodicity of 40 μs (= packet duration).

The received signal, s_{RX}, is the convolution of the transmitted signal, s_{TX}, with four impulse responses:

$$s_{RX}(t) = s_{TX}(t) \cdot h_{TX}^{el}(t) \cdot h_{TX}^{op} \cdot h_P(t) \cdot h_{RX}^{op} \cdot h_{RX}^{el}(t) + n(t) \tag{4-3}$$

where the second and sixth terms take into account the electronic conversion at the transmitter and receiver, respectively; the third and fifth terms represent the effects of the TX and RX optics, respectively; $h_P(t)$ represents the free-space light propagation; and n(t) is the Gaussian thermal noise at the receiver. In the frequency domain, this equation becomes:

$$S_{RX}(f) = S_{TX}(f) \cdot H_{TX}^{el}(f) \cdot H_{TX}^{op} \cdot H_P(f) \cdot H_{RX}^{op} \cdot H_{RX}^{el}(f) + N(f) \tag{4-4}$$

4.2.2. Experimental setup

The TX (shown in Figure 4-3) consisted of the LED light source and its current driver. A current of 0.7 A, required by the traffic light LEDs, was generated to provide the nominal luminous flux. A current modulation allowed for the insertion of the data stream into the optical carrier. The modulator was placed after a P-I regulation stage to stabilize the supply current from DC to ~1.5 kHz by adjusting the servo RC constant. In such a configuration, any modulation above the PI servo cut frequency (given by $f_{TX} = 1/2\pi RC \approx 1.5$ kHz) is not compensated by the P-I loop but added as a current modulation.

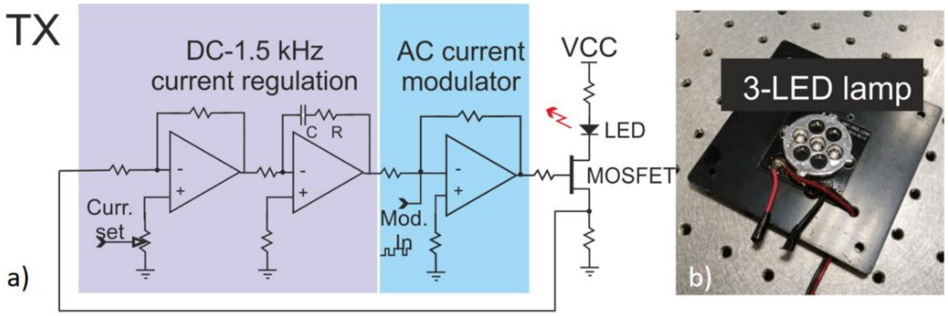

Figure 4-3. a) Schematics of the TX unit. A P-I regulation stage (purple area) stabilizes the DC current value in the RC BW for the LED to provide the required nominal light intensity. A modulation stage (cyan area) inserts a high-frequency current modulation in the LED source, shown in panel b).

The modulation waveform, provided by a function generator (Tektronix AFG1022), matched an OOK Manchester encoding (Figure 4-2), according to PHY I of standard IEEE 802.15.7 for outdoor VLC [57]. The red LED lamp (Lux Potentia OJ200-R07, 1 A, 12 V) of the traffic light consisted of three high-power LEDs. A red-colored Fresnel lens was used to shape the beam according to the standards.

The receiver hardware (Figure 4-4) consisted of an active PD (Thorlabs PDA36-A) with a physical AC decoupling of the chip from the first transimpedance amplification stage obtained *via* a multielement RLC network. The decoupling allowed to filter out any undesired low-frequency light variations (*e.g.*, vehicle headlights and sunlight) except the modulation signal. The photoreceiver gain was set at the highest value that could afford a BW > 150 kHz. The concentrator was a 25-mm diameter, 30-mm focal length, uncoated aspheric plastic lens. Data were collected through a 70-MHz, 1-Gs/sec digital oscilloscope (Tektronix TBS2074).

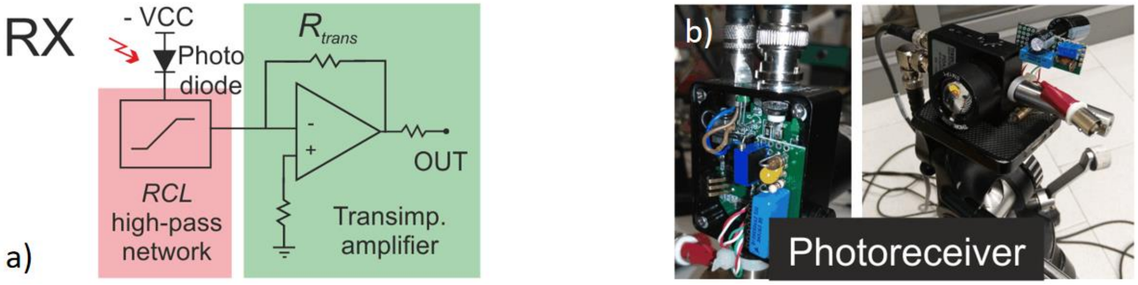

Figure 4-4. a) Schematics of the RX stage. b) Thorlabs PDA36-A detector modified through the physical insertion of a high-pass RCL network between the PD and the first stage of transimpedance amplification.

For the measurement campaign, we positioned the traffic light on the right side of the right-most lane, with a 0.75 m indentation and 2.83 m height (according to Italian regulations UNI11248 and UNI13201-2), as illustrated in Figure 4-5. The receiver was positioned in front of the TX along the points of a grid (Figure 4-6) centered at the position of the traffic light. The x axis corresponded to the road length, the y axis to the road width, and the z axis to the distance from the ground. The grid points along the x axis ranged from 3 to 30 m, with a higher density in the first 10 m (specifically, 3, 4, 5, 7, 10, 15, 20, 25, and 30 m). The measurement points were at 0.75, 1.75, 2.75, 3.75, 4.75, and 5.75 m. Such a grid was repeated along the z axis for three different heights: 0.75 m (corresponding to the standard height of car headlights), 1 m (dashboard), and 1.35 m (rear-view inside mirror). The RX optical axis was aligned toward the TX and, thanks to the lens used, the image was focused into the active area of the detector for all points on the grid. This configuration also presented the advantage of avoiding interference from reflections of the lamp signal on the tarmac, which can be demonstrated as follows.

Figure 4-5. Experimental setup used in the measurement campaign. Any stray light contribution was eliminated by the AC coupling of the PD.

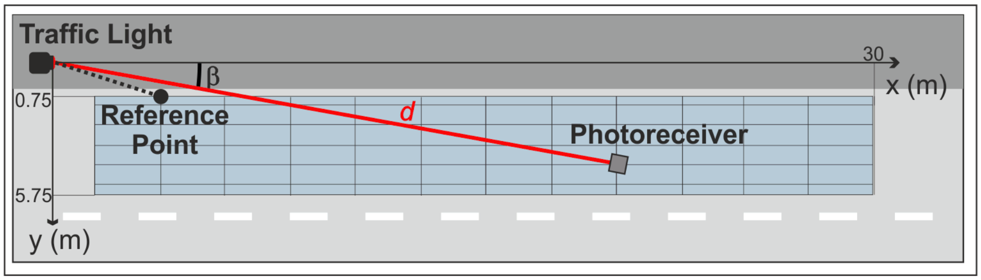

Figure 4-6. Measurement grid used in this work. The reference (0 dB) point is located at coordinates (4, 0.75, 1.35) m.

Let us consider the case of a receiver positioned along the optical axis of the traffic light lens as shown in Figure 4-7. The FoV θ of the receiver is:

$$\frac{\theta}{2} = \arctan\left(\frac{l}{2F}\right) \tag{4-5}$$

where l and F are, respectively, the width and lens focal length of the detector. For geometrical reasons, reflections from the tarmac (red line in Figure 4-7) cannot enter the detector's FoV when $\theta/2 \leq \gamma + \delta$, so the above expression becomes (see figure for a description of the parameters):

$$\arctan\left(\frac{l}{2\mathrm{F}}\right) \leq \arctan\left(\frac{\mathrm{Z}+\mathrm{S}}{\mathrm{D}}\right) + \arctan\left(\frac{\mathrm{Z}-\mathrm{S}}{\mathrm{D}}\right) \tag{4-6}$$

Given our experimental setup parameters, F = 30 mm and l = 6 mm, Equation (4-6) was always verified in our measurement grid for D < 35 m and the three receiver heights employed, except for very large distances (D ≥ 50 m). In the latter case, the detector's optical axis progressively leaned toward the horizontal plane for increasing distance, thus allowing reflection to enter the FoV cone.

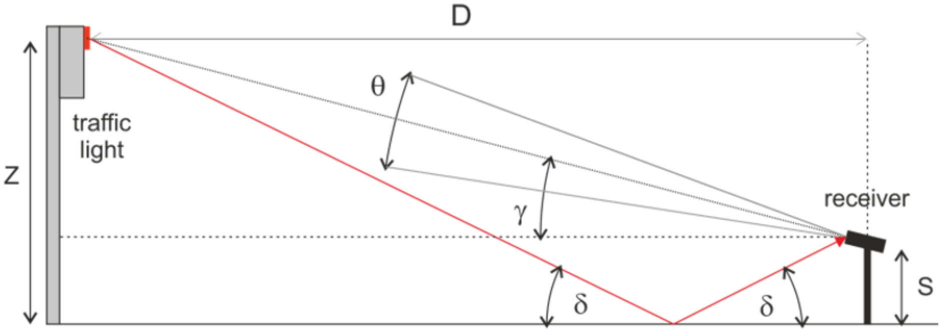

Figure 4-7. Reflections form tarmac (red line) in relation to parameters used in the text.

The detector was connected to an oscilloscope, and we collected 200.000 samples at a rate of 0.5 MSps, encompassing ten Manchester modulation periods. The measurements were performed during one day in sunny weather conditions. The raw data, recorded for each point of the grid, were processed to reduce the effects of high-frequency noise, and the received amplitude in the frequency domain was obtained. The data were also subjected to a binning procedure: briefly, we observed that the components of the received signal of frequencies higher than 500 kHz exhibited a negligible amplitude, and we applied a downsampling procedure to reduce the observation interval and filter out the unnecessary components. The binning procedure consisted in taking a cluster of consecutive samples and replacing it with their average value $N_{bin} = f_c/2f_{max}$ (where f_c is the initial sampling frequency and f_{max} the highest observation frequency), which was equal to 250 in our experiment (the oscilloscope sampling frequency being 250 MHz).

4.2.3. Results and discussion

For each point of the grid, we took into account the ratio between the transfer function (TF = $S_{RX}(f)/S_{TX}(f)$) of the system and that calculated for the reference position. The amplitudes ΔH_i for the i-th locations in the grid at the three chosen heights are defined as:

$$\Delta H_i = \frac{H_i(f)}{H_{ref}(f)} \tag{4-7}$$

$$H_i(f) = \frac{S_{RX_i}(f)}{S_{TX_i}(f)} \tag{4-8}$$

$$H_{ref}(f) = \frac{S_{RX_{ref}}(f)}{S_{TX_{ref}}(f)} \tag{4-9}$$

where $S_{TXi}(f)$ and $S_{RXi}(f)$ are the FFTs of the transmitted and received signal, respectively; $H_i(f)$ is the TF between the traffic light and the i-th point on the grid; and $H_{ref}(f)$ is the TF between the traffic light and the reference point. Namely, the reference point (*i.e.*, the point showing the maximum amplitude, corresponding to 0 dB) was located at coordinates (4, 0.75) m for a height of 1.35 m, as shown in the grid in Figure 4-6. Because all measurements were carried out on the same signal, $S_{TXi}(f) = S_{TXref}(f)$, and Equation (4-7) can be rewritten as follows:

$$\Delta H_i = \frac{S_{RX_i}(f)}{S_{RX_{ref}}(f)} \tag{4-10}$$

The amplitude values are reported in Figure 4-8 in a logarithmic scale (dB), where one can notice that the intensity decreases with increasing height.

The propagation of the VLC signal is typically approximated by the Lambertian path loss [98]:

$$I = \frac{I_0 \cos^{\nu} \varphi}{d^2} \tag{4-11}$$

where I_0 is the intensity in the axis of irradiance, φ the irradiance angle, ν a parameter reflecting the contribution of the lens, and *d* the TX-RX distance. The cosine propagation law presumes a homogeneous diffusion of light from its source, which may not be true in our case owing to the presence of a lens, which gives rise to a shaped beam pattern. For our mathematical characterization of the VLC signal propagation, we first considered that the intensity of the received signal over the grid depends on the receiver position in spherical coordinates (α, elevation; β, azimuth; and d, TX-RX distance).

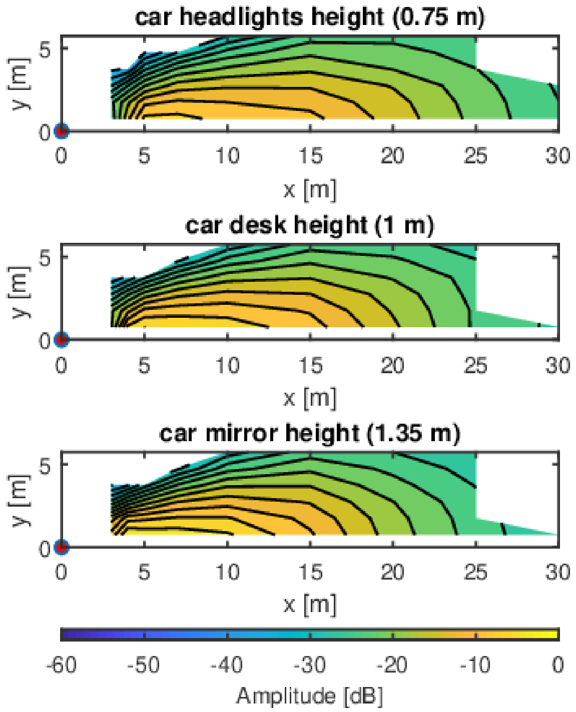

Figure 4-8. Map of measured amplitudes [dB] of the VLC signal H_i for the experimental grid in Figure 4-6 for three different heights: 0.75 m for car headlights, 1 m for car desk, and 1.35 m for car internal mirror.

Then, we proposed the following three models:

$$I_1(\alpha, \beta, d) = \frac{f(\alpha, \beta)}{d^2} \tag{4-12}$$

$$I_2(\alpha, \beta, d) = \frac{f(\alpha, \beta, d)}{d^2} \tag{4-13}$$

$$I_3 = f(\alpha, \beta, d) \tag{4-14}$$

where the first two equations are modifications of (4-11) in which the numerator has been generalized whilst retaining the dependence on the distance squared. An even more general approach is given by (33), where the optical intensity is a simple polynomial function of (α, β, d) without an explicit $1/d^2$ weight. The best fitting parameters for the three models were calculated through multiple generalized linear regression (MGLR), a useful method in those cases where more than one independent variable is present. The input parameters for the regression were: the model under assessment (I_1, I_2, or I_3); the maximum order of the variables in the polynomial function (1–9 for α and d, and 2–8 for β); and the error distribution (Normal, Poisson, Gamma), leading to the evaluation of nine models in total. The output of the regression was a set of polynomial coefficients of the function that fits the intensity. The interested reader is referred to ref. [28] for a detailed analysis of the procedure. Briefly, we calculated the root mean square error (RMSE) between the experimental data and the corresponding values of the polynomial fitting function over the entire grid. We found that the error decreased faster for model I_1, while the other two were more accurate at the expenses of introducing a higher number of polynomial terms; moreover, the error decreased faster using the Gamma and Poisson distributions than the Normal one. As a consequence, we chose to compare the following two models to define a propagation model valid for extrapolation at distances outside of our measurement range: I_1 with a Gamma distribution (fastest decrease in RMSE), Equation (4-15), and I_2 with a Poisson distribution (lowest error reached), Equation (4-16):

$$\begin{aligned} \mathrm{I}_1(\alpha,\beta,\mathrm{d}) = \frac{1}{\mathrm{d}^2}(&\mathrm{b}_1 + \mathrm{b}_2\alpha + \mathrm{b}_3\beta^2 + \mathrm{b}_4\alpha^2 + \mathrm{b}_5\alpha\beta^2 + \mathrm{b}_6\beta^4 + \mathrm{b}_7\alpha^3 + \mathrm{b}_8\alpha^2\beta^2 + \mathrm{b}_9\alpha\beta^4 \\ &+ \mathrm{b}_{10}\alpha^4 + \mathrm{b}_{11}\alpha^3\beta^2 + \mathrm{b}_{12}\alpha^2\beta^4)^{-1} \end{aligned} \tag{4-15}$$

$$\begin{aligned} \mathrm{I}_2(\alpha,\beta,\mathrm{d}) = \frac{1}{\mathrm{d}^2}\exp\{&\mathrm{b}_1 + \mathrm{b}_2\alpha + \mathrm{b}_3\beta^2 + \mathrm{b}_4\mathrm{d} + \mathrm{b}_5\alpha^2 + \mathrm{b}_6\alpha\beta^2 + \mathrm{b}_7\alpha\mathrm{d} + \mathrm{b}_8\beta^2\mathrm{d} + \mathrm{b}_9\alpha^2 \\ &+ \mathrm{b}_{10}\alpha^2\beta^2 + \mathrm{b}_{11}\alpha^2\mathrm{d} + \mathrm{b}_{12}\alpha\beta^2\mathrm{d}\} \end{aligned} \tag{4-16}$$

The values of the coefficients are given in Table 4-1. Figure 4-9 presents the intensity of the propagation models $I_1(\alpha, \beta, d)$ with a Gamma distribution (panel a), $I_2(\alpha, \beta, d)$ with a Poisson distribution (panel b), and the conventional Lambertian model (panel c). The intensities were extended an area of 100 × 50 m, which is larger than the measurement grid. The first two models were characterized by the same complexity (*i.e.*, 12 terms) and accuracy, as shown in the following.

Table 4-1. Values of coefficient b for the models $I_1(\alpha, \beta, d)$ with a Gamma distribution and $I_2(\alpha, \beta, d)$ with a Poisson distribution.

Coefficient	**Value for I_1 model**	**Value for I_2 model**
b_1	0.088395	6.1107
b_2	1.8365	20.436
b_3	0.53823	−9.8384
b_4	14.718	−0.09868
b_5	6.3874	47.629
b_6	0.92338	−12.142
b_7	46.406	−1.0858
b_8	26.178	−0.08044
b_9	−7.8413	52.16
b_{10}	52.665	13.944
b_{11}	39.219	−1.4756
b_{12}	−1.3364	0.90893

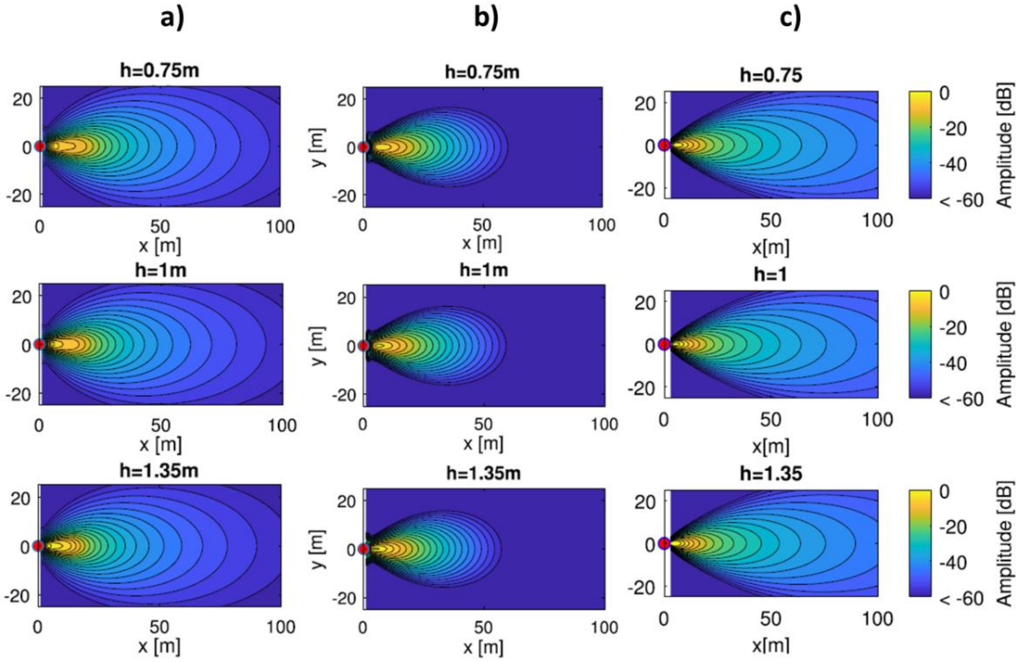

Figure 4-9. Intensity of the different models in an area of 100 × 50 m; the PD heights are 0.75, 1, and 1.35 m for each model. a) I_1 model with a Gamma distribution; the polynomial order is 4 for α and β. b) I_2 model with a Poisson distribution; the polynomial order is 3 for α, 2 for β, and 1 for d. c) Conventional Lambertian model.

To compare the two proposed models with the classic Lambertian one, their accuracies over the entire experimental grid were calculated as the percentage error of the model in comparison to the measured value for each point. The accuracy maps are presented in Figure 4-10, where the color scale ranges from lowest (blue) to highest (yellow) error. Interestingly, the conventional model presented a significantly higher RMSE compared to the two others: 0.097 for the Lambertian *versus* 0.030 and 0.029 for I_1 and I_2, respectively.

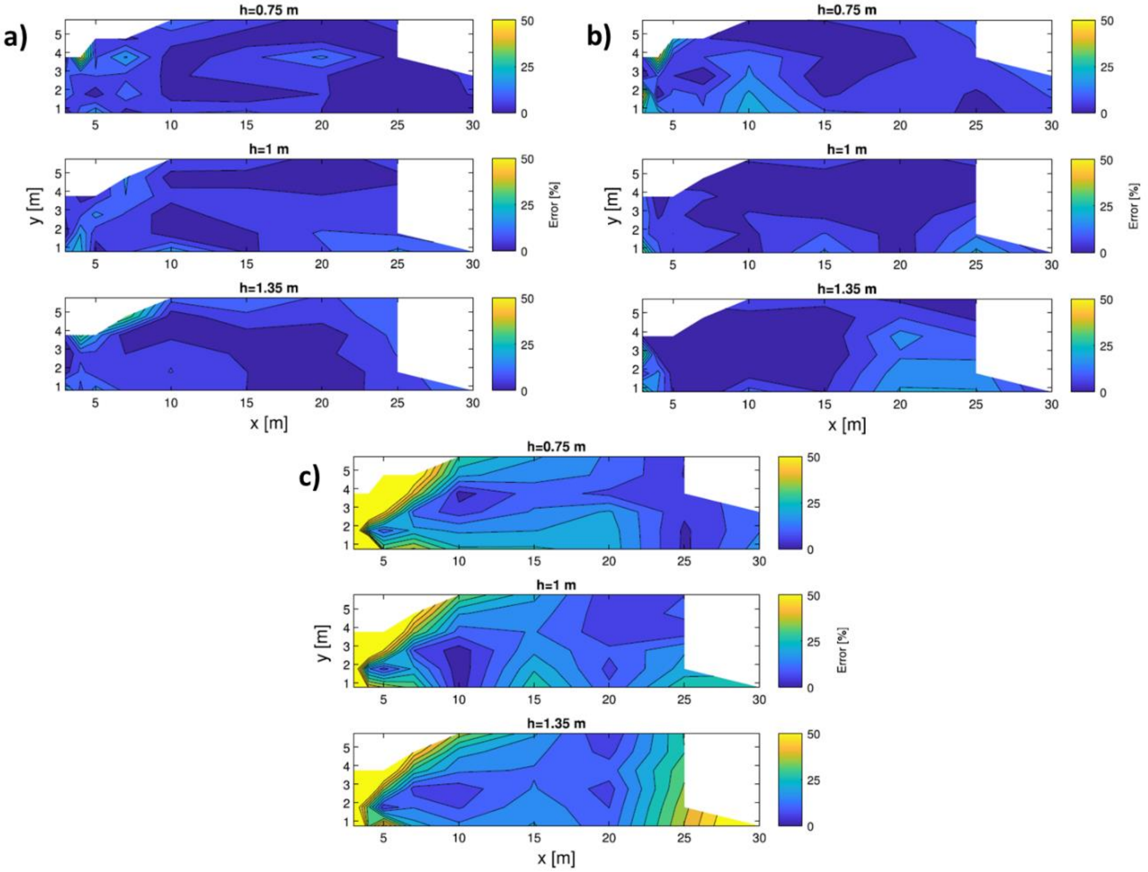

Figure 4-10. Accuracy of the three models in analysis in the measurement area for different heights (0.75, 1, and 1.35 m) of the PD. a) I_1 model with a Gamma distribution; the polynomial order is 4 for α and β. b) I_2 model with a Poisson distribution; the polynomial order for is 3 for α, 2 for β, and 1 for d. c) Conventional Lambertian model.

Using the accuracy maps, it is possible to select the most appropriate model according to the TX-RX distance and height of the receiver. When performing such a choice, however, one must also take into account the accuracy-complexity tradeoff of each model: in a dense urban scenario, where tens or hundreds of traffic-lights may be present, a global model of propagation might be difficult to attain in a reasonable time using a highly accurate model, as this would entail a higher order of parameters in the polynomial solution and, thus, higher computational complexity. Finally, although the bit error rate (BER) of the VLC link was not measured directly, it is possible to derive its performance analytically from the intensity measurements: as a result, the error probability is 10^{-3} for distances up to 30 m from the LED (Figure 4-10a,b).

4.3. Low-latency I2V VLC chain with active decode and relay

4.3.1. Experimental setup

The experimental setup consisted of a digital encoder/modulator, a standard traffic light as the light source, a fast and high-gain receiver, a digitizer/decoder, and an ADR digital stage. The transmitter included an AC modulation added on top of the DC supply required by the LED lamp obtained as described in the previous Section. The TX stage transmitted digital data, embedded in the optical carrier with OOK modulation and Manchester encoding, at rates up to 230 kbaud. The duty cycle of current driven into the LED source was 50%; to maximize the modulation intensity without affecting the regulatory intensity of the lamp, we performed a 0-200% modulation. No derating in the LED source characteristics was observed. The receiver consisted of a 36-mm^2 transimpedance PD with a variable secondary-stage gain and an aspherical 2" uncoated lens. To filter out any spurious DC stray light components (*i.e.*, sunlight or 100-Hz artificial light), the PD was physically AC-coupled before the first transimpedance stage, thereby retaining only the modulation component. The amplified analog signal was digitized by a variable-threshold comparator stage, and then analyzed and decoded by an Arduino DUE microcontroller platform. The message, once decoded, was compared bit-wise with a reference message and relayed only if all the bits were correctly received.

For this work, the experimental setup included an ultra-fast ADR stage intended for swift propagation of critical information through the vehicular chain. The collection lens was placed at approximately 105 cm from the ground, mimicking the typical height of a car dashboard (see Figure 4-11 for a sketch of the experimental configuration). The signal, after passing through the optical channel and being received by the PD, was actively decoded and interpreted by the Arduino DUE board, which checked for the correctly received bits as mentioned above. If no errors were detected, the message was re-encoded and sent to the modulator for relaying toward incoming units.

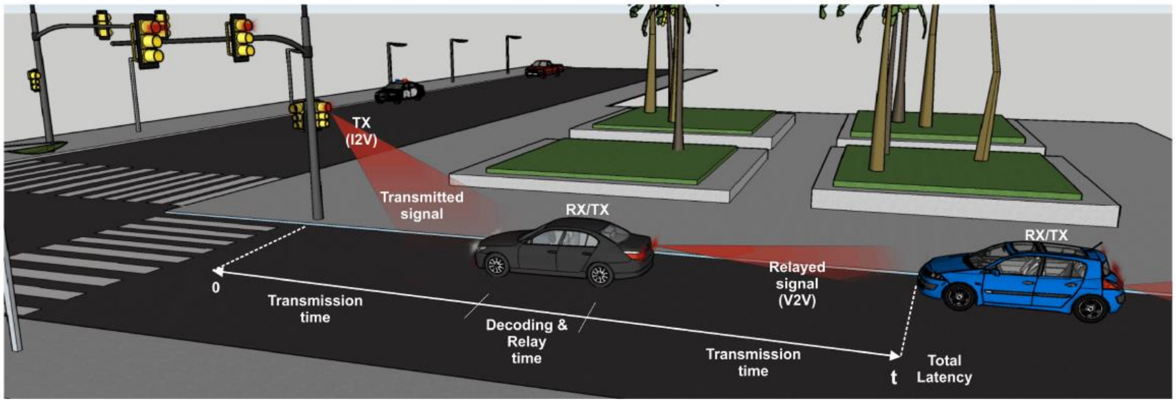

Figure 4-11. Illustration of the I2V2V ADR scenario simulated in this work: a traffic light sends a message to the first car (I2V) which acts as an active relaying node by decoding the message and relaying it to the next vehicle (V2V).

The measurements were carried out in a 55-m long corridor (see Figure 4-12), where the presence of artificial and ambient light sources led to multipath reflections, requiring a high robustness in noise rejection schemes. To maximize the received amplitude, the detector's optical axis was aligned with the center of the traffic light lamp. The distance between TX and RX was varied between 6 and 50 m while the gain was varied in steps of 10 dB to assess the system performance in a range of distance/gain configurations.

4.3.2. Results and discussion

The performance of the communications system was initially evaluated based on the following parameters:

- *PER:* the ratio between lost and total transmitted packets, where a packet is considered lost if a single bit is altered during transmission;
- *Latency:* the time elapsed between the first bit of transmitted message and the last bit of the relayed message after a correct reception and decoding process.

The total latency L_n was inferred from the raw data as a function of error cluster size:

$$\mathrm{L_n} = \mathrm{L_0} + \mathrm{N_{lost}}(\mathrm{IPD} + \mathrm{PT}) \tag{4-17}$$

where L_0 is the minimum time needed to relay a packet, N_{lost} the number of consecutively lost packets (*i.e.*, the cluster size), IPD the interpacket delay, and PT the packet duration (see also Figure 4-13).

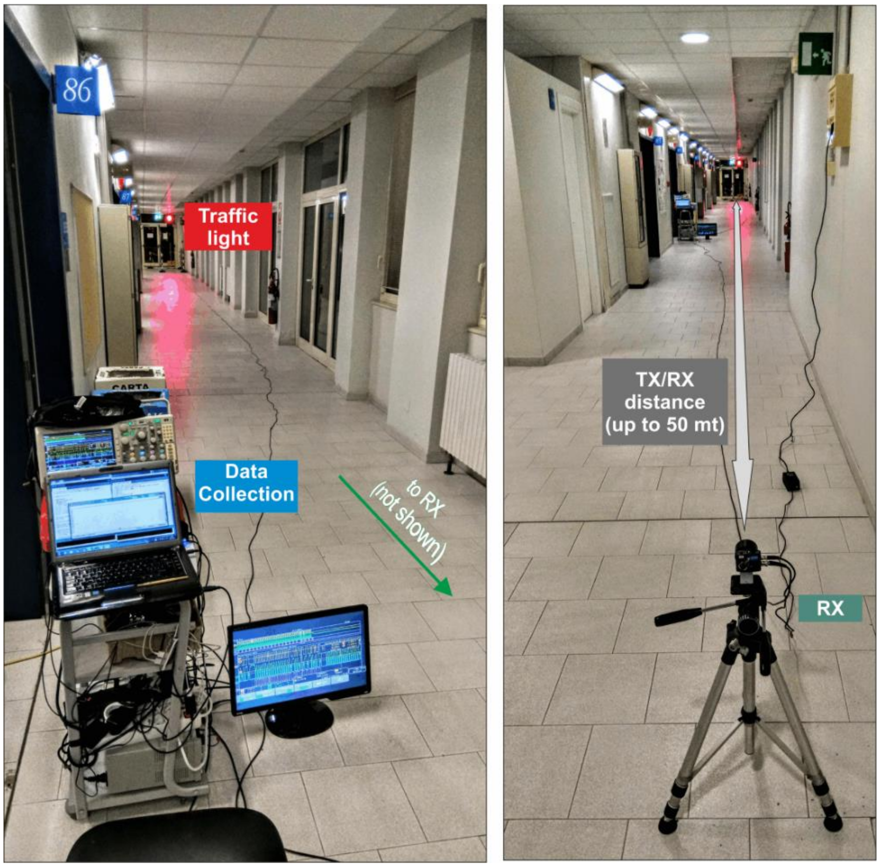

Figure 4-12. Experimental setup: a standard traffic light transmits a VLC signal to a photo-receiver stage equipped with an ADR block. The data collection unit includes a computer and an oscilloscope. The maximum distance between TX and RX units was 50 m in LoS configuration.

PER analysis was carried out by sending a predefined message between the TX and RX units at rates ranging between 230 and 19 kbaud. The PER values are presented in Figure 4-14 grouped by TX-RX distance, and the graphs clearly show that the performance of the system decreased with increasing distance following a decrease in the SNR received by the PD. However, the prototype successfully established communications up to the maximum available distance of 50 m at all tested baud rates, and a PER $< 10^{-5}$ (*i.e.*, lossless transmission in our observation window, since we fixed the number of sent packets as 100000, a trade-off between the time required for the measurement and acceptable PER) was obtained for a maximum distance of 42 m at the transmission rates of 19 and 57 kbaud. At ultra-low latency rates (230 kbaud), we observed a PER $< 10^{-4}$ at 30 m and PER < 0.3 at 50 m, while a near-lossless PER $= 2 \times 10^{-5}$ could be obtained at 50 m through a minor adjustment of the traffic light's vertical axis with respect to the standard orientation, which is typically optimized for maximum visibility in the range of 12–18 m [28].

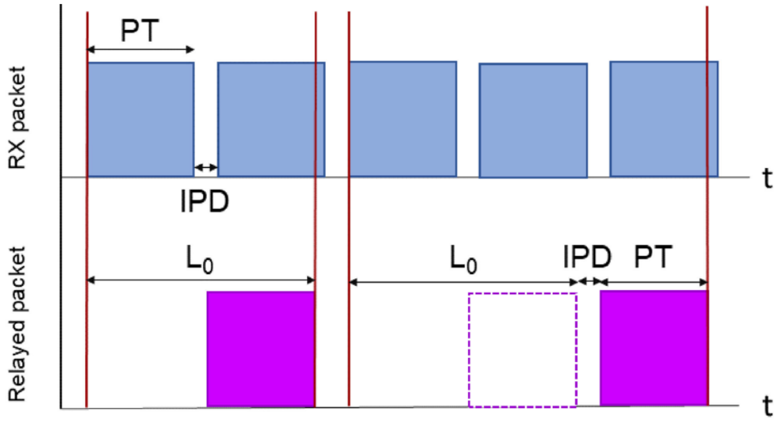

Figure 4-13. Reconstruction of latency from packet structure. L_0 = minimum time required to relay a packet. N_{Lost} = number of consecutively lost packets. IPD = interpacket delay. PT = packet size in time.

It should be noticed that we observed a drop in the RX-ADR block ability to correctly receive packets at approximately 20–40 mV, originating from the interference of a residual 100 Hz neon light signal. The presence of a higher number of neon sources, and consequently a higher noise, in a radius of 40 m could be the cause of the deviation in monotonic behavior in the PER *vs*. distance plots (Figure 4-14) at distances above 40 m and high baud rates. Nevertheless, it is worth reminding that the best experimental values estimated for PER and BER (respectively, $< 10^{-5}$ and $< 3 \times 10^{-7}$) correspond to those of a worst-case scenario because of the limited of number of transmitted packets.

Next, we moved on to an analysis of the latency of the system by testing its suitability for beaconing of situational information in one representative configuration (230 kbaud). The delay between packet transmissions was 100 ms, which is significantly higher than the packet time (280 μs), leading to a less constant data stream in comparison to the broadcast scenario (see also Section 2.6.). The data were relayed at sub-millisecond speeds (595 μs), and no loss of packets was observed, reinforcing the possibility of employing this setup for time-critical road safety applications in ITSs.

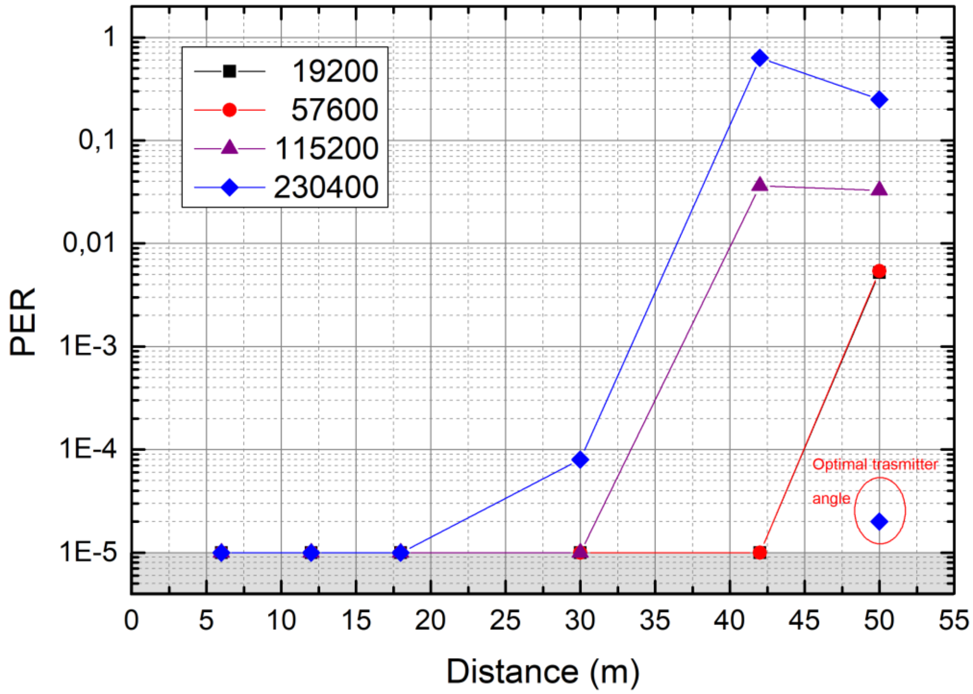

Figure 4-14. PER as a function of distance for different baud rates (230, 115, 57, and 19 kbaud). The shaded area is our lower limit in the observable PER (10^{-5}) owing to the transmitted number of packets. The point at 50 m (blue diamond) represents the best performance obtained at the highest baud rate if the traffic light vertical angle is optimized by a few degrees.

However, a more appropriate performance metric should be considered in the present case: the SAL value, which is a generalization of the packet inter-reception parameter [145] for ADR systems taking into account the distribution of errors in the transmission chain and, therefore, any possible clustering of errors occurring during the entire time interval. The SAL value thus represents the most probable latency value that may be observed for a certain PER, and it is more useful than the PER itself or a simple average of latencies when statistical response times and success rates must be accurately determined. Herein, we recorded the distribution of errors for different PER values. Entire data tracks were acquired in order to perform an accurate post-processing, and we restricted the analysis to values of PER $\geq 10^{-3}$, so that the total recorded number of lost packets in our observation window would be higher than 10 (limit value for a statistically relevant error dataset). The curves representing the number of occurrences as a function of the number of consecutively lost packets (*i.e.*, the cluster size) for different PER values are shown in Figure 4-15. The clustering in relaying messages increased with the PER value: the maximum cluster size was 26 for PER = 3×10^{-1}, while the minimum was 3 for PER = 3×10^{-3}.

Subsequently, we extracted the probability mass function (PMF) and cumulative distribution function of consecutively lost packets (CDF) [146] for the PER values 3×10^{-1}, 1×10^{-1}, and 5×10^{-2}. Three discrete distributions were tested to determine the best estimation for SAL: binomial, negative binomial, and Poisson. The best agreement for all the analyzed PER values was found with the negative binomial hypothesis; the PMF is given by:

$$f(k, r, p) = \binom{r + k - 1}{p} p^{k} (1 - p)^{r} \tag{4-18}$$

where k is the number of successes (*i.e.*, the number of consecutive packets received correctly), r that of failures (*i.e.*, the number of consecutive wrong packets), and p the success probability (*i.e.*, the probability of receiving correct packets).

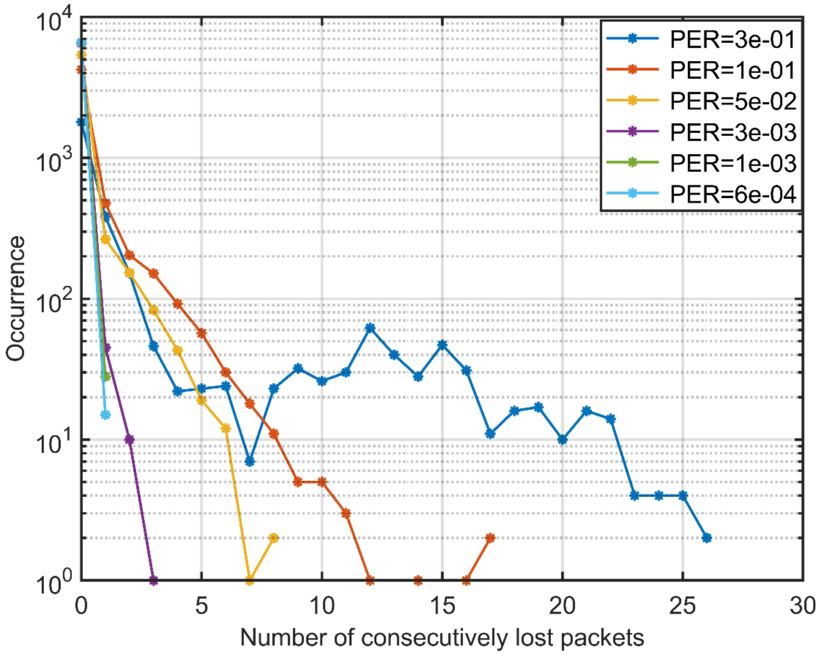

Figure 4-15. Number of total occurrences (*i.e.*, the total number of sent packets) as a function of the number of consecutively lost packets (*i.e.*, cluster size) obtained through measurements at various PER values. The legend indicates the different PERs considered in the latency analysis.

The CFD analysis of the cluster size yields the number of broadcast packet retransmissions that can achieve a specific success probability in the transmission chain, as shown by the solid lines in Figure 4-16. Such a packet number is connected to the corresponding latency using Equation (4-17), which gives us the right-hand axis of Figure 4-16 (obtained for 230 kbaud). In the figure inset, the dashed vertical lines correspond to three significant levels of probability of successful relaying (PSR): 95%, 99%, and 99.9%; the horizontal line indicates the sub-ms latency region. One can notice that, even for the worst PER value of 3×10^{-1} at 230 kbaud, a successful transmission can be achieved with a 99.9% confidence level in approximately 8 ms, whereas for PER $\leq 10^{-3}$ sub-ms latencies are obtained.

For the sake of clarity, the latency model parameters corresponding to the dash-dot lines in Figure 4-16 are summarized in Table 4-2. It can be noticed that best fitting PMF for the lowest PER values was a Poisson distribution with λ parameter owing to the low error rate in the measurements.

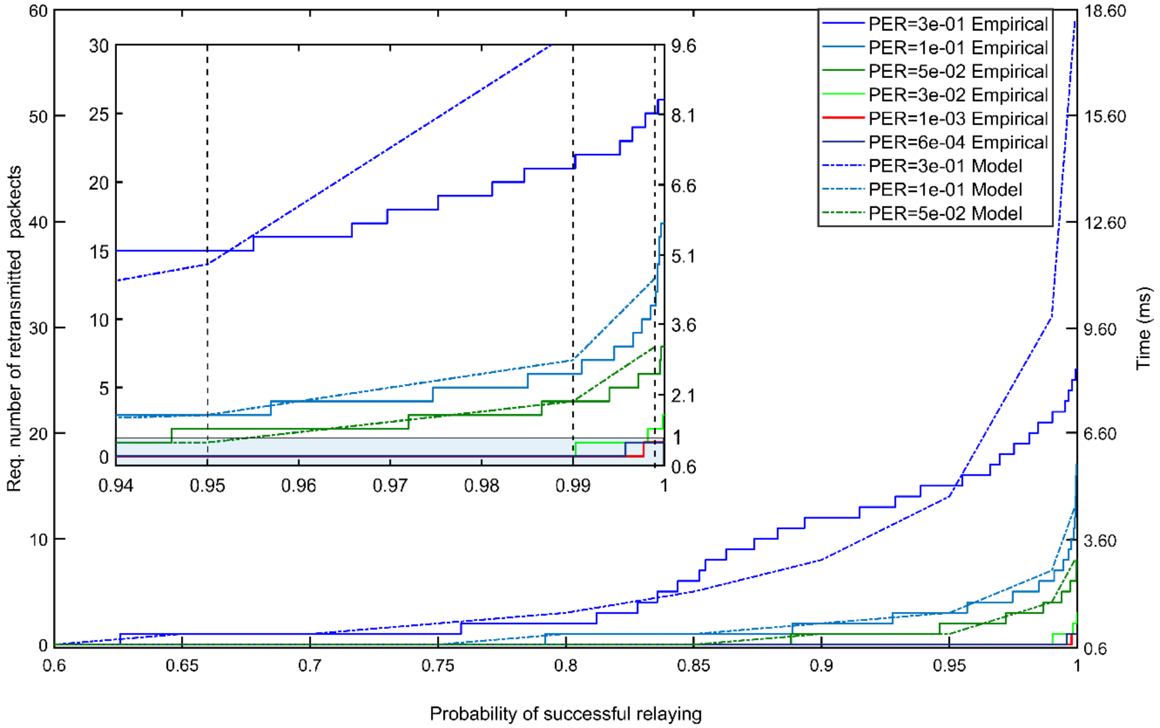

Figure 4-16. Performance of the analyzed system for road safety critical applications. The right-hand axis is calculated for 230 kbaud. Inset: zoom of the probability of successful relaying in the range 0.94–1.00. Vertical dash lines: PSR = 0.95, 0.99, and 0.999; dash-dot lines: negative binomial model.

One of the advantages of a low-latency system in terms of road safety is the reduction of the stopping distance of vehicles in response to a critical event, such as a traffic light turning red. Let us consider the total stopping distance as the sum of the perception-reaction distance $D_{p\text{-}r}$ and the braking distance D_{brake} [147]:

$$D_{stop} = D_{p-r} + D_{brake} = vt_{p-r} + \frac{v^2}{2\mu g} \quad (4\text{-}19)$$

where v is the speed of the vehicle, $t_{p\text{-}r}$ the reaction time, μ the friction coefficient (typically = 0.7 for a road in good conditions), and g the gravitational acceleration. In this calculation, we employed 57 kbaud as the transmission rate because lower baud rates are more reliable and provide low PER and SAL values for the present system, thus they are the best trade-off for safety-critical applications such as car braking. We considered three scenarios characterized by different initial speeds and distance-to-traffic-light (D) stopping distances for an average family car in dry road conditions: the corresponding latencies were calculated by considering the reaction time equal to latency (delay) in braking triggered by human, IEEE 802.11p, C-V2X, and VLC [148,149]. The reaction latency for VLC is the time interval between the start of a transmitted packet and the first correctly received packed at the RX, and it is obtained by subtracting the packet time from the ADR latency.

Table 4-2. Parameters of the best fitting PMF models for latency: negative binomial (with parameters r and p) for $3 \times 10^{-3} \leq \text{PER} \leq 3 \times 10^{-1}$; Poisson distribution (with parameter λ) for PER = 1×10^{-3} and 6×10^{-4}.

PER	Parameters	Target Probability			
		0.9	0.95	0.99	0.999
		Latency [nr. of packets]			
3×10^{-1}	r = 0.1691; p = 0.0638	8	14	31	59
1×10^{-1}	r = 0.1691; p = 0.0638	2	3	7	13
5×10^{-2}	r = 0.1691; p = 0.0638	1	1	4	8
3×10^{-3}	r = 0.1691; p = 0.0638	0	0	0	2
1×10^{-3}	λ = 0.0042	0	0	0	1
6×10^{-4}	λ = 0.0023	0	0	0	1

The results are compared in Table 4-3, where the reported reaction distance refers to automated braking systems that react immediately as the connectivity system receives the alert; the advantages of the VLC system in terms of total braking distance are evident. Moreover, it should be noticed that such a result cannot be obtained by RFC technologies: the maximum average latencies achieved by IEEE 802.11p and C-V2X standards are 100 and 140 ms, respectively, and such values are 10 and 14 times larger than the ones observed in our worst-case scenario tests (0.999 probability, 50 m, 230 kbaud).

Table 4-3. Reaction and stop distance for an average family car with good tires over dry asphalt. Comparison between VLC, IEEE802.11p (11p), C-V2X, and human latencies.

v [km/h]		40	60	90
D [m]		10	20	45
PER @ 57 kbaud		$\sim 10^{-5}$	$\sim 10^{-5}$	$\sim 10^{-4}$
Reaction latency @ 99% [ms]		~1.2	~1.2	~1.2
Brake distance [m] ($\mu = 0.7$)		9.00	20.25	45.55
Reaction distance [m]	**VLC**	0.01	0.02	0.03
	11p	1.11	1.67	2.50
	C-V2X	1.55	2.33	3.5
	Human	15.22	20.83	34.25
Stop distance [m]	**VLC**	9.01	20.27	45.58
	11p	10.11	21.92	48.05
	C-V2X	10.55	22.58	49.05
	Human	24.22	41.08	79.80

4.4. Optical characterization

4.4.1. Experimental setup

In this part of our work, we deepened the study of our VLC link by considering the effects of angular misalignment. More specifically, we characterized the AFoV of the receiver through an analysis of the signal amplitude and corresponding PER for various distances and RX-TX relative orientation in a realistic scenario. In particular, we focused on the effect of using a variety of lenses (aspherical/Fresnel) differing in diameter and focal lengths on the communication performances of the VLC system.

The experimental setup had the same structure as the one described in the previous Sections. Briefly, the transmitter unit was composed of a digital encoder/modulator consisting in an Arduino DUE microcontroller. This provided the digital modulation signal to be fed into the traffic light (red LED; nominal power = 6.5 W; Fresnel lens diameter = 30 cm). A continuous data stream was transmitted in broadcast mode with a maximum data rate of 230 Kbps. An OOK modulation with Non-Return-to-Zero (NRZ) data coding was employed. For PER analysis, the transmission consisted of 100000 packets of length 6 bytes sent through a direct modulation of the LED current *via* the UART protocol. The RX was positioned at a height of 105 cm (corresponding to a typical car dashboard), and the relative height between the traffic light lamp and RX was 178 cm as a result; the stage was placed on a tip/tilt platform with a 0.5° resolution in the horizontal and vertical orientation. An optical lens provided a high optical gain; inour analysis, we employed both molded glass aspheric lenses and plastic Fresnel ones, namely, AS1, AS2, FR1, and FR2 (see Table 3-2). The incoming light was collected by a custom large-area, variable-gain PD (Thorlabs PDA36A2), which was decoupled from the DC component: this allowed for the rejection of stray light and direct sunlight and provided a 30-dB attenuation of the 100-Hz artificial illumination. The gain was 30 or 40 dB for a rate of 230 or 115 kbaud, respectively. The analog signal went through a variable-threshold comparator to be digitized and then decoded by the Arduino receiver board, where it was eventually compared with a pre-stored message. Thus, the PER was measured as the number of correctly received packets. The received signal amplitude was recorded by a 1-Gs/s, 4-channel digital oscilloscope after subtraction of the 100-Hz component. The measurement configuration is presented in Figure 4-17.

4.4.2. Results and discussion

In Section 4.2., we presented the received signal of our VLC system measured as a function of TX-RX orientation and position on a three-dimensional grid and developed a model of the intrinsic intensity map as a function of the elevation angle α, azimuth β, and TX-RX distance d (see Figure 4-17b,c): I(α, β, d). Here, starting from such results, we used model I_1 from Section 4.2. and deepened our analysis of the VLC link to highlight the dependence of the received signal amplitude on the relative angular orientation of the traffic light and receiver unit. This is particularly useful in ITS applications because the angular limits of reception, within which the signal is received, must be correlated with the lane width (typically, a vehicle needs to receive information mainly from other units in the same lane).

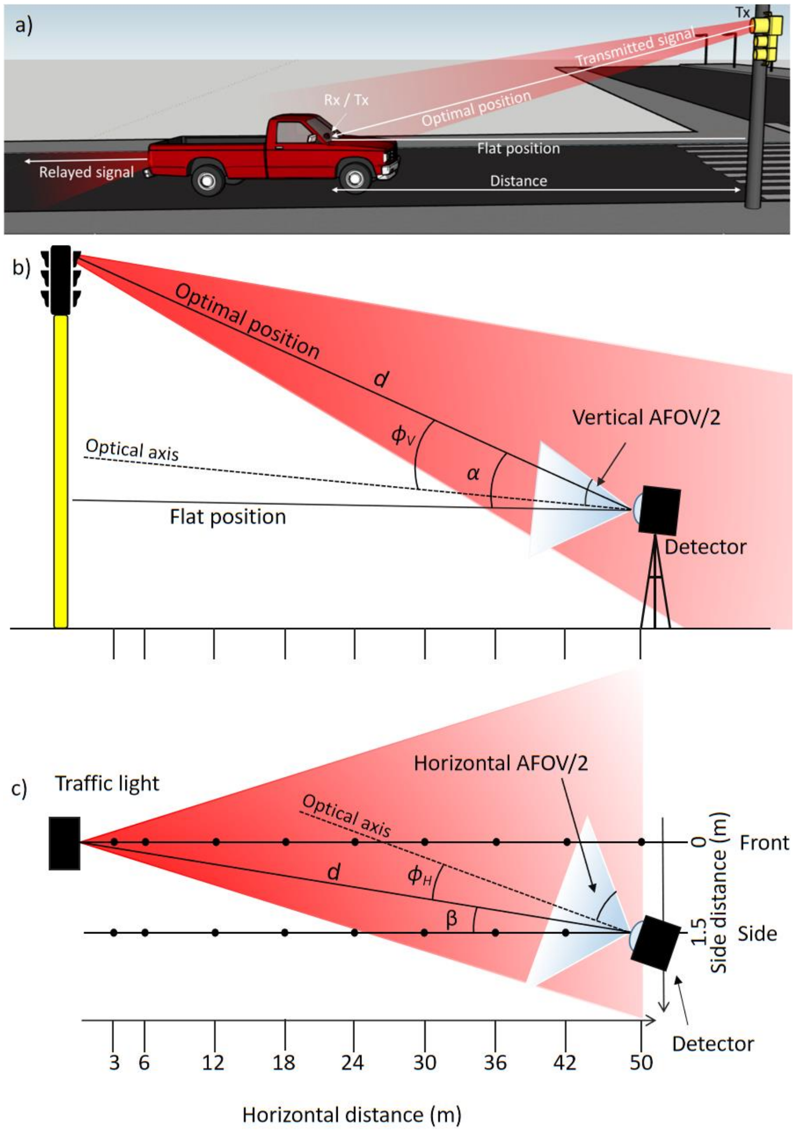

Figure 4-17. a) Prototype of I2V communication: a traffic light (TX) transmits information to a vehicle (RX/TX), which decodes and compares the message with a stored one and relays it only if all of the data were received correctly. Two configurations are considered: flat and optimal. b,c) Schematic side and top views of the measurement grid. The solid lines in b) highlight the two optimal and flat configurations for RX optical axis orientation, while the solid-dotted lines in c) highlight the two horizontal configurations used (front and 1.5 m side, respectively) across the measurement grid. The TX-RX distance, up to 50 m, is limited by the available LoS length in the building.

The AFoV is usually defined as the angular displacement of a source with respect to the optical axis for which its image is entirely formed in the active area of the detector:

$$\mathrm{AFoV} = 2\tan^{-1}\left(\frac{\mathrm{L}}{2\mathrm{f}}\right) \tag{4-20}$$

where f is the focal length of the lens, and L/2 is the half-size of the detector's active area for the case in which the object is located at a distance much higher than the focal length [127]. However, for non-ideal optical systems, such as the case in which the RX is tilted, the AFoV cannot be used to describe the effective amount of light reaching the detector owing to its dependence on the size and shape of the source image; an EFoV must be considered instead, which will be described further in the text. Let us first estimate the radius of the image, R. We start by assuming that the source is a uniform circular disk, 30 cm in diameter; R will be smaller than L for all distances considered in this work (ranging between 6 and 50 m).

The following possibilities arise:

1) the source image forms entirely on the PD;
2) the source image forms entirely outside the detector;
3) part of the source image forms on the PD.

Each of these can be obtained by varying the orientation of the RX stage. In case number 3, the inner and outer areas of the image are parametrized through an angle θ, as shown in Figure 4-18; the region lying outside the detector will be a circular segment of area

$$\mathrm{A} = \frac{\mathrm{R}^2}{2}(\theta - \sin\theta) \tag{4-21}$$

Let us now consider the optimal configuration in Figure 4-17b,c and assume a rotation of the receiver along one of its vertical axes; the correlation between θ and φ_V is given by:

$$\theta = 2\cos^{-1}\left(\frac{\mathrm{L}/2 - \mathrm{f}\tan(|\varphi_{\mathrm{V}}|)}{\mathrm{R}}\right) \tag{4-22}$$

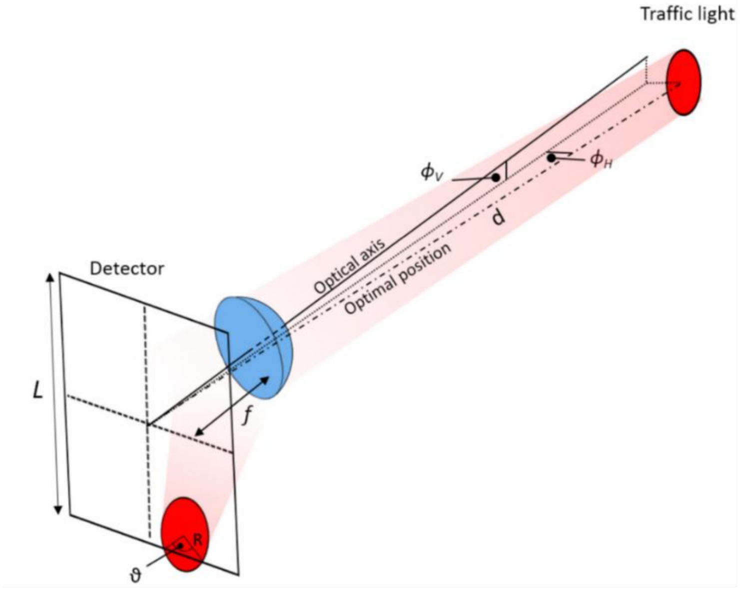

Figure 4-18. Dependence of AFoV on the size of the image *R*. The part of the image falling inside the PD area is parametrized in terms of the angle θ, which is correlated with the angles $\varphi_{H,V}$ in Figure 4-17b,c.

Therefore, the amplitude of the VLC signal S(α, β, d) depends on the area of the image formed at the detector and the angles $\varphi_1 = \tan^{-1}[(L/2 - R)/f]$ and $\varphi_2 = \tan^{-1}[(L/2 + R)/f]$, which define a region of non-sharp transition between maximum and zero collected power (*i.e.*, they provide the maximum angle of misalignment before a loss of the incoming signal occurs):

$$S(\alpha, \beta, d) = c \begin{cases} 0, & -\pi/2 < \varphi_V \leq -\varphi_2 \vee \varphi_2 \leq \varphi_V < \pi/2 \\ I(\alpha, \beta, d)\cos(\varphi_V), & -\varphi_1 \leq \varphi_V \leq \varphi_1 \\ I(\alpha, \beta, d)\cos(\varphi_V)\left(1 - \dfrac{\theta - \sin\theta}{2\pi}\right), & -\varphi_2 < \varphi_V < \varphi_1 \vee \varphi_1 < \varphi_V \leq \varphi_2 \end{cases} \tag{4-23}$$

where *c* is the scaling factor between the amplitude *S* and the intensity *I* of the signal, which can be measured on a point of the grid; we calculated it by normalizing the maximum amplitude at a distance of 6 m to the absolute value measured on this point. Figure 4-19 presents the amplitude map as a function of the elevation angle α for lens AS2 obtained through Equation (4-23) for a vertical rotation of the RX stage (for symmetry reasons, the same result is expected for a rotation around the horizontal axis). The EFoV is defined as the angle $\varphi_{H,V}$ below which the observed PER is better than 10^{-3}, *i.e.*, the commonly recommended threshold for reliable communication: indeed, by implementing forward error correction codes for these PER values, one would obtain a communication compatible with the internet one [150]. The EFoV is represented by the two horizontal lines in Figure 4-19, referring to conditions with and without interference by artificial light. By observing the figure, we can clearly notice that EFoV values reduce as the RX is moved away from the TX. Moreover, the transition region [φ_1, φ_2] becomes narrower for increasing distances owing to the demagnification of the optical system (*i.e.*, the image size is smaller).

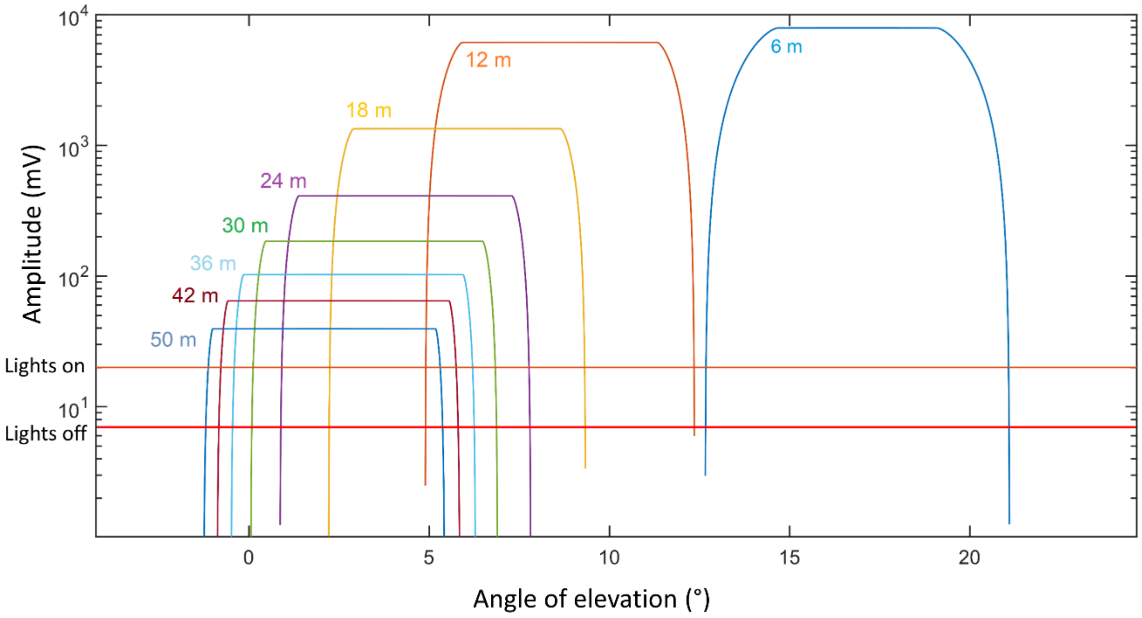

Figure 4-19. Signal amplitude as a function of the angle of elevation α calculated *via* our model for lens AS2 in the optimal configuration (see text). The horizontal lines represent the EFoV (PER = 10^{-3}) when artificial illumination is on (brown) and off (red).

The experimental campaign aimed at evaluating the optical performance of the system for various positions on the grid. For each reception position, we carried out an angular investigation to determine the EFoV, using the four lenses mentioned previously as well as in the absence of a lens. We simulated a realistic scenario by placing the detector a) in line with respect to the traffic light and b) displaced by 1.5 m on the side. We proceeded with our FoV analysis by recording the signal amplitude while scanning angles φ_H and φ_V in two configurations: the optimal condition, in which the RX axis was aligned with the center of the traffic light lamp (*i.e.*, simulating the active tracking of the lamp position by a vehicle's RX unit), and the flat condition, in which the optical axis of the receiver was horizontal and parallel to the longitudinal axis of the corridor in our setup (*i.e.*, representing the situation in which the RX of a vehicle is oriented along the direction of motion). The results are presented in Figure 4-20.

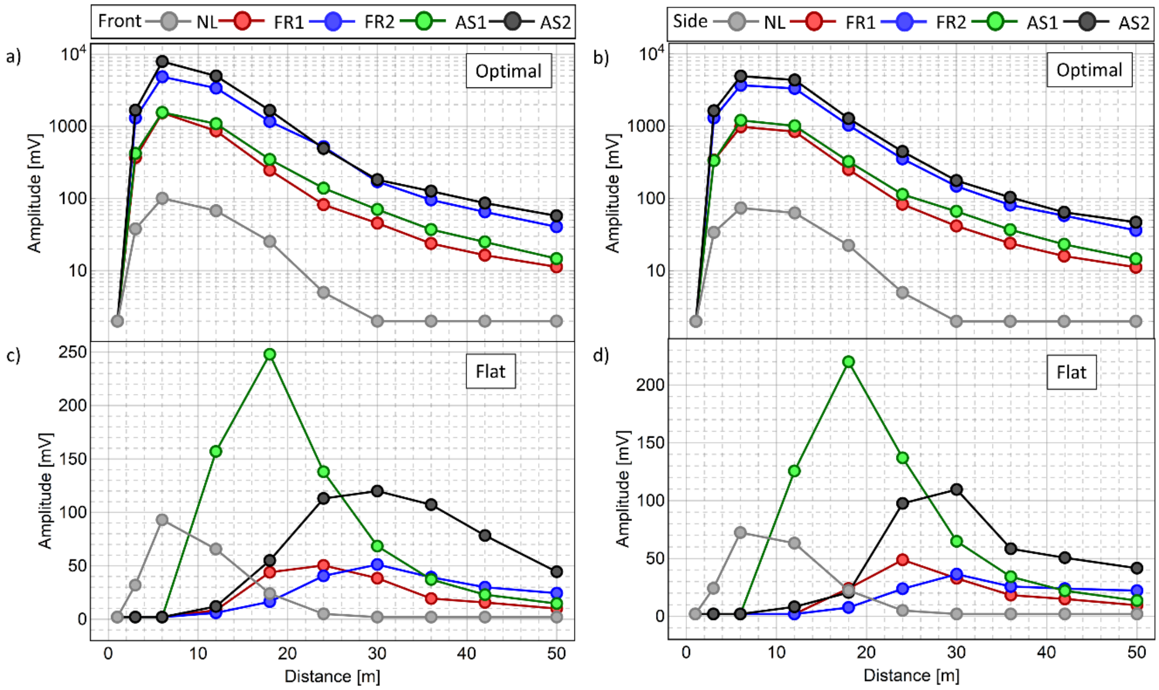

Figure 4-20. Amplitude of the received signal as a function of distance for the optical lenses used in this work (AS1, AS2, FR1, FR2; NL indicates the absence of a lens) and two receiver positions (front, aligned with TX, and side, 1.5 m from the alignment position). Panels (a) and (b) show the optimal configuration, in which the RX always points towards the TX. Panels (c) and (d) show the flat configuration, in which the optical axis of the RX is parallel to the floor.

The signal amplitude recorded in the optimal configuration (Figure 4-20a,b) represents the pattern of the traffic light intensity for φ_V and $\varphi_H = 0°$ (see Equation (4-23)). We can observe the same global trend taking place for all lenses: the amplitude first increased steeply for distances below 10 m and then decayed slowly. This was a consequence of the orientation of the traffic light lamp, which provided the maximum intensity in the 10–15 m range at ground level and 5–10 m at the chosen height of 105 cm (see Section 4.2.). The fact that the same trend, observed for high distances, was followed for all lenses is explained by the dependence of the incoming luminous flux on the lens diameter D according to a D^2 law: indeed, the ratio of amplitudes for the 2" and 1" lenses is constant and equal to approximately 4 over the entire grid, and no effects resulting from the different focal lengths or materials of the lenses are observed (we remind here that the FR lenses were plastic while the AS ones were glass). Finally, in the absence of lens (NL case in the figures), we recorded the lowest amplitude values owing to the lack of optical gain.

Panels c and d in Figure 4-20 present the flat configuration, in which the average amplitudes were globally lower than in the previously discussed case and presented a marked dependence on the lens used. This is an especially important configuration, as it is the simplest one in the absence of a tracking system. Short distances corresponded to large $\varphi_{H,V}$ values and low intensity levels for large α and β angles: as a consequence, the detected optical power was extremely low. In particular, lens AS1 exhibited the best performance for distances up to 25 m in both the front and side configurations owing to the short focal length: indeed, a larger AFoV requires a shorter focal length for a given aperture D. For distances > 25 m, where the FoV is less critical, the best performance in the front configuration was achieved by the 2" lenses owing to their larger optical gain as well as their size, which allowed for the image to form entirely inside the sensor.

The transmission performance of the VLC link was evaluated *via* PER measurements and analysis. First, we obtained a calibration of the entire measurement grid by acquiring the amplitude values and using Equation (2-12) to interpolate the experimental data; the results are shown in Figure 4-21 for both transmission rates: 115 and 230 kbaud (panels a and b, respectively). In the figure, the blue and red markers correspond to the PER values measured in the presence and absence of artificial illumination, respectively. The solid curves represent the fit to the experimental data obtained through Equation (2-12): in the fit procedure, the experimental error was used as a weight, while parameters T and σ were left free to vary.

As expected, the lower baud rate transmission exhibited a better performance than the higher baud rate one, and a few mV were sufficient to ensure an error-free transmission with our receiving unit, because the measured RMS noise was approximately 0.5 mV and, consequently, a few mV were required to achieve a high SNR. The results also show the impact of the 100 Hz illumination: a stronger VLC signal is required at the RX stage to achieve the same PER as the case without artificial lights. This is explained by considering that the slow fluctuations of the residual 100 Hz light cause a periodic shift in the signal with respect to the comparator detection threshold, resulting in periodic reading errors by the receiver board. Considering this aspect, the calibration curve obtained in the absence of artificial lights was then employed for PER performance determination in the rest of the work.

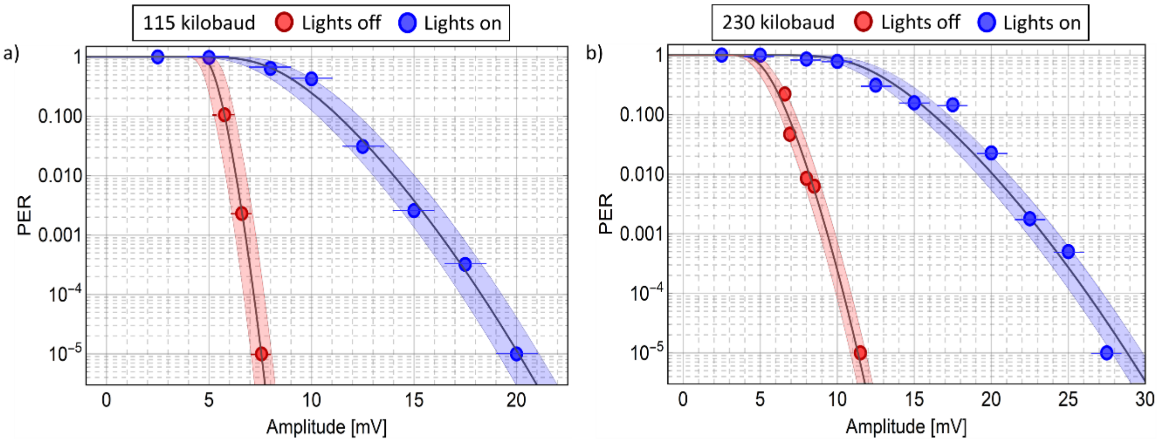

Figure 4-21. PER measurements for various received signal amplitudes at different baud rates: (a) 115 kbaud and (b) 230 kbaud. Blue and red symbols are the measured amplitudes with and without artificial lights, respectively; each marker represents the average of three consecutive measurements (error bars are smaller than the marker size). Black curves are fits to the experimental data; shaded areas represent the error associated to the fit procedure. Amplitude values are affected by a statistical error in the absence (± 0.5 mV) and presence (± 1 mV) of artificial lights.

The PER performance of our VLC link is presented in Figure 4-22 for all lenses used in this work and for both the optimal and flat orientations; specifically, the side configuration was used (*i.e.*, with a 1.5 m indentation on the right-hand side). The low baud rate (115 kbaud) transmission results are shown in panels (a) and (c): remarkably, the optimal orientation ensured an error-free (PER < 10^{-5}) communication at distances between 3 and 50 m with all lenses (except the no-lens case, NL, for which the performance decayed significantly after 18 m), while lenses AS1 and AS2 exhibited superior performances in the flat orientation at distances higher than 12 m. The results obtained for the high baud rate (230 kbaud) transmission are presented in panels (b) and (d): here, lenses FR2 and AS2 exhibited the best performance in the optimal orientation, owing to their 2" diameters ensuring higher gains, resulting in an error-free link between 3 and 50 m of distance. In the flat orientation, however, the only acceptable performances were achieved by lens AS1 at medium-short distances (12–30 m) and lens AS2 at large distances (up to 50 m).

These results, especially those concerning the high baud rate configuration, clearly demonstrate the importance of the condenser element in achieving a highly performing VLC link: indeed, the aspheric lenses AS1 and AS2 outperformed the Fresnel ones at both short and long distances. It is worth noticing that an error-free connection can be achieved at large angles (*i.e.*, largest attainable FoV) without using a lens, but this condition is not acceptable for distances higher than 12 m. Overall, the best performances were achieved by the aspheric condensers at 115 kbaud for distances between 12 and 50 m.

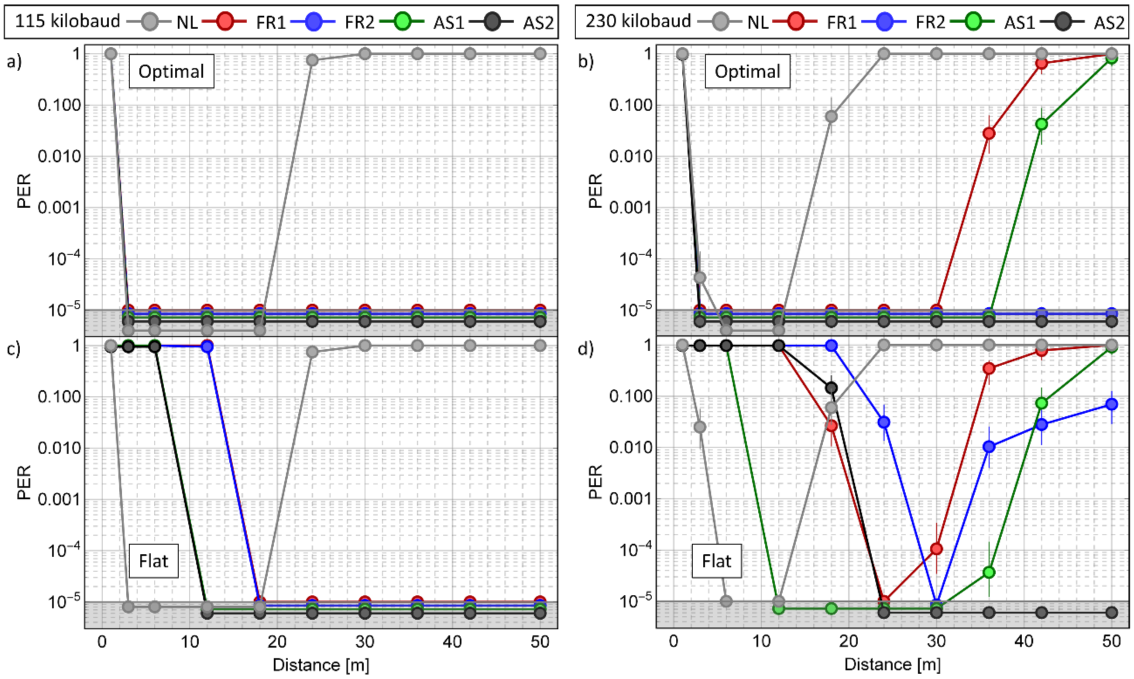

Figure 4-22. PER measured as a function of distance in the side configuration for all lenses used in this work (AS1, AS2, FR1, FR2; NL indicates the absence of a lens). Data transmission was carried out at two baud rates: 115 kbaud (panels (a) and (c)) and 230 kbaud (panels (b) and (d)). Upper panels: optimal configuration; bottom panels: flat configuration.

Next, we assessed the effects of a TX-RX angular misalignment on the VLC link performance by recording the signal amplitudes as a function of φ_H and φ_V with a resolution of 0.5° for various distances and using different condenser elements. Figure 4-23a reports an example of the amplitudes measured at 18 m during a φ_V scan in the optimal orientation using the AS2 element. Here, we can observe a significant contribution of reflections of the white floor of the corridor at low and negative angles that overlap in part with the direct VLC signal at higher α values. These data were modelled using a combined function consisting in the sum of the amplitude function (Equation (4-23)) and a Gaussian one in which all parameters (width, height, baseline, and center) were free. We accounted for aberrations (mainly coma, as shown by Figure 4-23b,c) and defocusing (no auto-focus feature was available on our RX) by considering the lamp image radius in Equation (4-23) as a free parameter. As shown in Figure 4-23a (blue and red line), this fit procedure yielded excellent results, allowing us to isolate the contribution of the reflections (*e.g.*, from the walls, floor, or ceiling) from each dataset and retrieve the actual amplitudes S(α, β, d).

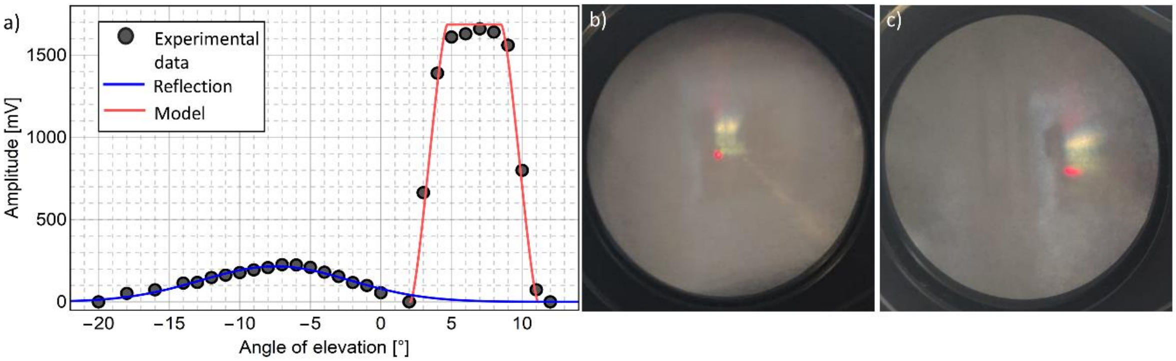

Figure 4-23. (a) Signal amplitude measured by the receiver unit as a function of the angle of elevation α. Black markers: experimental data (error bars are smaller than the symbol size); blue line: Gaussian fit for the contribution of the floor reflection; red line: fit to direct amplitude values using Equation (4-23). (b) Image of the traffic light lamp taken in the focal plane of the FR2 lens for the on-axis configuration. (c) Image of the traffic light lamp taken in the focal plane of the FR2 lens for the off-axis configuration, showing an evident coma effect with a pronounced tail on the right side of image. Both panels (b) and (c) refer to data taken at 18 m in the front case.

At this point, we proceeded to retrieve the PER as a function of $\varphi_{H,V}$ through the calibration procedure described previously. This allowed us to characterize the EFoV as a function of distance (6−50 m) for the different condensers used in this work as well as the no-lens case, as shown in Figure 4-24. Here, we can observe that the EFoV values in the absence of a condenser element reached 150° for short distances (< 20 m) but then dropped to zero owing to the low optical gain. The best performance was achieved by lens AS1, for which an EFoV of 25° was reached at 115 kbaud and short distances. Interestingly, this condenser was outperformed by AS2 at large distances owing to its larger diameter and consequent higher optical gain, which allowed it to attest an EFoV of ~10° over the entire range of distances.

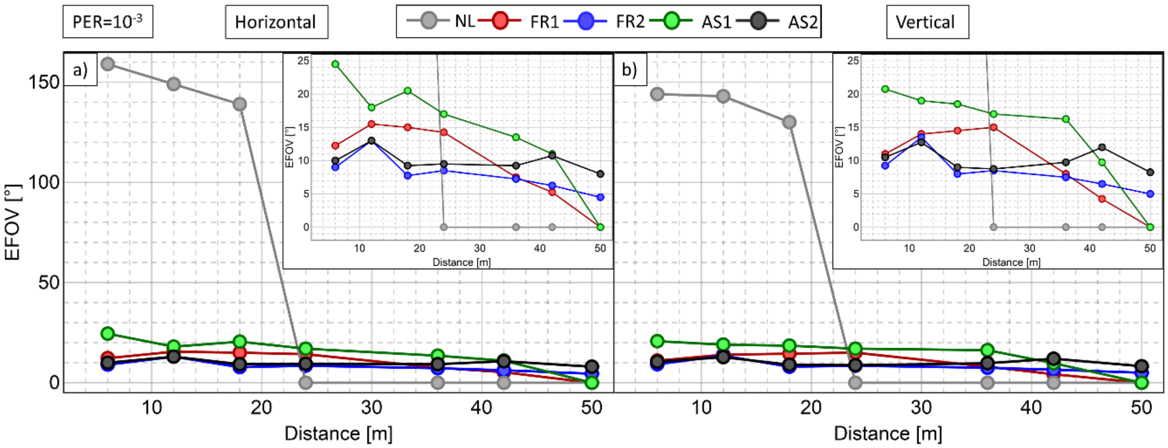

Figure 4-24. Experimental characterization of (a) horizontal and (b) vertical EFoV as a function of distance for a 115 kbaud transmission. EFoV values are shown for all lenses as well as the no-lens (NL) case. Insets: zoom of the lens data subsets. Error bars are smaller than the symbol size. PER = 1 × 10^{-3} is taken as a threshold value.

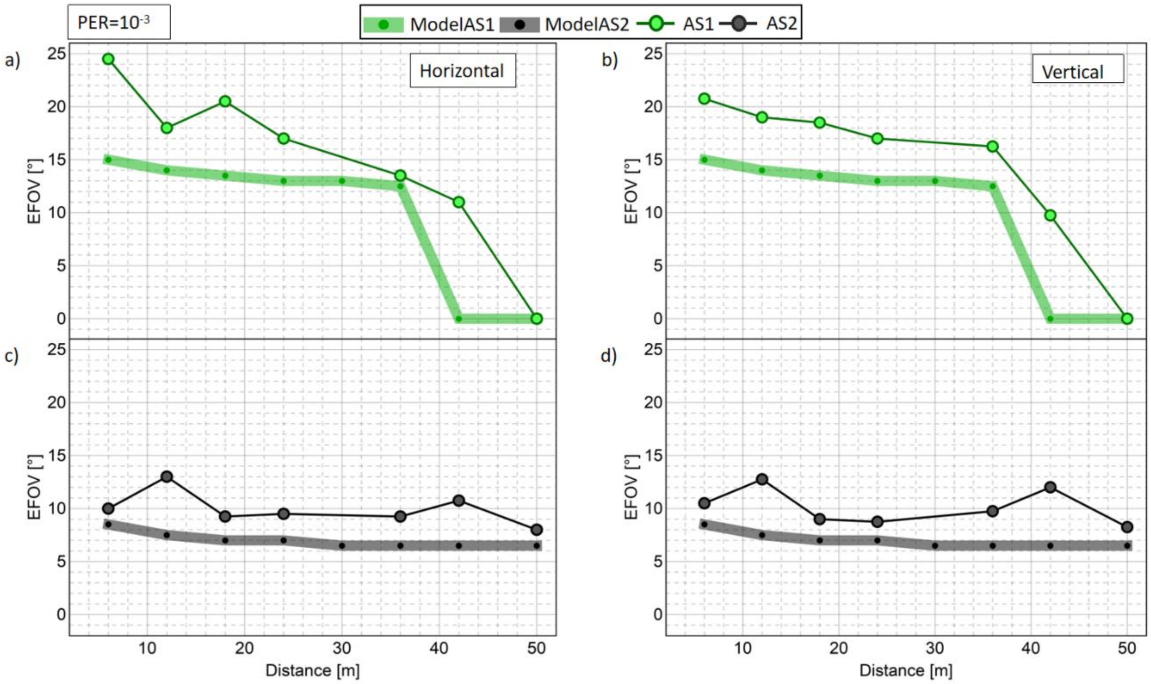

Figure 4-25. Comparison between measured (markers) and predicted (shaded areas) EFoV values for AS1 and AS2 condensers for 115 kbaud. Vertical error bars are smaller than the symbol size. The upper and lower bounds of the model (*i.e.*, the extension of the shaded areas) are calculated considering ± 0.5 mV as the uncertainty on amplitudes in model predictions.

To better elucidate this aspect, we compared the EFoV data for AS1 and AS2 with the predictions obtained using our model; the results are displayed in Figure 4-25. Clearly, the model was able to fully represent the global trend at short as well as large distances; only a modest underestimation of the experimental data can be observed, which can be explained by considering two main factors. First, the system PER performance depends significantly on the signal amplitude near the threshold, and even a difference of a few mV can determine a PER variation by orders of magnitude. Second, the angular rotation of the RX stage determines a dramatic decrease in amplitude in the intermediate region of the model. Considering both these factors, we can conclude that the observed discrepancy between measured values and model prediction is overall non-significant.

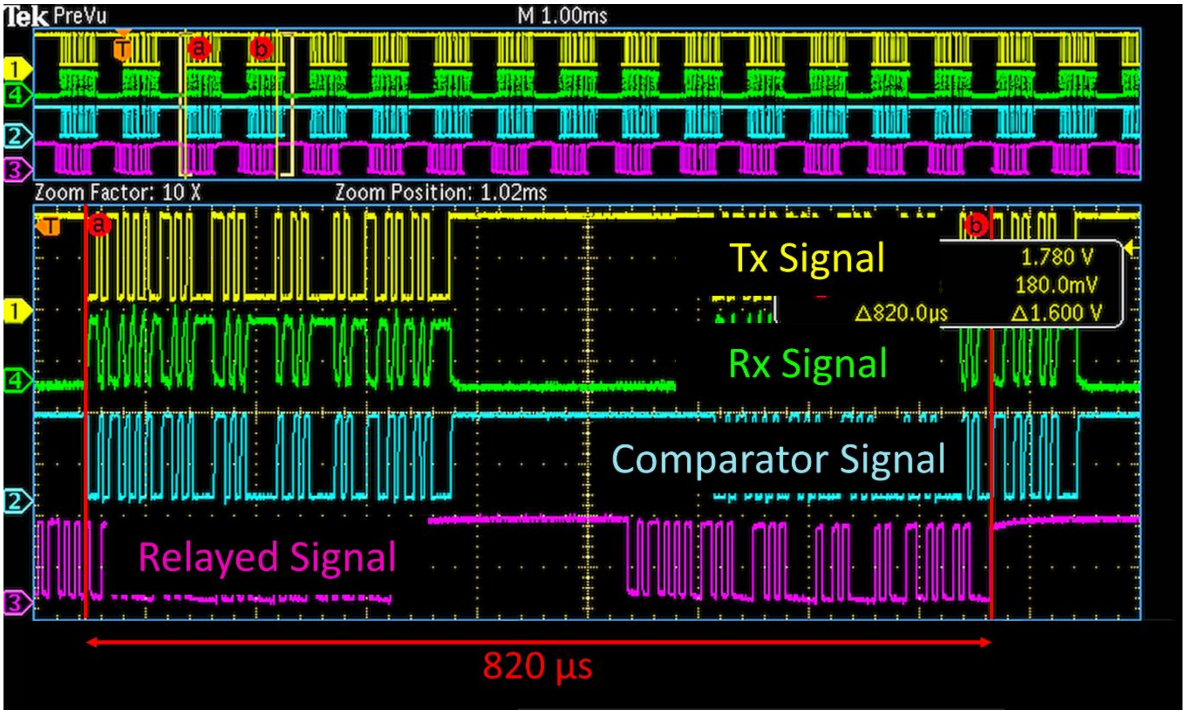

Figure 4-26. Information broadcast mode. Oscilloscope screen showing the transmitted (yellow), received (green), digitized (blue), and relayed (purple) signals. The observed latency was 820 ms at 230 kbaud for the full process.

The VLC link was further tested for continuous information broadcast and beaconing to assess its suitability for the exchange of situational information [25] (*e.g.*, traffic congestion, alternative routes, message broadcast during road accidents, *etc.*). The ability to handle both these modes is key feature of a VLC link for ITS applications. Indeed, the broadcast and beaconing modes differ from the optoelectronic point of view in that the latter does not ensure a constant root mean square (RMS) value of the detected signal. Therefore, the AC coupling of the receiving unit typically cannot filter the transients in isolated burst signals, which are thus difficult to detect. For this part of our work, we used the low-cost Fresnel lens as condenser elements owing to their ability to ensure the reliable and low-latency transmission of information. The results are shown in Figure 4-26 for the broadcast mode and Figure 4-27 for the beaconing mode. The latency was measured as 820 μs for 230 kbaud and 1.5 ms for 115 kbaud: these values even lower than those required by the IEEE802.11p standard and the newly introduced C-V2X [151].

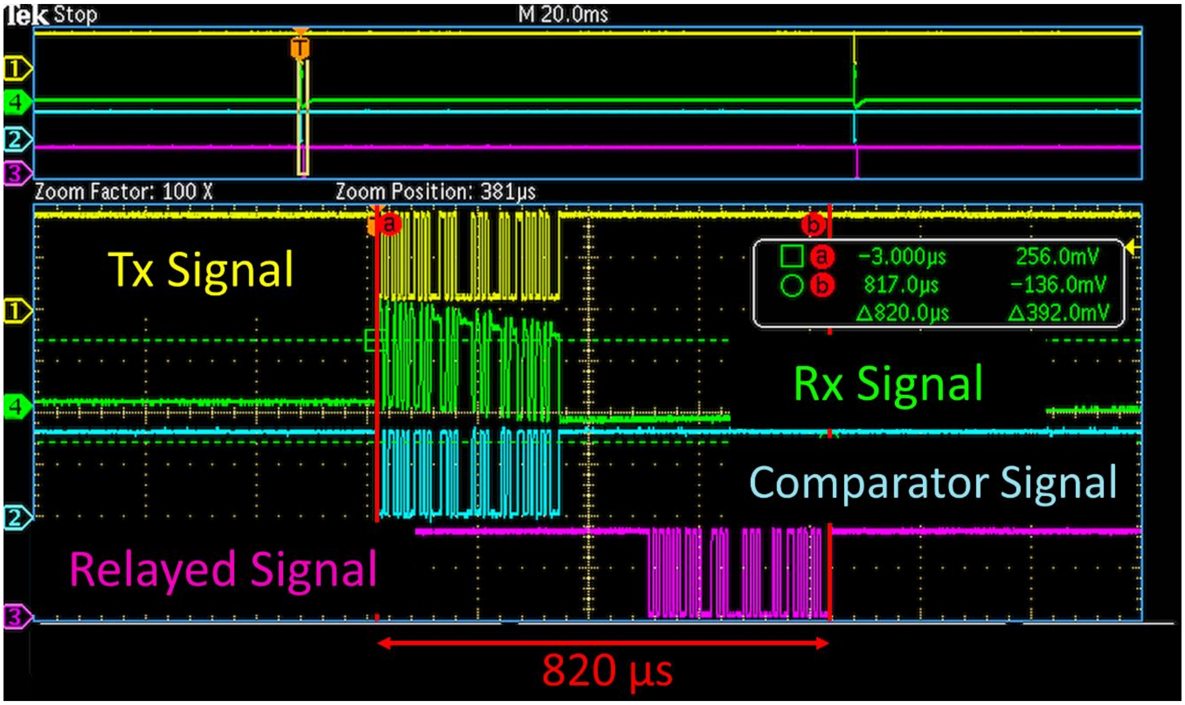

Figure 4-27. Beaconing mode. Oscilloscope screen showing the transmitted (yellow), received (green), digitized (blue), and relayed (purple) signals. The beaconing interval was set much higher than the packet size.

4.5. Bidirectional link

4.5.1. Experimental setup

The experimental setup used in this part of the work was different from that employed in the experiments described in Sections 4.2., 4.3., and 4.4. and is shown in Figure 4-28. Namely, the present system was composed by two transceiving stages, which will be referred to as TX1/RX2 and TX2/RX1, equipped with different LED lamps and each capable of receiving and decoding the VLC signal emitted by the other.

The TX1/RX2 stage is shown in Figure 4-28b, left panel. It was equipped with a commercial motorcycle headlight (HL) (white LED, Qiilu QL04156, 12 V 160 mA current DC value). The transmitter, TX1, consisted of the Arduino DUE board (see also Paragraph 3.2.1.) and custom analog current modulator stage (see also Paragraph 3.2.3.); it provided a continuous transmission of 9 byte-long data packets (maximum rate: 57 kbaud). The amplitude modulation was performed with a 0-200% NRZ-OOK scheme with Manchester encoding. The receiver, RX2, was a customized variable-gain PD (Thorlabs PDA100A2) with a large active area of 75 mm^2 and equipped with the AS2 lens (Thorlabs ACL50832U), characterized by a focal length of 32 mm and an FoV of 17°. The detector included a physical DC-block stage before the first transimpedance stage granting a large gain without the risk of saturating the amplifier stage (for example, owing to sunlight interference). To further reduce the effects of stray light interfering with the optical system, we placed a cylindrical shield (85 mm in diameter, 75 mm in height, 60° FoV) coaxially with the photoreceiver. The collecting lens was chosen to maximize the amplitude of the analog signal at high distances; this was then digitized by a variable-threshold custom comparator and decoded by a second Arduino DUE board. The TX2/RX1 unit, presented in Figure 4-28b, right panel, was equipped with a commercial motorcycle rear light (RL) (red LED, Alchemy Parts, UPC: 5060502564597, 12 V, 90 mA current nominal value) and was, in all other aspects, analogous to TX1/RX2.

As depicted in the sketch of Figure 4-28a, the TX1/RX2 stage (HL) transmitted a stream of packets toward TX2/RX1 (RL) with an inter-packet delay slightly larger than the packet duration, which would allow for the return packets to be received by the HL. Then, TX2/RX1 (RL) digitized and decoded the received signal, checking for possible errors in each packet. In the absence of errors, the TX2/RX1 board would send a return packet toward the HL through the RL to be received by TX1/RX2; this would then perform a similar decoding, count the total number of error, and estimate the PER of the entire bidirectional chain. This process was based on time division multiplexing

(TDM), allowing for each return packet from the RL to be sent back to the HL during the inter-packet delay. The synchronization between the two boards was achieved through a 2-byte preamble placed after the pre-equalization frame, as shown in Figure 4-29.

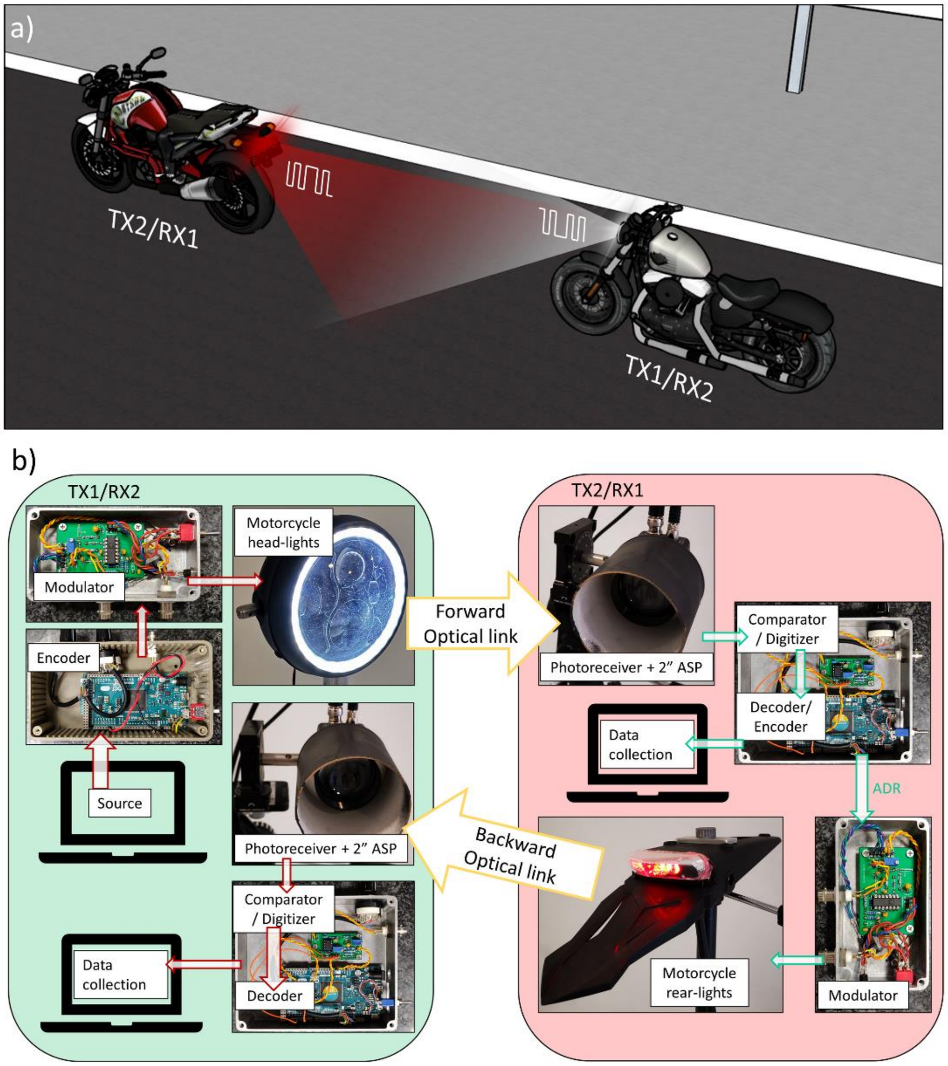

Figure 4-28. a) Sketch of the bidirectional communication simulated in this work: the TX1/RX2 unit (headlight) sends digital information to the TX2/RX1 one (rear light). The communication is actively decoded and sent back to TX1/RX2 to perform a bit-wise comparison of the data stream. b) VLC hardware blocks of our bidirectional V2V system. Left panel (green): TX1/RX2 block consisting of commercial motorcycle headlights and a variable-gain commercial PD. Right panel (red): TX2/RX1 block consisting of commercial motorcycle rear lights and a variable-gain commercial PD. Both units use Arduino DUE boards as the digital encoder and decoder.

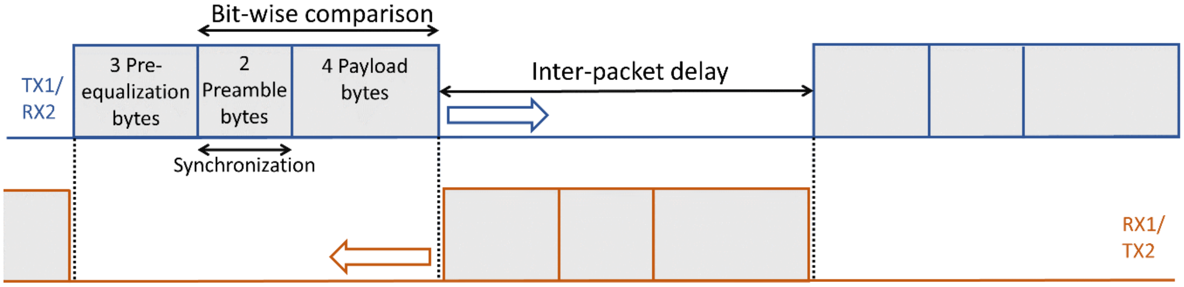

Figure 4-29. Packet structure. Three pre-equalization bytes are used for signal equalization. A bit-wise comparison is performed on the last six bytes (two preamble + four payload bytes). The two preamble bytes are used for synchronization. The inter-packet delay is slightly larger than the packet time.

4.5.2. Results and discussion

In a similar way to the experiments described previously, we realized a measurement grid as shown in Figure 4-30. We measured the received SNR and PER values for various distances and relative positions between HL and RL, extending up to 30 m of distance and 3 m of side displacement between the LEDs. The grid size was chosen to represent urban scenarios, where the average distance between vehicles ranges between 12 m (at rush hour) and 40 m (at late night) [152]. The detectors, HL, and RL were placed at a height of 750 mm with respect to the road plane to simulate the height of real motorcycle lamps. We only employed day lights for the tests because they are always lit during vehicle usage.

The SNR values were obtained by recording the RMS amplitude of the VLC signal at each stage with a 1 GSa/s digital oscilloscope (Siglent SDS 1204X-E). Such values were then compared against the measured RMS noise. In this way, we could obtain SNR maps for the two different configurations shown in Figure 4-30: in the flat orientation, the optical axis of the PD was oriented in the forward direction (*i.e.*, the most realistic configuration in road scenarios); in the optimal orientation, the PD aimed constantly at the source to obtain the maximal amplitude of the received signal for all points on the grid (*i.e.*, the expected scenario in the case of automatic tracking systems).

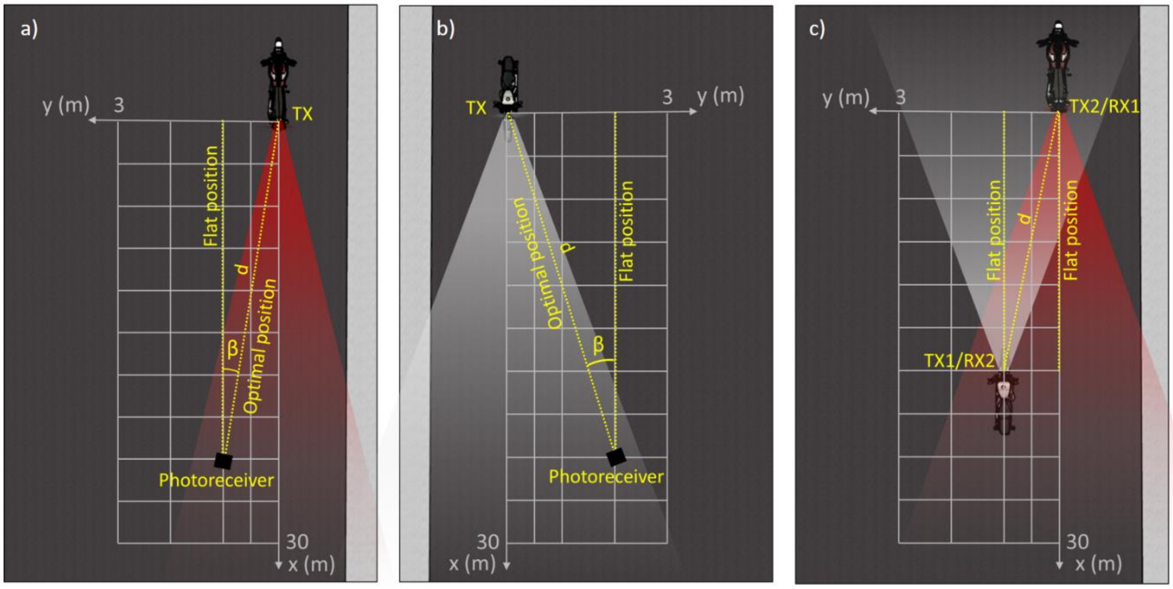

Figure 4-30. Experimental configuration for a) RL and b) HL. In the optimal configuration, the RX always aims at the source; only the amplitude is recorded for distances x up to 30 m and y up to 3 m. In the flat configuration, the RX is oriented in the forward direction. Both the amplitude and PER are recorded for distances x up to 30 m and y up to 1 m. c) In the bidirectional tests, amplitude and PER are evaluated only in the flat configuration.

Figure 4-31 presents the experimental amplitude SNR maps, recorded for both lights and configurations, for lateral displacements of 1, 2, and 3 m in the optimal configuration and 1 and 0.5 m in the flat one. The reference level of SNR = 0 dB matched that of the measured background RMS noise, σ = (4.2 ± 1.0) mV. The contour maps were obtained through a spline interpolation of the experimental data, corresponding to the black symbols. We can observe that the RL signal was more directional with respect to the HL one in the optimal orientation and presented a peculiar three-pronged intensity profile. HL, in contrast, was characterized by a more uniform intensity pattern in both the lateral and longitudinal directions owing to the circular arrangement of the LEDs. In the flat orientation, the behavior of the two lamps was similar especially at short distances (up to 6 m); nevertheless, HL presented globally higher SNR values because of its higher optical power (see Table 3-1).

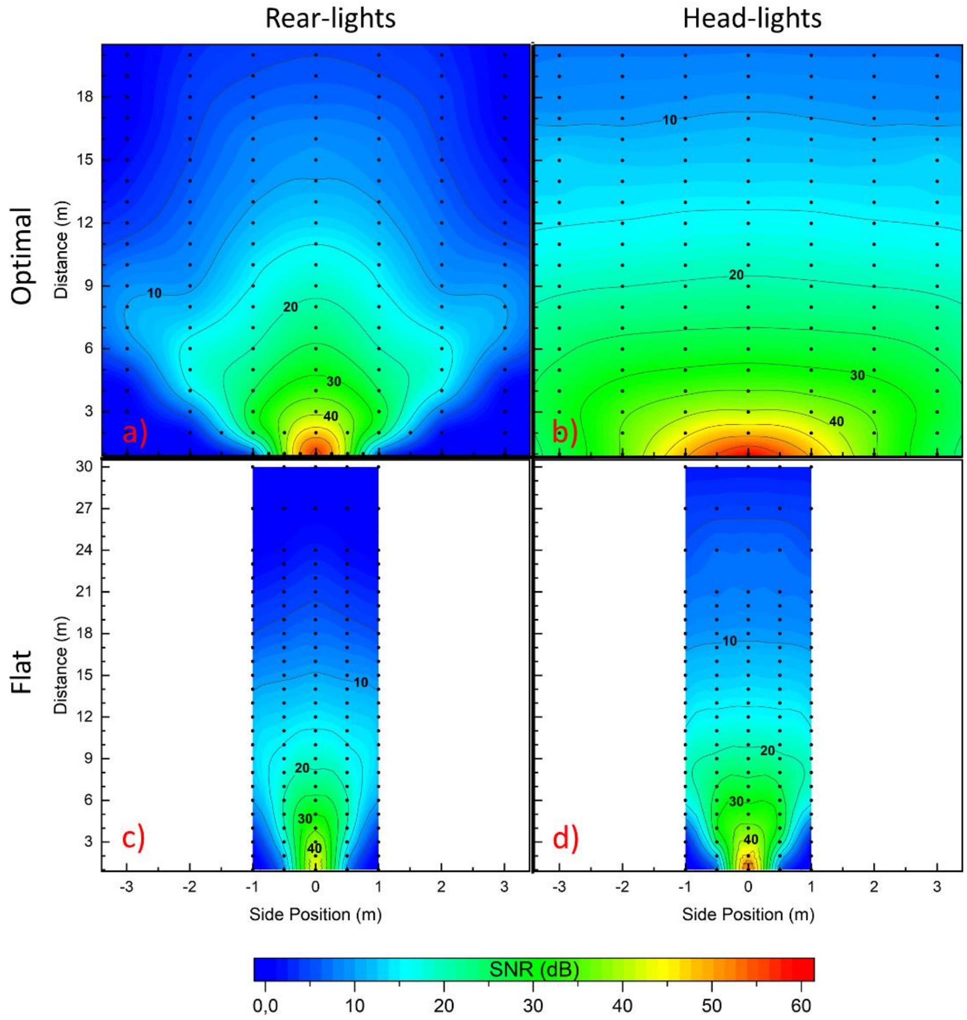

Figure 4-31. Experimental amplitude SNR maps for: a) RL in optimal configuration, b) HL in optimal configuration, c) RL in flat configuration, and d) HL in flat configuration. Color maps are obtained through a spline interpolation. The white regions are those for which no data were acquired owing to a too low SNR value.

Noticeably, a critical region existed for both configurations at short distances and large side displacements, in which the intensity exhibited a steep decrease caused by mechanical limitations as well as the directionality of the sources. This was due to a combination of the directional emission lobe of the LED lamps and the finite FoV of the receiving stage. To further increase the FoV, we would need to implement lenses with D > 2" or shorter focal length. However, these are not suitable for ITS applications: the former because of their sizes (they can be quite bulky), the latter because of their short focal length, high cost, and significant aberrations.

The PER was measured as the ratio between the incorrectly received packets and the total number of transmitted packets, as described previously (see Section 4.3.). These measurements were carried out only in the flat configuration, as this is the more realistic one. Owing to the transmission parameters (62500 packets, rate of 57 or 28 kbaud, and PD gain of 40 or 50 dB), the minimum achievable PER was 1.6×10^{-5}, corresponding to the error-free communication. The experimental PER values, reported as a function of distance for rates of 28 and 57 kbaud and for different side displacements, are displayed in Figure 4-32.

We can observe that the PER performances at 28 kbaud were globally better than those at 57 kbaud; this is easily explained by the fact that lower baud rates result in a higher energy per bit, thus larger PD gain and, consequently, larger SNR. The quality of the link was observed to decreased not only for larger distances but also for higher side displacements: this was due to the finite FoV of the RX units as well as the shape of the intensity profile of the lamps. However, different performances were observed depending on the lamp used.

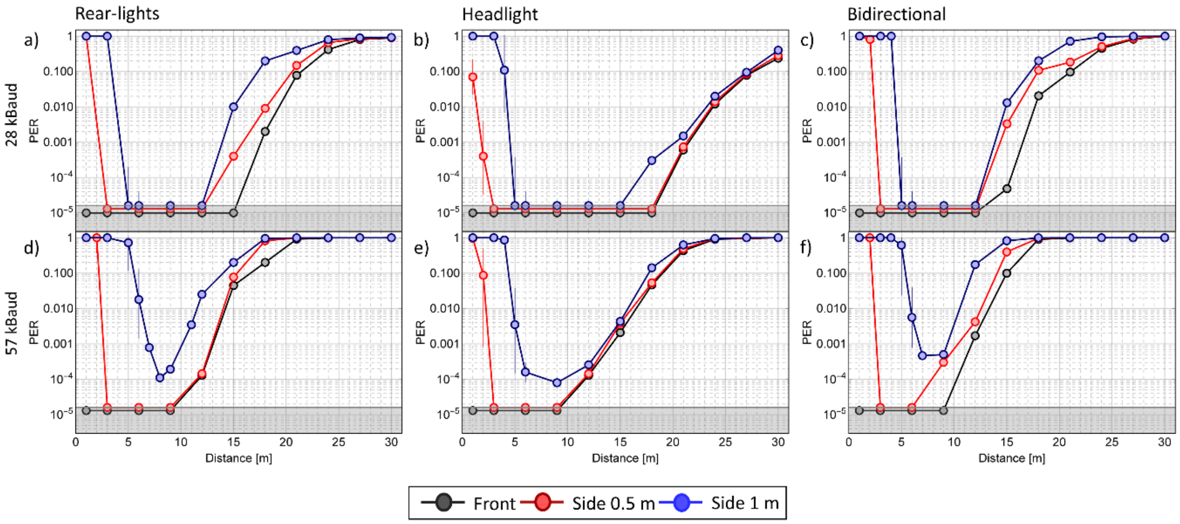

Figure 4-32. Experimental PER values as a function of distance measured in the flat configuration. a) RL unidirectional at 28 kbaud, b) HL unidirectional at 28 kbaud, c) bidirectional at 28 kbaud, d) RL unidirectional at 57 kbaud, e) HL unidirectional at 57 kbaud, and f) bidirectional at 57 kbaud. The round symbols represent the average PER value; error bars (maximum deviation from average values) are smaller than the symbol size; lines are a guide for the eye. Black curves = no horizontal displacement between the two units; red curves = horizontal displacement of 0.5 m; blue curves = horizontal displacement of 1 m. The gray shaded areas correspond to the lower bound for PER sensibility.

Let us analyze the PER performance for each type of link. In the unidirectional communication at 28 kbaud (Figure 4-32a), the RL achieved error-free communication for distances up to 15 m in the front configuration (*i.e.*, zero side displacement), 3–12 m for a 0.5 m side displacement, and 5–12 m for a 1 m side displacement. At 57 kbaud (Figure 4-32d), error-free communication was attained for distances below 9 m at zero side displacement and 3–9 m for 0.5 m displacement, while for the 1 m displacement, the PER value was 10^{-4} at a distance of 8 m. In the same conditions, the HL achieved a higher range of error-free communication distances: at 28 kbaud (Figure 4-32b), these were 18 m, 3–18 m, and 5–15 m for the zero, 0.5 m, and 1 m side displacements, respectively; at 57 kbaud (Figure 4-32e), they were $d < 9$ m and 3–9 m for zero and 0.5 m displacements, while in the 1 m case, the PER value was above the error-free threshold. As suggested by the intensity maps, the lower directionality and higher optical power of the HL allow for communications at longer distances (for both front and side displacements) compared to the RL. In the bidirectional communication, an error-free link was established for distances up to 12 m at 28 kbaud (Figure 4-32c) and for 9 m at 57 kbaud (Figure 4-32f), in both cases in the zero side displacement configuration. In the presence of a 0.5 m side displacement, the maximum achievable distances for a solid VLC link at 28 and 57 kbaud were 3–12 m and 3–6 m, respectively. Finally, for the 1 m displacement, the error-free range was 5–12 m for a rate of 28 kbaud, while the PER was above threshold at 57 kbaud. Generally speaking, in a bidirectional link, we would expect to be limited by the RL because of its directionality and lower power; indeed, by observing the ranges, we can notice that they match the RL ones, while the HL achieved an error-free communication in those same ranges.

We can derive a propagation model for the bidirectional communication link using the same mathematical procedure used in Section 4.2.. The SNR maps were used to predict the PER performances of a VLC link based on real LEDs for both unidirectional and bidirectional communication in the more realistic flat orientation. The intensity was assumed to be a function of the distance between TX and RX and the azimuth angle β; the elevation angle α was not taken in consideration because the two units TX1/RX2 and RX1/TX2 were placed at the same height. Once again, the coefficients of the polynomial model for the intensity of the HL and RL were calculated from the experimental data rather than using a Lambertian model, because using an empirical model allows for a better agreement with the experimental data. We employed the MGLR method to find the best fitting parameters for the model intensity, using the following inputs:

- the model function, $I = f(\beta, d)/d^2$;
- the maximum order of the polynomial function for each of the two variables;
- a Poisson error distribution.

We applied a *k*-fold method to avoid overfitting issues and derive the maximum order of the polynomial function for each variable that would give the lowest error [153]. The models for the RL and HL links in the optimal orientation are represented by Equations (4-24) and (4-25), respectively:

$$\begin{aligned}\mathrm{I}^{\mathrm{RL}}(\beta,\mathrm{d}) &= \frac{\mathrm{f}^{\mathrm{RL}}(\beta,\mathrm{d})}{\mathrm{d}^2} \\ &= \frac{1}{\mathrm{d}^2}\exp\{\mathrm{b}_1^{\mathrm{RL}} + \mathrm{b}_2^{\mathrm{RL}}\beta^2 + \mathrm{b}_3^{\mathrm{RL}}\mathrm{d} + \mathrm{b}_4^{\mathrm{RL}}\beta^2\mathrm{d} + \mathrm{b}_5^{\mathrm{RL}}\mathrm{d}^2 + \mathrm{b}_6^{\mathrm{RL}}\beta^2\mathrm{d}^2 \\ &\quad + \mathrm{b}_7^{\mathrm{RL}}\mathrm{d}^3\}\end{aligned} \tag{4-24}$$

$$\mathrm{I}^{\mathrm{HL}}(\beta,\mathrm{d}) = \frac{f^{\mathrm{HL}}(\beta,\mathrm{d})}{\mathrm{d}^2} = \frac{1}{\mathrm{d}^2}\exp\{\mathrm{b}_1^{\mathrm{HL}} + \mathrm{b}_2^{\mathrm{HL}}\beta^2 + \mathrm{b}_3^{\mathrm{HL}}\mathrm{d} + \mathrm{b}_4^{\mathrm{HL}}\beta^2\mathrm{d} + \mathrm{b}_5^{\mathrm{HL}}\mathrm{d}^2\} \tag{4-25}$$

where b_1, ..., b_7 are the polynomial coefficients; their values are listed in Table 4-4. The fact that the HL model only required five coefficients reflects its more regular emission pattern compared to the RL. Indeed, the HL exhibited an almost spherical emission profile, whereas the RL, owing to its shape and the arrangement of the LEDs (see Figure 4-28), has a more complex trilobate profile, requiring a higher number of coefficients for its accurate modeling.

Table 4-4. Coefficients of the propagation models for the RL (Equation (4-24)) and HL (Equation (4-25)) links.

Coefficient	RL	HL
b_1	2.59	2.45
b_2	−12.19	−0.78
b_3	−0.27	−0.015
b_4	2.09	−0.08
b_5	0.028	7.48×10^{-4}
b_6	−0.19	-
b_7	-7.53×10^{-4}	-

For the flat orientation, we weighed the optimal model predictions with an experimental coefficient accounting for the transfer function of the RX optics as a function of the azimuth angle: $H^{\text{RX-optic}} = SNR_{\text{flat}}/SNR_{\text{optimal}}$. This ratio does not depend on the light source used and can be calculated from the experimental amplitude maps for HL and RL. The values of $H^{\text{RX-optic}}$ are displayed as open symbols in Figure 4-33.

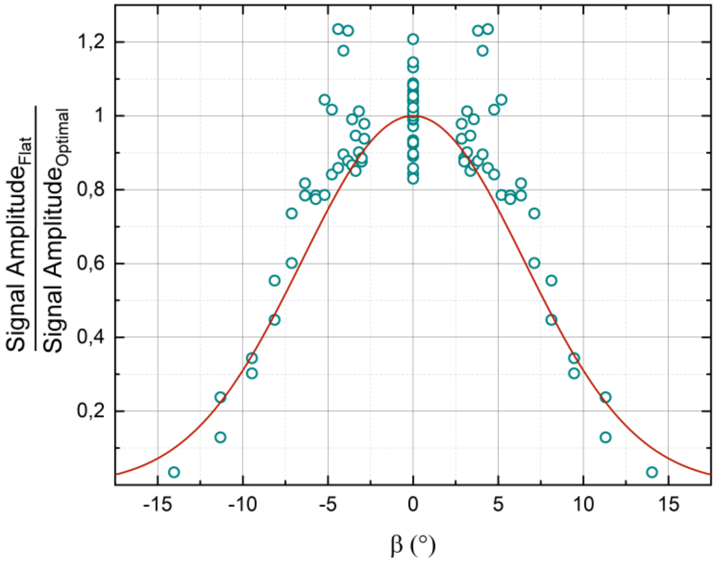

Figure 4-33. Experimental determination of the RX optics transfer function $H^{\text{RX-optic}}$ (open symbols) and the derived fitting curve (solid line) as a function of the azimuth angle β. The fit curve is normalized to 1.

The calculated values were fitted assuming a Gaussian dependence of the normalized transfer function on β (solid line in Figure 4-33):

$$H^{\text{RX-optic}}(\beta) = \exp\left\{-\frac{\beta^2}{2\sigma_{\text{opt}}^2}\right\} \tag{4-26}$$

where σ_{opt} represents the angular width of $H^{\text{RX-optic}}$. In this way, the amplitude maps of the flat orientation could be modeled by multiplying (43) and (44) by (45).

The model predictions thereby obtained are displayed in Figure 4-34 (panels a and b) and compared against the experimental SNR values (panels c and d). We could observe a very good global agreement between the predicted and measured SNRs for both lamps, except in some narrow regions at short lateral distances characterized by an underestimation of the amplitude. This was due to the specific emission patterns of the HL and RL, and to a higher sensitivity in positioning of the transmitter and receiver units for large angles.

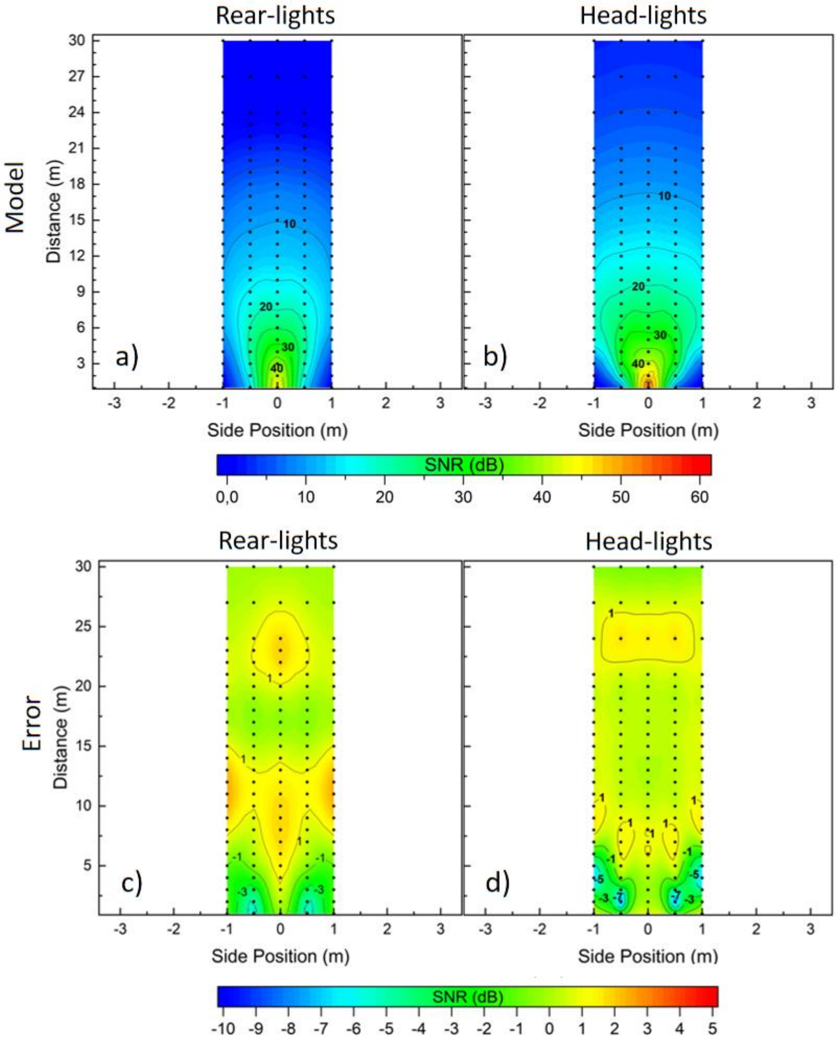

Figure 4-34. Amplitude maps for the flat configuration obtained using our model for RL (a) and HL (b). Map of the discrepancies (dB) between the SNR values measured during the experimental campaign and those obtained by the model for RL (c) and HL (d).

The SNR maps were used to predict the PER performances of a VLC link based on real LEDs for both unidirectional and bidirectional communication in the more realistic flat orientation. We calculated the BER considering possible synchronization errors stemming from the combination of clock signal and on-off keying of the NRZ-OOK scheme: namely, we considered the uncoded binary antipodal signal over an AWGN channel with imperfect timing, assuming a Gaussian distribution with zero mean for the normalized timing error; the standard deviation was assumed equal to 0.095 for the transmission at 57 kbaud and 0.0475 for that at 28 kbaud [154].

$$\mathrm{BER} = \frac{1}{4\pi\sigma_t}\int_{-\infty}^{+\infty} e^{\zeta/2\sigma_t}\int_{\sqrt{2\gamma}(1-2|\zeta|)}^{+\infty} e^{-\chi^2/2}\,d\chi\, d\zeta + \frac{1}{2\sqrt{2\pi}}\int_{\sqrt{2\gamma}}^{+\infty} e^{-\chi^2/2}\,d\chi \tag{4-27}$$

In Equation (4-27), σ_t is the standard deviation of the timing error, and $\gamma = E_b/N_0 = 1/\rho$ SNR is the ratio of the energy per bit and noise spectral density power; $\rho = R/B$ is the ratio between the data rate and the BW of the PD and is equal to $57/90$ for the 57 kbaud transmission and $28/28$ for the 28 kbaud one. For the measurements carried out at 57 kbaud, we used a PD gain G = 40 (BW = 90 kHz), while for those at 28 kbaud, we employed G = 50 (BW = 28 kHz). Therefore, the SNR can be calculated according to:

$$\mathrm{SNR} = \left(\frac{H^{RX-optic}(\beta)\ I(\beta, d) - T}{2\sqrt{2}\sigma}\right)^2 \tag{4-28}$$

where $H^{RX\text{-}optic}(\beta)\ I(\beta, d)$ is the amplitude of the VLC signal according to our model for the flat configuration; σ is the standard deviation of the background noise of the link; T accounts for a possible non-zero threshold in the receiver stemming from the presence of the comparator as a digitizing stage.

For the HL and RL links, the processes of error generation are statistically uncorrelated. Thus, we can calculate the PER of the bidirectional link assuming that the probability of success ($1 - PER^{BI}$) is given by the conditioned success probabilities of the unidirectional links:

$$1 - \mathrm{PER}^{BI} = (1 - \mathrm{PER}^{HL})(1 - \mathrm{PER}^{RL}) \tag{4-29}$$

The results of the procedure, obtained by setting T = 5 mV and $\sigma_t = 1.67$ μs, are reported in Figure 4-35; these two parameters were chosen based on our experimental observations of threshold and timing uncertainty of our digital boards. The PER values estimated by the model for the three links (unidirectional RL and HL and bidirectional) at 57 kbaud are plotted as a function of distance for the three side displacements (no displacement, 0.5 m, and 1 m) in the flat configuration. The percentage average error between the experimental values and the model was 17% for RL and 14% for HL. Visibly, the model was capable of predicting the PER performances of our link with remarkable accuracy.

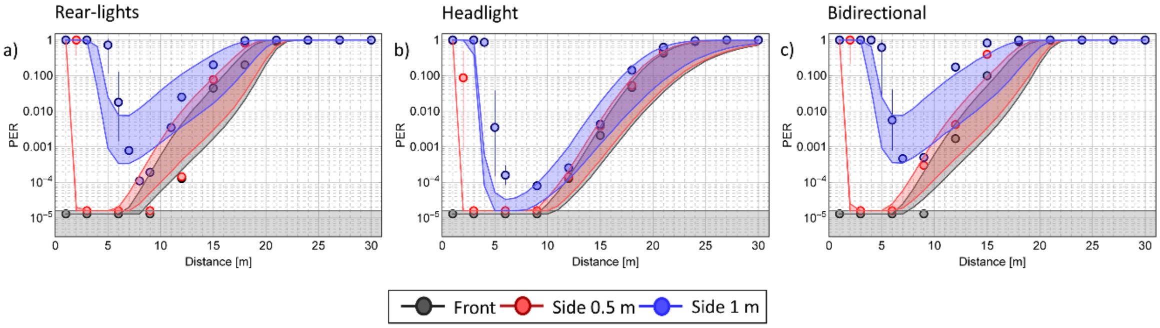

Figure 4-35. Experimental PER values compared with those estimated through our model as a function of distance in the flat configuration for: a) RL unidirectional 57 kbaud, b) HL unidirectional 57 kbaud, c) bidirectional 57 kbaud. The round markers refer to experimental data, whereas the shaded areas represent the model estimation embedding the model uncertainties.

4.6. Summary

In Section 4.2., we showed that the Lambertian model is less accurate than the ones proposed by us in describing the transmission and propagation of the VLC signal from traffic light to vehicle in a real scenario. Importantly, our models can be extended to distances exceeding those of the experimental campaign, allowing for a predictive value that can be extremely useful in urban settings where high accuracy is required. However, the two proposed polynomial models with 12 coefficients require a high computational cost, and this should be taken into account in mission-critical situations that necessitate high-speed communication and can tolerate higher error rates.

The experiments reported in Section 4.3. demonstrated the feasibility of a combined VLC I2V2V architecture based on an LED regulatory traffic light source and a custom PD detector. The entire prototype was based on a low-cost, open-source platform, entirely compliant with the IEEE 802.15.7 standard requirements. The system performance was evaluated through PER measurements for distances up to 50 m, revealing values of the order of 10^{-5} at the highest transmission rate used in this work (230 kbaud). A statistical analysis allowed us to obtain a predictive model for SAL below 1 ms with a 99.9% probability for PER = 5×10^{-3}. Therefore, our prototype can readily be integrated in the new 5G protocols for ITS applications in which high-quality safety standards are a pivotal requirement. For example, a decisive advantage of our VLC signaling system in a realistic road scenario would be a sudden braking over short distances or at high speeds, allowing a vehicle to stop with sufficient advance before crossing an intersection, as depicted in Figure 4-11.

The study reported in Section 4.4. represented the first detailed EFoV analysis for realistic ITS applications. We highlighted several nontrivial behaviors for different types of condenser elements which seem essential in the design of real VLC systems for ITSs. Depending on the specific VLC application, a higher importance can be placed on the use of short focal lengths with large acceptance angles (for example, when a high channel directionality is not required, such as typical indoor applications) or long-range transmission at the expense of the acceptance angle (*e.g.*, in I2V and V2V applications, for which a highly directional channel is paramount). Our optical model for received intensity and EFoV showed an excellent predictive ability and can be used to quantify the intrinsic performances of any VLC receiving unit consisting of an optical condenser and a PD. Further, the system based on Fresnel lenses was found suitable for both situational beaconing and event-triggered broadcast of information owing to its low latency. Overall, the prototype presented herein can ideally be integrated in real infrastructure and implemented with the current 5G-based ITSs.

In Section 4.5., we reported on the implementation and characterization of a bidirectional VLC link prototype, consisting of low-cost hardware as well as real motorcycle LED headlights and rear lights, in a realistic outdoor scenario. The transmission performances were assessed for different reciprocal orientations of the transmitting and receiving units by acquiring SNR amplitude maps and PER values at rates of 28 and 57 kbaud. As a result, we demonstrated the establishment of a successful VLC bidirectional communication ($\text{PER} \leq 10^{-1}$) for distances up to 21 m at 28 kbaud in the configuration with no TX-RX side displacement; error-free communication took place for distances up to 12 m. Importantly, a critical region was highlighted at short distances and large side displacements for the delivery of safety-critical information, which was a result of the LEDs' intensity patterns as well as the receiver's finite FoV. Finally, we introduced an accurate physical model of the bidirectional link taking into account the relative angles between the transmitter and receiver stages as well as the effect of finite FoV. The model was shown to predict the transmission quality of the link with remarkable accuracy for both the unidirectional and bidirectional configurations. The present model should be highly relevant for the design of novel VLC systems based on the bidirectional communication between consecutive vehicles in realistic ITS scenarios.

5. Indoor VLC: Museum application for pervasive communication and localization

5.1. Introduction to the Chapter

A key aspect of VLC is represented by the spatial directionality of the optical channel: in comparison to traditional RF fields, light fields can be readily shaped and contained by walls using low-cost optical elements. For this reason, one of the most promising applications of VLC is in localization protocols for users in indoor environments. Among these, museums and cultural heritage sites could benefit from the implementation of VLC channels to provide visitors with dedicated real-time information on the exposed artwork. However, studies exploring the suitability of VLC implementation in museum environments have been scarce. Existing research has so far reported proof-of-principle studies carried out in laboratory setups and focusing, for example, on VLC-based surveillance systems for the detection of inadequate behaviors of visitors [79,155]. In particular, there has been no characterization of a VLC system employing real museum lighting used to illuminate artwork. In such a scenario, it would be crucial to understand how light diffused by artwork could be exploited to transmit information; for this scope, a characterization of the OW channel should be performed in terms of PER as a function of position, relative angle, and distance from the artwork. To the best of our knowledge, such a characterization has never been carried out.

This Chapter presents the results of an extensive experimental campaign carried out in the Basilica of Santa Maria Novella in Florence (Italy) to characterize the performance of a VLC prototype in a real museum environment. We exploit the existing LED illumination in the Basilica to embed digital information within the light beams illuminating paintings and sculptures. In Section 5.2., we investigate the properties of our VLC channel through the analysis of the light diffused by two-dimensional artwork, including paintings by Masaccio, Vasari, and Ligozzi. We perform NLoS transmission tests and investigate the system performance through PER analysis as a function of relative distance and angle between the receiver and each of the artworks for realistic positions mimicking the locations of visitors looking at the artworks; furthermore, we quantify the effects of angular misalignment and lateral shifts. Then, in Section 5.3., we extend the characterization to a VLC link exploiting the diffusive illumination of three-dimensional wood and stone sculptures, in particular, masterpieces by Filippo Brunelleschi and Pagno Gherardo Bordoni. We characterize the optical channel in terms of SNR and PER patterns as a function of position and relative angle and distance from the three-dimensional artworks. The results presented herein could be relevant for different fields in addition to the cultural heritage sector: for example, the transmission of data streams through three-dimensional objects in NLoS could be implemented in both indoor and outdoor public structures such as offices, hospitals, and industries.

Figure 5-1. (a) Experimental setup for the characterization of VLC links in a museum environment; (b) and (c) receiving unit; (d) LED spotlights used for illumination and data transmission.

Our VLC system is presented in Figure 5-1. We exploit the existing spotlights of the Basilica, namely, commercial high-power dual white LEDs (Exenia Museo Mini 2L 609425042, with 2 × 9 W nominal power). The transmitter stage consists of a digital encoder/modulator. The signal is modulated using Manchester encoding to guarantee a constant average signal while maintaining a constant illumination (see Paragraph 3.2.3.). Moreover, the driver added a 0–200% AC current modulation on top of the DC nominal value (0.7 A), allowing a nominal light intensity on the artwork.

The receiver unit is mounted on a precision two-axis rotating stage (allowing for the determination of the angular position with an accuracy of 0.5°). The light diffused by the artwork is collected on a 75.4 mm^2 transimpedance PD with variable secondary-stage gain (Thorlabs PDA100A2, see also Paragraph 3.3.1.). As shown in Figure 5-1b, we insert an aperture stop consisting of a coaxial tube with the scope of limiting to the detector's FoV (which exceeds 110° with the bare PD). Since the horizontal dimensions of the artworks are ~4 m, by limiting the FoV within such a length, we can receive a data stream for a single piece of art. The dimensions of the tube are D = 25 mm and L = 20 mm, resulting in an optical angle of FoV of approximately 60° and a transverse linear FoV of approximately 5 m at a distance of 4 m.

To help suppress possible spurious DC stray light components, the PD is modified by the insertion of an AC-coupling network before the first transimpedance stage (as described in Section 4.2.). A digitizer/decoder stage carries out PER analysis in real time (see Paragraphs 3.3.3. and 3.3.4.). A 1 GSa/s digital oscilloscope records and analyzes the received signal.

The importance of this work lies in the demonstration of the ability of VLC technologies to function in museum environments by exploiting the light diffused by both 2D and 3D artworks. The very light used to illuminate the artworks can be employed as a means of communication. In this work, we show that such light can carry information about the artwork in an exclusive and practically directional (across distances of few meters) manner. For this scope, an in-depth knowledge of the optical systems is paramount for fine-tuning the geometric characteristics of the receivers: by tailoring the FoV, the best compromise between optical gain and interference rejection can be achieved.

5.2. VLC using LED light diffused by paintings

5.2.1. Experimental setup

Our system was tested on three different artworks characterized by different paints and positions in the main nave of the Basilica. The spotlights were installed on the floor at approximately 2.5–3.0 m from the artworks and in such a way so that their light cones were oriented upward, illuminating the center of the frames. Such a configuration, depicted in Figure 5-2, avoided the direct reflection of light toward the receiver, placed in front of the artwork at a height of 1.5 m (*i.e.*, mimicking the position of a visitor), and the only light component acquired by the RX unit was the diffused one.

We acquired intensity maps by recording the amplitude of the received VLC signal and measuring PER values for various distances and relative orientations of the receiving unit (Figure 5-2a). In addition, we performed an experimental determination of the threshold FoV of the receiver (see also Section 4.4.) to quantify the effect of angular misalignment between the optical axis of the RX and the artwork (Figure 5-2b). Finally, we investigated the effect of the lateral displacement of an observer (Figure 5-2c) on the quality of the VLC link. The measurements involved three different paintings, listed in Table 5-1 along with their salient characteristics.

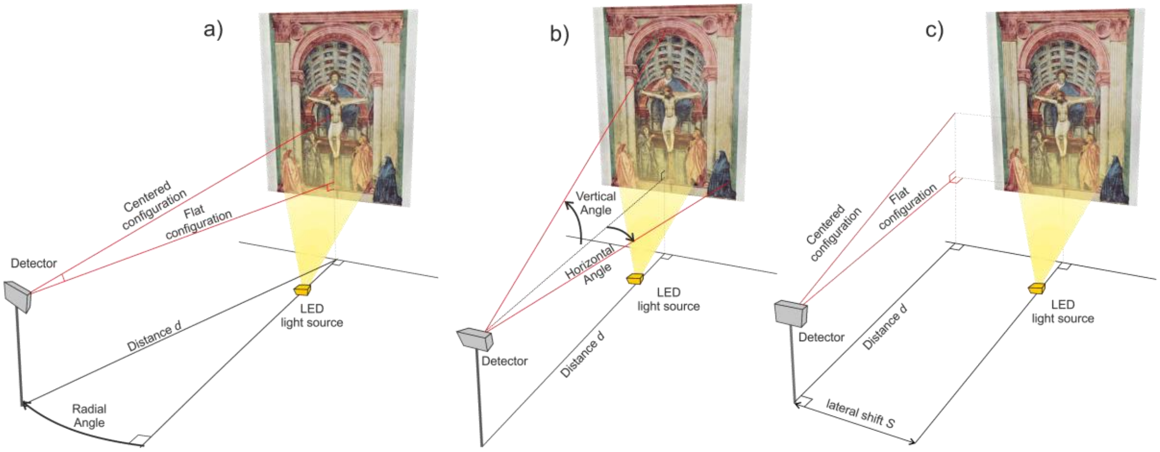

Figure 5-2. Configurations used in the experimental campaign. The detector was placed at various distances and angles from the artwork: (a) polar measurement, (b) FoV characterization, and (c) evaluation of lateral shift influence. The centered configuration was obtained by aiming the detector's optical axis toward the geometrical center of the painting, whereas in the flat configuration, the detector's optical axis was parallel to the floor.

Table 5-1. The three artworks analyzed in the experimental campaign.

Painting	**Year**	**Author**	**Support**	**Size w × h [m × m]**	**Distance to floor[a] [m]**
Trinity (Trinità)	1425–1426	Masaccio	Wall	3.17 × 6.67	0
Resurrection with four Saints (Resurrezione e quattro Santi)	1525–1574	G. Vasari	Canvas	2.95 × 4.07	1.95
St. Raymond of Penyafort resurrects a child (San Raimondo di Penyafort resuscita un fanciullo)	1620–1623	J. Ligozzi	Wood	2.95 × 4.07	1.95

[a] Distance from the bottom side of the painting to the floor level

5.2.2. Results and discussion

One of the main parameters determining the quality of a transmission channel is the SNR of the signal detected at the RX stage, because it is related to the communication performances (through Equation(2-12)). Therefore, it is paramount to acquire experimental SNR amplitude maps for our VLC prototype in relevant museum configurations. For each painting, the SNR values were recorded on a polar grid in front of the artwork for two distances (4 and 6 m) and for radial angles between 0° and 60° (error on angle determination = ± 1°). The experimental maps are presented in Figure 5-3: here, the black symbols represent the data, while the color maps are heuristic spline interpolations. The data refer to two different relative orientations of the RX, namely, flat and centered (depicted in Figure 5-2a and b, respectively): in the first, the optical axis of the receiver was parallel to the floor, while in the second, the vertical angle of the detector aimed at the center of the painting. We can observe a strong dependence of the recorded intensity on the specific artwork in both cases.

In the centered configuration, the main reason for such a dependence lied in the different nature of the paintings. The wall painting (Trinity by Masaccio, Figure 5-3a) was characterized by a rough surface, which would favor a strong diffusion of light toward a hypothetical visitor; moreover, light absorption would be strongly limited by the effects of aging on the painted layer. Here, the maximum recorded SNR was 21 dB (when facing the painting at a distance of 4 m), which decreased to 15 dB (6 m and 60° view angle). In contrast, the wood painting (Ligozzi's, Figure 5-3c) was characterized by a smooth substrate as well as the use of dark pigments: thus, the relevant reflectivity of the painted layer led to a significant decrease in the total amount of light reaching the detector. Here, the measured SNR range was 16–8 dB. Finally, the canvas by Vasari (Figure 5-3b) presented an intermediate diffusion of light owing to the intermediate brightness of its pigments and a higher roughness of the surface to Ligozzi's work.

In the flat configuration, the intensity of the diffused light was globally higher than that of the previously described case. This can be expected if we assume a uniform illumination and a Lambertian emission pattern for the diffused light [156], because the maximum diffusion line coincides with the orthogonal direction to the surface of the artwork. By increasing the relative angle between the normal direction and optical axis of the receiver, we could observe a decrease in the illuminance of the diffused light at the detector’s aperture.

The maximum and minimum SNR values were recorded for two different positions on the polar grid: the first corresponded to a distance of 4 m and 0°, while the second to 6 m and ± 60°; we defined these as frontal and angled, respectively. The recorded SNR values for such positions are summarized in Table 5-2. The most striking case was that of the frontal configuration: for example, for Vasari's canvas painting, a difference in SNR of 4 dB was observed between the frontal and centered positions. This was possibly due to the presence of bright white altar clothes placed in front of the artwork, resulting in a strong diffusion of light toward the detector when the optical axis of the receiver was horizontal; this object played a fundamental role in increasing the SNR and, consequently, the communication performances. In contrast, this component was practically negligible in the centered configuration: here, owing to the finite FoV of the detector, only the central portion of the paintings contributed to the VLC signal.

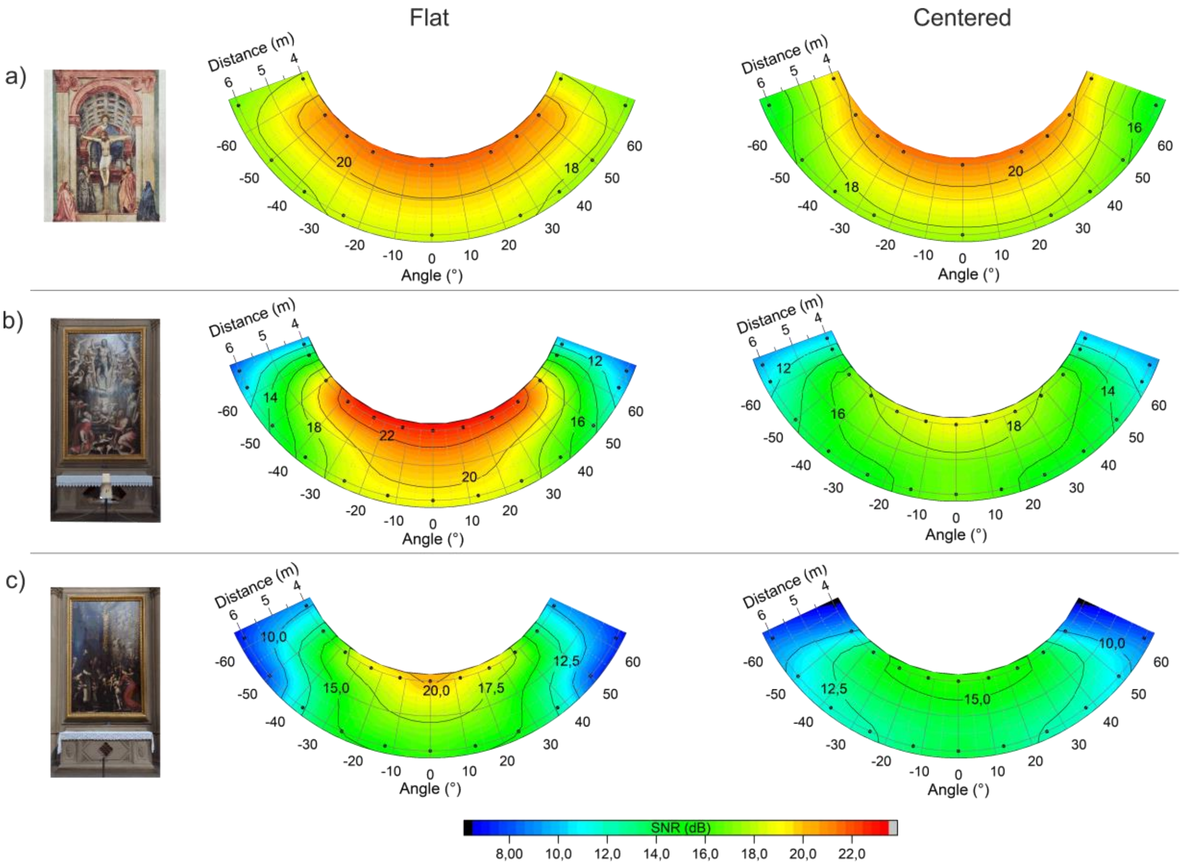

Figure 5-3. SNR maps acquired for the three different paintings listed in Table 5-1: (a) *Trinity*; (b) *Resurrection with four Saints*; and (c) *St. Raymond of Penyafort resurrects a child*. Data are recorded in both centered and flat configurations. The black dots represent the measurement grid; the color maps show a heuristic spline interpolation to the data.

VLC transmission tests

PER measurements were performed with the same experimental grid and configurations used to acquire the SNR amplitude maps. After some preliminary tests, in which we employed baud rates between 4.8 and 115.2 kbaud, we finally chose a transmission rate of 28 kbaud as the best trade-off between acceptable PER and latency values. The packets consisted of a 3-byte equalization frame, a 2-byte synchronization preamble, and a 4-byte data payload (see also Paragraph 3.2.2.). We employed the OOK scheme with Manchester encoding, as per IEEE 802.15.7 PHY 1 standard for VLC [142]. The PER analysis was carried out by recording a continuous stream of data packets; the digital board in the RX stage performed real-time, bitwise analysis. Such an analysis did not include the pre-equalization frame, whose scope was the stabilization of the data signal toward a steady RMS value corresponding to the comparator threshold. The overall acquisition length was limited to 50000 packets, setting the minimum detectable PER to 10^{-5} for an error-free transmission. The results are reported in Figure 5-4, where the maps present the PER values as a function of distance and radial view angle. The green symbols and areas correspond to the centered configuration, while the red ones to the flat configuration.

Table 5-2. Experimental SNR values (in dB) acquired for different configurations and positions (see also Figure 5-2) for the three paintings investigated in this work. The frontal viewpoint corresponds to a distance of 4 m and an angle of 0°, while the angled one refers to 6 m and ± 60°.

	Flat configuration		**Centered configuration**	
	Frontal [dB]	**Angled [dB]**	**Frontal [dB]**	**Angled [dB]**
(a) Masaccio (wall painting)	22	17	21	15
(b) Vasari (canvas)	23	9	19	10
(c) Ligozzi (wood painting)	20	8	16	8

The angular range pertaining to the present analysis was 0°–60°, as no significant variations were expected to take place in the symmetric quadrant between 0° and −60°. Let us first analyze the results obtained when the receiver was placed at a distance of 4 m. For the wall painting (Masaccio's, Figure 5-4a), we obtain PER < 10^{-4} in both configurations, reflecting the similar amplitude maps discussed previously for the same setting. A progressive degradation of PER could be observed for increasing radial angles (> 10^{-3} at 60°); however, these values would still ensure a reliable transmission, with no significant differences for the two configurations. In contrast, concerning Vasari's masterpiece, the performance of the link depended on the configuration used; the painting was capable of diffusing a larger amount of light owing to the clear paint used on the artwork as well as the presence of bright objects placed in front of the artwork. In the flat configuration, an error-free communication was achieved for angles up to ~35°; in the centered one, the minimum PER was 2×10^{-3}. Finally, Ligozzi's wood painting yielded the worst performance among the three cases, as suggested also by the SNR maps (a lower received signal equals a higher PER). However, the observed PER was still approximately 4×10^{-4} in the frontal flat position.

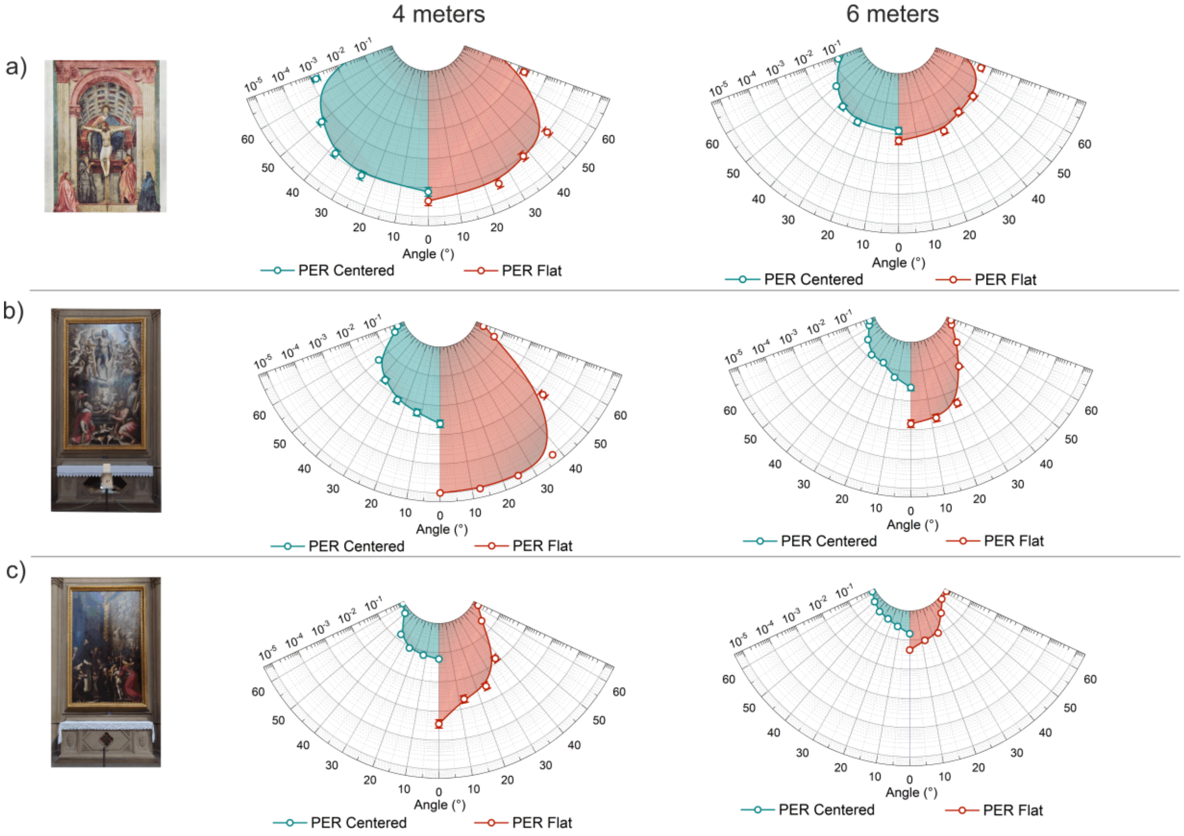

Figure 5-4. PER maps as a function of radial angle measured at distances of 4 and 6 m for the three artworks: (a) wall painting by Masaccio; (b) canvas by Vasari; (c) wood painting by Ligozzi. The open symbols represent the experimental data; the error bars representing the statistical average error are masked by the symbols. Lines are a spline interpolation used as a guide to the eye. The green and red color codes represent the centered and flat configurations, respectively.

For the distance of 6 m, the system performance was globally worse as a result of the lower intensity received at the RX. However, a PER of approximately 3×10^{-2} was observed for Masaccio's artwork in a large range of radial angles in the flat configuration. For Vasari's painting, the best observed PER was 10^{-3} in the same configuration. Finally, for the wood painting, we recorded a value of ~4×10^{-2} at 0°. These values are summarized in Table 5-3.

Table 5-3. PER values measured in relevant positions near the three paintings (see also Figure 5-2) investigated in this work. The frontal viewpoint corresponds to a distance of 4 m and an angle of 0°, while the angled one refers to 6 m and ± 60° (see Figure 5-2).

	Flat configuration		**Centered configuration**	
	Frontal	**Angled**	**Frontal**	**Angled**
(a) Masaccio (wall painting)	3×10^{-5}	2×10^{-2}	7×10^{-5}	8×10^{-2}
(b) Vasari (canvas)	1×10^{-5}	6×10^{-1}	2×10^{-3}	5×10^{-1}
(c) Ligozzi (wood painting)	4×10^{-4}	8×10^{-1}	6×10^{-2}	8×10^{-1}

According to these results, our VLC prototype can afford the transmission of digital information modulated through the light diffused by works of art and other objects placed in a museum room, covering a wide area in front of the artworks, where a typical visitor is expected to stand. If the value of PER ~10^{-3} is considered as the minimum quality threshold an error-free transmission [150], the performance of our VLC link in the flat configuration at a distance of 4 m achieved a successful delivery of information for a range of radial view angles between 0° to 55° in the case of the wall painting, up to 50° for the canvas painting, and up to 5° for the wood painting characterized in this study. Many factors are at play in the determination of a radial view angle, starting with the type of artwork (*e.g.*, canvas, fresco, wood painting...), paint, surface finish (such as the use of light-reflective oils), the presence of nearby objects that may reflect a large amount of light (such as, in our case, a white cloth placed on an altar below the artwork). In this scenario, further development in modeling the communication channel may involve a characterization of the chromatic yields and diffusion coefficients of the paintings.

To evaluate the possibility of employing VLC technology in real museum environments, it is important to assess the sensitivity of the RX to angular misalignment through a specific PER measurement campaign, which we performed focusing on Masaccio's wall painting. Indeed, angular measurements can provide information on realistic misalignments between TX and RX, help evaluate the aperture stop and, consequently, adjust the FoV in such a way as to isolate the contribution of each artwork (together with the lateral shift measurements). The receiver unit was placed in the frontal configuration (*i.e.*, 4 m and 0°), with both the horizontal and vertical angles equal to 0° as the reference position (see Figure 5-2b), and we scanned both orientations of the optical axis. The results of the campaign are shown in Figure 5-5; panel (a) reports the PER values obtained after a scan of the horizontal RX angle in the flat and centered configurations, while panel (b) presents those obtained for the variation in the vertical angle. We introduced here the threshold angle of field of view (TFoV), defined as the angle for which the measured PER was equal to a threshold value (= 10^{-3} in our case). From the data reported in Figure 5-5, we can estimate the horizontal and vertical TFoVs: namely, the horizontal TFoV values (panel (a)) were approximately 20° and 15° for the flat and centered configurations, respectively, while the vertical one (panel (b)) was approximately 30°. The difference in TFoV values resulted from the asymmetric light pattern: as shown in Figure 5-2, the experimental layout led to an elongated emission lobe in the vertical direction (wall surface). Nevertheless, these results suggest that our VLC channel can tolerate realistic misalignments such as those that might occur when a visitor is holding the receiver in their hand.

In those fields for which dedicated services and indoor localization are paramount, it is extremely useful to differentiate between neighboring receivers. In a museum scenario, the receiver held by a visitor may be intentionally pointed toward a nearby piece of art to acquire information on the latter: by increasing the view angle over the initial TFoV, the user would stop receiving data from the initial spotlight and move to the next without interference between the two data streams. To achieve this, the VLC transmission should be appropriately confined to a specific region near each piece of art. To assess the capability of our optical channel to withstand sidewise displacement, we acquired the PER variation with lateral distance for both configurations. The measurements were carried out only at the frontal distance of 4, and the results are presented in Figure 5-6. We can observe that the transmission was lost for side displacements higher than 1.5 m ($PER < 10^{-3}$), and the PER value was 1 beyond 4 m, corresponding to the absence of received packets at the RX. Because some real museum settings, such as the one presented herein, are characterized by a separation of at least 5 m between artworks, our VLC system could readily differentiate the data streams of neighboring hotspots. In other applications, naturally, an adjustment of the FoV might be necessary.

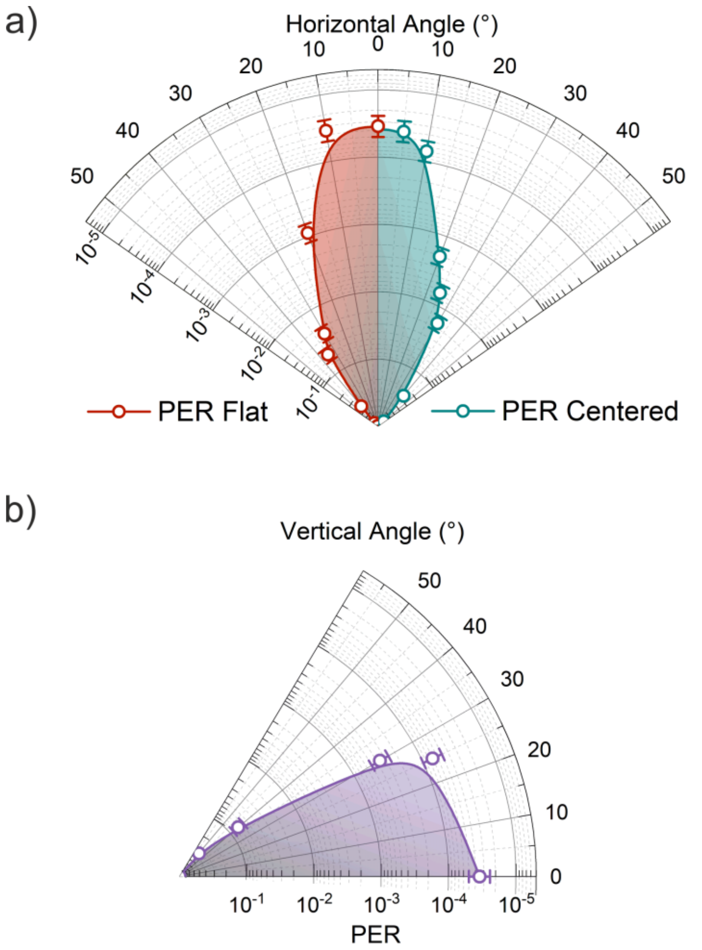

Figure 5-5. Determination of TFoV values through the PER values recorded for the wall painting by Masaccio by scanning the two angular positions of the receiver's optical axis: (a) horizontal (red symbols: flat configuration; green symbols: centered configuration) and (b) vertical. Error bars represent the statistical average error, equal to 40%, measured through 10 repeated measurements of the same PER and evaluated for different PER values.

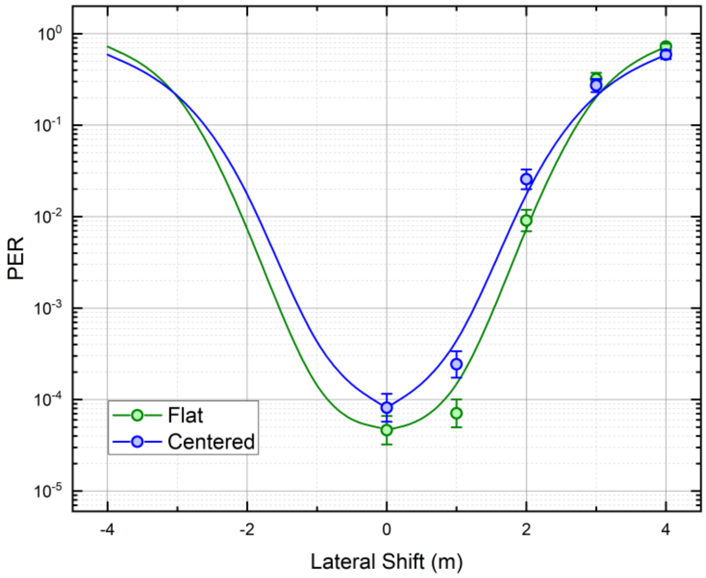

Figure 5-6. Effect of lateral displacement of the RX position on VLC transmission quality (wall painting by Masaccio). Data points show the measured PER for the flat (green symbols) and centered (blue symbols) configurations.

5.3. VLC using LED light diffused by sculptures

5.3.1. Experimental setup

After testing our VLC link in a real museum environment with two-dimensional artworks, we exploited our findings to further assess the possible implementation of this technology in the presence of three-dimensional art such as sculptures. Compared to two-dimensional artworks such as the painting analyzed in the previous Section, sculptures can give rise to a very different diffusive channel owing to the variable orientation of their surfaces. A new experimental campaign was carried out in the Basilica of Santa Maria Novella in Florence, Italy, this time focusing on the wooden Crucifix by Filippo Brunelleschi (1415) and the Holy Water Font by Pagno Gherardo Bordoni (XVII century). The hardware used for these experiments was the same as the one described in Section 5.2., while the experimental layout is sketched in Figure 5-7, where one can observe the two configurations chosen for our measurements: in the centered configuration, we mimicked the position of a visitor aiming the detector at the geometric center of the artwork (vertical angle ~20°), whereas in the flat configuration, the optical axis of the detector was parallel to the ground (vertical angle ~0°).

It should be noticed that the lighting positions were different for the two masterpieces considered herein: the Holy Water Font was illuminated from the floor level by a LED spotlight placed at a distance of 1 m, while the Crucifix was illuminated by a lamp positioned behind an altar, at a height of 1.5 m from the floor and a distance of 1.5 m from the Crucifix itself. Notably, the light was almost entirely directed upward, with only a minor diffused component, which made the communication more difficult. Therefore, because the RX stage was positioned at a height of 1.5 m from the floor in front of the artwork, the detector would mainly receive the diffused light.

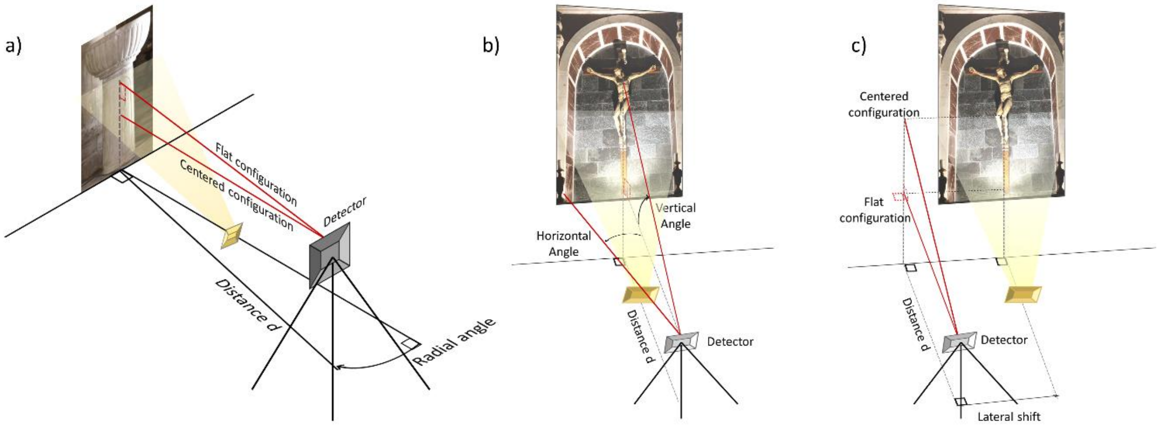

Figure 5-7. Experimental layouts for the SNR and PER measurements carried out on the three-dimensional pieces of art: (a) polar, (b) FoV, and (c) lateral displacement (see main text for descriptions).

Two different experimental grids were set for the artworks as follows. The Holy Water Font is a marble sculpture of cylindrical symmetry; placed in the main aisle, its observation range is quite large. As a result, we were able to perform measurements for angles up to 180° around the sculpture, with the most interesting configuration being the polar one, depicted in Figure 5-7a. We measured the PER and signal amplitude values to obtain intensity maps of the received VLC signal as a function of the TX/RX angle for different distances.

The Crucifix, in contrast, is placed against the back wall of a chapel that cannot be directly accessed by visitors. To accurately simulate the minimum distance of an observer from the artwork (6 m), we performed measurements aimed at determining the FoV of the RX (see Figure 5-7b) through angular scans in the vertical direction. These experiments allowed us to acquire information on the effects of angular misalignment between the optical axis of the receiver and the artwork, which yielded a thorough characterization of the VLC link quality as a function of an observer's lateral displacement with respect to the geometrical center of the Crucifix.

Further, we obtained a semi-quantitative assessment of the combined effects of channel noise, inter-symbol interference, and jitter in the VLC channel for the two artworks through eye diagrams realized for two different SNR values.

5.3.2. Results and discussion

A plot of the PER values as a function of SNR is presented in Figure 5-8: evidently, our VLC link achieves error-free communications in a diffusive NLoS configuration for SNR > 22 dB; however, successful communication, corresponding to PER < 0.1, was achieved for SNR > 15 dB. The data were accurately modelled using the already known relationship between PER and SNR through the Q function, according to Equation (2-12); the good quality of the fit confirmed the hypothesis of AWGN affecting the VLC channel.

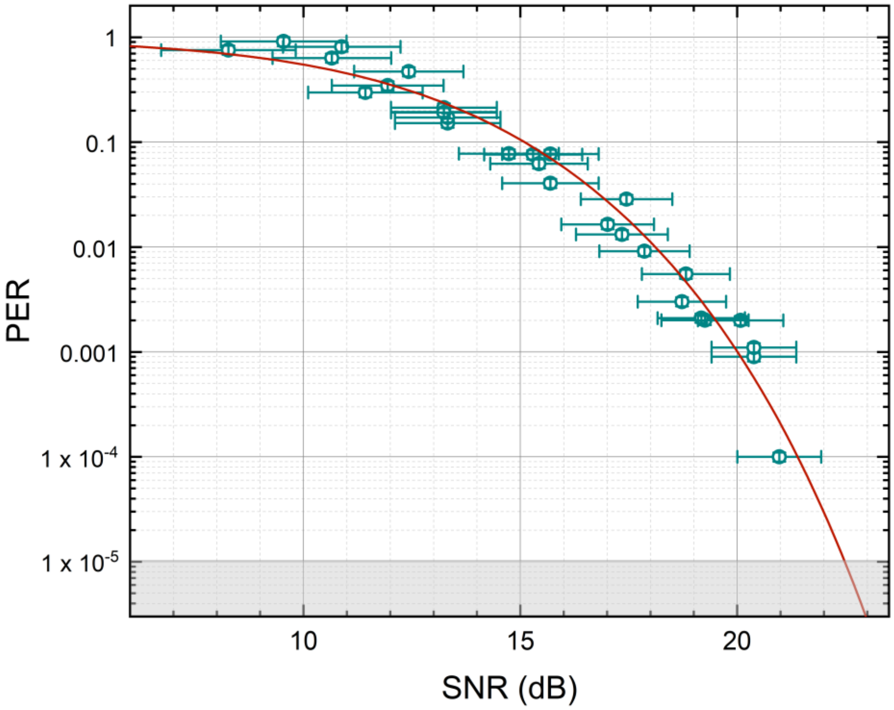

Figure 5-8. Typical PER values plotted as a function of SNR of the received signal amplitude. Green circles = experimental data; with horizontal error bars = uncertainty in amplitude; vertical error bars (smaller than symbols) = variance on the number of wrong packets on consecutive measurements; red line = best model fit to experimental data (see main text); shaded area = error-free region.

The eye diagrams are shown in Figure 5-9 for the two regions: low signal (SNR = 11 dB, PER ~0.5) and high signal (SNR = 22 dB, error-free). For each panel, three traces are reported, from top to bottom: i) the TX signal generated by the Arduino DUE board; ii) the analog output of the photoreceiver after the TIA; and iii) the digitized output of the comparator stage at the RX. The acquisition was self-triggered on the RX signal, thus, the horizontal spread of transition edges in the digitized signal contained information on the jitter in the reconstructed VLC digital signal.

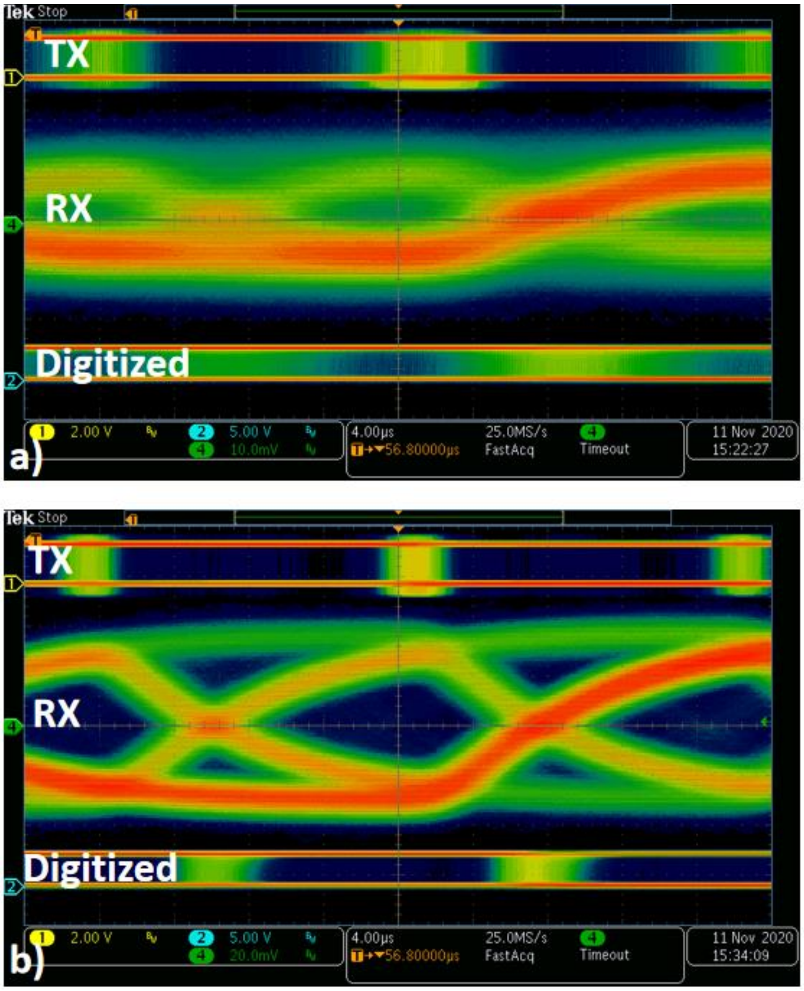

Figure 5-9. Heat maps showing eye diagrams for a) PER > 0.1 with SNR = 11 dB, and b) error-free communication with SNR = 22 dB. The shown traces are TX, RX, and the digitized signal after the comparator. The horizontal scale is 4 μs. The acquisition is self-triggered on the RX signal, so that the horizontal spread of the digitized signal corresponds to a jitter of 1–4 μs in the reconstructed VLC digital signal, depending on the SNR level.

In particular, we could observe a jitter of ~2 μs in the TX trace of the high-level signal eye diagram (Figure 5-9b) and one almost twice as large in the digitized signal, which can be attributed to the time limit of the Arduino DUE platform. This result can be explained by considering that TIA noise is usually the most important component of noise in indoor environments because the optical effects originating from air density fluctuations are negligible. The TIA is subjected to thermal and shot noises; for low signals, these contributions can be relevant and determine a random jitter [157,158]. In the low-level signal in Figure 5-9a, the noise fluctuations of the TIA are summed to the received amplitude, bringing the signal close to the threshold value T of the comparator. As a consequence, the comparator commuted faster and was thus more likely to induce a jitter of ~8 μs in the digitized signal, which caused the eye diagram to be less defined.

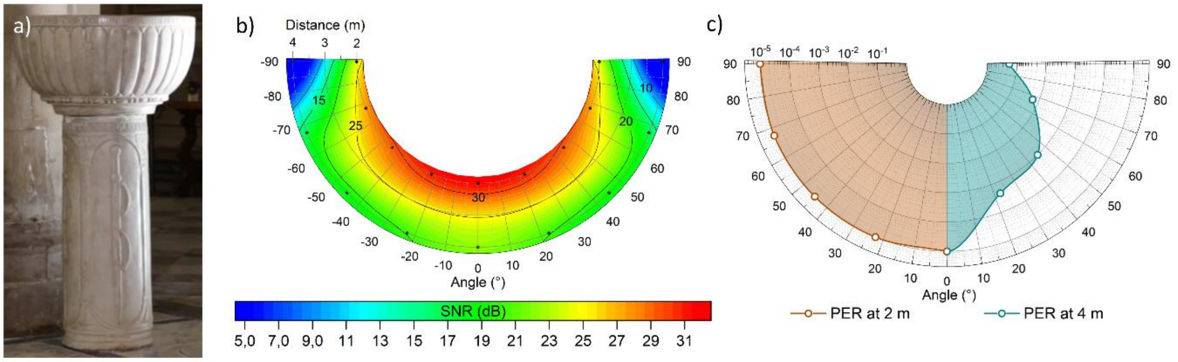

Figure 5-10. a) Photograph of Bordoni's sculpture, the Holy Water Font. b) Polar map of SNR amplitude values for a noise of RMS = 2.2 mV. Black symbols represent the experimental data, while the color map is a cubic spline interpolation. c) PER performance at distances of 2 m (orange) and 4 m (green) as a function of radial angles.

Let us first address the measurements performed on the Holy Water Font, shown in Figure 5-10a. We scanned the horizontal angular positions of the receiver around the Font in an angular range of ± 90°; the two radial distances considered were 2 and 4 m. The PD was kept facing the artwork at a fixed vertical angle allowing to collect the maximum amount of light diffused by the sculpture. This configuration will be referred to as optimal. The resulting SNR and PER maps are presented in Figure 5-10b and c, respectively. The results show that an error-free communication was achieved in the entire horizontal angular range for a distance of 2 m, where the SNR was always higher than 25 dB. At 4 m, the performance was predictably worse owing to the decrease in diffused light intensity; however, the PER was < 10^{-1}, indicating successful communication over the entire range of measured angles, and the error-free condition was achieved in the frontal position (angle = 0°). Nevertheless, it is worth remarking that PER values of ~10^{-1} can also ensure low-latency services [22].

We now discuss the results of the analysis on the wooden Crucifix sculpture by Brunelleschi, shown in Figure 5-11a. The artwork was located in a niche, standing against a wall, which implied that the movements of visitors could only take place in a narrow angular range. In addition, visitors could not approach the artwork further than a distance of 6 m. Clearly, such a configuration does not allow for polar tests for this piece of art. Therefore, we performed experiments to assess the FoV and the effects of side displacement on the quality of the VLC link. The results of PER measurements in the centered configuration are presented in Figure 5-11b, where the PER values are plotted as a function of the horizontal angular misalignment between the optical axis of the receiver and the sculpture. We can observe that a successful communication (PER > 0.1) occurred for the angular range between −10° and 15°, corresponding to an EFoV of 25°. Moreover, the light diffused by the stone wall behind the Crucifix contributed to the VLC signal, suggesting that the communication system could be improved by purposely placing three-dimensional artworks by walls. Notably, the projection of the measured FoV angle on such a wall covered a horizontal distance spanning approximately 2.6 m, suggesting that the latter would be the appropriate separation between pieces of art to avoid interference between data streams dedicated to each object. A similar set of measurements was carried out spanning the vertical angular orientation of the receiving stage. As shown in Figure 5-11c, a successful communication (PER < 0.1) was achieved for vertical angles between 10° and 30°; moreover, the minimum vertical separation between exposed objects to avoid data stream interference was estimated as 2 m through the same type of FoV analysis as above.

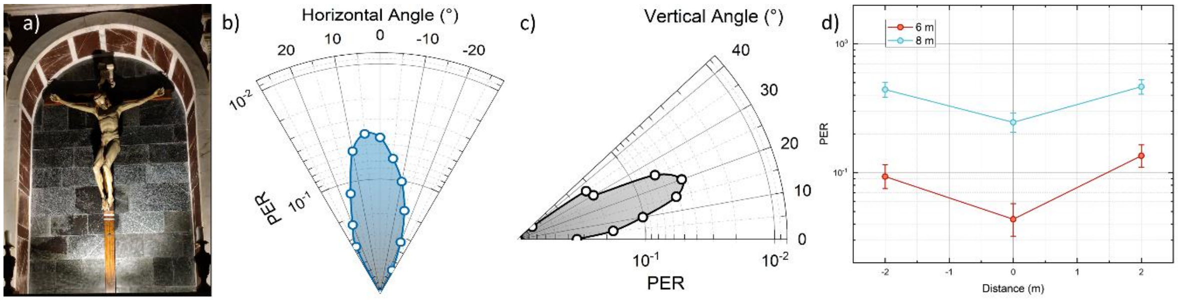

Figure 5-11. a–c) Experimental determination of EFoV through PER PER values measured for Brunelleschi’s Crucifix (photograph in panel a)) as a function of the horizontal b) and vertical c) angular orientations of the receiver's optical axis at a distance of 6 m. d) Measured PER for side shifts of ± 2 m at distances of 6 m (red) and 8 m (cyan) from the artwork.

Finally, we focused on the effect of a lateral displacement of the observer on the performance of our VLC prototype. The data are shown in Figure 5-11d, where the PER values are plotted as a function of the lateral shift of the receiver for two different distances. As a result, we observed a weak effect of lateral displacement on the link performance. The reason for this could lay in the localization of the sculpture in a 5 m long chapel niche made of reflective materials, which might contribute to an efficient diffusion of light and a consequent increase in the received SNR. Once again, this finding highlights the importance of exploiting light diffusion and reflection from items and structures placed near the works of art in a real museum scenario with the aim of enhancing the VLC signal quality.

5.4. Summary

This work represents the first detailed experimental characterization of an NLoS VLC system applied to a real museum environment. The study involved different types of supports, corresponding to different physical-chemical and geometric characteristics: from two-dimensional artworks (paintings) to three-dimensional ones (sculptures). We exploited the existing LED lighting system to embed information and direct it toward a receiver, representing a handheld device that could be used by museum visitors, which collected the light and VLC signal diffused by the artworks. Our analysis of the system performance highlighted the possibility of obtaining a stable VLC link in significant areas near each artwork even in conditions of TX-RX angular misalignment, simulating the movement of an observer across the room. Our prototype was found able to localize visitors and cast dedicated information for specific artwork. One way to reduce PER and increase system performances could consist in placing light-diffusing objects next to the artworks, such as the white cloths standing near the altars, which are able to increase the received signal amplitude. Notably, such a platform could be used for VLC-based localization in more general scenarios where diffusive illumination systems are present: envisaged applications concern the deployment of VLC links in indoor environments including, but not limited to, position-dependent alerting and dedicated advertisement services.

6. Mid-infrared free-space optical communication based on quantum cascade lasers

6.1. Introduction to the Chapter

FSOCSs have attracted significant interest in the reinforcement of 5G networks and for those applications that are difficult to implement with optic fiber cables, such as point-to-point and satellite-assisted communication infrastructures [159,160]. FSO technology presents several advantages, such as a higher carrier frequency and spatial directionality, wider bandwidth, lower cost, and simpler infrastructure compared to fiber links [161]. So far, FSOCSs have been developed in the near infrared (NIR) region of the spectrum, which covers the wavelength range between 0.75 and 3 μm, using well-established transmission and reception technologies mainly developed for optical fiber links. Most recently, the attention of researchers in the field has begun shifting to the MIR range ($\lambda > 3$ μm) to complement the NIR atmospheric transparency regions [162]. In particular, the MIR region is less sensitive to a number of factors, including: particle scattering, whose effect is proportional to λ^{-4} [163]; background noise originating from the black-body emission of the Sun, which peaks at approximately 500 nm and is substantially suppressed at longer wavelengths than 3 μm; and black-body emission of Earth, which peaks at $\lambda \approx 10$ μm and is suppressed for $\lambda < 5$ μm [164]. As a result, the MIR region can be more efficiently exploited for communication especially during night time and adverse weather conditions in comparison with the NIR one [165]. The development of MIR-based FSOCSs has progressed more rapidly since the advent of QCLs: these are chip-scale, semiconductor-heterostructured sources whose emission can cover a wide spectral range between 3 and 12 μm [166]. QCLs can operate at room temperature and be modulated both electrically and optically at high frequencies (up to several GHz) [167]. Recent proof-of-concept studies have shown FSOCSs with QCLs emitting at approximately 4.7 μm; successful transmissions in the tens of MHz range over distances of 2.5 m [168] and data rates of up to 4 Gb/s over distances of 5 cm have been demonstrated [19].

This work deals with the characterization of digital communications through a QCL source in the MIR range and a low-cost encoder platform. At the same time, it models the feasibility of using specific-wavelength QCLs for long-range communications. It should be noted that the communication performances of MIR FSOCSs based on QCLs still require a comprehensive evaluation for their effective application in real scenarios. In this work [31], we develop and characterize an MIR FSOCS based on a QCL emitting at 4.72 μm. The system, described in Figure 6-1, consists of a transmitter unit, in which a digital message is encoded in the MIR-range light emitted by the source using a current amplitude modulation (AM), and a receiver unit capable of detecting the optical signal, converting it to voltage, and decoding the message. Let us now analyze the experimental setup in detail.

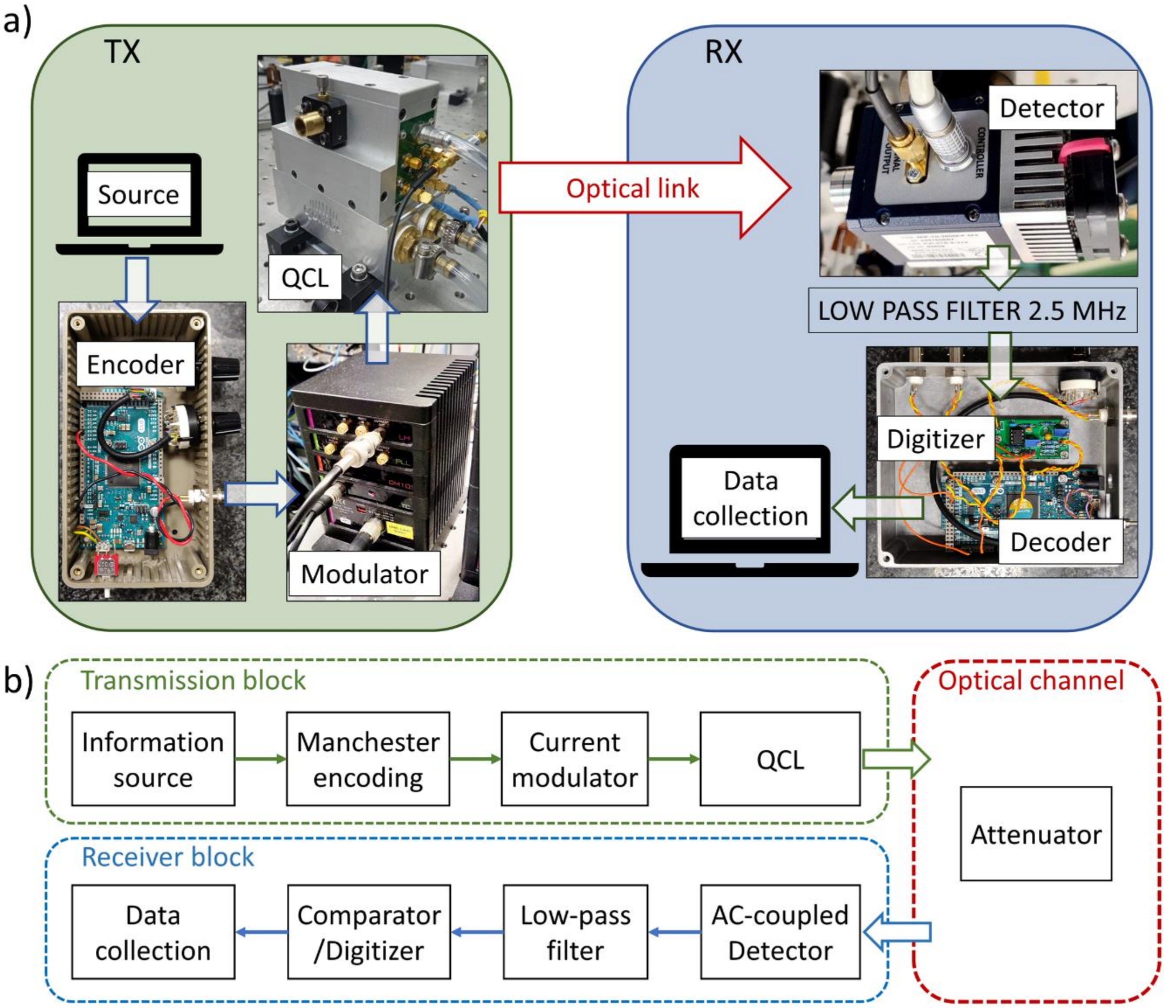

Figure 6-1. Photographs (a) and block diagrams (b) of the experimental setup highlighting the transmission block (green), optical channel (red), and receiver block (blue). The data stream is generated by a digital platform and encoded into the MIR light emitted by the QCL through the modulation of the laser driving current. Manchester encoding is used to ensure a constant average signal. The light travels through the optical channel, where it is attenuated to simulate long distances and then collected by a photovoltaic AC-coupled detector. The signal reaching the detector is filtered by a 2.5-MHz low-pass filter, digitized and compared with a pre-stored reference message.

6.2. Experimental setup

6.2.1. Transmitter and receiver

The MIR source was a custom Fabry–Pérot continuous-wave QCL fabricated at the Swiss Federal Institute of Technology (ETH, Zurich, Switzerland). Its emission wavelength was $\lambda = 4.72$ μm. The laser was capable of operating at $T = 18$ °C in a single-mode regime from the threshold current of 638 mA up to 680 mA; for $I > 680$ mA, it operated in a multi-mode regime. The current driver (QubeCL15-P from ppqSense srl) was characterized by a nominal current noise density of 200 pA/pHz and equipped with a low-noise current modulator (maximum modulation amplitude = 5 mA; modulation bandwidth = 1 MHz). The laser beam free-space propagation occurred through an optical path length of 3 m and a variable optical attenuator before reaching the receiver. Different attenuation regimes were applied to simulate realistic situations in outdoor FSOC. These were obtained by adjusting a rotating polarizer plate (WP25H-Z holographic wire grid polarizer, Thorlabs); indeed, because the QCL was linearly polarized, the amount of light was controlled by rotating the polarizer plate, and the residual optical power after the waveplate could be adjusted in a range between 14 and 52 dB. In particular, 14 dB was the minimum attenuation for an emitted optical power (P_{out}) of 13 mW to prevent detector saturation and degradation. At 52 dB, the maximum attenuation, the maximum power to perform a communication with OOK modulation (*i.e.*, the modulation used to turn the laser on and off) was $P_{out} = 1.66$ mW. The beam was focused on a two-stage transimpedance pre-amplified (MIP-10-250M-F-M4, Vigo System) MIR HgCdTe photovoltaic detector (PVI-4TE-5-2x2, Vigo System) having a nominal bandwidth of 180 MHz and operating in the range 2.5 μm $< \lambda <$ 5 μm. The detector was in its linear responsivity regime for $P < 1.2$ mW and would saturate at higher powers.

The information signal was generated by an Arduino DUE microcontroller (Encoder in Figure 6-1a) using an OOK scheme with Manchester encoding *via* the current driver, which adds the AC modulation on top of the laser DC driving current. The data stream, consisting of 62500 packets, was transmitted continuously at a rate up 115 kbaud, applying an inter-packet delay of 730 μs. Each packet consisted of 9 bytes (3 initial equalization bytes for signal pre-equalization, followed by 2 synchronization bytes and 4 data payload bytes, as shown in Figure 3-4). The receiver side (Figure 6-1b) was equipped with a 2.5 MHz low-pass filter (BLP-2.5+, Mini-Circuits) to cut off any frequency components higher than 10× the first harmonic of the modulation signal. The analog signal was digitized by a variable threshold comparator (Paragraph 3.3.3.), decoded in real-time by the RX

Arduino DUE board, and recorded by a 2.5 Gs/s 4-channel digital oscilloscope (Tektronix MDO3024 200 MHz).

6.2.2. Attenuation and noise regimes

The effective design of an FSOCS requires a correct evaluation of the noise contributions that can influence the SNR, including flaring, scintillation, and turbulence. A complete discussion would require the analysis of atmospheric factors; however, an analysis of the noises at the source and the detector in different regimes is a key aspect of the characterization of an FSOC link. In this work, we implemented two communication configurations corresponding to two realistic attenuation regimes. The first was a high attenuation regime (HAR), which was dominated by propagation and attenuation losses; the second was a low attenuation regime (LAR), in which the background noise of detector was overcome by the intensity noise of the laser. Let us now analyze each of these regimes.

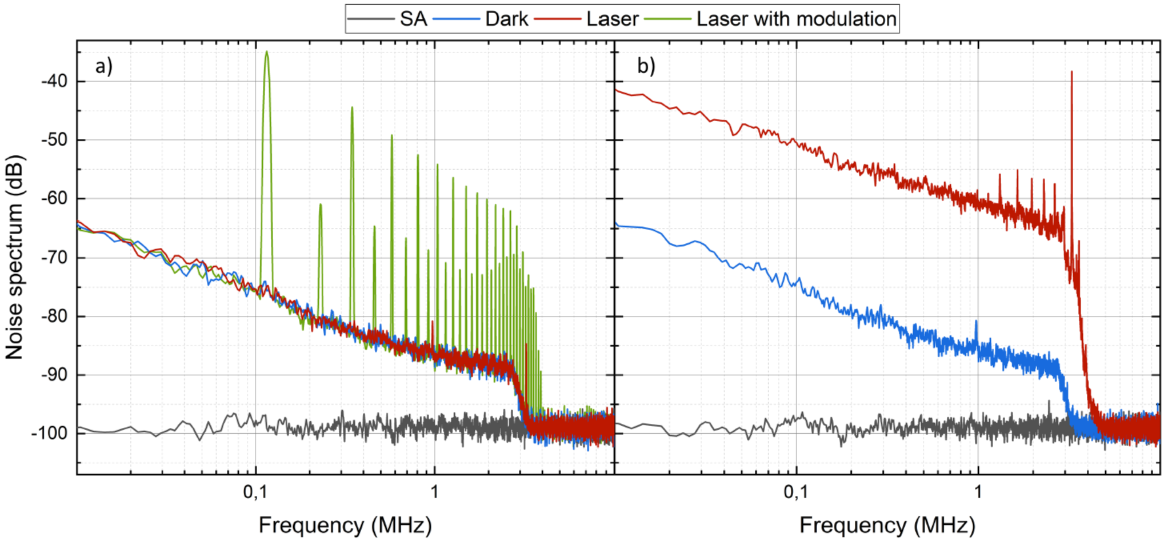

Figure 6-2. Signal noise spectra in the a) HAR and b) LAR regimes. The plots present the recorded spectrum analyzer background (*SA*, grey trace), the detector background (*dark*, blue trace), the laser+detector signal measured without beam modulation (*laser*, red trace) and in the presence of a digital modulation at 115.2 kHz with a 100% depth (*Laser with modulation*, green trace). The spectra were acquired *via* a handheld spectrum analyzer (Signal Hound USB-SA44B).

HAR conditions are connected to the case of a long-range outdoor FSOC, where the laser beam is strongly attenuated owing to absorption and scattering by atmospheric molecules and particles, possibly resulting in a significant extinction of the optical beam [169]. Therefore, the detector receives a very low residual intensity, and the detector background noise can overcome the intensity noise of the laser, as shown in Figure 6-2a. To accurately simulate such a scenario, we attenuated the incident optical power in such a way that the laser intensity noise baseline was lower than the detector background noise (red and blue traces, respectively, in Figure 6-2a). As a result, the graph in Figure 6-2a shows how the green trace, corresponding to the OOK AM signal, emerges above the noise floor. The laser was operated in two emission regimes, always remaining in its own single mode: one close to the lasing process threshold (driving current I = 642 mA; P_{out} = 1.66 mW) and the other well above such a threshold (I = 662 mA; P_{out} = 12.9 mW). The modulation depth (MD) values were, respectively, 100% and 12%, where MD is the ratio of the peak-to-peak amplitude to the DC component of the signal. After integration of the signal (green trace) on the receiver bandwidth, we calculated a corresponding SNR of 13 dB at the Manchester clock rate frequency of 115.2 kHz with an MD of 100%.

In the LAR case (Figure 6-2b), the laser noise contribution is significantly higher than the detector background noise (red and blue trace, respectively) because the RX stage collects a large amount of light. This regime simulates the beam attenuation of FSOCSs characterized by small channel losses, such as those in good weather outdoor conditions, indoor scenarios, or short-range transmission. For this scenario, we utilized a noise floor substantially higher than the background noise (up to 20 dB) and set the laser in a single-mode regime well above threshold (I = 662 mA, P_{out} = 12.9 mW). The tests were performed using an optical attenuation of 13 dB and different MDs. The resulting QCL intensity noise spectrum exhibited the typical 1/f trend of the flicker noise (see Figure 6-2) [170,171].

6.3. Theoretical overview

The performance of the communication system was characterized in terms of PER and SNR, which are interconnected by the relationships previously shown in Equation (2-12). The noise was approximated by an AWGN spectrum around the baseband frequency of 115.2 KHz; the SNR can be written as:

$$\mathrm{SNR}\ (\mathrm{dB}) = 20 \log\left(\frac{\mathrm{S_{RX}}}{2\sigma_{\mathrm{RMS}}}\right) \tag{6-1}$$

where S_{RX} is the received peak-to-peak AC signal, while σ_{RMS} is the RMS of the noise level. To better express the relationship between the measured parameters and the FSOC conditions, we can write the optical attenuation (OA) of the FSO channel as:

$$\mathrm{OA\ (dB)} = -10 \log\left(\frac{P_{inc}}{P_{out}}\right) = -10 \log\left(\frac{S_{RX}}{G\ R\ MD\ P_{out}}\right) \tag{6-2}$$

where $P_{inc} = S_{RX}/(GRMD)$ is the incident power on the detector; $G = 26.5$ is the gain of the AC transimpedance stage; and $R = 2793$ V/W is the detector responsivity. The maximal OA (MOA) is defined as the maximum tolerable channel attenuation to reach a certain threshold PER and can be estimated by replacing P_{out} with P_{max} in Equation (6-2), where P_{max} is the maximum output power ensuring a stable single-mode operation of the QCL (in our case, $P_{max} = 21$ mW).

As mentioned previously, our PER measurements in the LAR regime were performed for different MD values. Therefore, we have fixed P_{max}, G, and R in Equation (6-2), and we can write $S_{RX}/\sigma_{RMS} = k_i$, where the index *i* indicates each specific MD value. In contrast, in the HAR regime we measure the PER for various MOA values. Considering $P_{out} = P_{max}$ and combining the previous equations, we have:

$$\mathrm{SNR_i(dB)} = \begin{cases} k_i & \text{(LAR)} \\ D_i\ \mathrm{(dB)} - 2\mathrm{MOA\ (dB)} & \text{(HAR)} \end{cases} \tag{6-3}$$

where the constant parameters in our measurements are grouped as $D_i = 20 \log [(GRMD\ P_{max})/(2\sigma_{RMS})]$.

For a correct interpretation of the experimental data, we first modelled[1] common outdoor conditions in terms of the parameters that were going to be measured. To simulate the contributions of atmospheric attenuation, we considered a simplified scenario characterized by scattering and absorption by suspended particles and neglected the attenuation resulting from turbulence. In such a scenario, the atmospheric attenuation coefficient $\gamma(\lambda)$ can be written as [172]:

$$\gamma(\lambda) = \alpha_m(\lambda) + \alpha_a(\lambda) + \beta_m(\lambda) + \beta_a(\lambda) \tag{6-4}$$

---

[1] We acknowledge Nicola Corrias (Electronic Engineering MSc), Tecla Gabbrielli (PhD student), and Dr. Francesco Cappelli for developing this model within our collaboration.

where $\alpha_m(\lambda)$ and $\alpha_a(\lambda)$ are the molecular and aerosol absorption coefficients, respectively, and $\beta_m(\lambda)$ and $\beta_a(\lambda)$ are the scattering ones. These depend on the composition of the air, which can vary with altitude, latitudes, seasons, and environment. For the present study, the absorption coefficients were estimated through an atmospheric model of the HITRAN database named "USA model, mean latitude, summer, H = 0" [173], in which the altitude H = 0 is the sea level. For the scattering contribution, we considered both Rayleigh (molecules) and Mie (particles) scattering types. For the former, we used the available formula in the LOWTRAN code [174], while the latter was calculated as a function of the visibility V (in km); namely, V is the distance for which the optical power of a visible green light beam (λ_0 = 550 nm) is reduced to 2% of its original value:

$$\beta_a(\lambda) = 10\log(e)\frac{3.91}{V}\left(\frac{\lambda}{\lambda_0}\right)^{-p} \tag{6-5}$$

which is an empirical formula used to model fog conditions where the coefficient p accounts for the size distribution of the scattering particles [172]. Equation (6-5) can be adapted to simulate other weather conditions including heavy fog, haze, and clear sky. The p coefficients corresponding to different visibility values are summarized in Table 6-1.

Table 6-1. Values of the scattering coefficient p for different visibility conditions.

V	**p**
V > 50 km	1.6
6 km < V < 50 km	1.3
V < 6 km	$0.585\ V^{1/3}$

In our simulated FSOCS, we also considered a geometrical attenuation factor deriving from the Gaussian propagation of the laser beam, resulting in a $1/d^2$ scaling of the far-field intensity reaching the detector (d being the distance between transmitter and receiver). The geometrical attenuation also depends on the laser wavelength and the optical aperture at the receiver; thus, we considered 10 cm as a realistic value for the radii of both the transmitter and receiver apertures. Thus, the geometrical attenuation coefficient A_{geo} was estimated through:

$$A_{geo}(dB) = \begin{cases} 10\log\left(\frac{S_d}{S_{capture}}\right) & S_d > S_{capture} \\ 0 & \text{otherwise} \end{cases} \quad (6\text{-}6)$$

where S_d is the wavefront area of the transmitted beam as collected at the receiver after travelling a distance d, while $S_{capture}$ is the capture surface of the receiver. If $S_{capture}$ is larger than the beam area (*i.e.*, for short distances), all the light is collected and $A_{geo} = 0$; in our model, this is assumed only for distances lower than twice the Rayleigh length, while for higher distances, we considered a receiver aperture smaller than the diameter of the diverging beam.

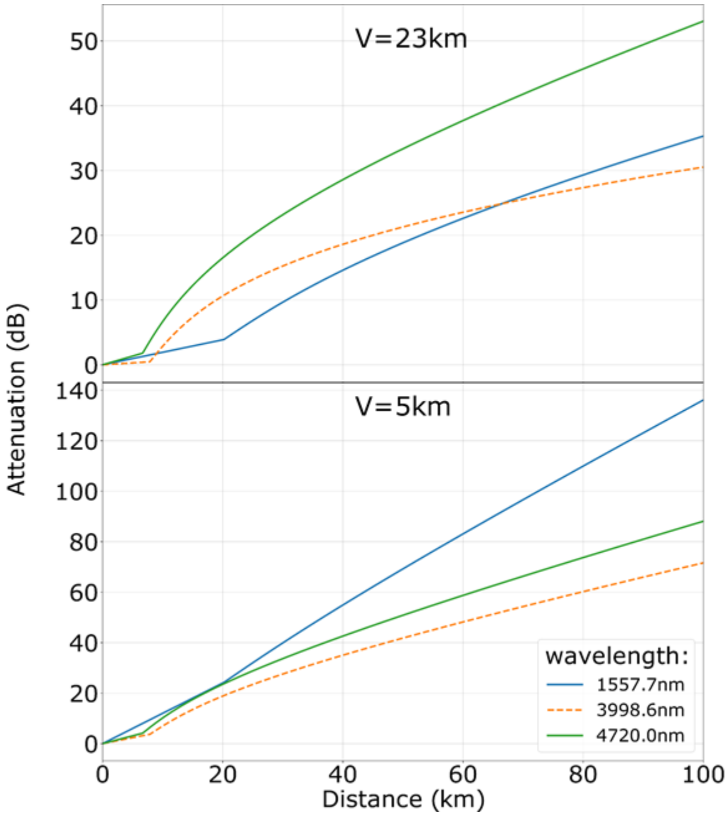

Figure 6-3. Simulation of the attenuation (in dB) as a function of the achievable communication distance (in km) for a terrestrial point-to-point FSOC at sea level. Two atmospheric conditions are taken into account: very clear air conditions (V = 23 km, top graph) and adverse weather conditions (V = 5 km, bottom graph).

The results of our simulations are presented in Figure 6-3, where we show the effects of combining the atmospheric and geometrical attenuation coefficients for two different visibility values. We compared the wavelength used in this work (λ = 4720.0 nm) with the optimal MIR value for air transmission (λ = 3998.6 nm) and the optimal telecom one (λ = 1557.7 nm); namely, the optimal MIR (NIR) wavelength is the one that is less affected by absorption and scattering effects in the MIR (NIR) region. The two latter values were provided by the HITRAN database [173]. The top graph in Figure 6-3 describes the case of very clear air conditions, with V = 23 km: we can observe that the optimal MIR wavelength is less attenuated than the NIR one for d > 65 km. In contrast, the bottom graph presents the simulation for low visibility conditions, with V = 5 km, where the attenuation is dominated by scattering effects. Notably, the MIR wavelength is less affected by losses than the NIR one for practically any distance. These results suggest that an MIR FSOCS operating at approximately 4.0 µm is very promising in case of low visibility conditions and can exceed the performances of the more common NIR FSOCSs.

6.4. Results and discussion

Let us first address the experiments carried out in the HAR. Our aim was to determine the performance of our system as a function of channel attenuation and estimate the tolerable MOA ensuring a reliable optical link for the required PER. Figure 6-4a shows the measured PER as a function of the SNR, taking into account the recorded noise value of σ_{RMS} = 2.3 mV measured after the detector. The experimental data were modeled using Equation (2-12), and the model shows a good agreement with the data points. Values of $PER < 1.6 \times 10^{-5}$, corresponding to error-free communication, were achieved for SNR > 14 dB. Panels b, c, and d in Figure 6-4 present the eye patterns recorded for the low-signal (SNR = 6 dB, PER ≈ 0.5), medium-signal (SNR = 10 dB, PER ≈ 0.02), and high-signal (SNR = 13.5 dB, error-free) configurations, respectively: these traces represent the self-triggered signal after the amplified PD stage of the receiver. One can observe a jitter on the transition edges of the eye patterns, which depends on the signal quality; its minimum value is a consequence of the time resolution of the Arduino DUE board.

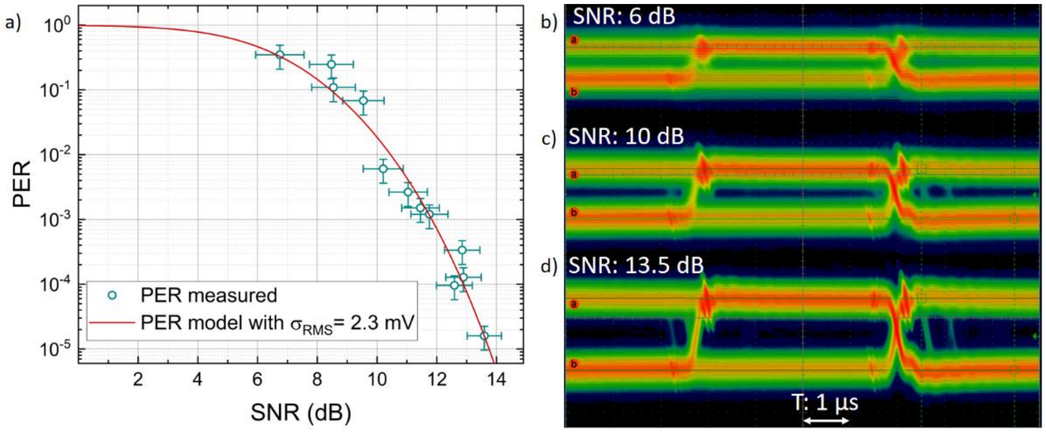

Figure 6-4. Link performance for the HAR scenario. a) PER as a function of SNR. Green circles represent measured data points; the red line is the model for σ_{RMS} = 2.3 mV, which corresponds to the measured RMS; the vertical error bars correspond to the standard deviation; the horizontal error bars are obtained after error propagation from measurements of σ_{RMS} and S_{RX} values. b–d) Eye patterns for SNR values of 6, 10, and 13 dB, respectively, corresponding to three different PER regimes. The horizontal scale is 1 µs/div; the vertical one is 10 mV/div.

The MOAs observed for the two MD values (12% and 100%) are reported as a function of PER in Figure 6-5: the error-free communication was achieved for MOA < 39 dB for MD = 12% and MOA < 48 dB for MD = 100%. The error bars were obtained after propagation of the statistical error obtained during signal and noise acquisitions. The oblique shaded lines in the figure (merely a guide for the eye and not a mathematical model) indicate an increase in MOA by 2 dB every three decades of PER before its saturation to 1 for both MD values. Such a behavior was in agreement with that expected according to the theoretical overview presented previously. If we consider two different values of MOA, such as 48.5 and 50.5, for MD = 100%, the corresponding values of SNR can be obtained from Equation (6-3): these would be, respectively, 13 and 9 dB. After converting these to a linear scale and replacing them in Equation (2-12), we obtain two PER values that differ approximately by three decades. In addition, we could observe a variation in MOA of approximately 9 dB between the data of the two studied MDs for a given PER: this is in agreement with the ratio of the two MD values.

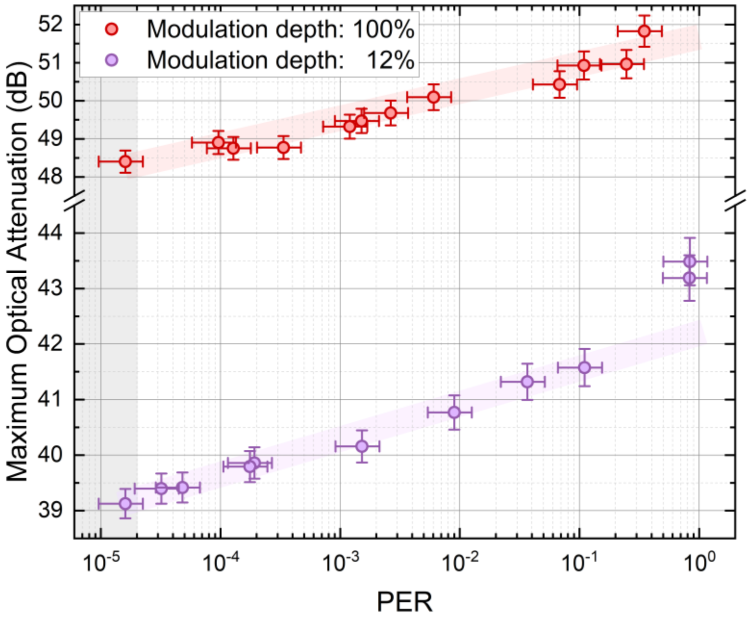

Figure 6-5. MOA as a function of PER for MD = 100% (red symbols) and MD = 12% (purple symbols) in the HAR. The shaded area represents the threshold for error-free communication. The oblique shaded lines are a guide to the eye highlighting the trends.

Moving to the LAR scenario, we expected both noise and signal amplitude to increase linearly with P_{out}, but the SNR was still expected to increase with the MD (Equations (6-2) and (6-3)). Therefore, we investigated the minimum MD value required for an error-free communication to identify the best working conditions for the setup in terms of high laser stability and spectral quality. The optical power and attenuation were fixed at 12.9 mW and ~13 dB, respectively. The communication performances were assessed as a function of the recorded SNR, and the results are shown in Figure 6-6a, where one can observe that the experimental values are best modelled by the PER curve obtained by using σ_{RMS} = 40 mV.

Such a σ_{RMS} value was slightly higher than the RMS measured in the absence of a transmission (32 mV). This discrepancy might originate from the occurrence of fast transients and glitches during the transmission; as a consequence, an intense electromagnetic noise might add to the overall transmission noise, owing to variations in the current during the modulation process. The eye patterns for three MD values are also shown in Figure 6-6: MD = 0.3% in panel b, 0.6% in panel c, and 1.3% in panel d; these correspond to the low (9 dB), medium (13 dB), and high (> 16 dB) SNR values, respectively, which in turn correspond to PER ≈ 0.2, 0.003, and 10^{-5}, respectively.

Finally, Figure 6-7 shows the linear dependence of PER with the MD, as highlighted by Equation (6-3): an error-free communication was achieved for MD > 1%.

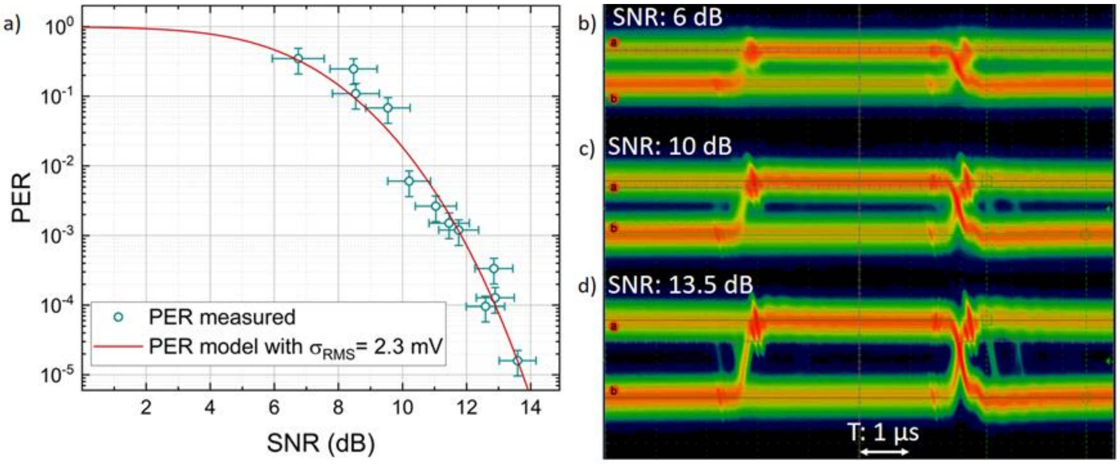

Figure 6-6. a) PER as a function of SNR for the LAR scenario. The green symbols represent the measured PER; the dashed blue line and the red solid line are, respectively, the models for σ_{RMS} = 32 mV (measured with an oscilloscope) and σ_{RMS} = 40mV (best agreement). b–d) Eye patterns for MD values of 0.3% (PER ≈ 0.2), 0.6% (PER ≈ 0.003), and 1.3% (error-free communication), respectively.

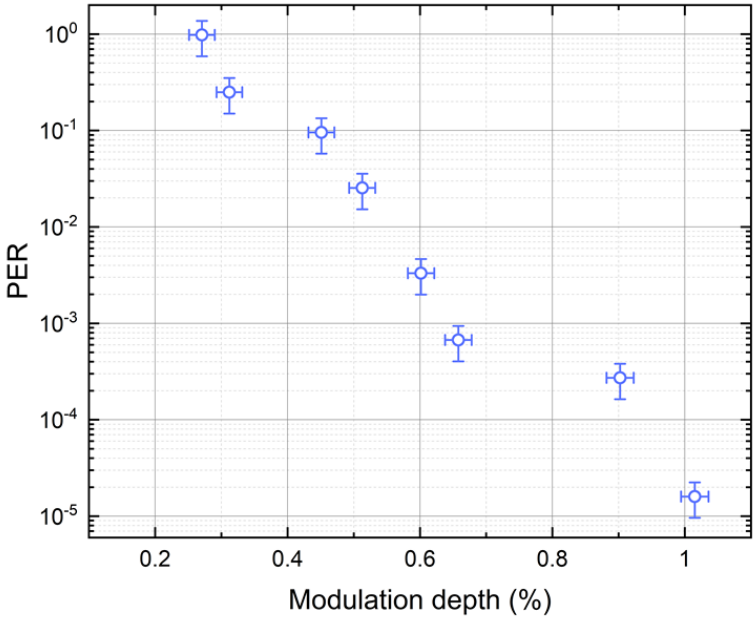

Figure 6-7. PER as a function of the MD for the LAR condition. The error bars are calculated as in the HAR case.

At this point, we examined the behavior of our system in the transition between the HAR and LAR conditions. To do so, we chose three MD values (0.5%, 0.7%, and 1%) and varied the attenuation of the optical link from 15 to 32 dB. The results are shown in Figure 6-8. In panel a, the trend of SNR as a function of the MOA clearly exhibits two distinct regimes: in the LAR, where the noise is dominated by the laser noise, the SNR does not show a straightforward dependency on the received optical signal, while in the HAR, and more specifically for MOA > 25 dB, the SNR decreases for increasing attenuation values with a rate of 2 dB/dB, which is in agreement with the predictions of Equation (6-3). These behaviors were reflected in the communication performances presented in Figure 6-8b. For the HAR condition, a steep increase in the PER was found above the 25 dB transition point. In contrast, in the LAR, the system featured stable communication performances regardless of the channel attenuation: this is explained by the fact that the main noise source in the detection stage was that of the QCL source.

Considering the application of the presently described system to realistic FSOC scenarios, we decided to estimate the maximum length of an FSO link employing our communication system under different atmospheric conditions. For this scope, the experimental results of Figure 6-5 and Figure 6-8 were combined with the expected channel attenuation predicted by the model (Figure 6-3). Table 6-2 reports the resulting maximum link lengths calculated for three different sources, namely, a telecom NIR source ($\lambda = 1.56$ μm), our MIR source ($\lambda = 4.72$ μm), and the ideal MIR wavelength ($\lambda = 4.00$ μm). These link lengths, expected to ensure minimal effects of atmospheric absorption and scattering, referred to the two different visibility conditions mentioned previously, that is, V = 5 and 23 km, corresponding to our HAR and LAR conditions. We considered an MD of 100% for the low visibility regime and 1% for the high visibility one.

Figure 6-8 shows that an error-free communication in high visibility conditions (1% MD) was achieved for MOA < 26 dB; here, the main contribution to the OA was represented by geometric attenuation. Using the model in Figure 6-3, we calculated the corresponding distances: for our MIR source, the error-free communication was achieved below 35 km, which was a shorter distance than that obtained with an NIR source (< 70 km). This result can be explained considering that the attenuation resulting from geometric factors is negligible for distances shorter than the Rayleigh length and increases for longer distances increases; therefore, its impact is more significant in the MIR than in the NIR. In contrast, in the low visibility regime, an error-free communication was achieved for MOA < 48 dB, corresponding to distances < 50 km for our MIR source: this value is substantially higher than that obtained for the NIR source (< 35 km), and this result is explained considering that scattering effects are more significant for shorter wavelengths, as expressed by Equation (6-5).

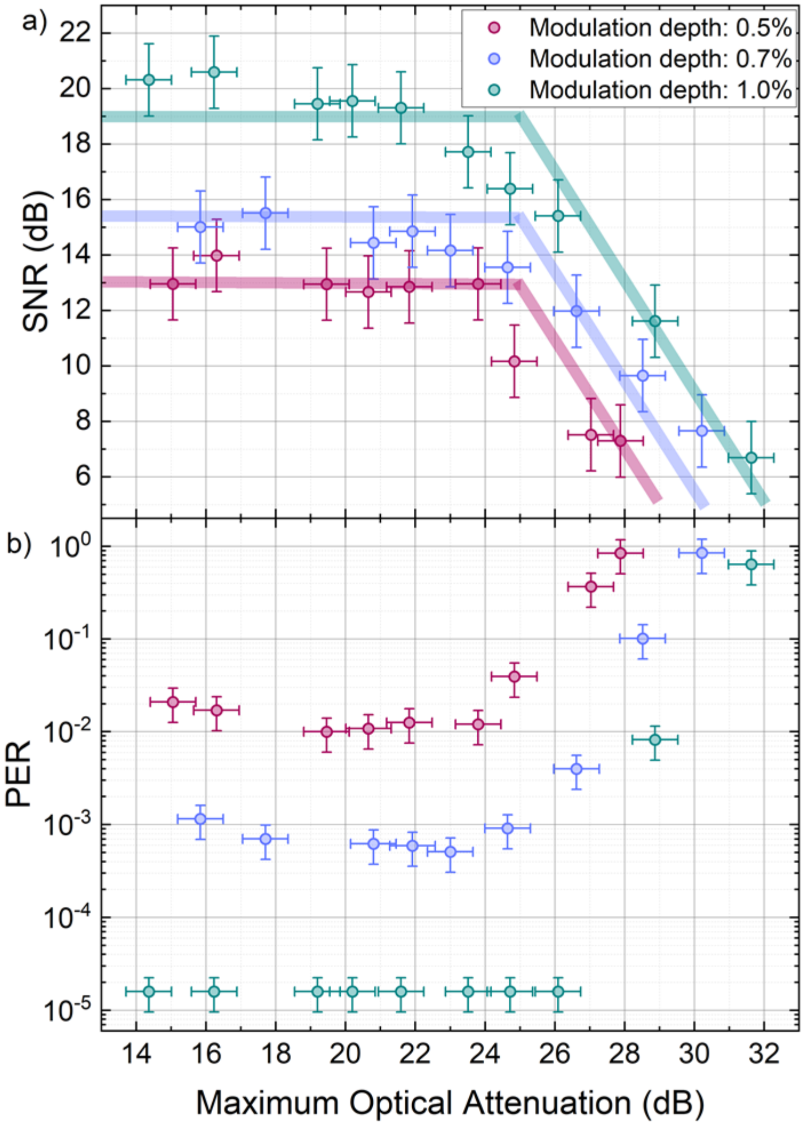

Figure 6-8. a) SNR as a function of the MOA for MD = 0.5% (purple markers), 0.7% (blue markers), and 1% (green markers). The shaded lines are merely guides to the eye highlighting the two different SNR regimes at low and high MOA values. b) PER as a function of MOA across the HAR-LAR transition region.

Table 6-2. Estimated distances for error-free communication at low (V = 5 km) and high (V = 23 km) visibility, corresponding to the HAR and LAR conditions, respectively, for three different sources. The values are estimated considering an MD of 100% for the HAR and 1% for the LAR.

	NIR source **(λ = 1.56 μm)**	**MIR source** **(λ = 4.72 μm)**	**MIR source** **(λ = 4.00 μm)**
V = 5 km	< 35 km	< 50 km	< 60 km
V = 23 km	< 70 km	< 35 km	< 75 km

6.5. Summary

This Chapter reported the first detailed characterization of an FSOCS based on an MIR QCL source. We highlighted the different communication performances taking place in two different noise regimes, HAR and LAR, in terms of transmission quality as a function of the optical channel attenuation. The experimental setup showed a significant versatility in the transition between the HAR and LAR conditions, and we were able to identify a clear crossing point between the two regimes. The system performance was also assessed in realistic operational conditions by combining our findings with the predictions of a propagation model: we considered the effects of geometrical and atmospheric absorption and scattering, and we estimated the error-free length of our communication link as well as those of NIR-based setups. Our analysis showed that the FSOCS herein developed requires further improvement, for example through the use of a wavelength other than 4.72 μm. Nevertheless, QCL-based MIR FSOCSs are extremely promising candidates for long-range FSO communications in real environments, especially those characterized by harsh weather or atmospheric conditions.

7. Preliminary study and characterization of a QD-doped optical antenna for long-range OWC

7.1. Introduction to the Chapter

The increasing congestion of the RF spectrum dedicated to wireless communication has inspired the research of alternative technologies which could meet the increasing demand for high-capacity communication. In VLC data links, high transmission rates can be achieved by employing PDs characterized by small active areas [107]. SNRs can be increased using focusing optical elements with large apertures; however, these work through reflection and refraction and thus conserve étendue, leading to reduced FoVs [108]. A recent solution to this problem is represented by the use of FC devices [108,115,123], which were originally developed back in the 1970s [109,110,175] but are still innovative from the point of view of their application in VLC and, as such, require further study and characterization. These consist in semitransparent substrates loaded with specific fluorophores capable of absorbing the impinging light in the UV-blue region and re-emit in the yellow-IR one following a Stokes conversion process [110]; the amount of converted light depends on the quantum yield (ϕ) [176]. The re-emitted light travels toward the edge of the substrate, acting as a waveguide, through internal reflection processes; the edge is coupled with a PD. An overview of the theoretical background and state-of-the-art on FC-based optical antennas for VLC has been given in Section 2.9.. Briefly, fluorescent antennas are able to exceed the étendue limit for gain because in fluorescence the number of photons is conserved. However, to the best of our knowledge, the only experimental assessments of FC optical antennas have concerned short-distance links [107,118,177]. In addition, only few studies have dealt with the capacity of FCs as RX stages for VLC application in partially illuminated environments [178] and none in conditions of direct solar irradiance. The lack of research on these aspects may reflect severe limitations in terms of photostability of the fluorophores as well as technical difficulties in designing receivers capable of rejecting solar and low-frequency stray irradiance [179].

Herein, we present a preliminary design, characterization, and testing of the first long-range (100 m) VLC link exploiting a large-area optical antenna based on an FC substrate, namely, CIS QDs (see also Paragraph 2.9.1. for further details on the efficiency model for the antenna) under direct solar irradiance. Following an assessment of the physical (conversion efficiency, FoV, temporal response to variable optical signal, and bandwidth) and telecom properties of the QD-based FC, we implemente such an optical antenna in a novel VLC setup employing a high-power 405 nm LED source and perform a comprehensive study of the communication performances for distances up to 100 m.

7.2. Experimental setup

QDs were chosen as fluorophores instead of organic dyes because they display high photoluminescence quantum efficiency, photostability, and short lifetime (up to 1 ns), and they can be engineered to selectively accept desired wavelengths [180,181]. Moreover, the Stokes shifts can be controlled to reduce re-absorption losses [182]. Furthermore, the use of QDs allowed for the application of novel fabrication processes and the production of the substrate in a large size. Notably, organic dyes also have the disadvantage of saturating at high light intensity, which may lead to non-linear responses [122].

As already mentioned in Section 2.9., we used a PMMA slab doped with CIS QDs obtained thanks to our collaboration with Glass to Power s.p.a., a spin-off company of UNIMIB (Università Milano - Bicocca). The absorption and fluorescence spectra of the QDs were presented earlier in the text in Figure 2-11. The slab was 38 cm wide and 8 cm high and enabled an FoV of approximately 120° (see Figure 3-12b). The so-obtained optical antenna was integrated in a custom RX stage by placing a rectangular Si PIN PD (Hamamatsu S3588-09, shown previously in Figure 3-9b) with active area $d \times L = 3 \times 30\ \mathrm{mm}^2$ and low parasitic capacitance in correspondence of the middle point of one of the short edges of the slab (shown previously in Figure 3-12b). The slab thickness, 3 mm, was matched to the size of the short side of the PD; this ensured a maximal light collection and minimal coupling loss. In contrast, the slab's height exceeded the PD size, which allowed part of the converted light to escape from the short side of the optical antenna (see also Section 2.9.). The photocurrent generated by the PD was voltage-amplified and converted by a TIA stage obtained through custom modifications of a commercial, variable-gain PD (Thorlabs, PDA100A2), in which the original PD was replaced with the S3588-09 one, maintaining the same gain/BW product as shown in Figure 3-11. A dedicated AC pre-filter stage was also present, which allowed rejection of unwanted light components at frequencies below 1 kHz, including sunlight and artificial illumination (see also Section 4.2.). This strategy could mitigate the effects of the solar radiation absorption by the QDs (see Figure 2-11), reduce the risk of saturating the detector and allow the use of our prototype under direct sunlight without significant degradation of the SNR.

7.3. Results and discussion

We carried out a characterization of the optical antenna in terms of FoV, response to digital signal, estimation of its BW, and communication performance in an outdoor environment under direct solar irradiation.

7.3.1. Dependence of photoluminescence signal on light spot position and field of view

As part of the characterization of our optical antenna, we investigated possible asymmetries originating from the specific position of the excitation spot on the FC area. For this scope, we recorded the signal amplitude as function of the excitation distance from the edge of the PD. We employed a 10 mW high-bandwidth LED source emitting at $\lambda = 405$ nm (Thorlabs LED405E), that is, near the absorption peak of the FC substrate. The current feeding the LED was amplitude-modulated at a frequency of 50 kHz *via* a square-wave pattern. The LED was placed in contact with the surface of the antenna and perpendicular to its surface. The light source was moved along the x direction in steps of different lengths: 1 cm steps when the source was at distances lower than 6 cm from the edge where the PD was positioned; then, 3 cm steps.

Figure 7-1a shows the RMS amplitude of the recorded signal; the markers represent the mean of five measurements, and the y-errors are the standard deviations from the mean. One can observe a bi-exponential decay for increasing distance, which could have resulted from a combined effect of the light escaping the waveguide and the QD re-absorption; this aspect, however, requires further and deeper investigation. The decay constants obtained from the fit procedure were $l_1 = 2 \pm 0.5$ cm^{-1} and $l_2 = 20 \pm 1$ cm^{-1}; as highlighted by Equation (2-17), these are correlated to various parameters: the absorption coefficient of the system, the roughness of borders and faces, and scattering [181].

The FoV of our antenna was determined by measuring the signal amplitude after illuminating the slab with the LED source and rotating the FC around its central axis in the x-z plane. We scanned the angle θ between the optical axis n and the direction of the incident light k (see Figure 7-1b) in steps of 10°. Two possible configurations were considered: one referring to a collimated source, in which the light spot is fully contained inside the FC surface, and the other representing a diffused source configuration, in which the light illuminates the FC uniformly.

Let us assume a uniform quantum yield across the slab. The signal impinging on the PD, corresponding to the number of photons converted by the FC, is a function of θ according to the following factors and fundamental laws of optics [183].

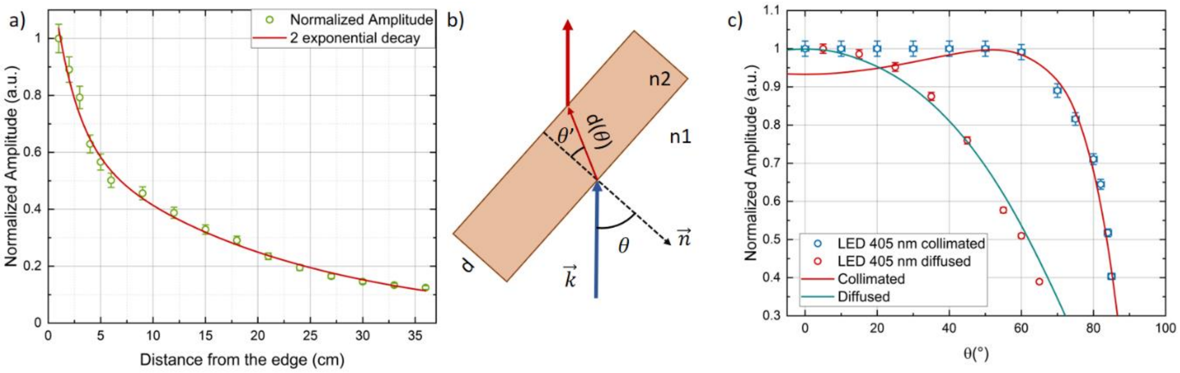

Figure 7-1. a) Normalized amplitude as a function of distance from the edge (the markers are the mean of the experimental values, and the y-error is the standard deviation of 5 measurements). A bi-exponential decay was used as the fit model with decay constants $l_1 = 2 \pm 0.5$ cm^{-1} and $l_2 = 20 \pm 1$ cm^{-1}. b) FoV measurement setup. This experiment was carried out both with a collimated light source (the light spot is collected for each angle inside the FC; n and k are the incident wave vector and the FC optical axis, respectively) and a diffused light source (the light illuminates the FC uniformly). c) Results of FoV measurements for the two configurations. Red trace = collimated configuration; green trace = diffused configuration. The markers represent the experimental data, while the curves are the model fits obtained with Equations (7-4) and (7-5). For each amplitude measurement, a relative statistical error of 4% is considered.

1) Part of the incident light is reflected by the slab owing to Fresnel's laws. Assuming such light to be non-polarized, we have:

$$R(\theta) = \frac{R_p(\theta) + R_s(\theta)}{2} \tag{7-1}$$

where R_p and R_s are the reflection coefficients for the p- and s-polarized light.

2) According to Snell's law, the optical path $d(\theta)$ of the light beam inside the FC increases with the incident angle θ when transitioning from a lower (n_1, air) to a higher refraction index (n_2, approximately 1.54 for PMMA):

$$d(\theta) = d\left(1 - \left(\frac{n_1}{n_2}\right)^2 \sin^2(\theta)\right)^{-1/2} \tag{7-2}$$

Following the Lambert–Beer law, this will exponentially increase the absorption conversion probability in the FC substrate.

3) In the diffused configuration, the optical power P(θ) collected on the FC surface decreases with respect to the orthogonal incidence configuration because of the projection of the FC area inside the intensity pattern:

$$P(\theta) = P(0°)\cos(\theta) \tag{7-3}$$

As a consequence, the signal amplitude after the TIA stage follows two distinct trends according to the specific illumination case:

$$S_{\text{coll}} \propto (1 - R(\theta))(1 - e^{-\alpha d(\theta)}) \tag{7-4}$$

$$S_{\text{diff}} \propto \left(1 - R(\theta)\right)\left(1 - e^{-\alpha d(\theta)}\right)\cos(\theta) \tag{7-5}$$

where the indexes "coll" and "diff" represent the collimated and diffused configuration, respectively.

The normalized signal amplitude recorded after the TIA stage is plotted in Figure 7-1c as a function of the angle θ. The amplitude recorded in the collimated configuration followed a broad plateau for low θ values, while that in the diffused one displayed a stronger angular dependence. The experimental data were compared with the results of the simulations obtained using Equations (7-4) and (7-5). For the collimated configuration, a non-monotonic behavior in signal amplitude was expected, exhibiting an increase in the signal at $\theta \approx 60°$. This may be explained by the opposite trend of optical path length and Fresnel reflection coefficients as a function of θ, resulting in a relative maximum of collection efficiency. At very low angles, a significant discrepancy could be observed between the experimental data and the simulation; this may depend on a non-ideal collimation of the LED emission pattern or polarization effects, which are not taken into account by our approximate model. In the diffused configuration, the efficiency decreased for increasing θ values owing to a vignetting effect, and the agreement between the data and model was excellent. At large angles, the Fresnel reflection effect was predominant in both cases, causing a sharp drop in the collected signal.

These results suggest a large FoV for our RX stage, ensuring a low sensitivity to angular misalignments. If we define the FoV as the θ value for which the signal drops to half the value observed for $\theta = 0°$, we obtain FoV $\approx$ 85° for the collimated configuration and FoV $\approx$ 60° for the diffused one; notably, the latter is the more probable one in long-range OWC/FSO applications.

7.3.2. Time response and bandwidth

The time response of the antenna was characterized by modulating the LED source with a square pulse (characterized by rise and fall times of 5 ns) produced *via* the waveform generator. The LED was kept in contact with the FC slab at 2 cm from the receiver, realized with CIS QDs dispersed in a PMMA slab provided by our partner Glass to Power s.p.a. (a spin-off company of UNIMIB, Università di Milano - Bicocca), and the converted light was acquired by an APD (Thorlabs, APD430A/M) characterized by a response time $\tau < 3$ ns (which is substantially shorter than the lifetime of the fluorophores). The temporal response of the substrate is shown in Figure 7-2a, where the black line represents the experimental data, and the red/green line is the double exponential rise/decay fit to take into account both the fast response of the LED and the slab response employed to calculate the rise and fall times. As a response time of the entire system, we considered the average weighed on the amplitude coefficients obtained from the exponential fit; thus, we obtained similar values for the rise time, $\tau_R = 650$ ns, and the fall time, $\tau_F = 620$ ns. From these, we were able to calculate a BW of the slab (−3 dB) of $0.35/\tau \approx 550$ kHz.

Regarding the direct measurement of the BW response for our FC substrate, three different lateral positions were considered for the BW measurements, that is, the following distances from the receiver: 2, 19, and 36 cm. The LED was kept in contact with the slab, and the light intensity was modulated with a digital current waveform of frequency f_{mod}. The signal amplitude was acquired after the APD stage as a function of f_{mod} between 10 kHz and 20 MHz. The results are shown in Figure 7-2b, where a different high-frequency cut (at −3 dB) can be observed for three different distances between the LED and receiver: 520 kHz at 2 cm, 390 kHz at 19 cm, and 350 kHz at 36 cm; notably, the first of these values was compatible with the step response shown in Figure 7-2a and discussed above. Such different BW cut-offs might be associated to the effect of light re-absorption by the QDs, increasing the propagation time of the signal within the slab.

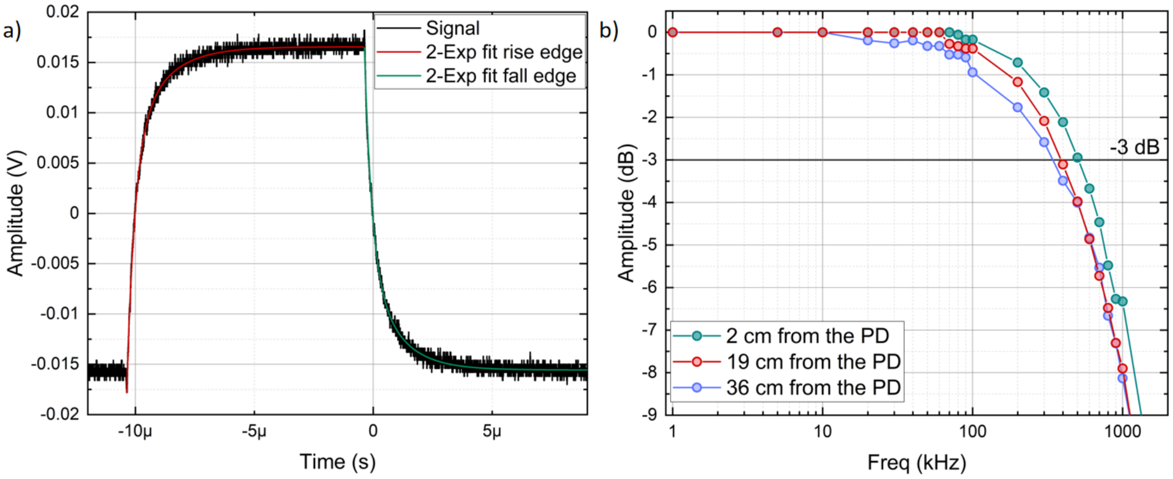

Figure 7-2. a) Time response to a square wave of the slab illuminated by the 405 nm LED. Both the rise and fall times were obtained through a double exponential model fit to take into account the different time constants of the light source and slab. (b) Digital BW of the FC substrate measured at three different distances from the receiver: 2, 19, and 36 cm.

Assuming an average BW ≈ 420 kHz (*i.e.*, the average of the three values) and employing an AWGN to drive the LED, the maximum channel capacity predicted by the Shannon–Hartley theorem for 2 bit/symbol modulations, such as OOK with UART & Manchester coding [184], is C ≈ 1 Mbps for SNR ≈ 11 dB. This theoretical value clearly does not take into account the limitations of the used hardware, which might reduce the channel capacity. In our prototype, the gain of the TIA can be increased up to G = 20 dB, leading to BW(−3 dB) = 1 MHz, which is larger than the intrinsic BW of the FC. This is an optimal configuration for our receiver unit, as it allows for the maximum SNR without further limiting the BW; moreover, the requested noise margin of 11 dB for a 1 Mbps capacity can be attained even in outdoor, long-range conditions.

7.3.3. Communication performance

The communication performances of the QD-based FC antenna in a long-distance outdoor link were assessed by embedding the device as a large-area RX stage in the VLC prototype (Figure 7-3a) and performing an measurement campaign at the Physics and Astronomy department of University of Florence during the month of July 2021.

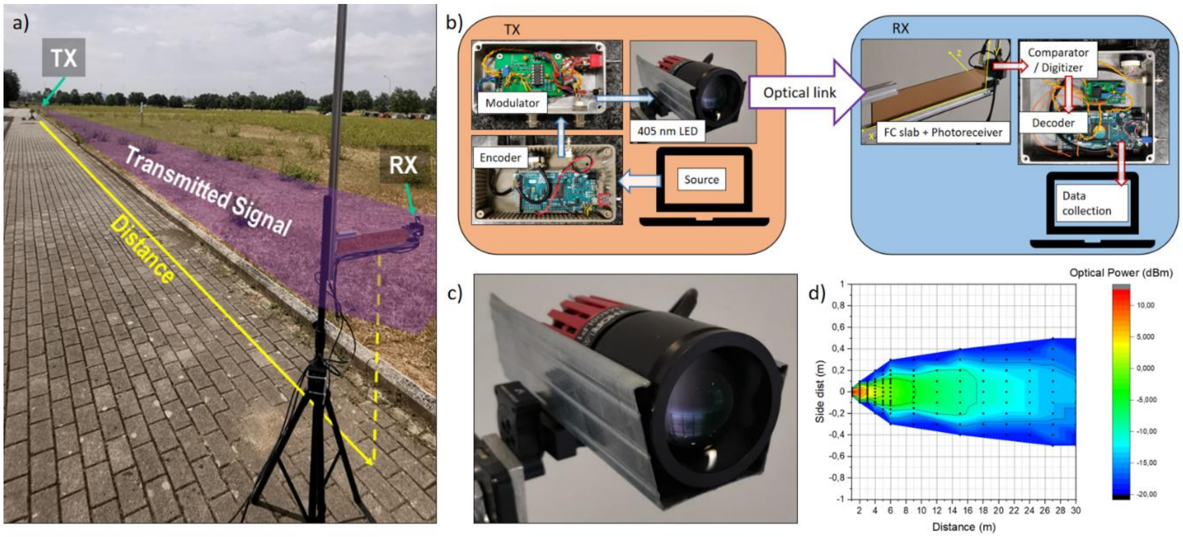

Figure 7-3. Summary of the experimental setup of the long-distance measurements. a) Photograph of the outdoor setup showing the TX and RX in LoS configuration. b) Overview of the TX and RX hardware. The left block displays the TX: the signal is generated by a digital controller based on an Arduino DUE board and encoded through a current modulator. The right block shows the receiver, composed of the FC slab and the PD. The output signal is digitized and compared with a pre-stored reference message. c) High-power LED used as the light source. (d) LED experimental irradiance map.

The block diagram of the experimental setup is reported in Figure 7-3b. The digital transmitter consisted of the high-power 405 nm LED source, a specific collimation lens (Figure 7-3c), and a current modulator controlled by a digital encoder (Figure 7-3b, left panel) based on an Arduino DUE digital microcontroller. A continuous stream of data was generated, containing identical 32-bit packets encoded as intensity modulation, while the current modulator controlled the LED optical intensity between 0% and 100% of the maximum current of 1.4 A, with a mean value corresponding to half the DC nominal value (*i.e.*, 0.7 A). The light was collected by the RX stage (Figure 7-3a,b) comprising the FC antenna as well as the PD and TIA (placed on the short side of the slab as described previously). The signal was then digitized by a single-threshold Schmitt-trigger comparator stage and decoded by a second Arduino DUE board. The acquired data were thus processed in real time: the digital board performed a bit-wise comparison of each received packet with a reference message and then recorded the errors occurring in the received stream. The communication performance was evaluated in terms of PER. Furthermore, the RX signal was also acquired by a 200 MHz digital oscilloscope (Tektronix, MDO3024) and an FFT spectrum analyzer (SignalHound, USB-SA44B) for direct SNR measurements and noise analysis.

The PER and SNR values were acquired on an experimental grid for link distances up to 100 m. The LED and FC were positioned at a height of 115 cm from the floor, in LoS configuration. Two setups were tested: 1 Mbaud UART and 500 kbaud OOK with Manchester encoding, both featuring a 500 kHz clock rate. For the UART (Manchester) configuration, the most effective TIA gain was G = 20 dB (G = 10 dB). Such a discrepancy may be explained by the fact that Manchester encoding is not the native one for the Arduino DUE board, which would negatively affect the RX board and result in a lower timing tolerance by the microcontroller board in the digitized waveform during the bit decoding process. In our case, this effect was exacerbated by the BW-limited waveform; therefore, the Manchester configuration required a lower TIA gain setting, corresponding to the larger TIA BW value of 1.5 MHz.

The measured SNR values are plotted in Figure 7-4a as a function of the distance D. Assuming a digital square waveform, the SNR is defined as in Equation (6-1) in Section 6.3.. Since we observed background noise RMS values σ_{RMS} = 0.7 mV for G = 10 (500 kbaud Manchester) and σ_{RMS} = 0.8 mV for G = 20 (1 Mbaud UART), the SNR value at 500 kbaud (Manchester) would be lower than the one at 1 Mbaud (UART). In the far-field region, the signal amplitude (which is related to the optical power of the light source) should decrease as $1/D^2$. Indeed, a light source emits a relatively uniform far-field wave pattern, whose electromagnetic field amplitude decays as 1/D; as a consequence, its optical power decays as $1/D^2$. Therefore, as shown by the solid lines in Figure 7-4a, we modelled the SNR data through a function $I(D) \propto 20 \log(A/D^2)$, where A was a free fit parameter. The SNR trend was in agreement with the expected behavior at large distances for both baud rates, while strong deviations were observed for D < 10 m (inset of Figure 7-4a), where S_{RX} is no longer proportional to $1/D^2$. For even lower D values, the spot size was almost equal to the surface of the FC antenna; therefore, the SNR did not vary significantly for different D values. However, a comprehensive description of the observed behavior is still necessary and will require the introduction of a detailed modeling of the processes of light conversion and propagation within the antenna.

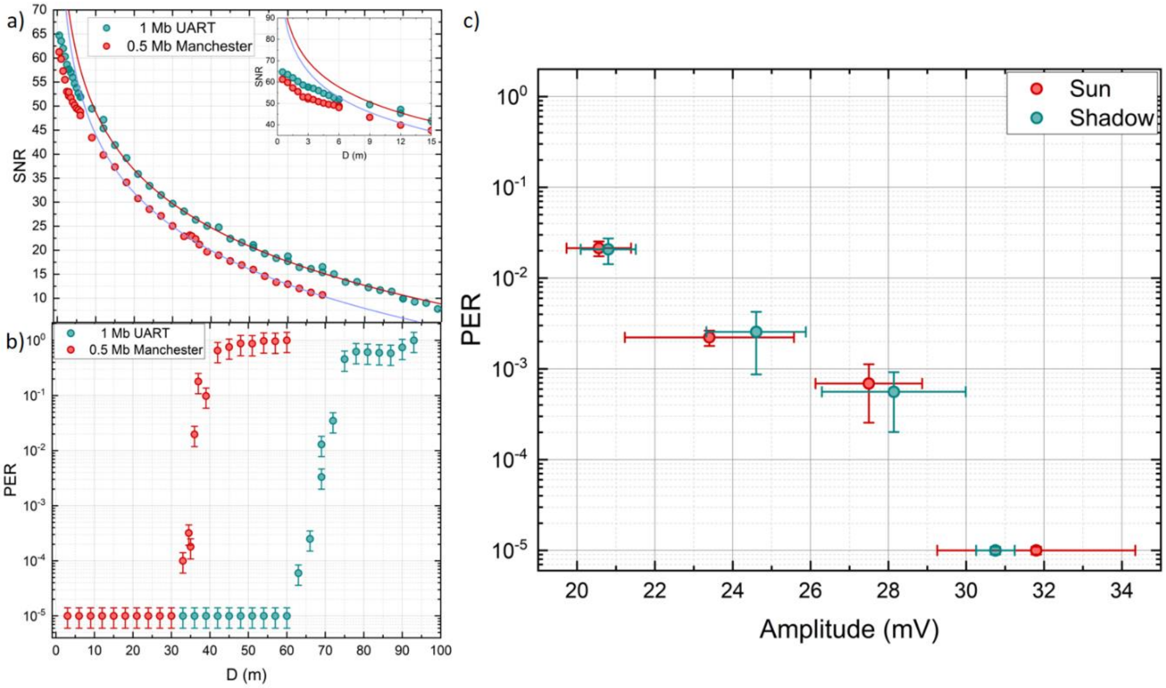

Figure 7-4. a) SNR as a function of distance (D) for 1 Mbaud UART (green circles) and 500 kbaud Manchester (red circles). The markers represent the experimental data, while the solid lines are fits in the far-field propagation region (see text). The inset highlights the short-distance deviations of data from the far-field trend. (b) PER as a function of D for 1 Mbaud UART (green markers) and 500 kbaud Manchester (red markers). The error-free threshold for our measurements is PER ≤ 10^{-5}. Error bars refer to the repeatability uncertainty on the relative positioning between TX and RX. c) PER as a function of the signal received in conditions of shadow (green markers) and under direct sunlight (red markers); no significant differences between the two cases are observed. The reported values are averages and standard deviations of five measurements.

In the PER experiments, the total number of packets per measurement was 105, which set the error-free detection to a minimum PER of 10^{-5}. The results are presented in Figure 7-4b, where the PER values are plotted as a function of D. Interestingly, our prototype exhibited error-free transmission capabilities for D < 60 m in the 1 Mbaud UART and D < 30 m in the 500 kbaud Manchester configuration, providing better performance than any previously related work involving FC antennas. Notably, while the lower performance recorded for the Manchester configuration reflects the lower SNR values discussed in the previous Section, the Shannon–Hartley limit predicted error-free transmission for SNR ≥ 11 dB, *i.e.*, D ≥ 85 m, for the 1 Mbaud configuration, which is only slightly larger than the experimental result. Therefore, the agreement between theoretical and empirical data is remarkable.

In order to highlight the possible effects on the quality of VLC transmission, PER measurements were also conducted under conditions of *sun* (direct sunlight, intensity > 70000 lux) and *shadow* (no direct illumination, intensity ∼10000 lux) conditions. The measurements were performed on different days with clear sky conditions, and a time window approximately between 12:00 and 14:00 was chosen to maximize the solar irradiance on the RX stage; the *shadow* condition was obtained by artificially shading the RX stage. The results, reported in Figure 7-4c, show no substantial variations in the VLC link performances between two configurations. This finding confirms that the combination of electrical and physical-chemical properties of our FC-based RX stage is effective in delivering a stable, long-range VLC link even under strong solar irradiance.

7.4. Summary

In conclusion, the combination of the physical-chemical properties of the QD fluorophores, together with the DC rejection provided by our RX stage design, allowed for error-free VLC link distances up to 60 m and a baud rate of 1 Mb/s. Notably, this outcome was mostly limited by the temporal response of the FC substrate. We were able to determine a BW of ~500 kHz and an FoV of ~170°. Interestingly, the signal was found to decay according to a double-exponential trend as the luminous spot moved further away from the border where the PH was placed. It is important to remind that these are preliminary results and require further investigation to provide a comprehensive explanation for the observed phenomena. Nevertheless, this work represents the first example of a long-range VLC link under strong solar irradiance, extending the boundaries of current long-range FSO applications by means of large-area, UV-resistant substrates based on QDs. Therefore, these results may prompt the development of novel VLC technologies in real life applications, solar energy harvesting, and communication capabilities.

8. Conclusions

In this Thesis, the first one dealing with VLC at LENS, we tackled several aspects of communication through visible and IR light, thanks to our ability to manipulate light. The project focused on the study and implementation of an extremely versatile system that, with minimal modifications and adjustments, allowed for the characterization and investigation of VLC in several application scenarios. We showed the capabilities and potential of optical wireless communication, which could be used in synergy with radiofrequency-based technologies to accomplish a pervasive communication network. Moreover, the use of LED light sources was shown to be key to implementing safe, long-range communications, delivering information over times approximately one order of magnitude shorter than those achieved in radiofrequency transmissions. This, in turn, allows for increased safety in vehicular applications (Section 4.3.). Within the intelligent transportation systems field, on which most of our work has focused, we studied and modeled the transmission channels (Section 4.2.) as well as the receiving system (Section 4.4.). Further, we implemented an active decode-and-relay system for the transmission, decoding, and forwarding of typical messages for platooning applications (Section 4.3.). Finally, we characterized a bidirectional link in a real environment, using commercial source and modeling the communication system.

This work also provided some original indoor NLoS applications of VLC for the transmission of specific data (Chapter 5). We exploited the illumination systems of works of art as a means to deliver dedicated information. The main evidence shown by these studies is represented by the directionality of the source, which, contrary to other technologies such as Bluetooth, is not affected by interferences between transmissions. A possible development, that was outside the scope of this Thesis, could be the realization of a positioning system to track the localization and movement of the receiving devices and, thus, the people employing them.

We have further demonstrated the possibility of implementing long-range communications *via* a mid-IR source based on a quantum cascade laser (Chapter 6). We evaluated the performances of such a system in different regimes, namely, when dominated by the noise of the detector or that of the source, as well as in the transition between such conditions. We modeled the behavior of a source that would minimize the effects of atmospheric absorption and scattering and evidenced the possibility of developing long-range free-space optical communications in a more efficient way compared with those using near-infrared sources.

Finally, we began the study of an FC-based optical antenna as a receiver capable of overcoming the étendue limit, obtained by doping a PMMA slab with CIS QDs and coupling it with a customized PD (Chapter 7). Our preliminary characterization regarded the conversion efficiency, temporal response to optical signals, and FoV of this innovative receiving system. A set of outdoor measurements was carried out under strong solar irradiance to demonstrate the transmission properties of the prototype in a realistic outdoor scenario.

The main achievements and findings of this project can be summarized as follows:

1) The realistic simulation of a road scenario using a real, VLC-capable traffic light and a receiver positioned at different heights corresponding to car headlights, dashboard, and internal mirror. The transmission pattern and the propagation channel were mathematically modeled: the conventional Lambertian model was found the least accurate in describing the channel properties, yielding an average error of 25%, while our proposed polynomial models achieved 8% with 12 coefficients. The results of an experimental measurement campaign highlighted that an uncoded error probability of 10^{-3} could be achieved for a distance of 30 m (Section 4.2.).

2) The design and implementation of a low-cost, low-latency VLC prototype for I2V communications based on a commercial LED-based traffic light as the transmitter and a PD with inexpensive lenses of different materials (glass or plastic) as the receiver. The system was tested at two baud rates (115 and 230 kbaud), and the results highlighted the possibility of obtaining error-free transmission using a 2" Fresnel lens for distances up to 36 m with a sub-millisecond (820 μs) latency of the entire process at 230 kbaud (Section 4.4.).

3) The deployment of a novel, IEEE 802.15.7-compatible I2V2V communication system embedding a digital ADR stage for decoding and relaying real-time road information over a vehicular chain, using a regular LED traffic light as the transmitter. A thorough statistical analysis of PER distribution showed that this VLC system attained ultra-low, sub-ms latencies for distances up to 30 m. A latency below 10 ms was still achieved for distances of 50 m at a 99.9% confidence level (Section 4.3.).

4) The development of a bidirectional VLC system for V2V vehicular applications exploiting low-cost hardware and real motorcycle LED headlights and rear lights. The tests were performed in a realistic outdoor scenario under direct solar irradiance using different baud rates (28 and 57 kbaud). A successful VLC bidirectional link was established for distances up to 21 m at 28 kbaud, and error-free communication was observed up to 12 m (Section 4.5.).

5) The first report of a successful NLoS VLC data transfer in a real museum by exploiting the existing LED illumination system and the light diffused by two-dimensional (paintings) and three-dimensional (sculptures) works of art. The prototype was tested on different masterpieces in their original locations, recording PER and SNR maps as a function of the position of the RX stage, which mimicked realistic positions of the visitors. Error-free transmissions were achieved for baud rates up to 28 kbaud and different distances and angular displacements depending on the material and shape of the specific artwork being considered. Most importantly, we demonstrated that the diffusive VLC data stream was highly directional and could be exploited for casting dedicated information to visitors observing a specific piece of art (Chapter 5).

6) The extensive characterization of a novel FSOCS based on an MIR QCL source under two different noise regimes obtained by applying different optical channel attenuations to simulate different weather conditions. The results showed a very different response of the system in the two cases. In high attenuation conditions, the predominant noise contribution originated from the detector, and error-free communication ($PER < 1.6 \times 10^{-5}$) was achieved for a maximum optical attenuation MOA of 48 dB for 100% modulation depth and 115.2 kbaud. In the low attenuation regime, the channel was mainly affected by the source noise, and the PER was almost constant independently of the optical attenuation. We proposed a simplified propagation model considering geometrical and atmospheric absorption and scattering effects, which allowed us to estimate the error-free link length as 50 km in low-visibility conditions ($V = 5$ km), yielding a better outcome than the performances standard NIR sources in the telecom range (Chapter 6).

7) The preliminary characterization of a new reception system consisting of an optical antenna coupled with a PD, which overcame the étendue principle and ensured 1 Mbaud UART communications up to 100 m (60 m with 0.5 Mbaud Manchester). Interestingly, this prototype demonstrated a field of view of approximately 160° in an outdoor scenario, regardless of whether the system performed under direct sunlight or shadow conditions (Chapter 7).

9. Future perspectives

Several changes could be implemented with the scope of improving our VLC system. For example, the low-cost Arduino DUE digital platforms could be replaced by Software Defined Radios; although more expensive, these would allow for a paradigm shift in the data processing capabilities, providing outstanding performances in noise rejection. Moreover, different digital data encoding methods could be employed, such as QAM and OFDM modulations, and forward correction errors could be used. More generally, multiple challenges and future perspectives can be listed for the field of VLC. One of these is the possibility of implementing the technology in environments typically affected by the issue of interference between radio signals, such as airplanes, hospitals, or heavy industries. Moreover, visible light sources, particularly those emitting at 400–450 nm, are attracting increasing interest for use in underwater optical wireless communication, owing to the negligible absorption by water in that spectral region [185].

Another challenge is found in the efforts to increase the BW of commercial LEDs: the current bottleneck in the development of VLC technology is the inability to perform ultra-fast communication except with LED prototypes. A possible solution might be provided by atomic layer deposition [186]. One more issue is the reduction of the dark current in the receiver; to mitigate this, Huang *et al.* [187] have proposed a rapid thermal annealing and hydrogenated surface passivation.

A major challenge is represented by mass commercialization: in the near future, lighting companies and phone manufacturers will need to develop new devices to accommodate the current VLC technologies for use in future applications. Data transmission through LEDs requires further study to overcome the existing issues with misalignment and outages. Another concern is related to possible hazards for eye safety and effects on circadian rhythm following long-term exposure to high-intensity light. Conventional LEDs are characterized by limitations in allowable bandwidths and transmission rates in Li-Fi systems, and they may be replaced by micro-LEDs.

Quantum communication is also being applied to the VLC system: this consists in a way to transfer quantum states from the transmitter (Alice) to the receiver (Bob). Quantum key distribution, proposed by Bennett and Brassard in 1984, is an example of quantum cryptography [188]. Different photon states (polarization, period, frequency, phase, and space) can accomplish various protocols; the essence of one of these, named BB84, is to pressure an eavesdropper (Eve) to perform a quantum measurement that will expose their existence, by sending a series of individual photons to Bob. While a large number of these photons never arrive or are not detected, some are kept and used as key material, while the rest are used to hunt for Eve.

In FSO technology, a polarization-based BB84 QKD protocol is often employed. When this is applied to optical fiber networks, the transmission distance is limited by polarization-dependent loss and polarization mode dispersion [189]. A beam-steering system is used so that Alice can direct the beam to Bob with no need to actually move the system; this can be obtained through a liquid crystal spatial light modulator or a micro-electromechanical system [190]. A single-photon source is necessary for this scope because the BB84 protocol is implemented through the use of a high-attenuation laser, which can produce weak coherent state pulses [191]. The coherent state is characterized by a high probability that there is no more than one photon. Thus, we can express the number state $| n >$ in terms of the ground state $| 0 >$ using the creation operator, $| n > = (a^{+})^{n} | 0 > / (n!)^{0.5}$, where a is the annihilation operator. The density operator of a coherent state is $\rho = | \alpha >< \alpha |$, where $| \alpha >$ is the coherent state vector. The probability to find n photons in the coherent state, according to a Poisson distribution, is $P(n) = |< n | \alpha >|^{2} = \exp(-\mu (\mu^{n} / n!))$, where $\mu = |\alpha|^{2}$ is the photon number. Because the probability of more than one photon being sent is not zero, a photon number splitting attack can be deployed, allowing Eve to acquire information.

As a possible solution, Lo *et al*. have introduced a decoy-state-based quantum key distribution [192] in which Alice and Bob are able to detect whether Eve is capturing photons because the average number of sent photons is higher in random time slots. Depending on which method Bob employs, two QKD schemes can be applied: a discrete variable- or a continuous variable-QKD. These allow for measuring the field quadrature by making use of a single-photon detector and a homodyne/heterodyne detection mode, respectively. In discrete variable-QKD, the security of the system is ensured by the unclonability and indistinguishability theorems of arbitrary quantum states. The former states that a quantum state is unique and cannot be copied: even the most powerful of computers cannot allow Eve to clone a non-orthogonal quantum state [193]; the latter asserts that we cannot clearly differentiate non-orthogonal states: this means that Eve's attempt to gather information will interfere with the constancy of the quantum states, which will allow Bob to detect the attempt. In contrast, the continuous variable-QKD is based on the uncertainty principle and affirms that it is not possible to accurately measure the in-phase and quadrature components of the coherent state at the same time. The most recent developments of QKD have had a significant positive impact from both a theoretical and experimental point of view. For example, an LED-based decoy-state QKD has been proposed, in which the replacement of a laser source with an LED achieves lower costs and sufficient security of the QKD system.

References

[1] O. Borowski, B. Howell, T. Sever, Communication by fire (and smoke) signals in the Kingdom of Judah, 1998.

[2] J.A. Kingman, The Isle of Capri: An Imperial Residence and Probable Wireless Station of Ancient Rome, Nature Geographic Magazine, 1919.

[3] P.A. Clayton, M. Price, The seven wonders of the ancient world, Routledge, 1988.

[4] G.J. Holzmann, B. Pehrson, The Early History of Data Networks, IEEE Computer Society Press, United States, 1995.

[5] H. Elgala, A Study on the Impact of Nonlinear Characteristics of LEDs on Optical OFDM. PhD Thesis., Jacobs University Bremen, 2010.

[6] C.H. Sterling, Military Communications: From Ancient Times to the 21st Century, Abc-Clio Inc., 2007.

[7] A.G. Bell, ART. XXXIV.--On the Production and Reproduction of Sound by Light, American Journal of Science. 20 (1880) 305.

[8] G. Marconi, Improvements in Transmitting Electrical impulses and Signals, and in Apparatus therefor. US patent, USRE11913E, 1901.

[9] T.H. Maiman, Stimulated Optical Radiation in Ruby, Nature. 187 (1960) 493–494. https://doi.org/10.1038/187493a0.

[10] J. Hecht, City of Light: The Story of Fiber Optics, Oxford University Press, 1999.

[11] A.E. Ibhaze, P.E. Orukpe, F.O. Edeko, High capacity data rate system: Review of visible light communications technology, Journal of Electronic Science and Technology. 18 (2020) 100055. https://doi.org/10.1016/j.jnlest.2020.100055.

[12] Y. Tanaka, S. Haruyama, M. Nakagawa, Wireless optical transmissions with white colored LED for wireless home links, in: 11th IEEE International Symposium on Personal Indoor and Mobile Radio Communications. PIMRC 2000. Proceedings (Cat. No.00TH8525), IEEE, London, UK, 2000: pp. 1325–1329. https://doi.org/10.1109/PIMRC.2000.881634.

[13] M. Uysal, H. Nouri, Optical wireless communications — An emerging technology, in: 2014 16th International Conference on Transparent Optical Networks (ICTON), IEEE, Graz, Austria, 2014: pp. 1–7. https://doi.org/10.1109/ICTON.2014.6876267.

[14] L.U. Khan, Visible light communication: Applications, architecture, standardization and research challenges, Digital Communications and Networks. 3 (2017) 78–88. https://doi.org/10.1016/j.dcan.2016.07.004.

[15] O. Ergul, E. Dinc, O.B. Akan, Communicate to illuminate: State-of-the-art and research challenges for visible light communications, Physical Communication. 17 (2015) 72–85. https://doi.org/10.1016/j.phycom.2015.08.003.

[16] Z. Zhang, A. Chaaban, L. Lampe, Physical layer security in light-fidelity systems, Phil. Trans. R. Soc. A. 378 (2020) 20190193. https://doi.org/10.1098/rsta.2019.0193.

[17] D. Karunatilaka, F. Zafar, V. Kalavally, R. Parthiban, LED Based Indoor Visible Light Communications: State of the Art, IEEE Commun. Surv. Tutorials. 17 (2015) 1649–1678. https://doi.org/10.1109/COMST.2015.2417576.

[18] M.A. Umair, M. Meucci, M. Seminara, M. Fattori, S. Brovelli, F. Meinardi, J. Catani, Long-range, Mbit-class optical wireless communication system based on a large-area, quantum-dot fluorescent antenna, To Be Submitted to Laser & Photonics Reviews. (2022).

[19] X. Pang, O. Ozolins, L. Zhang, R. Schatz, A. Udalcovs, X. Yu, G. Jacobsen, S. Popov, J. Chen, S. Lourdudoss, Free-Space Communications Enabled by Quantum Cascade Lasers, Phys. Status Solidi A. 218 (2021) 2000407. https://doi.org/10.1002/pssa.202000407.

[20] H. Chun, A. Gomez, C. Quintana, W. Zhang, G. Faulkner, D. O’Brien, A Wide-Area Coverage 35 Gb/s Visible Light Communications Link for Indoor Wireless Applications, Sci Rep. 9 (2019) 4952. https://doi.org/10.1038/s41598-019-41397-6.
[21] K. Cui, G. Chen, Z. Xu, R.D. Roberts, Traffic light to vehicle visible light communication channel characterization, Appl. Opt. 51 (2012) 6594. https://doi.org/10.1364/AO.51.006594.
[22] T. Nawaz, M. Seminara, S. Caputo, L. Mucchi, F.S. Cataliotti, J. Catani, IEEE 802.15.7-Compliant Ultra-Low Latency Relaying VLC System for Safety-Critical ITS, IEEE Trans. Veh. Technol. 68 (2019) 12040–12051. https://doi.org/10.1109/TVT.2019.2948041.
[23] F. Nizzi, T. Nawaz, J. Catani, M. Seminara, T. Pecorella, S. Caputo, L. Mucchi, R. Fantacci, M. Bastianini, C. Cerboni, A. Buzzigoli, A. Fratini, Data dissemination to vehicles using 5G and VLC for Smart Cities, in: 2019 AEIT International Annual Conference (AEIT), IEEE, Florence, Italy, 2019: pp. 1–5. https://doi.org/10.23919/AEIT.2019.8893380.
[24] M. Seminara, T. Nawaz, S. Caputo, L. Mucchi, J. Catani, Characterization of Field of View in Visible Light Communication Systems for Intelligent Transportation Systems, IEEE Photonics J. 12 (2020) 1–16. https://doi.org/10.1109/JPHOT.2020.3005620.
[25] T. Nawaz, M. Seminara, S. Caputo, L. Mucchi, J. Catani, Low-Latency VLC System with Fresnel Receiver for I2V ITS Applications, JSAN. 9 (2020) 35. https://doi.org/10.3390/jsan9030035.
[26] D. Marabissi, L. Mucchi, S. Caputo, F. Nizzi, T. Pecorella, R. Fantacci, T. Nawaz, M. Seminara, J. Catani, Experimental Measurements of a Joint 5G-VLC Communication for Future Vehicular Networks, JSAN. 9 (2020) 32. https://doi.org/10.3390/jsan9030032.
[27] M. Meucci, M. Seminara, T. Nawaz, S. Caputo, L. Mucchi, J. Catani, Bidirectional Vehicle-to-Vehicle Communication System Based on VLC: Outdoor Tests and Performance Analysis, IEEE Trans. Intell. Transport. Syst. (2021) 1–11. https://doi.org/10.1109/TITS.2021.3104498.
[28] S. Caputo, L. Mucchi, F. Cataliotti, M. Seminara, T. Nawaz, J. Catani, Measurement-based VLC channel characterization for I2V communications in a real urban scenario, Vehicular Communications. 28 (2021) 100305. https://doi.org/10.1016/j.vehcom.2020.100305.
[29] M. Seminara, M. Meucci, F. Tarani, C. Riminesi, J. Catani, Characterization of a VLC system in real museum scenario using diffusive LED lighting of artworks, Photon. Res. 9 (2021) 548. https://doi.org/10.1364/PRJ.414394.
[30] M. Meucci, M. Seminara, F. Tarani, C. Riminesi, J. Catani, Visible Light Communications through Diffusive Illumination of Sculptures in a Real Museum, JSAN. 10 (2021) 45. https://doi.org/10.3390/jsan10030045.
[31] M. Seminara, T. Gabbrielli, N. Corrias, S. Borri, L. Consolino, M. Meucci, F. Cappelli, J. Catani, Mid-infrared free-space optical communication based on quantum cascade lasers: experimental analysis of noise regimes, Submitted to Photonics Research. (2021).
[32] E. Desurvire, Classical and quantum information theory: an introduction for the telecom scientist, Cambridge University Press, Cambridge, UK ; New York, 2009.
[33] T.-C. Yu, W.-T. Huang, W.-B. Lee, C.-W. Chow, S.-W. Chang, H.-C. Kuo, Visible Light Communication System Technology Review: Devices, Architectures, and Applications, Crystals. 11 (2021) 1098. https://doi.org/10.3390/cryst11091098.
[34] F.E. Schubert, Light-emitting diodes, 3rd ed., E. Fred Schubert, New York, USA, 2018.
[35] L.E.M. Matheus, A.B. Vieira, L.F.M. Vieira, M.A.M. Vieira, O. Gnawali, Visible Light Communication: Concepts, Applications and Challenges, IEEE Commun. Surv. Tutorials. 21 (2019) 3204–3237. https://doi.org/10.1109/COMST.2019.2913348.
[36] D.A. Steigerwald, J.C. Bhat, D. Collins, R.M. Fletcher, M.O. Holcomb, M.J. Ludowise, P.S. Martin, S.L. Rudaz, Illumination with solid state lighting technology, IEEE J. Select. Topics Quantum Electron. 8 (2002) 310–320. https://doi.org/10.1109/2944.999186.

[37] S. Muthu, F.J.P. Schuurmans, M.D. Pashley, Red, green, and blue LEDs for white light illumination, IEEE J. Select. Topics Quantum Electron. 8 (2002) 333–338. https://doi.org/10.1109/2944.999188.

[38] C.-H. Yeh, Y.-L. Liu, C.-W. Chow, Real-time white-light phosphor-LED visible light communication (VLC) with compact size, Opt. Express. 21 (2013) 26192. https://doi.org/10.1364/OE.21.026192.

[39] C.-T. Tsai, C.-H. Cheng, H.-C. Kuo, G.-R. Lin, Toward high-speed visible laser lighting based optical wireless communications, Progress in Quantum Electronics. 67 (2019) 100225. https://doi.org/10.1016/j.pquantelec.2019.100225.

[40] A.M. Khalid, G. Cossu, R. Corsini, P. Choudhury, E. Ciaramella, 1-Gb/s Transmission Over a Phosphorescent White LED by Using Rate-Adaptive Discrete Multitone Modulation, IEEE Photonics J. 4 (2012) 1465–1473. https://doi.org/10.1109/JPHOT.2012.2210397.

[41] G. Cossu, A.M. Khalid, P. Choudhury, R. Corsini, E. Ciaramella, 34 Gbit/s visible optical wireless transmission based on RGB LED, Opt. Express. 20 (2012) B501. https://doi.org/10.1364/OE.20.00B501.

[42] H.S. Wasisto, J.D. Prades, J. Gülink, A. Waag, Beyond solid-state lighting: Miniaturization, hybrid integration, and applications of GaN nano- and micro-LEDs, Applied Physics Reviews. 6 (2019) 041315. https://doi.org/10.1063/1.5096322.

[43] K. Rae, P.P. Manousiadis, M.S. Islim, L. Yin, J. Carreira, J.J.D. Mckendry, B. Guilhabert, I.D.W. Samuel, G.A. Turnbull, N. Laurand, H. Haas, M.D. Dawson, Transfer-printed micro-LED and polymer-based transceiver for visible light communications, Opt. Express. 26 (2018) 31474. https://doi.org/10.1364/OE.26.031474.

[44] A. Salehi, X. Fu, D. Shin, F. So, Recent Advances in OLED Optical Design, Adv. Funct. Mater. 29 (2019) 1808803. https://doi.org/10.1002/adfm.201808803.

[45] P. Deng, M. Kavehrad, Effect of white LED DC-bias on modulation speed for visible light communications, ArXiv:1612.08477 [Physics]. (2016). http://arxiv.org/abs/1612.08477 (accessed January 25, 2022).

[46] A. Žukauskas, M. Shur, R. Gaska, Introduction to solid-state lighting, J. Wiley, New York, 2002.

[47] P.H. Pathak, X. Feng, P. Hu, P. Mohapatra, Visible Light Communication, Networking, and Sensing: A Survey, Potential and Challenges, IEEE Commun. Surv. Tutorials. 17 (2015) 2047–2077. https://doi.org/10.1109/COMST.2015.2476474.

[48] G. Wyszecki, W.S. Stiles, Color science: concepts and methods, quantitative data, and formulae, Wiley classics library ed, John Wiley & Sons, New York, 2000.

[49] J.F. Cox, Fundamentals of linear electronics: integrated and discrete, 2nd ed, Delmar Thomson Learning, Albany, 2002.

[50] S. Hranilovic, Wireless optical communication systems, Springer, New York, 2005.

[51] K. Cui, G. Chen, Z. Xu, R.D. Roberts, Line-of-sight visible light communication system design and demonstration, in: 2010 7th International Symposium on Communication Systems, Networks & Digital Signal Processing (CSNDSP 2010), IEEE, Newcastle upon Tyne, 2010: pp. 621–625. https://doi.org/10.1109/CSNDSP16145.2010.5580360.

[52] K. Lee, H. Park, J.R. Barry, Indoor Channel Characteristics for Visible Light Communications, IEEE Commun. Lett. 15 (2011) 217–219. https://doi.org/10.1109/LCOMM.2011.010411.101945.

[53] W. Tomasi, Electronic communications systems: fundamentals through advanced : laboratory manual, Prentice Hall Career & Technology, Englewood Cliffs, NJ, 1994.

[54] T. Komine, M. Nakagawa, Fundamental analysis for visible-light communication system using LED lights, IEEE Trans. Consumer Electron. 50 (2004) 100–107. https://doi.org/10.1109/TCE.2004.1277847.

[55] D. Milovancev, T. Jukic, N. Vokic, P. Brandl, B. Steindl, H. Zimmermann, VLC Using 800-µm Diameter APD Receiver Integrated in Standard 0.35-µm BiCMOS Technology, IEEE Photonics J. 13 (2021) 1–13. https://doi.org/10.1109/JPHOT.2020.3036549.

[56] K.-T. Ho, R. Chen, G. Liu, C. Shen, J. Holguin-Lerma, A.A. Al-Saggaf, T.K. Ng, M.-S. Alouini, J.-H. He, B.S. Ooi, 32 Gigabit-per-second Visible Light Communication Link with InGaN/GaN MQW Micro-photodetector, Opt. Express. 26 (2018) 3037. https://doi.org/10.1364/OE.26.003037.

[57] IEEE Std. 802.15.7-2018, IEEE Standard for Local and metropolitan area networks--Part 15.7: Short-Range Optical Wireless Communications, IEEE, 2018. https://doi.org/10.1109/IEEESTD.2019.8697198.

[58] A. Boucouvalas, P. Chatzimisios, Z. Ghassemlooy, M. Uysal, K. Yiannopoulos, Standards for indoor Optical Wireless Communications, IEEE Commun. Mag. 53 (2015) 24–31. https://doi.org/10.1109/MCOM.2015.7060515.

[59] J.M. Kahn, J.R. Barry, Wireless infrared communications, Proc. IEEE. 85 (1997) 265–298. https://doi.org/10.1109/5.554222.

[60] M.S. Rea, ed., The IESNA lighting handbook: reference & application, 9. ed, Iluminating Engineering Society of North Amercia, New York, NY, 2000.

[61] S.M. Berman, D.S. Greenhouse, I.L. Bailey, R.D. Clear, T.W. Raasch, Human Electroretinogram Responses to Video Displays, Fluorescent Lighting, and Other High Frequency Sources, Optometry and Vision Science. 68 (1991) 645–662. https://doi.org/10.1097/00006324-199108000-00012.

[62] J. Vucic, C. Kottke, S. Nerreter, K. Habel, A. Buttner, K.D. Langer, J.W. Walewski, 125 Mbit/s over 5 m wireless distance by use of OOK-modulated phosphorescent white LEDs, 2009 35th European Conference on Optical Communication. IEEE. (2009) 1–2.

[63] T.Y. Elganimi, Studying the BER performance, power- and bandwidth- efficiency for FSO communication systems under various modulation schemes, in: 2013 IEEE Jordan Conference on Applied Electrical Engineering and Computing Technologies (AEECT), IEEE, Amman, Jordan, 2013: pp. 1–6. https://doi.org/10.1109/AEECT.2013.6716426.

[64] B. Sklar, Digital communications: fundamentals and applications, 2nd ed, Prentice-Hall PTR, Upper Saddle River, N.J, 2001.

[65] R. Khalili, K. Salamatian, A New Analytic Approach to Evaluation of Packet Error Rate in Wireless Networks, in: 3rd Annual Communication Networks and Services Research Conference (CNSR'05), IEEE, Halifax, NS, Canada, 2005: pp. 333–338. https://doi.org/10.1109/CNSR.2005.14.

[66] H. Elgala, R. Mesleh, H. Haas, Indoor optical wireless communication: potential and state-of-the-art, IEEE Commun. Mag. 49 (2011) 56–62. https://doi.org/10.1109/MCOM.2011.6011734.

[67] J. Gancarz, H. Elgala, T. Little, Impact of lighting requirements on VLC systems, IEEE Commun. Mag. 51 (2013) 34–41. https://doi.org/10.1109/MCOM.2013.6685755.

[68] Y. Fan, B. Bai, R.J. Green, PPMPWM: A new modulation format for wireless optical communications, in: 2010 7th International Symposium on Communication Systems, Networks & Digital Signal Processing (CSNDSP 2010), IEEE, Newcastle upon Tyne, 2010: pp. 604–609. https://doi.org/10.1109/CSNDSP16145.2010.5580364.

[69] S.H. Lee, K.-I. Ahn, J.K. Kwon, Multilevel Transmission in Dimmable Visible Light Communication Systems, J. Lightwave Technol. 31 (2013) 3267–3276. https://doi.org/10.1109/JLT.2013.2281209.

[70] W. Popoola, E. Poves, H. Haas, Generalised space shift keying for visible light communications, in: 2012 8th International Symposium on Communication Systems,

Networks & Digital Signal Processing (CSNDSP), IEEE, Poznan, Poland, 2012: pp. 1–4. https://doi.org/10.1109/CSNDSP.2012.6292784.

[71] E. Monteiro, S. Hranilovic, Design and Implementation of Color-Shift Keying for Visible Light Communications, J. Lightwave Technol. 32 (2014) 2053–2060. https://doi.org/10.1109/JLT.2014.2314358.

[72] M.Z. Afgani, H. Haas, H. Elgala, D. Knipp, Visible light communication using OFDM, in: 2nd International Conference on Testbeds and Research Infrastructures for the Development of Networks and Communities, 2006. TRIDENTCOM 2006., IEEE, Barcelona, 2006: p. 6 pp. – 134. https://doi.org/10.1109/TRIDNT.2006.1649137.

[73] J. Armstrong, OFDM for Optical Communications, J. Lightwave Technol. 27 (2009) 189–204. https://doi.org/10.1109/JLT.2008.2010061.

[74] CIE, Commission Internationale de l'Eclairage Proc., Cambridge Univ. Press, 1931.

[75] Y. Gu, A. Lo, I. Niemegeers, A survey of indoor positioning systems for wireless personal networks, IEEE Commun. Surv. Tutorials. 11 (2009) 13–32. https://doi.org/10.1109/SURV.2009.090103.

[76] J. Armstrong, Y. Sekercioglu, A. Neild, Visible light positioning: a roadmap for international standardization, IEEE Commun. Mag. 51 (2013) 68–73. https://doi.org/10.1109/MCOM.2013.6685759.

[77] S. Pergoloni, Z. Mohamadi, A.M. Vegni, Z. Ghassemlooy, M. Biagi, Visible Light indoor positioning through colored LEDs, in: 2017 IEEE International Conference on Communications Workshops (ICC Workshops), IEEE, Paris, France, 2017: pp. 150–155. https://doi.org/10.1109/ICCW.2017.7962649.

[78] S.-K. Lim, K. Ruling, I. Kim, I. Jang, Entertainment lighting control network standardization to support VLC services, IEEE Commun. Mag. 51 (2013) 42–48. https://doi.org/10.1109/MCOM.2013.6685756.

[79] M. Kim, T. Suh, A Low-Cost Surveillance and Information System for Museum Using Visible Light Communication, IEEE Sensors J. 19 (2019) 1533–1541. https://doi.org/10.1109/JSEN.2018.2879606.

[80] J. Cosmas, B. Meunier, K. Ali, N. Jawad, H.-Y. Meng, F. Goutagneux, E. Legale, M. Satta, P. Jay, X. Zhang, C. Huang, J. Garcia, M. Negru, Y. Zhang, T. Kourtis, C. Koumaras, C. Sakkas, L.-K. Huang, R. Zetik, K. Cabaj, W. Mazurczyk, M.E. Cakan, A. Kapovits, 5G Internet of radio light services for Musée de la Carte à Jouer, in: 2018 Global LIFI Congress (GLC), IEEE, Paris, 2018: pp. 1–6. https://doi.org/10.23919/GLC.2018.8319095.

[81] L. Gokrem, M. Durgun, Y. Durgun, Indoor Location Control with Visible Light Communication, in: 2019 3rd International Conference on Advanced Information and Communications Technologies (AICT), IEEE, Lviv, Ukraine, 2019: pp. 314–316. https://doi.org/10.1109/AIACT.2019.8847765.

[82] F. Viani, A. Polo, P. Garofalo, N. Anselmi, M. Salucci, E. Giarola, Evolutionary Optimization Applied to Wireless Smart Lighting in Energy-Efficient Museums, IEEE Sensors J. 17 (2017) 1213–1214. https://doi.org/10.1109/JSEN.2017.2647827.

[83] H. Haas, L. Yin, Y. Wang, C. Chen, What is LiFi?, J. Lightwave Technol. 34 (2016) 1533–1544. https://doi.org/10.1109/JLT.2015.2510021.

[84] M.M. Céspedes, B.G. Guzmán, V.P.G. Jiménez, Lights and Shadows: A Comprehensive Survey on Cooperative and Precoding Schemes to Overcome LOS Blockage and Interference in Indoor VLC, Sensors. 21 (2021) 861. https://doi.org/10.3390/s21030861.

[85] S. Chatterjee, D. Sabui, G.S. Khan, B. Roy, Signal to interference plus noise ratio improvement of a multi-cell indoor visible light communication system through optimal parameter selection complying lighting constraints, Trans Emerging Tel Tech. 32 (2021). https://doi.org/10.1002/ett.4291.

[86] S.A.H. Mohsan, H. Amjad, A comprehensive survey on hybrid wireless networks: practical considerations, challenges, applications and research directions, Opt Quant Electron. 53 (2021) 523. https://doi.org/10.1007/s11082-021-03141-1.

[87] R. Pernice, A. Andò, M. Cardinale, L. Curcio, S. Stivala, A. Parisi, A.C. Busacca, Z. Ghassemlooy, J. Perez, Indoor free space optics link under the weak turbulence regime: measurements and model validation, IET Communications. 9 (2015) 62–70. https://doi.org/10.1049/iet-com.2014.0432.

[88] A. Vavoulas, H.G. Sandalidis, D. Varoutas, Weather Effects on FSO Network Connectivity, J. Opt. Commun. Netw. 4 (2012) 734. https://doi.org/10.1364/JOCN.4.000734.

[89] S. Zafar, H. Khalid, Free Space Optical Networks: Applications, Challenges and Research Directions, Wireless Pers Commun. 121 (2021) 429–457. https://doi.org/10.1007/s11277-021-08644-4.

[90] H. Kaushal, G. Kaddoum, Underwater Optical Wireless Communication, IEEE Access. 4 (2016) 1518–1547. https://doi.org/10.1109/ACCESS.2016.2552538.

[91] N. Saeed, A. Celik, T.Y. Al-Naffouri, M.-S. Alouini, Underwater optical wireless communications, networking, and localization: A survey, Ad Hoc Networks. 94 (2019) 101935. https://doi.org/10.1016/j.adhoc.2019.101935.

[92] R.M. Hagem, D.V. Thiel, S.G. O'Keefe, T. Fickenscher, Optical wireless communication for real time swimmers feedback: A review, in: 2012 International Symposium on Communications and Information Technologies (ISCIT), IEEE, Gold Coast, QLD, 2012: pp. 1080–1085. https://doi.org/10.1109/ISCIT.2012.6380853.

[93] G. Cossu, R. Corsini, A.M. Khalid, S. Balestrino, A. Coppelli, A. Caiti, E. Ciaramella, Experimental demonstration of high speed underwater visible light communications, in: 2013 2nd International Workshop on Optical Wireless Communications (IWOW), IEEE, Newcastle upon Tyne, United Kingdom, 2013: pp. 11–15. https://doi.org/10.1109/IWOW.2013.6777767.

[94] I.C. Rust, H.H. Asada, A dual-use visible light approach to integrated communication and localization of underwater robots with application to non-destructive nuclear reactor inspection, in: 2012 IEEE International Conference on Robotics and Automation, IEEE, St Paul, MN, USA, 2012: pp. 2445–2450. https://doi.org/10.1109/ICRA.2012.6224718.

[95] M. Kong, J. Lin, C.H. Kang, C. Shen, Y. Guo, X. Sun, M. Sait, Y. Weng, H. Zhang, T.K. Ng, B.S. Ooi, Toward self-powered and reliable visible light communication using amorphous silicon thin-film solar cells, Opt. Express. 27 (2019) 34542. https://doi.org/10.1364/OE.27.034542.

[96] N. Kumar, N. Lourenco, D. Terra, L.N. Alves, R.L. Aguiar, Visible light communications in intelligent transportation systems, in: 2012 IEEE Intelligent Vehicles Symposium, IEEE, Alcal de Henares , Madrid, Spain, 2012: pp. 748–753. https://doi.org/10.1109/IVS.2012.6232282.

[97] S.-H. Yu, O. Shih, H.-M. Tsai, N. Wisitpongphan, R.D. Roberts, Smart automotive lighting for vehicle safety, IEEE Commun. Mag. 51 (2013) 50–59. https://doi.org/10.1109/MCOM.2013.6685757.

[98] M. Akanegawa, Y. Tanaka, M. Nakagawa, Basic study on traffic information system using LED traffic lights, IEEE Trans. Intell. Transport. Syst. 2 (2001) 197–203. https://doi.org/10.1109/6979.969365.

[99] M. Uysal, Z. Ghassemlooy, A. Bekkali, A. Kadri, H. Menouar, Visible Light Communication for Vehicular Networking: Performance Study of a V2V System Using a Measured Headlamp Beam Pattern Model, IEEE Veh. Technol. Mag. 10 (2015) 45–53. https://doi.org/10.1109/MVT.2015.2481561.

[100] A. Memedi, F. Dressler, Vehicular Visible Light Communications: A Survey, IEEE Commun. Surv. Tutorials. 23 (2021) 161–181. https://doi.org/10.1109/COMST.2020.3034224.

[101] S. Iwasaki, C. Premachandra, T. Endo, T. Fujii, M. Tanimoto, Y. Kimura, Visible light road-to-vehicle communication using high-speed camera, in: 2008 IEEE Intelligent Vehicles Symposium, IEEE, Eindhoven, Netherlands, 2008: pp. 13–18. https://doi.org/10.1109/IVS.2008.4621155.

[102] H. Binti Che Wook, Visible Light Communication with LED Traffic Lights Using 2-Dimensional Image Sensor, IEICE Transactions on Fundamentals of Electronics, Communications and Computer Sciences. E89-A (2006) 654–659. https://doi.org/10.1093/ietfec/e89-a.3.654.

[103] M. Elamassie, M. Karbalayghareh, F. Miramirkhani, R.C. Kizilirmak, M. Uysal, Effect of Fog and Rain on the Performance of Vehicular Visible Light Communications, in: 2018 IEEE 87th Vehicular Technology Conference (VTC Spring), IEEE, Porto, 2018: pp. 1–6. https://doi.org/10.1109/VTCSpring.2018.8417738.

[104] A. Bazzi, B.M. Masini, A. Zanella, A. Calisti, Visible light communications as a complementary technology for the internet of vehicles, Computer Communications. 93 (2016) 39–51. https://doi.org/10.1016/j.comcom.2016.07.004.

[105] A. Bazzi, G. Cecchini, M. Menarini, B.M. Masini, A. Zanella, Survey and Perspectives of Vehicular Wi-Fi versus Sidelink Cellular-V2X in the 5G Era, Future Internet. 11 (2019) 122. https://doi.org/10.3390/fi11060122.

[106] S. Ariyanti, M. Suryanegara, Visible Light Communication (VLC) for 6G Technology: The Potency and Research Challenges, in: 2020 Fourth World Conference on Smart Trends in Systems, Security and Sustainability (WorldS4), IEEE, London, United Kingdom, 2020: pp. 490–493. https://doi.org/10.1109/WorldS450073.2020.9210383.

[107] Y. Dong, M. Shi, X. Yang, P. Zeng, J. Gong, S. Zheng, M. Zhang, R. Liang, Q. Ou, N. Chi, S. Zhang, Nanopatterned luminescent concentrators for visible light communications, Opt. Express. 25 (2017) 21926. https://doi.org/10.1364/OE.25.021926.

[108] P.P. Manousiadis, S. Rajbhandari, R. Mulyawan, D.A. Vithanage, H. Chun, G. Faulkner, D.C. O’Brien, G.A. Turnbull, S. Collins, I.D.W. Samuel, Wide field-of-view fluorescent antenna for visible light communications beyond the étendue limit, Optica. 3 (2016) 702. https://doi.org/10.1364/OPTICA.3.000702.

[109] W.H. Weber, J. Lambe, Luminescent greenhouse collector for solar radiation, Appl. Opt. 15 (1976) 2299. https://doi.org/10.1364/AO.15.002299.

[110] J.S. Batchelder, A.H. Zewai, T. Cole, Luminescent solar concentrators 1: Theory of operation and techniques for performance evaluation, Appl. Opt. 18 (1979) 3090. https://doi.org/10.1364/AO.18.003090.

[111] C. Corrado, S.W. Leow, M. Osborn, I. Carbone, K. Hellier, M. Short, G. Alers, S.A. Carter, Power generation study of luminescent solar concentrator greenhouse, J. Renewable Sustainable Energy. 8 (2016) 043502. https://doi.org/10.1063/1.4958735.

[112] S.F.H. Correia, P.P. Lima, E. Pecoraro, S.J.L. Ribeiro, P.S. André, R.A.S. Ferreira, L.D. Carlos, Scale up the collection area of luminescent solar concentrators towards metre-length flexible waveguiding photovoltaics: Scale up of luminescent solar concentrators, Prog. Photovolt: Res. Appl. 24 (2016) 1178–1193. https://doi.org/10.1002/pip.2772.

[113] P.P. Manousiadis, K. Yoshida, G.A. Turnbull, I.D.W. Samuel, Organic semiconductors for visible light communications, Phil. Trans. R. Soc. A. 378 (2020) 20190186. https://doi.org/10.1098/rsta.2019.0186.

[114] G. Smestad, H. Ries, R. Winston, E. Yablonovitch, The thermodynamic limits of light concentrators, Solar Energy Materials. 21 (1990) 99–111. https://doi.org/10.1016/0165-1633(90)90047-5.

[115] A. Riaz, S. Collins, A Slab Fluorescent Concentrator for Visible Light Communications, in: 2019 2nd IEEE Middle East and North Africa COMMunications Conference

(MENACOMM), IEEE, Manama, Bahrain, 2019: pp. 1–4. https://doi.org/10.1109/MENACOMM46666.2019.8988526.

[116] I.A. Carbone, K.R. Frawley, M.K. McCann, Flexible, Front-Facing Luminescent Solar Concentrators Fabricated from Lumogen F Red 305 and Polydimethylsiloxane, International Journal of Photoenergy. 2019 (2019) 1–9. https://doi.org/10.1155/2019/8680931.

[117] S. Zhang, D. Tsonev, S. Videv, S. Ghosh, G.A. Turnbull, I.D.W. Samuel, H. Haas, Organic solar cells as high-speed data detectors for visible light communication, Optica. 2 (2015) 607. https://doi.org/10.1364/OPTICA.2.000607.

[118] T. Peyronel, K.J. Quirk, S.C. Wang, T.G. Tiecke, Luminescent detector for free-space optical communication, Optica. 3 (2016) 787. https://doi.org/10.1364/OPTICA.3.000787.

[119] I. Tavakkolnia, L.K. Jagadamma, R. Bian, P.P. Manousiadis, S. Videv, G.A. Turnbull, I.D.W. Samuel, H. Haas, Organic photovoltaics for simultaneous energy harvesting and high-speed MIMO optical wireless communications, Light Sci Appl. 10 (2021) 41. https://doi.org/10.1038/s41377-021-00487-9.

[120] W.G.J.H.M. van Sark, K.W.J. Barnham, L.H. Slooff, A.J. Chatten, A. Büchtemann, A. Meyer, S.J. McCormack, R. Koole, D.J. Farrell, R. Bose, E.E. Bende, A.R. Burgers, T. Budel, J. Quilitz, M. Kennedy, T. Meyer, C.D.M. Donegá, A. Meijerink, D. Vanmaekelbergh, Luminescent Solar Concentrators - A review of recent results, Opt. Express. 16 (2008) 21773. https://doi.org/10.1364/OE.16.021773.

[121] K. Barnham, J.L. Marques, J. Hassard, P. O'Brien, Quantum-dot concentrator and thermodynamic model for the global redshift, Appl. Phys. Lett. 76 (2000) 1197–1199. https://doi.org/10.1063/1.125981.

[122] S. Collins, D.C. O'Brien, A. Watt, High gain, wide field of view concentrator for optical communications, Opt. Lett. 39 (2014) 1756. https://doi.org/10.1364/OL.39.001756.

[123] P.P. Manousiadis, H. Chun, S. Rajbhandari, D.A. Vithanage, R. Mulyawan, G. Faulkner, H. Haas, D.C. O'Brien, S. Collins, G.A. Turnbull, I.D.W. Samuel, Optical Antennas for Wavelength Division Multiplexing in Visible Light Communications beyond the Étendue Limit, Adv. Optical Mater. 8 (2020) 1901139. https://doi.org/10.1002/adom.201901139.

[124] Atmel SMART ARM-based MCU, SAM3X / SAM3A datasheet, (2015). https://ww1.microchip.com/downloads/en/devicedoc/atmel-11057-32-bit-cortex-m3-microcontroller-sam3x-sam3a_datasheet.pdf.

[125] Arduino reference text: "Setup" function, (2019). https://www.arduino.cc/reference/en/language/structure/sketch/setup/.

[126] A. Mirvakili, V.J. Koomson, High efficiency LED driver design for concurrent data transmission and PWM dimming control for indoor visible light communication, in: 2012 IEEE Photonics Society Summer Topical Meeting Series, IEEE, Seattle, WA, USA, 2012: pp. 132–133. https://doi.org/10.1109/PHOSST.2012.6280761.

[127] Understanding focal length and field of view. Application Notes, Edmund Optics, (2015). https: //www.edmundoptics.com/knowledge-center/application-notes/imaging/understanding-focal-length-and-field-of-view/.

[128] World Health Organization, Road traffic injuries, (2018). https://www.who.int/en/news-room/fact-sheets/detail/road-traffic-injuries.

[129] M.Y. Abualhoul, M. Marouf, O. Shagdar, F. Nashashibi, Platooning control using visible light communications: A feasibility study, in: 16th International IEEE Conference on Intelligent Transportation Systems (ITSC 2013), IEEE, The Hague, Netherlands, 2013: pp. 1535–1540. https://doi.org/10.1109/ITSC.2013.6728448.

[130] F. Arena, G. Pau, A. Severino, A Review on IEEE 802.11p for Intelligent Transportation Systems, JSAN. 9 (2020) 22. https://doi.org/10.3390/jsan9020022.

[131] G. Karagiannis, O. Altintas, E. Ekici, G. Heijenk, B. Jarupan, K. Lin, T. Weil, Vehicular Networking: A Survey and Tutorial on Requirements, Architectures, Challenges, Standards and Solutions, IEEE Commun. Surv. Tutorials. 13 (2011) 584–616. https://doi.org/10.1109/SURV.2011.061411.00019.

[132] A. Correa, A. Hamid, E. Sparks, Li-Fi Based Smart Traffic Network, in: 2018 IEEE Transportation Electrification Conference and Expo (ITEC), IEEE, Long Beach, CA, USA, 2018: pp. 217–219. https://doi.org/10.1109/ITEC.2018.8450245.

[133] I. Yaqoob, I.A.T. Hashem, Y. Mehmood, A. Gani, S. Mokhtar, S. Guizani, Enabling Communication Technologies for Smart Cities, IEEE Commun. Mag. 55 (2017) 112–120. https://doi.org/10.1109/MCOM.2017.1600232CM.

[134] T. Yamazato, I. Takai, H. Okada, T. Fujii, T. Yendo, S. Arai, M. Andoh, T. Harada, K. Yasutomi, K. Kagawa, S. Kawahito, Image-sensor-based visible light communication for automotive applications, IEEE Commun. Mag. 52 (2014) 88–97. https://doi.org/10.1109/MCOM.2014.6852088.

[135] A. Cailean, B. Cagneau, L. Chassagne, S. Topsu, Y. Alayli, J.-M. Blosseville, Visible light communications: Application to cooperation between vehicles and road infrastructures, in: 2012 IEEE Intelligent Vehicles Symposium, IEEE, Alcal de Henares , Madrid, Spain, 2012: pp. 1055–1059. https://doi.org/10.1109/IVS.2012.6232225.

[136] A.M. Vegni, M. Biagi, R. Cusani, Smart vehicles, technologies and main applications in vehicular ad hoc networks, in: Vehicular Technologies, Intech, Rijeka, Croatia, 2013.

[137] D. Wang, T. Lan, Design of a gradient-index lens with a compound parabolic concentrator shape as a visible light communication receiving antenna, Appl. Opt. 57 (2018) 1510. https://doi.org/10.1364/AO.57.001510.

[138] X. Ning, R. Winston, J. O'Gallagher, Dielectric totally internally reflecting concentrators, Appl. Opt. 26 (1987) 300. https://doi.org/10.1364/AO.26.000300.

[139] I. Takai, S. Ito, K. Yasutomi, K. Kagawa, M. Andoh, S. Kawahito, LED and CMOS Image Sensor Based Optical Wireless Communication System for Automotive Applications, IEEE Photonics J. 5 (2013) 6801418–6801418. https://doi.org/10.1109/JPHOT.2013.2277881.

[140] Satoshi Okada, Tomohiro Yendo, Takaya Yamazato, Toshiaki Fujii, Masayuki Tanimoto, Yoshikatsu Kimura, On-vehicle receiver for distant visible light road-to-vehicle communication, in: 2009 IEEE Intelligent Vehicles Symposium, IEEE, Xi'an, China, 2009: pp. 1033–1038. https://doi.org/10.1109/IVS.2009.5164423.

[141] L. Mucchi, F.S. Cataliotti, L. Ronga, S. Caputo, P. Marcocci, Experimental-based propagation model for VLC, in: 2017 European Conference on Networks and Communications (EuCNC), IEEE, Oulu, Finland, 2017: pp. 1–5. https://doi.org/10.1109/EuCNC.2017.7980780.

[142] S. Rajagopal, R. Roberts, S.-K. Lim, IEEE 802.15.7 visible light communication: modulation schemes and dimming support, IEEE Commun. Mag. 50 (2012) 72–82. https://doi.org/10.1109/MCOM.2012.6163585.

[143] S.J. Lee, J.K. Kwon, S.Y. Jung, Y.H. Kwon, Simulation modeling of visible light communication channel for automotive applications, in: 2012 15th International IEEE Conference on Intelligent Transportation Systems, IEEE, Anchorage, AK, USA, 2012: pp. 463–468. https://doi.org/10.1109/ITSC.2012.6338610.

[144] K. Cui, G. Chen, Z. Xu, R.D. Roberts, Experimental characterization of traffic light to vehicle VLC link performance, in: 2011 IEEE GLOBECOM Workshops (GC Wkshps), IEEE, Houston, TX, USA, 2011: pp. 808–812. https://doi.org/10.1109/GLOCOMW.2011.6162566.

[145] M.E. Renda, G. Resta, P. Santi, F. Martelli, A. Franchini, IEEE 802.11p VANets: Experimental evaluation of packet inter-reception time, Computer Communications. 75 (2016) 26–38. https://doi.org/10.1016/j.comcom.2015.06.003.

[146] A. Papoulis, S.U. Pillai, Probability, random variables, and stochastic processes, 4. ed., internat. ed., Nachdr, McGraw-Hill, Boston, Mass., 2009.

[147] J.Y. Wong, Theory of ground vehicles, 4th ed, Wiley, Hoboken, N.J, 2008.

[148] M. Zhuk, V. Kovalyshyn, Y. Royko, K. Barvinska, Research on drivers' reaction time in different conditions, EEJET. 2 (2017) 24–31. https://doi.org/10.15587/1729-4061.2017.98103.

[149] Md. Noor-A-Rahim, G.G.Md.N. Ali, H. Nguyen, Y.L. Guan, Performance Analysis of IEEE 802.11p Safety Message Broadcast With and Without Relaying at Road Intersection, IEEE Access. 6 (2018) 23786–23799. https://doi.org/10.1109/ACCESS.2018.2829897.

[150] S.G. Wilson, Digital modulation and coding, Prentice Hall, Upper Saddle River, N.J, 1996.

[151] M. Emara, M.C. Filippou, D. Sabella, MEC-Assisted End-to-End Latency Evaluations for C-V2X Communications, in: 2018 European Conference on Networks and Communications (EuCNC), IEEE, Ljubljana, Slovenia, 2018: pp. 1–9. https://doi.org/10.1109/EuCNC.2018.8442825.

[152] F.M. Alsalami, N. Aigoro, A.A. Mahmoud, Z. Ahmad, P.A. Haigh, O.C.L. Haas, S. Rajbhandari, Impact of Vehicle Headlights Radiation Pattern on Dynamic Vehicular VLC Channel, J. Lightwave Technol. 39 (2021) 3162–3168. https://doi.org/10.1109/JLT.2021.3064811.

[153] G. James, D. Witten, T. Hastie, R. Tibshirani, eds., An introduction to statistical learning: with applications in R, Springer, New York, 2013.

[154] J.J. Stiffler, Theory of synchronous communications, Prentice-Hall, Englewood Cliffs, N.J, 1971.

[155] S. Udtewar, D. Dsouza, A. Aghamkar, Visible Light Information System for Museums, IJSRP. 9 (2019) p8602. https://doi.org/10.29322/IJSRP.9.02.2019.p8602.

[156] R. Lu, ed., Light scattering technology for food property, quality and safety assessment, CRC Press/Taylor & Francis Group, Boca Raton, 2016.

[157] J. Hancock, Jitter—Understanding it, Measuring It, Eliminating It. Part 1: Jitter Fundamentals, High Frequency Electronics. 4 (2004) 44–50.

[158] B. Gary, Analyzing Signals Using the Eye Diagram, High Frequency Electronics. 4 (2005) 50–53.

[159] H.A. Willebrand, B.S. Ghuman, Fiber optics without fiber, IEEE Spectr. 38 (2001) 40–45. https://doi.org/10.1109/6.938713.

[160] M.A. Esmail, A.M. Ragheb, H.A. Fathallah, M. Altamimi, S.A. Alshebeili, 5G-28 GHz Signal Transmission Over Hybrid All-Optical FSO/RF Link in Dusty Weather Conditions, IEEE Access. 7 (2019) 24404–24410. https://doi.org/10.1109/ACCESS.2019.2900000.

[161] S. Dang, O. Amin, B. Shihada, M.-S. Alouini, What should 6G be?, Nat Electron. 3 (2020) 20–29. https://doi.org/10.1038/s41928-019-0355-6.

[162] S. Bloom, E. Korevaar, J. Schuster, H. Willebrand, Understanding the performance of free-space optics [Invited], J. Opt. Netw. 2 (2003) 178. https://doi.org/10.1364/JON.2.000178.

[163] A.J. Cox, A.J. DeWeerd, J. Linden, An experiment to measure Mie and Rayleigh total scattering cross sections, American Journal of Physics. 70 (2002) 620–625. https://doi.org/10.1119/1.1466815.

[164] J. Faist, F. Capasso, D.L. Sivco, C. Sirtori, A.L. Hutchinson, A.Y. Cho, Quantum Cascade Laser, Science. 264 (1994) 553–556. https://doi.org/10.1126/science.264.5158.553.

[165] P. Corrigan, R. Martini, E.A. Whittaker, C. Bethea, Quantum cascade lasers and the Kruse model in free space optical communication, Opt. Express. 17 (2009) 4355. https://doi.org/10.1364/OE.17.004355.

[166] L. Tombez, F. Cappelli, S. Schilt, G. Di Domenico, S. Bartalini, D. Hofstetter, Wavelength tuning and thermal dynamics of continuous-wave mid-infrared distributed feedback quantum cascade lasers, Appl. Phys. Lett. 103 (2013) 031111. https://doi.org/10.1063/1.4813753.

[167] R. Paiella, R. Martini, F. Capasso, C. Gmachl, H.Y. Hwang, D.L. Sivco, J.N. Baillargeon, A.Y. Cho, E.A. Whittaker, H.C. Liu, High-frequency modulation without the relaxation oscillation resonance in quantum cascade lasers, Appl. Phys. Lett. 79 (2001) 2526–2528. https://doi.org/10.1063/1.1411982.

[168] C. Liu, S. Zhai, J. Zhang, Y. Zhou, Z. Jia, F. Liu, Z. Wang, Free-space communication based on quantum cascade laser, J. Semicond. 36 (2015) 094009. https://doi.org/10.1088/1674-4926/36/9/094009.

[169] J.C. Ricklin, S.M. Hammel, F.D. Eaton, S.L. Lachinova, Atmospheric channel effects on free-space laser communication, J Optic Comm Rep. 3 (2006) 111–158. https://doi.org/10.1007/s10297-005-0056-y.

[170] B.-B. Zhao, X.-G. Wang, J. Zhang, C. Wang, Relative intensity noise of a mid-infrared quantum cascade laser: insensitivity to optical feedback, Opt. Express. 27 (2019) 26639. https://doi.org/10.1364/OE.27.026639.

[171] S. Borri, S. Bartalini, P.C. Pastor, I. Galli, G. Giusfredi, D. Mazzotti, M. Yamanishi, P. De Natale, Frequency-Noise Dynamics of Mid-Infrared Quantum Cascade Lasers, IEEE J. Quantum Electron. 47 (2011) 984–988. https://doi.org/10.1109/JQE.2011.2147760.

[172] H. Kaushal, Free space optical communication, Springer Berlin Heidelberg, New York, NY, 2016.

[173] L.S. Rothman, I.E. Gordon, Y. Babikov, A. Barbe, D. Chris Benner, P.F. Bernath, M. Birk, L. Bizzocchi, V. Boudon, L.R. Brown, A. Campargue, K. Chance, E.A. Cohen, L.H. Coudert, V.M. Devi, B.J. Drouin, A. Fayt, J.-M. Flaud, R.R. Gamache, J.J. Harrison, J.-M. Hartmann, C. Hill, J.T. Hodges, D. Jacquemart, A. Jolly, J. Lamouroux, R.J. Le Roy, G. Li, D.A. Long, O.M. Lyulin, C.J. Mackie, S.T. Massie, S. Mikhailenko, H.S.P. Müller, O.V. Naumenko, A.V. Nikitin, J. Orphal, V. Perevalov, A. Perrin, E.R. Polovtseva, C. Richard, M.A.H. Smith, E. Starikova, K. Sung, S. Tashkun, J. Tennyson, G.C. Toon, Vl.G. Tyuterev, G. Wagner, The HITRAN2012 molecular spectroscopic database, Journal of Quantitative Spectroscopy and Radiative Transfer. 130 (2013) 4–50. https://doi.org/10.1016/j.jqsrt.2013.07.002.

[174] F.X. Kneizys, U.S.A.F.G. Laboratory, Atmospheric Transmittance/radiance, Computer Code LOWTRAN 5, Optical Physics Division, Air Force Geophysics Laboratory, 1980. https://books.google.it/books?id=kJB3twEACAAJ.

[175] A. Goetzberger, W. Greube, Solar energy conversion with fluorescent collectors, Appl. Phys. 14 (1977) 123–139. https://doi.org/10.1007/BF00883080.

[176] G. Hamilton, H. Sanabria, Multiparameter fluorescence spectroscopy of single molecules, in: Spectroscopy and Dynamics of Single Molecules, Elsevier, 2019: pp. 269–333. https://doi.org/10.1016/B978-0-12-816463-1.00006-7.

[177] R. Mulyawan, H. Chun, A. Gomez, S. Rajbhandari, G. Faulkner, P.P. Manousiadis, D.A. Vithanage, G.A. Turnbull, I.D.W. Samuel, S. Collins, D. O'Brien, MIMO Visible Light Communications Using a Wide Field-of-View Fluorescent Concentrator, IEEE Photon. Technol. Lett. 29 (2017) 306–309. https://doi.org/10.1109/LPT.2016.2647717.

[178] W. Ali, P. Manousiadis, D.C. O'Brien, G. Turnbull, I. Samuel, S. Collins, A Gigabit VLC receiver that incorporates a fluorescent antenna and a SiPM, J. Lightwave Technol. (2021) 1–1. https://doi.org/10.1109/JLT.2021.3095398.

[179] M.S. Islim, S. Videv, M. Safari, E. Xie, J.J.D. McKendry, E. Gu, M.D. Dawson, H. Haas, The Impact of Solar Irradiance on Visible Light Communications, J. Lightwave Technol. 36 (2018) 2376–2386. https://doi.org/10.1109/JLT.2018.2813396.

[180] S. Sadeghi, H. Bahmani Jalali, R. Melikov, B. Ganesh Kumar, M. Mohammadi Aria, C.W. Ow-Yang, S. Nizamoglu, Stokes-Shift-Engineered Indium Phosphide Quantum Dots for Efficient Luminescent Solar Concentrators, ACS Appl. Mater. Interfaces. 10 (2018) 12975–12982. https://doi.org/10.1021/acsami.7b19144.

[181] F. Meinardi, H. McDaniel, F. Carulli, A. Colombo, K.A. Velizhanin, N.S. Makarov, R. Simonutti, V.I. Klimov, S. Brovelli, Highly efficient large-area colourless luminescent solar concentrators using heavy-metal-free colloidal quantum dots, Nature Nanotech. 10 (2015) 878–885. https://doi.org/10.1038/nnano.2015.178.

[182] F. Meinardi, A. Colombo, K.A. Velizhanin, R. Simonutti, M. Lorenzon, L. Beverina, R. Viswanatha, V.I. Klimov, S. Brovelli, Large-area luminescent solar concentrators based on 'Stokes-shift-engineered' nanocrystals in a mass-polymerized PMMA matrix, Nature Photon. 8 (2014) 392–399. https://doi.org/10.1038/nphoton.2014.54.

[183] G. Giusfredi, Physical optics: concepts, optical elements, and techniques, Springer, Cham, 2019.

[184] R. Gallager, Channels, modulation, and demodulation, Cambridge University Press, 2008.

[185] C.-Y. Li, H.-H. Lu, W.-S. Tsai, Z.-H. Wang, C.-W. Hung, C.-W. Su, Y.-F. Lu, A 5 m/25 Gbps Underwater Wireless Optical Communication System, IEEE Photonics J. 10 (2018) 1–9. https://doi.org/10.1109/JPHOT.2018.2842762.

[186] S.-W.H. Chen, Y.-M. Huang, Y.-H. Chang, Y. Lin, F.-J. Liou, Y.-C. Hsu, J. Song, J. Choi, C.-W. Chow, C.-C. Lin, R.-H. Horng, Z. Chen, J. Han, T. Wu, H.-C. Kuo, High-Bandwidth Green Semipolar (20–21) InGaN/GaN Micro Light-Emitting Diodes for Visible Light Communication, ACS Photonics. 7 (2020) 2228–2235. https://doi.org/10.1021/acsphotonics.0c00764.

[187] S. Huang, Q. Wu, Z. Jia, X. Jin, X. Fu, H. Huang, X. Zhang, J. Yao, J. Xu, Black Silicon Photodetector with Excellent Comprehensive Properties by Rapid Thermal Annealing and Hydrogenated Surface Passivation, Adv. Optical Mater. 8 (2020) 1901808. https://doi.org/10.1002/adom.201901808.

[188] C.H. Bennett, G. Brassard, Quantum cryptography: Public key distribution and coin tossing, Theoretical Computer Science. 560 (2014) 7–11. https://doi.org/10.1016/j.tcs.2014.05.025.

[189] I. Djordjevic, Physical-layer security and quantum key distribution, Springer, Cham, 2019.

[190] H.-H. Chou, W.-T. Huang, Wavelength Tunable Asymmetric B-OWC System Based on Self-Injection Locking for TDM-PONs, IEEE Photon. Technol. Lett. 33 (2021) 370–372. https://doi.org/10.1109/LPT.2021.3064650.

[191] X.-X. Xia, Z. Zhang, H.-B. Xie, X. Yuan, J. Lin, S.-K. Liao, Y. Liu, C.-Z. Peng, Q. Zhang, J.-W. Pan, LED-based fiber quantum key distribution: toward low-cost applications, Photon. Res. 7 (2019) 1169. https://doi.org/10.1364/PRJ.7.001169.

[192] H.-K. Lo, X. Ma, K. Chen, Decoy State Quantum Key Distribution, Phys. Rev. Lett. 94 (2005) 230504. https://doi.org/10.1103/PhysRevLett.94.230504.

[193] W.K. Wootters, W.H. Zurek, A single quantum cannot be cloned, Nature. 299 (1982) 802–803. https://doi.org/10.1038/299802a0.

List of abbreviations

5G: Fifth Generation

μ-LED: micro Light-Emitting Diode

AC: Alternate Current

ADR: Active Decode-and-Relay

AFoV: Angle of Field of View

AM: Amplitude Modulation

ASK: Amplitude Shift Keying

AWGN: Additive White Gaussian Noise

BER: Bit Error Rate

BPSK: Binary Phase Shift Keying

BW: Bandwidth

CAP: Contention Access Period

CDF: Cumulative Distribution Function

CFP: Contention Free Periods

CIS: $CuInS_2$

CKS: Color Shift Keying

CSMA: Carrier Sense Multiple Access

C-V2X: Cellular Vehicle-to-everything

DC: Direct Current

EPCF: effective photon-concentrating factor

EFoV: Effective Field of View

FFT: Fast Fourier Transform

FoV: Field of View

FSOC: Free-space optical communication

FSOCS: Free-space optical communication system

GPS: Global Positioning Systems

GSSK: Generalized Space Shift Keying

HAR: High Attenuation Regime

I2V/V2I: Infrastructure-to-Vehicle

I2V2V: infrastructure-to-Vehicle-to-Vehicle

IFFT: Inverse Fast Fourier Transform

InGaN: Indium-Gallium Nitride

IR: Infrared

IRC: Infrared Communication

IrDA: Infrared Data Association

ITS: Intelligent Transportation System

JEITA: Japan Electronics and Information Technology Industries Association

LAN: Local Area Network

LAR: Low Attenuation Regime

LED: Light-Emitting Diode

Li-Fi: Light Fidelity

LoS: Line of Sight

LSC: Luminescent Solar Concentrator

MAC: Medium Access Control

MGLR: Multiple Generalized Linear Regression

MIR: Mid Infrared

MOA: Maximal Optical Attenuation

NIR: Near Infrared

NLoS: Non-Line of Sight

NRZ: Non-Return-to-Zero

OA: Optical Attenuation

OCDMA: Optical Code Division Multiple Access

OFDM: Orthogonal Frequency Division Multiplexing

OFDMA: Orthogonal Frequency Division Multiple Access

OOC: Optical Orthogonal Code

OOK: On-Off Keying

OLED: Organic Light-Emitting Diode

OWC: Optical Wireless Communication

PAM: Pulse Amplitude Modulation

pc-LED: Phosphor Converted Light-Emitting Diode

PD: Photodiode

PDP: Power Delay Profile

PER: Packet Error Rate

PMF: Probability Mass Function

PMMA: Poly(Methyl Methacrylate)

PSR: Probability of Successful Relaying

PWM: Pulse Width Modulation

QAM: Quadrature Amplitude Modulation

QCL: Quantum Cascade Laser

RC: Resistor-Capacitor

rc-LED: Resonant Cavity Light-Emitting Diode

RF: Radio Frequency

RFC: Radio Frequency Communication

RLL: Run Length Limited

RMS: Root Mean Square

RMSE: Root Mean Square Error

RX: Receiver Stage

SAL: Statistically-Averaged Latency

SNR: Signal-to-Noise Ratio

TDM: Time Division Multiplexing

TF: Transfer Function

TFoV: Threshold angle of Field of View

TIA: Transimpedance Amplifier

TIR: Total Internal Reflection

TX: Transmitter Stage

UART: Universal Asynchronous Receiver-Transmitter

V2V: Vehicle-to-Vehicle

VLC: Visible Light Communication

VLP: Visible Light Positioning

YAG: Yttrium-Aluminum Garnet

List of figures

List of tables